

# Dynamics of disordered Rydberg lattice gases with constraints

**Maike Ostmann**

Thesis submitted to the University of Nottingham for the degree  
of Doctor of Philosophy



**University of  
Nottingham**

UK | CHINA | MALAYSIA

School of Physics and Astronomy

University of Nottingham

October 2019

# Abstract

Recent advances in the manipulation of cold atoms within a tailored optical tweezer array allow for the production of Rydberg quantum simulators. In this thesis we analyze disordered and constrained many-body dynamics by utilizing such a system. Using a one-dimensional quantum simulator platform, we employ single-site addressing to analyze three distinct protocols based on the Rydberg blockade mechanism. These protocols allow for the preparation of an antiferromagnetic GHZ state and a matrix product state, as well as the transport of a quantum state.

Furthermore, Rydberg simulators allow for the study of many-body dynamics under the so-called facilitation condition. Under this condition, the system can be represented by a single-particle hopping model on a synthetic lattice that features flat bands supporting localized states. We discuss the dynamics of this system in a ladder geometry focusing on the localization properties under the influence of disorder originating from an uncertainty of the atomic position in the optical tweezer.

Additionally, we explore an interacting spin chain with kinetic facilitation constraints and disorder in the many-particle sector. This system can be mapped onto an XX-chain with an unconventional non-local disordered interaction resulting in interesting non-ergodic behavior. We analyze the localization properties using theoretical tools from the domain of many-body localization and find signatures indicating a crossover between a localized and delocalized phase.

In the final part of the thesis, we study the constrained dynamics of an effectively open, two-dimensional system of hard-core bosons. The constraint enters the system through the Zeno effect due to strong, non-local pair loss instead of energy barriers, as in the previous considerations. This system, which can be studied in a Rydberg atom setup, exhibits intriguing localization phenomena, even in the absence of disorder.

# List of Publications

## Chapter 4:

*Non-adiabatic quantum state preparation and quantum state transport in chains of Rydberg atoms*; Maike Ostmann, Jiří Minář, Matteo Marcuzzi, Emanuele Levi and Igor Lesanovsky, New J. Phys. 19 123015 (2017) [1].

I modelled the effect of the three-different protocols in the presence of a non-perfect Rydberg blockade and disorder, as well as the limitations of the protocols due to spontaneous decay. Furthermore, I analyzed the numerical results and wrote the manuscript of the publication with help from Jiří Minář and Igor Lesanovsky.

## Chapter 5:

*Synthetic lattices, flat bands and localization in Rydberg quantum simulators*; Maike Ostmann, Matteo Marcuzzi, Jiří Minář and Igor Lesanovsky, Quantum Sci. Technol. 4, 02LT01 (2019) [2].

I carried out the transfer matrix approach and the detangling procedure, calculated the eigenvalues of the transfer matrix and the band structure of the Lieb ladder. I simulated the localization lengths of the system as a function of disorder, extracted the scaling exponent, and wrote up my results for this publication.

## Chapter 6:

*Localization in spin chains with facilitation constraints and disordered interactions*; Maike Ostmann, Matteo Marcuzzi, Juan P. Garrahan and Igor Lesanovsky, Phys. Rev. A 99, 060101(R) (2019) [3].

I was responsible for the numerical results presented in this paper. I modelled the behavior of the constrained spin chain in the presence of disorder, analyzed my findings and wrote the manuscript together with Matteo Marcuzzi and Igor Lesanovsky.

# Contents

<b>1</b>	<b>Introduction</b> <sup>1</sup>	<b>1</b>
<b>2</b>	<b>Interacting Rydberg gases</b>	<b>5</b>
2.1	Introduction to Rydberg quantum simulators . . . . .	5
2.2	From a real atom to a two-level system . . . . .	8
2.3	Interacting Rydberg atoms . . . . .	11
2.3.1	Dipole-dipole interaction . . . . .	11
2.3.2	Van der Waals interaction . . . . .	13
2.3.3	Blockade and facilitation effect . . . . .	15
2.4	Rydberg lattice <sup>2</sup> . . . . .	17
2.4.1	Rydberg gases in optical tweezer arrays . . . . .	19
<b>3</b>	<b>Localization phenomena</b>	<b>21</b>
3.1	Anderson localization . . . . .	21
3.1.1	Localization length . . . . .	24
3.2	Introduction to many-body localization . . . . .	28
3.2.1	Thermalization . . . . .	28
3.2.2	Many-body localization . . . . .	30
<b>4</b>	<b>Non-adiabatic quantum state preparation and quantum state transport in chains of Rydberg atoms</b>	<b>38</b>
4.1	Introduction . . . . .	38
4.2	Setup, state preparation and state transport protocols . . . . .	39
4.2.1	GHZ state preparation . . . . .	44
4.2.2	Dimer-MPS preparation . . . . .	46
4.2.3	Quantum state transport . . . . .	49
4.3	Imperfections . . . . .	49
4.3.1	Non-perfect Rydberg blockade . . . . .	50

---

<sup>1</sup>This chapter is adapted from References [1–3]

<sup>2</sup>Parts of this section are taken from Ref. [2] and its supplementary material.

4.3.2	Non-perfect blockade and position disorder . . . . .	54
4.3.3	Limitations due to spontaneous decay . . . . .	59
4.4	Outlook and Conclusion . . . . .	62
<b>5</b>	<b>Synthetic lattices, flat bands and localization in Rydberg quantum simulators</b>	<b>64</b>
5.1	Introduction . . . . .	64
5.2	Facilitation, Hilbert space structure and flat bands . . . . .	65
5.2.1	Hilbert space reduction and restricted Hamiltonian . . . . .	67
5.2.2	Hilbert space lattice structure . . . . .	72
5.3	Disordered Lieb ladder . . . . .	73
5.3.1	Transfer matrix approach . . . . .	75
5.3.2	Localization and scaling exponents . . . . .	78
5.4	Localized flat band state dynamics . . . . .	81
5.5	Outlook and Conclusion . . . . .	89
<b>6</b>	<b>Localization in spin chains with facilitation constraints and disordered interactions</b>	<b>90</b>
6.1	Introduction . . . . .	90
6.2	Setup . . . . .	91
6.3	Constrained spin chain . . . . .	92
6.3.1	Constrained Rydberg gas with disorder . . . . .	94
6.4	Numerical results . . . . .	95
6.4.1	Domain wall imbalance . . . . .	97
6.4.2	Half-chain entanglement entropy (HCEE) . . . . .	99
6.4.3	Level statistic ratio . . . . .	100
6.4.4	ETH plots . . . . .	101
6.5	Localization in the full model . . . . .	103
6.6	Outlook and Conclusion . . . . .	105
<b>7</b>	<b>Dynamics of hard-core bosons on a two-dimensional lattice with non-local loss</b>	<b>106</b>
7.1	Introduction . . . . .	106
7.2	System . . . . .	107
7.3	Classical loss dynamics . . . . .	109
7.3.1	Quantum evolution . . . . .	111
7.3.2	Quantum dynamics versus classical diffusion . . . . .	114
7.4	Ladder system . . . . .	116

7.4.1	Localized zero-energy states . . . . .	119
7.5	Conclusion and Outlook . . . . .	121
<b>8</b>	<b>Outlook and Conclusions</b>	<b>123</b>
<b>A</b>	<b>Interacting Rydberg gases</b>	<b>144</b>
A.1	Approximate Gaussian distribution of the atoms . . . . .	144
A.2	Distribution of the distances and interactions for a single chain . .	146
A.2.1	From the distribution of the atomic positions to the distri- bution of the distances . . . . .	147
A.2.2	Marginal distribution for a single pair of atoms . . . . .	149
<b>B</b>	<b>Non-Adiabatic quantum state preparation and quantum state transport</b>	<b>152</b>
B.1	Toffoli gate . . . . .	152
B.2	Dimer-MPS . . . . .	153
B.2.1	Derivation of the recurrence formulae . . . . .	153
<b>C</b>	<b>Synthetic lattices, flat bands and localization in Rydberg quan- tum simulators</b>	<b>158</b>
C.1	Bound on the number of flat bands . . . . .	158
C.1.1	Example: the triangular lattice . . . . .	163
C.1.2	Example: the honeycomb lattice . . . . .	165

# List of Figures

2.1	<b>Rydberg atom, two-level scheme.</b> (a) Model of an alkali atom in a Rydberg state. The valence electron (dark blue) is in a highly excited s-state ( $n \gg 1, l = 0$ ). The nucleus is shielded by the non-excited electrons (blue shaded region) leading to a positive charge equal to a hydrogen nucleus which allows a description of the Rydberg atom as hydrogen with a small correction accounting for the finite size of the nucleus. (b) Two-level atom. A laser couples the ground state $ \downarrow\rangle$ with a highly excited Rydberg state $ \uparrow\rangle$ . . . . .	6
2.2	<b>Interacting dipoles.</b> Two highly excited Rydberg atoms, which are separated by $R_0$ , can be described as two-interacting dipoles. The positively charged atomic core of atom $i$ and the negatively charged electron $e_i^-$ are separated by $\mathbf{r}_{e_i}$ . . . . .	12

2.3	<p><b>Rydberg blockade and facilitation.</b> (a) Illustrates the Rydberg blockade mechanism for the example of two atoms trapped in optical tweezers. When the first atom (red) is excited to a Rydberg state, the excited state of the second atom (blue) gets shifted by the van der Waals interaction <math>-V_0</math>. In the regime of <math> V_0  \gg \Omega</math>, a laser of Rabi frequency <math>\Omega</math> and zero detuning <math>\Delta = 0</math> cannot excite the second atom (blue) to the shifted Rydberg state. (b) Illustrates the facilitation (anti-blockade) effect. When the detuning of the laser matches the facilitation condition <math>\Delta = -V_0</math>, the probability of exciting an atom to a Rydberg state is strongly enhanced by an already excited neighbor. (c) Depicts the energies of the pair state as a function of the interatomic separation. When the interaction energy is strong enough to shift the doubly excited state out of resonance, the transition is blockaded. The blue spheres represent ground state atoms <math> 0\rangle</math>, while the red spheres are atoms in the excited Rydberg state <math> 1\rangle</math> blockaded atoms. The doubly excited state shifts by <math>V(R_i) = C_6/R_i^6</math>. Adapted from Ref. [4]. . . . .</p>	16
2.4	<p><b>Rydberg atoms trapped in chain of optical tweezers.</b> One-dimensional lattice of three optical tweezers each loaded with a single atom. The optical traps are arranged along the <math>z</math> direction and are separated by <math>R_0</math>. The ground state <math> \downarrow\rangle</math> is resonantly coupled to the Rydberg state (of a single atom) <math> \uparrow\rangle</math> via a laser of Rabi frequency <math>\Omega</math>. <math>V_0</math> indicates the nearest-neighbor interaction energy between the atoms. The second atom is in a Rydberg state that shifts the first and third atom out of resonance (Rydberg blockade). The position of the atoms in the traps follows a Gaussian distribution of width <math>\sigma</math>. . . . .</p>	18
3.1	<p><b>Mobility edge.</b> Density of states (DOS) as a function of energy <math>E</math> for a system featuring a mobility edge <math>E_c</math>. The mobility edge separates localized (purple shaded region) from extended states energetically. . . . .</p>	23

3.2	<b>Comparison of the density profile of an ergodic and an MBL system.</b> An interacting quantum system initially prepared in a staggered configuration. In a disorder-free system (left), the system thermalizes under unitary time evolution, and each lattice site is equally populated leading to a uniform density. On the other hand, when the atoms are located in a disordered potential $V(x)$ (right), the system evolves into a many-body localized state retaining some memory of the initial state. Adapted from Ref. [5].	32
3.3	<b>Entanglement entropy and distribution of energy levels for ergodic and localized systems.</b> (a) Entanglement entropy (EE) as a function of the logarithm of the time. An ergodic system shows a ballistic growth of the EE (red). The EE in an MBL system is strongly suppressed compared to the thermalizing case; the EE growth logarithmically (green). In the case of Anderson localization, the EE saturates and does not spread through the system (blue) even for $t \rightarrow \infty$ . (b) The spacing between adjacent energy levels $s = \epsilon_\alpha - \epsilon_{\alpha+1}$ , in a MBL system follows a Poisson distribution (dark red), while the spacing in an ergodic system follows the Wigner distribution (black).	35
4.1	<b>Setup, level schemes for two and three level systems, and GHZ protocol.</b> (a): Setup for $N = 2$ atoms. The optical traps are arranged along the $x_3$ direction and are separated by $R_0$ . The atomic positions are spread with uncertainty $\sigma_i$ around their equilibrium values [6]. (b): Level scheme for an effective two level system, where the state $ 0\rangle$ is coupled to the Rydberg state $ 1\rangle$ by a laser with Rabi frequency $\Omega$ . (c): Energy levels of an effective three-level system as it is assumed in the GHZ protocol, where $\tilde{\Omega}$ couples the Rydberg state $ 1\rangle$ to another hyperfine state $ \tilde{1}\rangle$ . (d) GHZ protocol in the three-level scheme. The blue arrows represent laser pulses coupling the $ 0\rangle \rightarrow  1\rangle$ state, while the red arrows represent laser pulses driving the $ 1\rangle \rightarrow  \tilde{1}\rangle$ . This figure is adapted from Ref. [1].	41

4.2	<b>Representation of the MPS preparation and state transport protocol.</b> (a): Representation of the dimer-MPS for a chain of $N = 6$ atoms. This state is a superposition of all possible configurations without neighboring Rydberg excitations. The parameter $z$ is weighting the number of excitations in the particular component of the superposition state. (b): Circuit for the transport of a single qubit state $ \psi\rangle$ from the first to the $N$ th qubit in the chain. All qubits except the first one, are prepared in the ground state. The CNOT gate as well as the Toffoli gate correspond to a $\pi$ -pulse with Rabi frequency $\Omega$ applied to the particular atom. In the post processing, the $\hat{G}^N$ -gate is applied to the state on the $N$ th qubit, in order to obtain the correct state $ \psi\rangle$ . Taken from Ref. [1]. . . . .	47
4.3	<b>Fidelity of the GHZ state preparation protocol for a two-level, and three-level atom.</b> Fidelity of the GHZ state preparation protocol for a two-level description of the atoms (a), as well as the three-level scheme (b) as a function of $V_0/\Omega$ . In the three-level implementation of the protocol, atoms are excited to the Rydberg state to effectuate the blockade mechanism and are subsequently transferred to a stable hyperfine state, see text for details. The fidelity is given for chains of length $N = 2, 4, 6, 8$ , respectively. Taken from Ref. [1]. . . . .	52
4.4	<b>Fidelity of the dimer-MPS preparation protocol.</b> Fidelity of the dimer-MPS preparation protocol for $N = 2$ up to $N = 7$ atoms as a function of $V_0/\Omega$ and for $z=0.1, 0.5, 1, 0$ (a-d). See text for details (Taken from Ref. [1]). . . . .	53
4.5	<b>Fidelity of the transport process for different initial states.</b> (a): Fidelity of a coherent transport process for $N = 4, 5, 6$ as a function of $V_0/\Omega$ . The transferred state is $ \psi_1\rangle = 1/\sqrt{2}( 0\rangle +  1\rangle)$ . (b): Comparison of the fidelity of the transport process for different initial states $ \psi_1\rangle$ for $N = 4$ . The parameter $\alpha$ ( $\beta = \sqrt{1 - \alpha^2}$ ) of the state $ \psi_1\rangle = \alpha 0\rangle + \beta 1\rangle$ is varied (Taken from Ref. [1]). . . . .	55
4.6	<b>Fidelity of the GHZ protocol including the effect of non-perfect blockade and disorder.</b> Fidelity of the GHZ state preparation protocol including the effect of non-perfect blockade and disorder for $N = 4$ (a) and $N = 6$ (b) as a function of $V_0/\Omega$ with no (solid red), isotropic (dotted blue) and anisotropic (dashed green) disorder (Taken from Ref. [1]). . . . .	57

4.7	<b>Fidelity of the dimer-MPS protocol including a non-perfect Rydberg blockade and disorder.</b> Fidelity of the dimer-MPS protocol as a function of $V_0/\Omega$ including the effect of a non-perfect Rydberg blockade and disorder for $N = 4$ (a,c), $N = 7$ (b,d), and $z = 1$ (a,b) and $z = 10$ (c,d). The solid red, dotted blue and dashed green lines correspond to no, isotropic and anisotropic disorder, respectively. Here, $F$ is obtained for 100 realizations of the disorder. (Taken from Ref. [1].) . . . . .	57
4.8	<b>Fidelity of the state transport protocol including a non-perfect Rydberg blockade and disorder.</b> Fidelity of the state transport protocol as a function of $V_0/\Omega$ for the initial state $ \psi_1\rangle = 1/\sqrt{2}( 0\rangle +  1\rangle)$ and for $N = 4$ (a), $N = 5$ (b), $N = 6$ (c), and $N = 7$ (d). The solid red, dotted blue and dashed green lines correspond to no, isotropic and anisotropic disorder, respectively. (Taken from Ref. [1].) . . . . .	58
4.9	<b>Fidelity of the GHZ protocol as a function of the system size.</b> Fidelity of the GHZ protocol as a function of the number of atoms in the chain $N$ for $V_0/\Omega = 7.2$ (a) and $V_0/\Omega = 15.5$ (b). The red crosses, blue squares and green diamonds correspond to no, isotropic and anisotropic disorder, respectively. The solid lines represent an exponential function fitted to the data points, see text for details. Data obtained by averaging over 100 realizations of the disorder. (Taken from Ref. [1].) . . . . .	60
4.10	<b>Fidelity of the dimer-MPS protocol as a function as a function of the system size.</b> Fidelity of the dimer-MPS protocol as a function of the number of atoms in the chain $N$ for $V_0/\Omega = 17.1$ for even (e) and $V_0/\Omega = 15.6$ for odd (o) number of atoms in the chain and $z = 10$ in a logarithmic scale. The red crosses, blue squares and green diamonds correspond to no, isotropic and anisotropic disorder, respectively. The solid lines represent an exponential function fitted to the data points, see text for details. Data obtained by averaging over 100 realizations of the disorder. (Taken from Ref. [1].) . . . . .	60

4.11	<b>Fidelity of the state transport protocol as a function of the number of atoms.</b> Fidelity of the state transport protocol as a function of the number of atoms in the chain $N$ for $V_0/\Omega = 6.9$ (a) and $V_0/\Omega = 15.5$ (b) in a logarithmic scale. The red crosses, blue squares and green diamonds correspond to no, isotropic and anisotropic disorder, respectively. The solid lines represent an exponential function fitted to the data points, see text for details. Data obtained by averaging over 1000 realizations of the disorder. (Taken from Ref. [1].) . . . . .	62
5.1	<b>Splitting of the Hilbert space.</b> Under the facilitation condition the Hilbert space splits into subspaces separated by energies much larger than the Rabi frequency (adapted from Ref. [6]). . . . .	66
5.2	<b>Real space lattice, synthetic Lieb lattice and the respective band structure.</b> Left column: basic local site configuration within a square, triangular, and honeycomb lattices. The gray dots depict the positions of the optical tweezers, while the lines provide a guide to the eye. $R_0$ and $R_1$ represent nearest and next-nearest neighbor distances, respectively. Middle column: respective "synthetic lattices" in the Hilbert space under facilitation conditions. The blue dots represent one-excitation states while the red ones are pair states. Right column: Cut through the Brillouin zone for each lattice geometries at $k_y = 0$ . Each lattice features (at least) a flat band. The momentum scales for the three lattices (from top to bottom) are $\eta = (1, \frac{4}{3}, \frac{4}{3})$ . This figure is taken from Ref. [2]. . . . .	68
5.3	<b>Definition of the set of <math>\mathcal{F}_k</math> and <math>\mathcal{S}_k</math></b> We define the set $\mathcal{F}_k$ (violet) which consists of all nearest-neighbor sites of site $k$ (dark red). The set $\mathcal{S}_k$ (green) are all sites within a distance of $2R_0$ from $k$ , which are not site $k$ itself, or site in set $\mathcal{F}_k$ . . . . .	69

- 5.4 **Lieb ladder, “detangled” Lieb ladder, eigenvalues of the transfer matrix and band structure.** (a) Lieb ladder; blue (red) dots correspond to one-excitation (pair) states. We denote by  $A_n, B_n, C_n, D_n, E_n$  the five sites in the  $n$ -th unit cell (shaded in gray). (b) A change of basis – the so-called “detangling”, introducing the new linear combinations  $X_n^\pm = (A_n \pm B_n)/\sqrt{2}$  and  $Y_n^\pm = (C_n \pm D_n)/\sqrt{2}$  [7,8] maps the Lieb ladder onto two decoupled chains; a stub lattice (orange) and a chain (green). The  $\sqrt{2}$  factor denotes that the hopping amplitude on the vertical link of each unit cell is amplified by that same amount. (c) Eigenvalues of the transfer matrix in log-linear scale. The dotted lines corresponds to the energies  $\epsilon = \{1, \sqrt{2}, 1.8, 2, \sqrt{6}\}$  at which the scaling of the localization lengths is investigated in Fig. 5.5. (d) Band structure of the Lieb ladder. The bands corresponding to the stub lattice are given in orange and bands of the ordinary 1D chain are shown in green. This figure can be found in Ref. [2] . . . . . 74
- 5.5 **Localization lengths.** (a) Color map of the localization lengths  $\xi_1, \xi_2$  as a function of the energy  $\epsilon$  and the disorder strength  $s = \sigma/R_0$ . (b) Localization lengths  $\xi_1$  (thick lines),  $\xi_2$  (thin lines) in log-log scale for five different values of the energy, reported above the panel and highlighted in (a) via horizontal, solid lines. For small disorder all curves are approximately linear, making it possible to assign power law exponents  $\nu$  characterizing the small-disorder behavior  $\xi_i \sim s^\nu$ : grouping them by energy  $\epsilon$ , they read  $\nu(\epsilon = 1) \approx \{0, 2.2\}$ ,  $\nu(\epsilon = \sqrt{2}) \approx \{0.7, 2.2\}$ ,  $\nu(\epsilon = 1.8) \approx \{2.0, 1.9\}$ ,  $\nu(\epsilon = 2) \approx \{1.1, 1.1\}$ ,  $\nu(\epsilon = \sqrt{6}) \approx \{0, 0.6\}$ . Here we have chosen a dipole-dipole interaction ( $\alpha = 3$ ) with an interaction strength of  $V(R_0) = 300\Omega$ . It is apparent that the lowermost curves bend down in the rightmost part of panel (b). For the estimation of the slope, we have considered the data between  $s = 5 \times 10^{-6}$  and  $s = 5 \times 10^{-5}$ . This Figure is adapted from Ref. [2]. 79

- 5.6 **Localization length  $\xi_2$  for zero energy.** Localization lengths (a)  $\xi_1$  and (b)  $\xi_2$  for zero energy  $\epsilon = 0$  and experimental disorder acting on the pair states of the lattice (red sites in Fig. 5.4). We used a dipole-dipole interaction ( $\alpha = 3$ ) with an interaction strength of  $V(R_0) = 300\Omega$ . (c) Localization length  $\xi_2$  with flat disorder drawn from the interval  $[-W/2, W/2]$  acting on the pair states (red sites in Fig. 5.4). (d)  $\xi_2$  with flat disorder forced to act on all lattice states (all sites in Fig. 5.4). In all panels, the colours correspond to the system sizes listed in (b). . . . . 82
- 5.7 **Time evolution of the localized state.** (a) Schematic representation of the spin configuration corresponding to the initial state  $|\psi_{\text{loc}}\rangle$  localized at rungs  $i, i + 1$  of the ladder. (b) The averaged probability of excitations  $p_i$  given by the time evolution of the localized state. Initially the state has support in the middle (rungs 10 and 11) of the ladder of length 20 for  $s = 0.0014$ . The left (right) panel shows the time evolution in the upper (lower) leg of the ladder. The horizontal red lines denote three different times for which the respective value of  $\Delta x$  is shown as a black circle in (c). (c) Standard deviation of the excitation positions  $\Delta x$  as a function of the disorder strength  $s$  for three different times. Blue (red) solid lines, which are virtually indistinguishable correspond to upper (lower) leg of the ladder respectively. Results obtained for 100 disorder realizations and  $V(R_0) = 200\Omega$ . This plot can be found in Ref. [2]. . . . . 87
- 5.8 **Spin dynamics in the effective and full model.** (a) Width  $\Delta x$ , Eq. (5.49), of the excitation positions in the  $s - \Omega/V(R_0)$  plane. Here,  $\Delta x$  was obtained by evolving the initial state  $|\psi_{\text{loc}}\rangle$  located at rungs 10 and 11 in the middle of the ladder of length  $L = 20$  by the effective Hamiltonian  $H_{\text{eff}}$ . The two red solid lines correspond to a cut for fixed values of  $\Omega/V(R_0)$ ,  $\Omega/V(R_0) = 1/20$  (upper line) and  $\Omega/V(R_0) = 1/200$  (lower line). (b) Comparison between the evolution of  $|\psi_{\text{loc}}\rangle$  generated by  $H$ , Eq. (5.1), dashed line and  $H_{\text{eff}}$ , solid line, in a ladder of  $L = 4$  and for  $\Omega/V(R_0) = 1/20$ . (c) Same as (b) with  $\Omega/V(R_0) = 1/200$ . Here we have fixed the time so that  $\Omega t/2\pi = 4.3$  irrespective  $\Omega$  and averaged over 100 disorder realizations. This Figure is taken from the supplementary material in Ref. [2]. . . . . 88

6.1	<b>Setup of the one-dimensional Rydberg lattice with kinetic facilitation constraints.</b>	Setup and basic principle. In a one-dimensional lattice atoms in their electronic ground state, $ \downarrow\rangle$ , are coupled to a highly-excited Rydberg state, $ \uparrow\rangle$ , with a laser of Rabi frequency $\Omega$ and detuning $\Delta$ . The atomic positions in the local traps are distributed according to a Gaussian distribution of width $\sigma$ . For small values of $\sigma$ excitations, initially prepared at time $t = 0$ in a state $ \uparrow\uparrow\downarrow\downarrow\uparrow\uparrow\downarrow\downarrow\rangle$ , spread throughout the chain. With increasing value of $\sigma$ localization sets in and the systems remains localized in a state close to the initial configuration. (Taken from Ref. [3]). . . . .	91
6.2	<b>Domain wall imbalance and average of the local density of domain walls.</b>	(a) Domain wall imbalance in the long-time limit ( $\Omega t = 10^5$ ) for a chain of $N = 8$ (brown, solid line), $N = 10$ (blue, long dashes) and $N = 12$ (red, short dashes) atoms. The shaded area is plus/minus the standard deviation for 100 disorder realizations at $t = 10^5$ for a chain of $N = 8$ atoms. (b) Imbalance as a function of time (up to $\Omega t = 10^3$ ) for seven values of the trap width $\sigma$ for $N = 8$ atoms; in increasing order: $\sigma = 0.0006$ (purple, star), 0.0031 (dark blue, pentagon), 0.0071 (light blue, rhombus), 0.0306 (green, square), 0.0506 (dark green, circle), 0.08 (orange, triangle), 0.135 (red, cross). (c) Average local density of domain walls $\langle \hat{n}_j^{(DW)} \rangle$ in the initial state and at long times ( $\Omega t = 10^5$ ) for all values of the disorder displayed on the left and $N = 10$ . A crossover from a quasi-uniform and delocalized average to configurations more and more similar to the initial state is observed as $\sigma$ is increased. (This figure can be found in Ref. [3]). . . . .	96

6.3	<b>Half-chain entanglement entropy (HCEE), and level statistic ratio.</b>	(a,b) HCEE as a function of time in a chain for various $N = 8, 10, 12$ , and $\sigma$ . The color code and symbols correspond to those in Fig. 6.2(a), i.e. $\sigma = 0.0006$ (purple) [only $N = 10, 12$ shown], $0.0071$ (light blue), $0.0306$ (green) and $0.135$ (red) [ $N = 10$ and $N = 12$ overlap] . (b) The $\sigma = 0.08$ (orange) case, is displayed on its own to highlight the emergence of a logarithmic growth of the HCEE as $N$ is increased (the black curve, indicating logarithmic behavior, is a guide to the eye). (c) LSR of the effective disordered Hamiltonian in the restricted Hilbert space containing $N_{cl} = 2$ clusters as a function of $\sigma$ for different $N$ . The LSR is compatible with a Poissonian distribution of level spacings at very low and large disorder. In the former case, the system is close to being integrable, whereas in the latter this is due to the effects of the disorder and the phase is MBL-like. In between there is a crossover regime in which the LSR shows GOE statistics, suggesting the presence of an ergodic window at intermediate values of $\sigma \approx 10^{-2}$ . Shaded areas: plus/minus the standard deviation for 100 disorder realizations for $N = 8$ atoms. (This figure is adapted from Ref. [3]). . . . .	98
6.4	<b>Finite size effects of the level statistic ratio and the imbalance.</b>	(a): Imbalance of an equal superposition state containing $N_{cl} = 2$ clusters at $\Omega t = 0$ as a function of system size $N$ . (b): Level statistic ratio for zero disorder in the restricted Hilbert space containing $N_{cl} = 2$ clusters as a function of system size $N$ . The dashed line gives the LSR of a Poissonian distribution of the level spacing. . . . .	99
6.5	<b>ETH plot of the magnetization.</b>	ETH plot of the magnetization $\langle M_z \rangle$ for a chain of $N = 12$ atoms for nine different trap width, where $ E_\alpha\rangle$ is the eigenstate of the Hamiltonian with eigenenergies $E_\alpha$ . We compare the magnetization for the full Hilbert space (gray) and the restricted Hilbert space containing $N_{cl} = 2$ clusters (colored) for nine different disorder strengths . (b-h) The colors and the symbols correspond to the trap width in Fig. 6.2. (a,i) Magnetization for zero disorder and the maximal disorder $\sigma = 1$ . . .	102

6.6	<b>Half-chain entanglement entropy and imbalance under the full dynamics.</b> Half-chain entanglement entropy as a function of time and trap width $\sigma$ for a chain of $N = 8$ atoms. The full dynamics is considered (6.1) for van der Waals interaction $\alpha = 6.0$ and for a long ranged interaction with exponent, $\alpha = 1.0$ (b). The color code and the symbols correspond to the ones in Fig. 6.2. (c) Imbalance $\langle I(\Omega t = 10^5) \rangle$ of the full Hamiltonian for $\alpha = 6, 1$ . . .	104
7.1	<b>Dynamics and constraint of the lattice bosons.</b> (a) Dynamics and constraint of the lattice bosons which leads to the non-local loss when two atoms are separated by the critical distance $R_c$ . (Adapted from [9]). (b) Representation of the constrained hopping model on the example of a $N = 6 \times 6$ lattice where the initial state consists of four occupied sites (black circles) forming a square (left) and a $Z$ (right). The white and red circles show unoccupied and forbidden sites, respectively, for a critical distance $R_c = 2$ . The square configuration is surrounded by forbidden sites and is therefore immobile for all times, while the $Z$ -configuration has the ability to leave its initial configuration (in two directions).	108
7.2	<b>Kinetic Monte Carlo method and final boson density.</b> (a) Illustration of the kinetic Monte Carlo (MC) method. The system is initially prepared in a Mott insulator state. In every jump two boson at the critical distance $R_c$ are removed from the system. In our model, any jump happens with transfer rate $\Gamma = 1$ but the choice of jump is randomly selected. This process is repeated until the Zeno subspace is reached; i.e. there no longer exists particles separated by the critical distance $R_c$ . (b) Final boson density $\langle p(t_f) \rangle$ as a function of $N_x$ (with $N = N_x \times N_x$ ) for various constraints $R_c$ . Initially, the system is prepared in a Mott insulator state and atoms located at the critical distance $R_c$ are removed until the Zeno subspace is reached. The density is averaged over 20 MC runs. . . . .	110

7.3	<b>Comparison of the constrained and free dynamics for a <math>Z</math>-configuration.</b> Upper panel: Autocorrelator as a function of time $c(t)$ for a constrained system (red) with a critical distance of $R_c = 2$ and a system without any constraints (blue) as a function of time. We are considering $N = 4 \times 4$ lattice sites with $N_p = 4$ particles initially prepared in the $Z$ -configuration shown in the inset. Lower panel: Evolution of the populations $\langle \hat{n}_i \rangle$ for a constrained (red) and an unconstrained system (blue) on a $N = 5 \times 5$ lattice with $N_p = 4$ particles initially prepared in a $Z$ -configuration. We are using OBC for both the simulation of the autocorrelation function and the evolution of the population. . . . .	112
7.4	<b>Scan of the autocorrelation function for constrained and free quantum dynamics, and constrained classical diffusion.</b> Scan of the two-time correlation function $c(t)$ over all possible initial product states for a $N = 4 \times 4$ lattice sites with $N_p = 2$ particles and open boundary conditions. We are considering a system under (a) quantum dynamics with constraint $R_c = 2$ , (b) quantum dynamics without constrained and (c) classical diffusion with constraint. We indicate three of the localized states in the quantum dynamics. . . . .	115
7.5	<b>Scan of the autocorrelation function for a system with high boson density.</b> Scan of the two-time correlation function $c(t)$ over all possible product states of a constrained system ( $R_c = 2$ ) of $N = 4 \times 4$ lattice sites with $N_p = 4$ particles (OBC) under (a) quantum dynamics, and (b) under classical diffusion. The trivially localized states (black bands) coincide in the quantum and the classical case. . . . .	117

7.6	<b>Constrained model on a ladder.</b> (a) Quasi one-dimensional lattice expanding in the $x$ -direction and restricted in the $y$ -direction to two rows (ladder). We are considering two particles (black) in the lattice, the red spheres indicate the lattice sites that are forbidden for this specific configuration with $R_c = 2$ . (b) Graph representation of the constrained model for a $N = 4 \times 2$ ladder with PBC ( $N_p = 2$ ). We show all allowed product state configurations and their connections under the action of the constrained Hamiltonian. (c) Ratio of the number of zero-energy eigenstates (ZE) and the size of the reduced Hilbert space (HS) as a function of system size $N = N_x \times 2$ for $R_c = 2$ for open (blue) and periodic (orange) boundary conditions. . . . .	118
7.7	<b>Graph representation of the Hilbert space and localized zero-energy eigenstates.</b> Graph of the adjacency matrix for a $N = 4 \times 2$ (a) and $N = 6 \times 2$ (b) ladder with two particles ( $R_c = 2$ , PBC). We show the configurations of the $N_x$ transitionally invariant zero-energy eigenstates which can be constructed in any $N_x \times 2$ ladder with PBC. . . . .	120
7.8	<b>Scan of the autocorrelation function for a ladder.</b> Scan of the two-time correlation function $c(t)$ over all possible product states of a constrained system ( $R_c = 2$ ) of $N = 10 \times 2$ lattice sites with $N_p = 2$ particles evolving under (a) quantum dynamics, and (b) under classical diffusion (PBC). . . . .	122
A.1	<b>Distribution of energy shifts.</b> Probability distribution function for the dimensionless energy shift (A.32) for $s = 0.3$ (blue) and $s = 0.1$ (red). . . . .	149

# List of Tables

2.1	<b>Properties of Rydberg atoms.</b> Selected properties of Rydberg atoms and their scaling with the principal quantum number $n$ . This table is taken from reference [10]. . . . .	7
3.1	<b>Properties of the thermal, Anderson and MBL phase.</b> Comparison of the properties of the ETH, the Anderson localized and the MBL-phase (taken from Ref. [11]). Note, the third row compares the properties of the entanglement entropy (EE) as a function of system size. . . . .	33
4.1	<b>Protocol for the GHZ and MPS state preparation, and the state teleportation.</b> Pulse sequence for the preparation of a GHZ state (left column), the dimer-MPS state (middle column) and the state transport (right column) in a chain of $N$ Rydberg atoms. In the case of the GHZ state, the Rydberg atoms are described as an effective three-level system. However, the GHZ protocol can also be adapted to a two-level description of the atoms by neglecting step (iv). For the dimer-MPS as well as the state transport protocol, each atom is approximated as a two-level system. $ \Psi_{\text{in}}\rangle$ is the initial state for the particular protocol. Taken from Ref. [1]. . . . .	45
4.2	<b>Fit of the system size dependence for the GHZ, dimer-MPS state preparation and state transport protocols.</b> The coefficients of the function $f(N) = a \exp(-b(N - 2))$ fitted to the data points in Figs. 4.9, 4.10 and 4.11 for the GHZ, dimer-MPS state preparation and state transport protocols, respectively. The abbreviations correspond to “no dis” = no disorder, “iso” = isotropic disorder, “aniso” = anisotropic disorder parameterized according to the values reported in the main text. (Taken from Ref. [1].) . . . . .	61

5.1	<b>Scaling exponents.</b> Scaling exponents $\nu$ for different energies $\epsilon$ obtained from fitting the behaviour of the localization lengths $\xi$ . $\xi_i \sim s^{\nu_i}$ for the first and $\xi_i \sim W^{\nu_i}$ for the second to fourth columns, see text for details. Experimental disorder refers to disorder stemming from the Gaussian position distribution of the atoms which acts only on the pair states in the system. The range of $s$ and $W$ in the first row denote the interval of the disorder parameter over which the fit was performed. Values in the first column are obtained for $\alpha = 3$ and $n = 10^6$ , where $n$ is the number of random matrix realizations entering (5.37). In the third and fourth column we used $n = 10^6$ and $10^5$ , respectively (see Ref. [2]). . . . .	80
B.1	Truth table of the Toffoli gate . . . . .	153

# Chapter 1

## Introduction <sup>1</sup>

Over the past few decades, technological advances have allowed for increasingly precise manipulation of cold atomic gases rendering them invaluable in the quest towards achieving quantum information processing (QIP) and exceedingly viable as a versatile quantum simulation platform [12, 13]. Several paradigmatic many-body models have been studied experimentally using cold atomic gases. One dimensional models include Luttinger liquids [14] and Tonks-Girardeau gases [15] which model the interaction of identical fermions and bosons, respectively. Other examples are the Bose-Hubbard model [16, 16] which describes the behavior of spinless lattice bosons, and the Fermi-Hubbard model [17] which approximates the behavior of fermions in a solid. The experimental investigation of these models has allowed for the direct observation of phenomena such as quantum revivals [18], Lieb-Robinson bounds [19], and topological phase transitions [20]. Though there are many contenders for the building block of a quantum simulator, ensembles of Rydberg atoms [10, 21, 22] have proved particularly suitable due to their strong interactions, which give rise to an intricate phenomenology, including devil's staircases [23–25], aggregate formation and melting [26, 27], Rydberg crystals [28], optical bistability [29, 30], phase transitions [31–33] and protected zero modes [34].

Experimental progress in manipulating Rydberg atoms now allows the simulation of, for example, quantum Ising spin system [35], quantum information processing [21, 36] and the implementation of quantum gates [37, 38] utilizing the so-called *Rydberg blockade* effect which prevents the simultaneous excitation of two neighboring atoms to a Rydberg state.

The subject matter of this thesis centres around quantum simulators based on Rydberg atoms trapped in optical tweezer arrays. Current technology allows

---

<sup>1</sup>This chapter is adapted from References [1–3]

for the creation of various lattice geometries [39] that have been recently used to deterministically obtain an optical lattice with close-to-unit filling [40,41]. Importantly, techniques allowing single-site addressing in such arrays have been developed [42–45] opening new possibilities for *non-adiabatic* quantum state engineering. This might be an approach to overcome limitations imposed by the required timescales by adiabatic procedures, where detrimental relaxation effects may become important [46]. First steps in this direction were taken in Ref. [47] which considered optimal control techniques for creation of ferromagnetic Greenberger-Horne-Zeilinger (GHZ), crystalline or Fock superposition quantum states in Rydberg atoms. Several among these instances employ the so-called *facilitation* (or *anti-blockade*) mechanism (see e.g., Refs. [48–53]), meaning that Rydberg states can only be excited next to an already existing excitation, actuating a form of quantum transport.

In contrast to the Rydberg blockade, facilitation depends strongly on the interatomic separation (see Chapter 2.3.3). In optical tweezer arrays, where there is an uncertainty in the atomic position (a type of disorder), facilitation and therefore transport are hindered. In general, disorder can heavily affect quantum transport, as it can cause destructive interference effects resulting in the localization of eigenstates. This disorder induced localization of the wavefunction, known as *Anderson localization* [54], appears, for example, in the case of metals with impurities where the conductivity vanishes. Anderson localization was initially discussed for non-interacting quantum particles in disordered potential landscapes.

Localization phenomena are not limited to disordered systems. In lattices with specific geometries like in a *Lieb lattice*, localization occurs via macroscopically degenerate flat bands formed by localized zero-energy eigenstates. Interestingly, when disorder is present in such a Lieb lattice, it can destroy the localized flat-band states which is counter intuitive. Understanding the competition between localization due to flat bands and Anderson localization is an interesting problem which we will investigate in this thesis (see Chapter 5).

Since the introduction of Anderson localization, the focus has increasingly shifted to the many-body domain, partially fueled by the development of refined techniques to experimentally engineer and probe many-body systems with cold atoms [12]. Evidence has been found that in isolated, one-dimensional, interacting systems the presence of disorder induces a transition from a thermal to a many-body localized phase where ergodicity breaks down [55–72]. Experiments have confirmed theoretical predictions [72–75], and signatures of many-body localiza-

tion (MBL) have also been identified in two-dimensional systems [76]. A second mechanism for interesting quantum relaxation is via constraints in the dynamics. Quantum systems with kinetic constraints can display very slow and complex relaxation [77–79] and can be used to probe the possibility of MBL-like physics in the absence of disorder [80–90]. Constraints can further impose restrictions on the dynamics either by removing states from the Hilbert space or by cutting off transition pathways between states. Supplemented by the presence of disorder, it is expected that constrained systems become prone to localization [91].

In summary, we will focus on quantum phenomena in Rydberg quantum simulator systems. We utilize the natural occurrence of disorder in optical tweezer arrays to investigate how disorder affects quantum state engineering protocols as well as systems with localized flat bands. Furthermore, we consider kinetic constraints occurring via the facilitation condition to study many-body localization. In Rydberg lattice gases, constraints can also occur via strong dissipation resulting in the dissipative localization of states.

In Chapter 2, we introduce the concept of a Rydberg atom quantum simulator, give a theoretical description of Rydberg atoms, describe the interaction between them, and then explain the many-body behavior of a Rydberg lattice gas under the influence of disorder in the system. Chapter 3 begins with disorder induced single-particle or Anderson localization and how the localization properties are described in terms of the localization length. The natural progression is to then introduce interactions to a localized system leading to many-body localization. We consider the impact of interactions and disorder on localizing systems which can result in a phase transition between an ergodic and an MBL phase.

We consider in Chapter 4 quantum information processing using a Rydberg atom platform with single-site addressing. We focus on the preparation of three different protocols for the non-adiabatic engineering of quantum states and the state transport in a one-dimensional lattice. In particular, we discuss protocols for the creation of an antiferromagnetic GHZ state, a specific kind of matrix product state (MPS) which is related to Rydberg crystals, and the transport of a single-qubit quantum state from the first to the last qubit of the chain. The protocols are based on the Rydberg blockade mechanism. Furthermore, we identify system parameters that optimize the fidelity and allow that the operation of the protocols is shorter than the lifetime of the Rydberg states. We discuss the influence of imperfections like a non-perfect Rydberg blockade, positional disorder of the atoms, and radiative decay of the Rydberg state, on the resulting state.

Chapter 5 covers the quantum many-body dynamics of a Rydberg quantum sim-

ulator under the facilitation constraint. This results in a Hilbert space structure where many-body states organize into a synthetic lattice featuring flat bands that support immobile states. We focus on a quasi-one dimensional lattice, a Lieb ladder, in the presence of quenched disorder, caused by an uncertainty in the atomic position, that results in Anderson localization. The localization properties of this system are characterized through two length scales (localization lengths) that display anomalous scaling behavior at certain band edges. Moreover, we discuss the experimental preparation of an immobile localized state, and analyze disorder-induced propagation effects.

A natural progression from our study of single-particle localization is to consider many-body localization phenomena in a Rydberg quantum simulator systems. In Chapter 6, we analyze many-body effects in spin chains with facilitated kinetic constraints and disorder originating from spin-spin interactions. This system can be described by an  $XX$ -model, a standard MBL system, though it has an unusual non-local disordered interaction potential. We analyze how the connection between interaction and disorder affects the localization compared to standard MBL models. In Chapter 7, we analyze the dynamics of hard-core bosons on a two-dimensional lattice with non-local, distance selective loss that can be engineered using Rydberg atom simulators. The evolution of the system separates into two timescales, the fast dissipative dynamics into a Zeno subspace, followed by the coherent dynamics which can be treated as a constrained hopping model. This constrained dynamics results in interesting relaxation behavior and exhibits trivially localized eigenstates even in the absence of disorder.

# Chapter 2

## Interacting Rydberg gases

### 2.1 Introduction to Rydberg quantum simulators

In 1982, Feynman proposed the so-called analog quantum computer [92], or quantum simulator, which is based on the idea of letting nature solve complex quantum physical many-body problems too difficult to study analytically. In quantum physics, the Hilbert space scales exponentially with the number of particles  $N$  in the system. Due to this exponential growth, quantum systems are too complex to be described analytically even for small particle numbers, while numerical approaches to solve the Schrödinger equation are quickly limited by computer memory. A quantum simulator is not a programmable machine performing any given algorithm, but instead it consists of a precisely engineered system that, when allowed to evolve in time, perfectly models the dynamics of the desired quantum system. The observable of interest is measured after the system has evolved and the experiment has to be repeated until the quantum mechanical distribution of the observable in the final state is resolved. A disadvantage of quantum simulators is that they cannot be used to solve a broad range of problems. This is aim of quantum computers, which are based on the design of specific algorithms utilizing the quantum properties of systems, such as linear superpositions of states and entanglement. As classical computation relies on collections of binary variables (bits), quantum computation acts on on collections of quantum two-level systems called quantum bits (qubits [93]). Using classical algorithms on a quantum computer will not give a significant gain in the efficiency as these algorithms do not take the quantum nature of the system into account. Quantum computers are not restricted to solving quantum mechanical problem; classical problems that may be tackled by quantum computers are: the Deutsch-Josza algorithm [94,95]

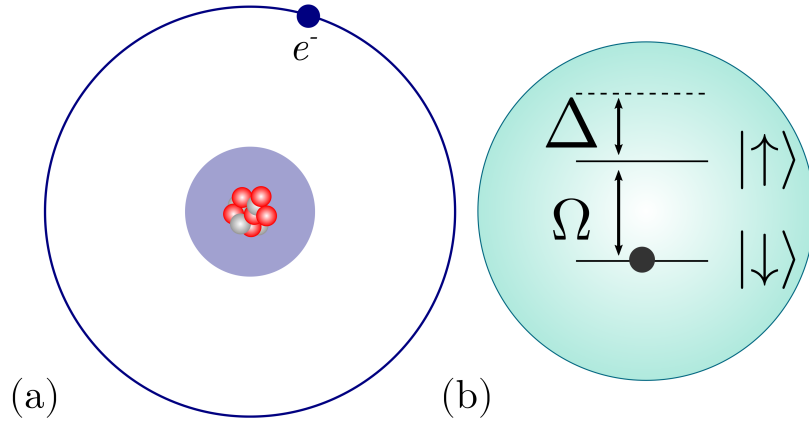


**Figure 2.1: Rydberg atom, two-level scheme.** (a) Model of an alkali atom in a Rydberg state. The valence electron (dark blue) is in a highly excited s-state ( $n \gg 1$ ,  $l = 0$ ). The nucleus is shielded by the non-excited electrons (blue shaded region) leading to a positive charge equal to a hydrogen nucleus which allows a description of the Rydberg atom as hydrogen with a small correction accounting for the finite size of the nucleus. (b) Two-level atom. A laser couples the ground state  $|\downarrow\rangle$  with a highly excited Rydberg state  $|\uparrow\rangle$ .

for the generation of truly random numbers, the Grover algorithm for the efficient data-bank search [96], and the Shor algorithm for the factorization of large numbers [97]. There also exist algorithms to solve the time-dependent Schrödinger equation (TDSE) such as the quantum Fourier transform algorithm, which is a part of the Shor algorithm.

There have been a variety of different proposals for the implementation of qubits, for example optical qubits using linear optics [98], superconducting qubits using Josephson junctions [99], or atomic qubits like neutral atoms [100] or trapped ions [101]. An advantage of neutral atomic qubits is the possibility of encoding quantum information in long-living hyperfine states. Moreover, resonant laser pulses are very effective in both manipulating the qubit states, as well as reading out the information stored in the atoms. The interaction of neutral atoms, which is necessary for conditional qubit gates acting on multiple qubits at the same time, is strongly dependent on their state. We will focus in this work on neutral atom qubits, more precisely on Rydberg atom quantum simulator platforms. Rydberg atoms are atoms with one or more electrons in a highly excited energy state with a large principal quantum number  $n \gg 1$  (see Fig. 2.1 (a)). Although it is possible to have multiple highly excited electrons per atom these systems are unstable because autoionization destroys the doubly excited state very quickly. Most quantum simulator platforms which are based on neutral atoms therefore

utilize alkali atoms with only a single valence electron [36, 40, 41]. We will restrict our considerations to alkali atoms with a single electron in a Rydberg state. The valence electron is largely unaffected by the structure of the atomic core, which it sees approximately as a point charge, due to the large separation. The core, non-excited electrons together with the atomic nucleus display a net positive electrical charge (equal to a single protonic charge). Thus, the energy states of the Rydberg atom can effectively be described by a hydrogen atom with a small correction accounting for the finite size of the core, the quantum defect  $\delta_{n,l}$ , where  $n$  and  $l$  denote the principal and angular momentum quantum numbers, respectively. Hence, the energy levels of an atom in a Rydberg state are

$$\epsilon_{nlj} = -\frac{R_y}{(n - \delta_{n,l})^2}, \quad (2.1)$$

where  $R_y = 13.61$  eV is the Rydberg constant, and  $j = s + l$  being the total angular momentum quantum number composed of the spin  $s$  and the orbital angular momentum quantum number  $l$ .

Rydberg atoms interacting with a laser field resonantly coupling two atomic energy states can be described as a two-level system (see Section 2.2 for the derivation). Thus, Rydberg atoms naturally represent spin systems, in which different atomic levels correspond to spin states. A common choice is to use the ground or a low-lying excited state of the atom as  $|\downarrow\rangle$ -spin, and a Rydberg state to represent the  $|\uparrow\rangle$ -spin. Consequently, Rydberg atoms can be used to simulate various spin models like the Ising spin system [35] or the  $XY$ -model [102]. In Chapter 6, we use a Rydberg lattice system to study the dynamics of a spin chain with kinetic constraints.

In quantum computation platforms utilizing Rydberg atoms as qubits, there are multiple ways of encoding the information in the atom. The simplest method

Properties	$n$ dependence
Binding energy of the electron	$n^{-2}$
Energy between adjacent levels	$n^{-3}$
Radius of the Orbit	$n^2$
Dipole moment	$n^2$
Polarizability	$n^7$
Radiative lifetime	$n^3$

**Table 2.1: Properties of Rydberg atoms.** Selected properties of Rydberg atoms and their scaling with the principal quantum number  $n$ . This table is taken from reference [10].

employs a two-level atom as a qubit, where the ground state represents the logical zero  $|\downarrow\rangle \hat{=} |0\rangle$ , and the Rydberg state represents the logical one  $|\uparrow\rangle \hat{=} |1\rangle$ . This description is based on the long lifetime of the highly excited atom, scaling as  $n^3$  (see table 2.1) and typically in the range of hundreds of microseconds. The long lifetime can be explained by the weak coupling of the ground-state wavefunction and the highly excited Rydberg state which results in a very slow decay. However, the lifetime of the Rydberg states is finite leading to relaxation processes such as spontaneous decay to the ground state. Alternatively, a three-level scheme can be used where the logical zero and one are both hyperfine ground states with a very long lifetime, and the function of the Rydberg state is to allow gate operations. The population of the Rydberg level is transferred to one of the hyperfine states to avoid losses due to effects such as spontaneous emission [21, 103]. In Chapter 4, we will explain the two different level schemes and their application in quantum information processing in more detail.

The idea of using Rydberg atoms to build quantum gates is based on the Rydberg-blockade effect which prevents the excitation of two neighboring atoms to an excited state and will be introduced in detail later in this chapter (see Section 2.3.3). This blockade mechanism allows to naturally implement controlled qubit gates as we will show in Chapter 4, using the example of a Toffoli gate (see appendix B.1). One of the main advantages of Rydberg atoms is the scalability and control of their interaction strength as a function of the interatomic separation  $R_0$  which can be tuned over 12 orders of magnitude [21]. This control allows fast gate operations (up to the sub-microsecond level [104]), which are beneficial for quantum information processing (QIP) and quantum computation. It is sufficient to cool the Rydberg system to temperatures around  $50\mu\text{K}$  [105] to obtain high fidelity quantum gates, as the fidelity depends only weakly on the center of mass motion of the atoms. Due to the long-range interaction, gates can be implemented between atoms that can be optically resolved. The fidelity of the gates is, however, limited by the finite lifetime  $\tau$  of a real atom due to radiative decay leading to loss of coherence. Table 2.1 gives the scaling of selected properties of the Rydberg atom with the principal quantum number  $n$ .

## 2.2 From a real atom to a two-level system

As discussed in the previous chapter, an atom interacting with a laser field that resonantly couples two of the states can be described as a two-level system. In this section we will explain how an atom interacts with a laser in order to understand,

for example, how neutral atoms can be exploited as qubits, how quantum gates can be applied to a Rydberg system, and how the interaction in quantum gates is switched on and off. (Throughout this thesis we are working in natural units  $\hbar = 1$ .) The time-dependent Schrödinger equation (TDSE) describing the time evolution of a quantum mechanical system is given by

$$i \frac{\partial \Psi(\mathbf{r}, t)}{\partial t} = \hat{H} \Psi(\mathbf{r}, t). \quad (2.2)$$

In the semi-classical description, the Hamiltonian of a single atom interacting with a laser field is defined as

$$\hat{H} = \hat{H}_0 + \hat{H}_{\text{int}}, \quad (2.3)$$

where  $\hat{H}_0$  is the atomic Hamiltonian in the Schrödinger representation and  $\hat{H}_{\text{int}}$  describes the light-matter interaction.

The dipole approximation can be used to describe this interaction by assuming that the wavelength of the laser is much larger than the size of the atom, allowing us to neglect the spatial dependence of the electric field. The interaction Hamiltonian in length gauge, with the light-matter interaction defined via the electric field times the position vector of the electron  $\hat{\mathbf{r}}$ , is then given by

$$\begin{aligned} \hat{H}_{\text{int}} &= -e \mathbf{E}(t) \cdot \hat{\mathbf{r}}, \\ &= -e E_0 \cos(\omega t) \boldsymbol{\varepsilon} \cdot \hat{\mathbf{r}}, \end{aligned} \quad (2.4)$$

where  $e$  is the elementary charge,  $E_0$  is the amplitude of the electric field,  $\omega$  is the angular frequency of the laser, and  $\boldsymbol{\varepsilon}$  is the unit polarization vector. The complete set of eigenfunctions of the atomic Hamiltonian  $\hat{H}_0$  is

$$\hat{H}_0 |\varphi_n\rangle = \epsilon_n |\varphi_n\rangle, \quad (2.5)$$

where  $\omega_n = \epsilon_n$  ( $\hbar = 1$ ), and the time evolution of the wavefunction in (2.2) is then given by

$$|\Psi(t)\rangle = \sum_n c_n(t) e^{-i\omega_n t} |\varphi_n\rangle. \quad (2.6)$$

Inserting Eq. (2.6) into (2.2) gives the differential equation for the time-dependent expansion coefficients  $c(t)$

$$i \sum_n \dot{c}_n(t) e^{-i\omega_n t} |\varphi_n\rangle = -e E_0 \cos(\omega t) (\boldsymbol{\varepsilon} \cdot \hat{\mathbf{r}}) \sum_n c_n(t) e^{-i\omega_n t} |\varphi_n\rangle. \quad (2.7)$$

Multiplication from the left with  $\langle \varphi_m | e^{i\omega_m t}$  gives

$$i \dot{c}_m(t) = E_0 \cos(\omega t) \sum_n c_n(t) \mathfrak{d}_{mn} e^{i(\omega_m - \omega_n)t}, \quad (2.8)$$

where  $\omega_{mn} = \omega_m - \omega_n$  is the transition frequency, and the transition dipole matrix element  $\mathfrak{d}_{mn} = \mathfrak{d}_{nm} = -e \langle \varphi_m | \boldsymbol{\varepsilon} \cdot \hat{\mathbf{r}} | \varphi_n \rangle$  determines the coupling strength between two states and the laser field. The large separation between the nucleus and core electrons, and the highly excited valence electron results in a strong dipole moment proportional to  $n^2$  that can induce a very strong interaction between Rydberg atoms.

We are using the rotating wave approximation (RWA) [106], where fast oscillating terms with frequency  $\omega_{mk} + \omega$  are neglected. Such terms can be neglected on the time scale of the relevant processes such as transitions or radiative decays. Thus terms which oscillate at optical frequencies can be averaged to zero which is a reasonable assumption as optical detectors cannot respond on these fast timescales. Additionally, we apply the two-level approximation, where a laser couples two of the atomic states near resonance  $\omega \approx \omega_{mk}$ , and all other atomic levels can be neglected. Hence, the atom can be effectively described as a two-level system and the wavefunction (2.6) takes the form

$$|\Psi(t)\rangle = c_g(t) |\varphi_g\rangle e^{-i\omega_g t} + c_e(t) |\varphi_e\rangle e^{-i\omega_e t}. \quad (2.9)$$

In this description  $|\varphi_g\rangle$  is the ground state and  $|\varphi_e\rangle$  is the excited state with  $\epsilon_g < \epsilon_e$ , and  $\epsilon_e - \epsilon_g \approx \omega$ . With this ansatz for the wavefunction, we obtain a system of coupled differential equations for the coefficients

$$i \dot{c}_g(t) = \frac{\Omega}{2} c_e(t) [e^{i(-\omega_{eg} + \omega)t} + e^{-i(\omega_{e,g} + \omega)t}], \quad (2.10)$$

$$i \dot{c}_e(t) = \frac{\Omega}{2} c_g(t) [e^{i(\omega_{eg} + \omega)t} + e^{i(\omega_{e,g} - \omega)t}], \quad (2.11)$$

where  $\Omega = E_0 \mathfrak{d}_{g,e}$  is the Rabi frequency. We perform a transformation of the coefficients into a rotating coordinate system, with the coefficients  $\tilde{c}_g(t) = e^{i\Delta t/2} c_g(t)$  and  $\tilde{c}_e(t) = e^{-i\Delta t/2} c_e(t)$ , where  $\Delta = \omega_{eg} - \omega$  is the detuning of the laser from the resonant transition between the ground and excited states. By applying the rotating wave approximation, we obtain the coupled differential equations for the coefficients in matrix representation

$$i \begin{pmatrix} \dot{\tilde{c}}_e(t) \\ \dot{\tilde{c}}_g(t) \end{pmatrix} = \frac{1}{2} \begin{pmatrix} \Delta & \Omega \\ \Omega & -\Delta \end{pmatrix} \begin{pmatrix} \tilde{c}_e(t) \\ \tilde{c}_g(t) \end{pmatrix}. \quad (2.12)$$

Since a two-level atom can represent a spin system ( $|\varphi_g\rangle = |\downarrow\rangle$ ,  $|\varphi_e\rangle = |\uparrow\rangle$ ), the Hamiltonian describing the coupling of a two level atom with a laser is given by

$$\hat{H} = \frac{1}{2} [\Delta (|\uparrow\rangle \langle \uparrow| - |\downarrow\rangle \langle \downarrow|) + \Omega (|\uparrow\rangle \langle \downarrow| + |\downarrow\rangle \langle \uparrow|)]. \quad (2.13)$$

To obtain the standard form of the Hamiltonian used in Rydberg setups, we add the global phase shift zero in energy  $\frac{1}{2}\Delta \cdot \mathbb{1}$  to Eq. (2.13) resulting in

$$\hat{H} = \left[ \Delta |\uparrow\rangle \langle \uparrow| + \Omega (|\uparrow\rangle \langle \downarrow| + |\downarrow\rangle \langle \uparrow|) \right] \quad (2.14)$$

with the eigenenergies of the system  $\epsilon_{\pm} = \frac{1}{2} (\Delta \pm \sqrt{\Delta^2 - 4\Omega^2})$ . This Hamiltonian can describe the time-evolution of a two-level atom where the levels are coupled by a laser with Rabi frequency  $\Omega$  and detuning  $\Delta$ .

## 2.3 Interacting Rydberg atoms

Rydberg atoms show very strong dipole-dipole interactions scaling with  $C_3/r^3$  at short interatomic separation, and van der Waals behavior scaling as  $C_6/r^6$  on longer distances. The form of the interaction depends on the separation between the atoms and on the principal quantum number  $n$  of the Rydberg state.

### 2.3.1 Dipole-dipole interaction

For short interatomic separations, Rydberg atoms show, due to their large dipole moment, a very strong interaction which is dependent on the interatomic separation  $R_0$  between the atoms. The Hamiltonian of a pair of interacting Rydberg atoms is

$$\hat{H} = \hat{H}_1 + \hat{H}_2 + \hat{H}_{\text{int}}, \quad (2.15)$$

where  $\hat{H}_i$  is the Hamiltonian of a single atom  $i$  and  $\hat{H}_{\text{int}}$  describes the interaction between the atoms. We neglect any retardation effect as the spacing between the atoms is much smaller than the wavelength of light from the Rydberg-Rydberg transition. Furthermore, we assume that the interatomic distance is sufficiently large to ensure that the electronic wavefunctions do not overlap. The interaction Hamiltonian is given by the interactions between all four charges (two atomic cores and two electrons) in the system,

$$\hat{H}_{\text{int}} = \frac{e^2}{4\pi\epsilon_0} \left( \frac{1}{R_0} - \frac{1}{|\mathbf{R}_0 + \mathbf{r}_{e_2}|} - \frac{1}{|\mathbf{R}_0 - \mathbf{r}_{e_1}|} + \frac{1}{|\mathbf{R}_0 + \mathbf{r}_{e_2} - \mathbf{r}_{e_1}|} \right), \quad (2.16)$$

where  $\mathbf{R}_0$  is the vector between the two atomic cores, and  $\mathbf{r}_{e_i}$  is the vector between core  $i$  and its respective electron  $e_i$ . Assuming that  $|\mathbf{R}_0| \gg |\mathbf{r}_{e_1}|, |\mathbf{r}_{e_2}|$ , we can perform a multipole expansion which leads to

$$\begin{aligned} \frac{1}{|\mathbf{R}_0 - \mathbf{r}_1|} &= \sum_{k=0}^{\infty} \frac{1}{k!} (\mathbf{r}_1 \cdot \nabla_{\mathbf{r}_1})^k \frac{1}{|\mathbf{R}_0 - \mathbf{r}_1|} \Big|_{\mathbf{r}_1=0} \\ &= \frac{1}{R_0} + \frac{\mathbf{R}_0 \cdot \mathbf{r}_1}{R_0^3} + \frac{3(\mathbf{R}_0 \cdot \mathbf{n})^2 - (R_0 r_1)^2}{2R_0^5} + \mathcal{O}(1/R_0^5), \end{aligned} \quad (2.17)$$

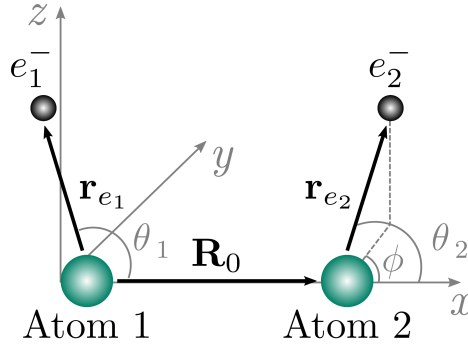


**Figure 2.2: Interacting dipoles.** Two highly excited Rydberg atoms, which are separated by  $R_0$ , can be described as two-interacting dipoles. The positively charged atomic core of atom  $i$  and the negatively charged electron  $e_i^-$  are separated by  $\mathbf{r}_{e_i}$ .

where  $\mathbf{n} = \mathbf{R}_0/R_0$  is the normalized vector between the atomic cores. The terms in (2.17) correspond to monopole, dipole and quadrupole terms, respectively. With this, we obtain for the third term in (2.16)

$$\frac{1}{|\mathbf{R}_0 - \mathbf{r}_{e_1}|} \simeq \frac{1}{R_0} + \frac{\mathbf{n} \cdot \mathbf{r}_{e_1}}{R_0^2} + \frac{3(\mathbf{n} \cdot \mathbf{r}_{e_1})^2 - r_{e_1}^2}{2R_0^3}, \quad (2.18)$$

and the other terms can be similarly calculated. Inserting (2.18) into (2.16) gives us the resonant dipole-dipole coupling as dominant term

$$\hat{H}_{\text{DD}} = \frac{e^2}{4\pi\epsilon_0} \left( \frac{\mathbf{r}_{e_2} \cdot \mathbf{r}_{e_1} - 3(\mathbf{n} \cdot \mathbf{r}_{e_1})(\mathbf{n} \cdot \mathbf{r}_{e_2})}{R_0^3} \right) \quad (2.19)$$

$$= \frac{\mathbf{d}_{e_2} \cdot \mathbf{d}_{e_1} - 3(\mathbf{n} \cdot \mathbf{d}_{e_1})(\mathbf{n} \cdot \mathbf{d}_{e_2})}{4\pi\epsilon_0 R_0^3}, \quad (2.20)$$

where  $\mathbf{d}_{e_i} = e \mathbf{r}_{e_i}$  is the electric dipole moment. Thus, in this parameter regime, the interaction Hamiltonian (2.16) can be approximated by the dipole-dipole interaction (2.20), i.e.  $\hat{H}_{\text{int}} \approx \hat{H}_{\text{DD}}$  [107]. The interaction Hamiltonian depends on the orientation of the dipoles through  $\theta_1, \theta_2$ , the angles between the dipole and the connection vector  $\mathbf{n}$ , through  $\phi$  which is the dihedral angle between the vectors  $\mathbf{r}_{e_1}$  and  $\mathbf{r}_{e_2}$ . Note, defining the vector  $\mathbf{r}_{e_1}$  to lie in the  $xy$ -plane, the dihedral angle  $\phi$  is the rotation of  $\mathbf{r}_{e_2}$  against the  $xy$ -plane as shown in Fig. 2.2. With this, we obtain the orientation dependent expression of the dipole-dipole interaction

$$\hat{H}_{\text{DD}} = -\frac{d_1 d_2}{4\pi\epsilon_0 R_0^3} (2 \cos \theta_1 \cos \theta_2 - \sin \theta_1 \sin \theta_2 \cos \phi). \quad (2.21)$$

In the case of parallel dipoles ( $\theta_1 = \theta_2 = \theta$  and  $\phi = 0$ ), the interaction only depends on the angle  $\theta$ , the angle between the direction of the dipole and the vector connecting them,

$$\hat{H}_{\text{DD}} = \frac{d_1 d_2}{4\pi\epsilon_0 R_0^3} (1 - 3 \cos^2 \theta) . \quad (2.22)$$

This equation yields the so-called magic angle,  $\theta_m = 54.74^\circ$ , where the dipole-dipole interaction vanishes.

### 2.3.2 Van der Waals interaction

Two atoms interacting via the dipole-dipole interaction in Eq. (2.20) experience an eigenvalue shift as a function of the interatomic separation  $R_0$ . This shift can be determined via perturbative approaches resulting in an estimation of the interaction potential. For small interatomic separations the potential shows a dipole-dipole scaling  $\propto 1/R_0^3$ , while for large interatomic separations, the potential has a short-range van der Waals scaling  $\propto 1/R_0^6$ . We derive this energy shift caused by the dipole-dipole interaction. In order to do this, we consider a very simple one-dimensional model of two interacting atoms, each represented by a harmonic oscillator, which allows analytical calculations to be carried out. The structure of these calculations can then be straightforwardly generalised to other cases (we follow the considerations in Ref. [108]). The Hamiltonian of our model system is given by

$$\hat{H} = \hat{H}_0 + \hat{H}_{\text{int}} , \quad (2.23)$$

where  $H_0$  describes the two harmonic oscillators

$$\hat{H}_0 = \frac{1}{2m} p_1^2 + \frac{1}{2} m \omega_0^2 x_1^2 + \frac{1}{2m} p_2^2 + \frac{1}{2} m \omega_0^2 x_2^2 . \quad (2.24)$$

In this example,  $x_k$  plays the role of the distance between the nucleus and electron of atom  $k$ ,  $p_k$  defines the momentum of atom  $k$ , and  $\omega_0$  is the angular frequency of the harmonic oscillator. Assuming a large interatomic separation, the interaction Hamiltonian (2.20) simplifies to

$$\hat{H}_{\text{int}} \approx \frac{-2e^2 x_1 x_2}{4\pi\epsilon_0 R_0^3} \quad (2.25)$$

which is the dipole-dipole interaction Hamiltonian from Eq. (2.20) in one dimension. Because of the odd parity of the interaction operator, the first-order term vanishes when both harmonic oscillators are in the ground state  $|0\rangle$

$$\Delta\epsilon^{(1)} = \langle 0 | \hat{H}_{\text{int}} | 0 \rangle , \quad (2.26)$$

and the leading term of the ground-state energy shift is given by second order perturbation theory

$$\Delta\epsilon^{(2)} = V_{\text{vdW}}(R_0) = \sum_{n \neq 0} \frac{\langle 0 | \hat{H}_{\text{int}} | n \rangle \langle n | \hat{H}_{\text{int}} | 0 \rangle}{\epsilon_0 - \epsilon_n}, \quad (2.27)$$

where the summation runs over all oscillator states  $|n\rangle$  dipole coupled to the ground state. The van der Waals potential is then given by

$$V_{\text{vdW}}(R_0) = \left( \frac{2e^2}{4\pi R_0^3} \right)^2 \sum_{n_1, n_2} \frac{\delta_{n_1,1} \delta_{n_2,1} |\langle n_1 n_2 | \hat{x}_1 \hat{x}_2 | 0 0 \rangle|^2}{-\omega_0(n_1 + n_2)} \quad (2.28)$$

$$= -\frac{e^4}{32\pi^2 m^2 \omega_0^3 R_0^6}, \quad (2.29)$$

with the matrix element of a simple harmonic oscillator  $\langle n | \hat{x} | 0 \rangle = \delta_{n,1} \sqrt{1/(2m\omega_0)}$ . Introducing the electric polarizability  $\alpha_E = 2e^2/4\pi m\omega_0^2$ , the van der Waals interaction can be written in the London form [109]

$$V_{\text{vdW}}(R) = -\frac{\alpha_E^2 \omega_0}{8R_0^6}. \quad (2.30)$$

Using this result, we can now estimate the energy shift for the oscillator model of two real interacting atoms (three dimensional). We consider two atoms, each in the atomic state  $|\psi_{nlm}\rangle$ , interacting via the dipole-dipole interaction (2.20). The van der Waals energy shift of the pair state given by second order perturbation theory is

$$V(R_0) = \Delta\epsilon_2 = \left( \frac{e^2}{4\pi\epsilon_0 R_0^3} \right)^2 \sum_{\substack{n', l', m' \\ n'', l'', m''}} \frac{|\langle \psi_{n'' l'' m''} \psi_{n' l' m'} | \hat{H}_{\text{DD}} | \psi_{nlm} \psi_{nlm} \rangle|^2}{2\epsilon_{nl} - \epsilon_{n'l'} - \epsilon_{n''l''}}. \quad (2.31)$$

This result can be expressed in terms of the van der Waals coefficient  $C_6$  and shows the predicted short-ranged  $1/R_0^6$  behavior

$$V(R_0) = \frac{C_6}{R_0^6}. \quad (2.32)$$

From Table 2.1, we know that the dipole moments of a Rydberg atom scale as  $n^2$ , resulting in  $|\langle \psi_{n'' l'' m''} \psi_{n' l' m'} | \hat{H}_{\text{DD}} | \psi_{nlm} \psi_{nlm} \rangle|^2 \propto (n^4)^2$ , and the spacing between adjacent energy levels is proportional to  $n^{-3}$ . Thus, the van der Waals interaction between two Rydberg atoms scales as  $V(R_0) \propto \frac{n^{11}}{R_0^6}$ . This shows that the van der Waals interaction is strongly dependent on the state of the Rydberg atom. Switching between the dipole-dipole regime to the van der Waals regime can be achieved by tuning the interatomic separation  $R_0$ , as well as the van der Waals constant  $C_6$  by changing the principal quantum number  $n$  of the Rydberg atom [21].

### 2.3.3 Blockade and facilitation effect

In the previous section, we described the van der Waals interaction of two highly excited Rydberg atoms which results in an energy shift of the pair state. We now explain how the interaction of atoms with a laser field can result in interesting effects such as the Rydberg blockade where the simultaneous excitation of two atoms to a Rydberg state is strongly suppressed. Fig. 2.3(a) illustrates the blockade effect on the example of two Rydberg atoms in an optical lattice. In the blockade regime of  $V_0 \gg \Omega$ , a laser of Rabi frequency  $\Omega$  and zero detuning  $\Delta = 0$  cannot overcome the energy cost of having two neighboring atoms excited to a Rydberg state. When the first atom is resonantly excited to a Rydberg state  $|\uparrow\rangle$  (highlighted in red) by a laser of Rabi frequency  $\Omega$ , the van der Waals interaction shifts the Rydberg state of the neighboring atom (highlighted in gray) by the interaction energy  $V_0$ . If the shift of the doubly excited state  $|\uparrow\uparrow\rangle$  is large enough  $V_0 \gg \Omega$ , the laser is off-resonance with this transition resulting in the blockade of any further excitations.

The shift of the doubly excited state is given by the van der Waals potential  $V(r) = C_6/r^6$  with the van der Waals coefficient  $C_6$ . Figure 2.3(c) shows the dependence of the energy shift of the state  $|\uparrow\uparrow\rangle$  on the interatomic separation  $r_i$ . All other states in the two-atom system,  $|\downarrow\downarrow\rangle$ ,  $|\uparrow\downarrow\rangle$  and  $|\downarrow\uparrow\rangle$ , only interact weakly, thus, we can treat these states as unshifted. For an atomic separation smaller than the blockade radius,  $r_i < R_b$ , the doubly excited Rydberg state  $|\uparrow\uparrow\rangle$  is shifted by a large value  $V(r)$  and the blockade works almost perfectly resulting in a strong suppression of the transition to the doubly excited state. However, the shift  $V(r)$  decreases with an increasing interatomic separation. When the separation between the atoms is equal to the blockade radius  $r_i = R_b$ , the blockade effect breaks down. Further increasing the separation  $r_i > R_b$  leads to a negligible shift of the doubly-excited state and the laser can excite both atoms to the Rydberg state. A single excited Rydberg atom can not only blockade the excitation of a single atom but it prevents the excitation of all atoms inside a volume with blockade radius  $R_b$ . This is the collective Rydberg blockade which can be utilized for the production of collective Rydberg ensemble states, used for the creation of long distance entanglement, as well as light-atom quantum interfaces. We will restrict our considerations to a blockade radius equal to the interatomic separation  $R_b = R_0$ . Shining a laser with zero detuning on two neighboring atoms with a separation smaller than the blockade radius,  $r_i < R_b$ , creates the entangled state  $|\Psi_+\rangle = \frac{1}{\sqrt{2}}(|\downarrow\uparrow\rangle + |\uparrow\downarrow\rangle)$ . Note, the antisymmetric state has zero transition dipole moment and is therefore not coupled to the laser. Thus,

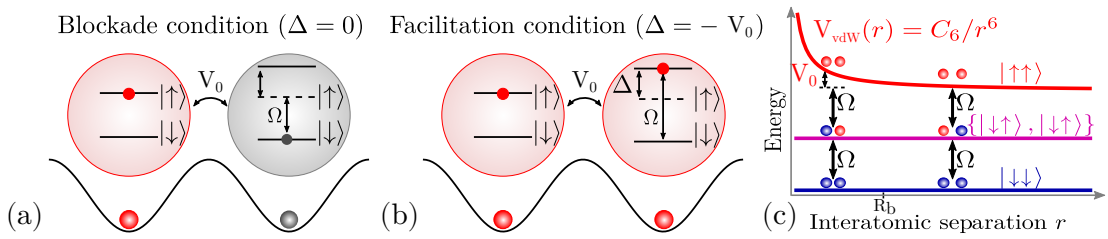


**Figure 2.3: Rydberg blockade and facilitation.** (a) Illustrates the Rydberg blockade mechanism for the example of two atoms trapped in optical tweezers. When the first atom (red) is excited to a Rydberg state, the excited state of the second atom (blue) gets shifted by the van der Waals interaction  $-V_0$ . In the regime of  $|V_0| \gg \Omega$ , a laser of Rabi frequency  $\Omega$  and zero detuning  $\Delta = 0$  cannot excite the second atom (blue) to the shifted Rydberg state. (b) Illustrates the facilitation (anti-blockade) effect. When the detuning of the laser matches the facilitation condition  $\Delta = -V_0$ , the probability of exciting an atom to a Rydberg state is strongly enhanced by an already excited neighbor. (c) Depicts the energies of the pair state as a function of the interatomic separation. When the interaction energy is strong enough to shift the doubly excited state out of resonance, the transition is blocked. The blue spheres represent ground state atoms  $|0\rangle$ , while the red spheres are atoms in the excited Rydberg state  $|1\rangle$  blocked atoms. The doubly excited state shifts by  $V(R_i) = C_6/R_i^6$ . Adapted from Ref. [4].

the Rydberg blockade is a mechanism which naturally creates entangled states. Another interesting effect which can occur in a system of Rydberg atoms when interacting with a laser is the anti-blockade or facilitation mechanism Fig. 2.3(b), which was first predicted by [48, 110], where the excitation of an atom to a Rydberg level is strongly enhanced by an excited neighbor. In order to achieve a population of the doubly excited Rydberg state  $|\uparrow\uparrow\rangle$ , the system is driven by a laser with detuning  $\Delta = -V_0$ , i.e. the laser detuning matches exactly the shift of the doubly excited Rydberg state  $|\uparrow\uparrow\rangle$ . This results in a strong enhancement of the excitation of two neighboring atoms to the doubly-excited state. In contrast to the blockade effect, facilitation requires a fine-tuning protocol to work in optical lattices, since small differences in the distance between the atoms can result in dramatic effects on the energetic shifts.

## 2.4 Rydberg lattice <sup>1</sup>

So far, we have introduced the two-level description of a single Rydberg atom, considered the van der Waals interaction between two atoms excited to a Rydberg state, and explained the resulting Rydberg blockade and facilitation mechanism when the system is coupled to a laser. We will now expand our discussion to a many-body Rydberg system with  $N > 2$  atoms which will be the setup in chapter 4, 5 and 6.

We study the physics of a cold Rydberg lattice gas where the atoms are trapped in  $N$  optical tweezers, each loaded with a single atom (see Fig. 2.3(a)). For sufficiently low temperatures, the optical tweezers can be approximated by a harmonic trap, as explained in more detail in the appendix A.1. The atoms in the trap are separated by the nearest-neighbor distance  $R_0$ . Shining a laser with a Rabi frequency  $\Omega$  and detuning  $\Delta$  with respect to the atomic transition between the electronic ground state  $|\downarrow\rangle$  and a Rydberg level  $|\uparrow\rangle$  couples the two states of the atom. Atoms in the Rydberg state  $|\uparrow\rangle$  interact, at distance  $d$ , via an algebraically-decaying potential  $V(d) = C_\alpha/d^\alpha$ , with  $\alpha = 3$  for dipole-dipole or  $\alpha = 6$  for van der Waals interactions. Within the rotating wave approximation the Hamiltonian of this system reads

$$\hat{H} = \Omega \sum_{k=1}^N \hat{\sigma}_x^{(k)} + \Delta \sum_{k=1}^N \hat{n}_k + \frac{1}{2} \sum_{\substack{k=1 \\ m \neq k}}^N V(d_{km}) \hat{n}_m \hat{n}_k, \quad (2.33)$$

---

<sup>1</sup>Parts of this section are taken from Ref. [2] and its supplementary material.

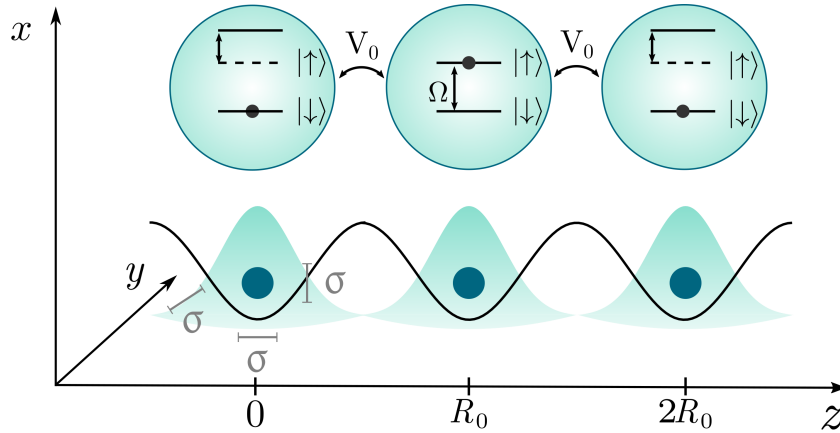


**Figure 2.4: Rydberg atoms trapped in chain of optical tweezers.** One-dimensional lattice of three optical tweezers each loaded with a single atom. The optical traps are arranged along the  $z$  direction and are separated by  $R_0$ . The ground state  $|\downarrow\rangle$  is resonantly coupled to the Rydberg state (of a single atom)  $|\uparrow\rangle$  via a laser of Rabi frequency  $\Omega$ .  $V_0$  indicates the nearest-neighbor interaction energy between the atoms. The second atom is in a Rydberg state that shifts the first and third atom out of resonance (Rydberg blockade). The position of the atoms in the traps follows a Gaussian distribution of width  $\sigma$ .

where  $k$  and  $m$  are lattice indices,  $d_{km}$  denotes the distance between atoms in sites  $k$  and  $m$ ,  $\hat{\sigma}_x^{(k)} = |\uparrow_k\rangle\langle\downarrow_k| + |\downarrow_k\rangle\langle\uparrow_k|$  and  $\hat{n}_k = |\uparrow_k\rangle\langle\uparrow_k|$ .

### Effective Hamiltonian

The Hamiltonian (2.33) describes the general dynamics of a Rydberg lattice system interacting with a laser. In our work, we fix the laser parameters to fulfill either the blockade (chapter 4) or the facilitation condition (chapter 5 and 6) and restrict the interactions to nearest neighbors. Describing the dynamics of the systems with an effective Hamiltonian can simplify analytical calculations and reduce the Hilbert space dimensions therefore allowing the simulation of more complex and larger systems. In chapter 4 we consider an effective three-body Hamiltonian (4.10) which has the Rydberg blockade mechanism directly built into it. In chapter 5 the effective Hamiltonian (5.18) describes the facilitated dynamics of the system which is restricted to a Hilbert subspace with at most two neighboring atoms excited to a Rydberg state. The effective Hamiltonian (6.2) in chapter 6 describes the constraint dynamics in the many-body sector of the Hilbert space allowing excitations to spread through the system.

In order to derive the effective Hamiltonian for each of the models, we trans-

form the Hamiltonian (2.33) into an interaction picture by applying the unitary transformation

$$\hat{H} = \hat{U}^\dagger \hat{H} \hat{U} - i\hat{U}^\dagger \left( \partial_t \hat{U} \right), \quad (2.34)$$

with a unitary operator  $\hat{U}$ . After the unitary transformation (2.34), large energy differences in the Hilbert space, which cannot be overcome dynamically, only appear in fast rotating terms. By applying the rotating wave approximation, the Hilbert space splits into subspaces which are no longer coupled through the Hamiltonian as discussed in more detail in Sec 5.2.1. The splitting of the Hilbert space into energy sectors leads to the reduction of the dimensionality mentioned before by restricting the dynamics to one specific energy subspace. The specific form of the unitary operator  $\hat{U}$  depends on the parameter regime being explored and will be specified in each of the chapters.

### 2.4.1 Rydberg gases in optical tweezer arrays

Even small degrees of disorder can be detrimental to the exploitation of facilitation effects. Even if the positioning of the optical tweezers can be achieved with remarkable precision, an additional source of randomness has to be accounted for coming from the non-vanishing width of the traps and an uncertainty in the atomic positions due to the finite temperature of the setup. Small displacements from the center of the traps are sufficient to significantly shift the atomic transitions off resonance from the laser frequency, thereby hindering the facilitation mechanism [6]. The interaction potential experienced by an atom at a distance  $r = R_0 + \delta r$  from an excitation will be  $V(r) = V(R_0 + \delta r) \equiv V(R_0) + \delta V$ , with  $\delta V$  representing the random shift. We derive in appendix A.2 the correlated distribution of the energy shifts between atomic pairs. To characterize the impact of this type of disorder, we denote by  $\omega$  the optical tweezer trapping frequency (assumed hereafter to be isotropic in space), by  $m$  the atomic mass and by  $T$  the temperature. The probability distribution of a trapped atom can then be approximately described as a Gaussian of width  $\sigma$  around the trap center as indicated in Fig 2.4. We now require that (I)  $k_B T \gg \hbar\omega$ : this implies that one can use the semiclassical estimate  $\sigma \approx \sqrt{k_B T / m\omega^2}$  [6] and moreover that the thermal de Broglie wavelength of the atom is much smaller than the distribution width. In other words, the atom can be considered approximately localized somewhere within the trap according to a classical probability distribution. (II)  $\omega\Delta t \ll 1$ , with  $\Delta t$  the duration of an experiment: this ensures that the atoms will not appreciably move from their positions in this time frame and thus the

disorder is quenched. (III)  $\Omega\Delta t \gtrsim 1$ : the internal degrees of freedom are much faster than the kinetic ones, so that within an experiment the dynamics induced by the disordered Hamiltonian can be probed. In particular, one sees that (II) and (III) imply that  $\Omega/\omega \gg 1$ . While challenging, a regime of this kind is in principle reachable. For instance, in Ref. [6] this ratio is of order 10 (if one takes, as an upper bound,  $\omega$  from the short side of the elongated traps). In the supplementary material of Ref. [6] the role of interatomic repulsion is also discussed and shown to be of the same order as thermal motion, in which case it can be similarly reduced by decreasing  $\Delta t$ .

# Chapter 3

## Localization phenomena

### 3.1 Anderson localization

In 1958, P.W. Anderson predicted a localization effect of electronic wavefunctions in a solid which is caused by the presence of randomly distributed impurities in the lattice. This localization corresponds to a complete absence of charge carrier diffusion leading to a vanishing conductivity. This localization manifests in the electronic wavefunctions being sharply peaked within the lattice, instead of resembling plane waves. The absence of these extended modes hinders charge transport and can lead indeed to a vanishing conductivity for sufficiently large doping/concentration of impurities.

At that time, it was known that defects in a medium are the cause of resistance and hinder the conductivity, but the complete cancellation of diffusion was a new phenomenon. In a localized system, the electronic wavefunction can no longer be described as a Bloch wave  $\Psi(\mathbf{r}) \sim \exp(i\mathbf{k}\mathbf{r})$ , which is implying the ability of an electron to freely propagate through the periodic potential of the solid and is extended over the whole lattice. Instead, it is typically peaked at some position within the lattice and has exponentially suppressed tails decaying according to  $\Psi(\mathbf{r}) \sim \exp(-|\mathbf{r}|/\xi)$  with the localization length  $\xi$ . Due to the vanishing diffusion of localized states, systems that undergo Anderson localization can preserve information of the initial state and therefore have some degree of memory of the initial conditions.

Considering an electron hopping in a disordered lattice, the disorder in the system hinders the energy transport by shifting the potential energies at each lattice site out of resonance. Even if the hopping of the electrons is not prevented, the amplitudes of different hopping paths cancel each other out resulting in a localized state. Anderson localization can also occur in a wave model where the

wavefunction is scattered by impurities, resulting in the destructive interference of multiple scattering paths localizing the wave.

In order to explain this localization effect Anderson studied a tight-binding model, neglecting the interaction between the electrons

$$H = J \sum_{\langle i,j \rangle} (\hat{c}_i^\dagger \hat{c}_j + \hat{c}_j^\dagger \hat{c}_i) + \sum_i U_i \hat{c}_i^\dagger \hat{c}_i, \quad (3.1)$$

where the  $\hat{c}_i^\dagger$  ( $\hat{c}_i$ ) denotes the spinless fermionic creation (annihilation) operator acting on site  $i$ ,  $\langle i,j \rangle$  specifies that the summation is restricted to nearest neighbors in the lattice,  $J$  is the nearest-neighbor hopping amplitude, and  $U_i$  is the random onsite potential acting on site  $i$ . The  $U_i$  are independent and identically distributed variables drawn from a uniform distribution  $U_i \in [-W/2, W/2]$  with amplitude  $W$ . This model verifies that in the case of zero disorder  $W = 0$ , the electron is hopping in a periodic lattice and the eigenfunctions of the Hamiltonian are extended plane waves. When the disorder is switched on, which randomly shifts the energies at each lattice site out of resonance, localization occurs.

By changing the disorder strength it is possible to induce a metal-insulator (Anderson) transition, which is, in contrast to the Mott-insulator transition, not considering electron-electron interactions but is strongly dependent on the dimension of the medium. At absolute zero, the conductivity in the Anderson localized phase is zero and the system is a perfect insulator. However, at finite temperatures, the electrons in the system can hop between localized states due to thermally-activated hopping, whereas in the metallic phase, the system is conducting even at  $T = 0\text{K}$ . In one- and two-dimensional systems, all eigenstates of the Hamiltonian 3.1 are exponentially localized when disorder is introduced, independent of its strength. These low-dimensional systems do not exhibit a phase transition. This does not mean that the conductivity in a thin wire has to be negligibly small, as the localized modes in a finite wire can couple to form a so-called *necklace state* leading to full conductivity [111]. In three- or more dimensions, there exists a phase transition, the so-called Anderson transition, occurring at a critical disorder strength  $W_c$ . For weak disorder  $W < W_c$ , some eigenstates of the Hamiltonian remain extended over the whole system, while for strong disorder  $W > W_c$  all wavefunctions are localized.

At intermediate disorder strengths, these systems feature a mobility edge  $E_c$  separating localized and delocalized states by their energy (see Fig. 3.1). The Ioffe-Regel criterion defines this threshold by stating that states with a mean free path between successive scattering events  $l$  smaller than  $\lambda/2\pi$ , with  $\lambda$  being the wavelength of a wavefunction, are localized.

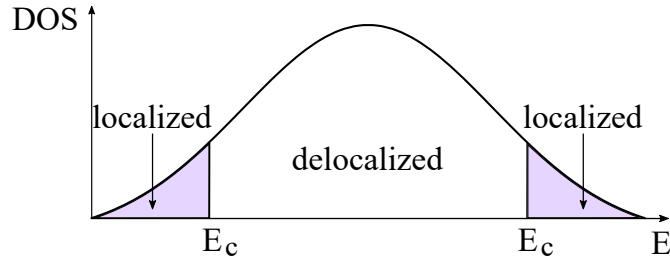


**Figure 3.1: Mobility edge.** Density of states (DOS) as a function of energy  $E$  for a system featuring a mobility edge  $E_c$ . The mobility edge separates localized (purple shaded region) from extended states energetically.

Due to their large wavelength, states in the centre of the bands will not be affected by small potential fluctuations as much as the states close to the band edge. Increasing the disorder strength will localize more and more states, which increases the area of localized states till a critical disorder strength  $W_c$  is reached where all states are localized and the mobility edge disappears. This is referred to as the Anderson transition. For a localized state, the localization length takes a finite value and reaches infinity for an extended state.

In 1979, the scaling theory of localization [112] was introduced as a tool to describe and understand the localization transition in finite media. It states that, close to the mobility edge, the conductivity of a material is system size dependent. Therefore, a dimensionless conductance  $g$  is introduced which depends on the size of the system  $L$ ,

$$g(L) = \frac{G(L)}{e^2/2\hbar}, \quad (3.2)$$

where  $G(L)$  is the conductance in the system. States are localized when the scale parameter  $g < 1$ , and are delocalized (metallic) for  $g > 1$ . Additionally, two critical exponents are predicted, one describes how the conductivity vanishes with energy when approaching the mobility edge, the other describes the divergence of the localization length for energies approaching the mobility edge from the localized side. Anderson localization can be observed in the transport of electromagnetic waves, acoustic waves, quantum and spin waves, among others.

An interesting platform with which to study Anderson localization is an optical lattice of trapped cold atoms. The interactions can be tuned in a wide range, including the opportunity to switch from repulsive to attractive interactions, as well as reduced to a level where a free-particle description is appropriate. Furthermore, the localization process can be directly observed using absorption or fluorescence imaging techniques.

### 3.1.1 Localization length

A measure for the localization of a wavefunction is the localization length  $\xi$ , defining the width of a wavefunction. In one- and quasi-one dimensional systems, the localization length can be computed using the limiting behaviour of random matrices. To be more precise, the localization length can be extracted as the inverse of the so-called Lyapunov exponent  $\xi = \gamma^{-1}$ , which characterizes the exponential growth of the length of a vector with the number of random matrices subsequently applied to it. The Lyapunov exponent depends only on the disorder distribution and not on the specific realization of the disorder. A system is in a localized state when the Lyapunov exponent is greater than zero  $\gamma > 0$  and is delocalized when the Lyapunov exponent vanishes  $\gamma = 0$ . We give a brief introduction into Random matrix theory and the calculation of the Lyapunov exponent, related to the the localization length, which we will use to characterize the localization properties of the synthetic Lieb ladder discussed in Chapter 5.

#### Random matrix theory

In complex systems, such as heavy nuclei, chaotic systems, and disordered lattices, it is often impossible to exactly describe a system quantum mechanically, the exact Hamiltonian might be unknown or the eigenvalue problem  $\hat{H} |\varphi_n\rangle = E_n |\varphi_n\rangle$  too complicated to be solved. A solution can be the extraction of distinct statistical properties such as the distribution or density of energy levels of those systems, using random matrix theory (RMT). This method cannot predict the exact position of the energy levels, which is a function of the specific realization of the disorder, however it can give insight into the overall appearance of the spectrum. We are interested in the application of RMT to the description of the localization behavior in a quasi one-dimensional disordered lattice system. In a random matrix, some or all elements of the matrix are random variables drawn from a probability distribution, and the symmetry of the Hamiltonian defines the ensemble from which random elements are drawn. As such, the random matrix carries only the most fundamental properties of the Hamiltonian it aims to describe. Thus, it is expected to reproduce relevant features of the Hamiltonian only when the corresponding system is amenable to a statistical description, i.e. typically if it comprises of an extensive number of degrees of freedom.

We will focus our considerations on random matrices  $R$  belonging to the Gaussian orthogonal ensemble (GOE) because it models systems with time-reversal symmetry, which are invariant under orthogonal conjugation. The GOE considers

real symmetric random matrices of dimension  $M$ , where the  $M(M+1)/2$  matrix elements on and above the main diagonal,  $R_{ij}$  with  $i \leq j$ , are independent Gaussian variables. The ensemble of random variables is independent and identically distributed (iid)

$$P(R) = \prod_{i \leq j} f(R_{ij}), \quad (3.3)$$

with the Gaussian probability distribution  $f$  with zero mean and unit variance, while the remaining elements are determined by the matrix being symmetric  $R_{ij} = R_{ji}$ . Furthermore, the probability density,  $P(R)$  is invariant under a transformation with an orthogonal matrix  $Q$

$$P(Q^T R Q) = P(R). \quad (3.4)$$

Since the elements of the matrix are random Gaussian variables they satisfy  $\langle R_{ij} \rangle = 0$  and  $\langle R_{ij}^2 \rangle = 1$  for  $i \leq j$ . The distribution  $P_M(x)$  of eigenvalues  $x$  of the random matrix is given by Wigner's semicircular law as

$$\lim_{M \rightarrow \infty} P_M(x) = P(x) = \frac{1}{2\pi} \sqrt{4 - x^2}, \quad (3.5)$$

This states that the density of energy levels of a large class of symmetric random matrices converge to a semicircular distribution. Wigner's surmise on the other hand, which we will discuss later, describes the distribution of the level spacing. We will discuss the statistics of the eigenvalue spacing of real, symmetric, random matrices later in this chapter in more detail as it is related to the statistics of the energy levels of chaotic systems, and can be used to distinguish between an ergodic (chaotic), and an integrable system (that exhibits an extensive number of conserved quantities).

### Lyapunov exponent

We explain the concept and calculation of the Lyapunov exponent  $\gamma$  for the example of a one-dimensional hopping model with a random potential on each lattice site, as described in Ref. [113]. In order to calculate the Lyapunov exponent, we apply the transfer matrix method, which can be used to solve the one-dimensional Schrödinger equation of the Anderson model (3.1) [54, 54],

$$\psi_{i+1} + \psi_{i-1} + U_i \psi_i = \epsilon \psi_i. \quad (3.6)$$

Here, the  $\psi_i$  denotes the value of the wave function on site  $i$  and  $\epsilon$  is the eigenenergy of the system. For simplicity, we set the hopping amplitude  $J = 1$ . Equation

(3.6) can then be written in a recursive form

$$\begin{pmatrix} \psi_{i+1} \\ \psi_i \end{pmatrix} = \hat{\mathbf{T}}_i \begin{pmatrix} \psi_i \\ \psi_{i-1} \end{pmatrix}, \quad (3.7)$$

with the random transfer matrix

$$\hat{\mathbf{T}}_i = \begin{pmatrix} \epsilon - U_i & -1 \\ 1 & 0 \end{pmatrix}. \quad (3.8)$$

To obtain the Lyapunov exponent, we have to calculate the product  $\mathbf{P}_N$  of the transfer matrices describing how a state translates through the system

$$\mathbf{P}_N = \prod_{i=1}^N \hat{\mathbf{T}}_i \quad (3.9)$$

which satisfies the Oseledec theorem [113]. This theorem states that in the case of a single Lyapunov exponent defining the localization in the system for  $N \rightarrow \infty$ , the Lyapunov exponent  $\gamma$  can be extracted from the largest eigenvalue  $\Lambda$  of the product of random transfer matrices  $\mathbf{P}_N$

$$\gamma = \frac{1}{\xi} = \lim_{N \rightarrow \infty} \frac{1}{N} \ln(\Lambda). \quad (3.10)$$

The smallest Lyapunov exponent describes longest localization length for a system in the thermodynamic limit.

### Algorithm for multiple transmission channels

In Chapter 5, we see, for the example of a Lieb ladder, how the transfer matrix is constructed and then used to calculate the localization length of a system. However, the method described above has to be adapted to account for multiple transition channels for the dispersive wavefunctions and, consequently, multiple localization lengths  $\xi_i$ . The number of channels depends on the connectivity of the hopping matrix. In order to calculate the first  $k$  leading Lyapunov exponents in a system with  $p$  channels ( $k < p$ ), we use the algorithm outlined in Ref. [113]. The sum of the first  $p$  Lyapunov exponents is given by

$$\gamma_1 + \gamma_2 + \dots + \gamma_p = \lim_{N \rightarrow \infty} \frac{1}{N} \ln \{ \text{VOL}_p [\mathbf{P}_N z^{(1)}(0), \dots, \mathbf{P}_N z^{(p)}(0)] \}, \quad (3.11)$$

where  $\text{VOL}_p [z^{(1)}(k), z^{(2)}(k) \dots z^{(p)}(k)]$  is the volume of a  $p$ -dimensional parallelepiped spanned by  $p$  different randomly chosen vectors  $z^{(q)}(k)$ . Each vector  $z^{(q)}(k)$  can be obtained from its predecessor  $z^{(q)}(k-1)$  via the recursion relation

$$z^{(q)}(k+1) = \hat{\mathbf{T}}(k) z^{(q)}(k) \quad \text{with} \quad q \in \{1, \dots, p\}. \quad (3.12)$$

Now, the extraction of Lyapunov exponents needs to follow a more subtle procedure than simple matrix multiplication: let us focus for simplicity on a single Lyapunov exponent. Calculating  $\gamma_1$  in a straightforward way by simple matrix multiplication will lead to a memory overflow as the calculation of  $\mathbf{P}_N z^{(q)}(k)$  diverges exponentially with  $\exp(\gamma_1 N)$ . To avoid the overflow, we normalize the vectors  $z^{(q)}(k)$  after a set number  $m$  of iterations:  $w^{(q)}(k) = z^{(q)}(k)/|z^{(q)}(k)|$ . The normalized vector  $w^{(q)}(k)$  is then evolved with

$$w^{(q)}(k+1) = \frac{\mathbf{P}_m^{(km)} w^{(q)}(k)}{R_m(k+1)}, \quad (3.13)$$

where  $R_m(k+1)$  ensures that the evolved vector  $w(k+1)$  is normalized to one

$$R_m(k+1) = |\mathbf{P}_m^{(km)} w^{(q)}(k)|, \quad \text{for } k \geq 1, \quad (3.14)$$

and  $\mathbf{P}_m^{(s)}$  is the product of  $m$  matrices given for the  $s$ th time the normalization procedure was applied

$$\mathbf{P}_m^{(s)} = \prod_{i=s}^{s+m} \hat{\Gamma}(i). \quad (3.15)$$

Note, to avoid exceeding the overflow limit, the number of iterations  $m$  for the normalization procedure must not be too large. The Lyapunov is then given by

$$\gamma_1 = \lim_{N \rightarrow \infty} \frac{1}{Nm} \sum_{i=1}^N \ln(R_m(i)). \quad (3.16)$$

Another problem emerges from the calculation of the second (or  $n$ th) Lyapunov exponent. When  $\gamma_1 \neq \gamma_2$ , the angle between  $\mathbf{P}_N z^{(q)}(k)$  and  $\mathbf{P}_N z^{(r)}(k)$  becomes very small and one experiences problems with the precision of the result. This can be avoided by replacing the vector  $z^{(q)}$  after every  $m$ th iteration with the orthonormalized vector  $w^{(q)}(k)$  ( $q = 1, 2, \dots, p$ ), which can be calculated by using the Gram-Schmidt algorithm. The spectrum of the Lyapunov exponents is then given by

$$\gamma_1 + \dots + \gamma_p = \lim_{N \rightarrow \infty} \frac{1}{Nm} \sum_{k=1}^N \ln \left[ \text{VOL}_p \left[ \mathbf{P}_m^{(km)} w^{(1)}(k), \dots, \mathbf{P}_m^{(km)} w^{(p)}(k) \right] \right]. \quad (3.17)$$

With this algorithm, we first compute the first Lyapunov exponent and extract the following exponents step by step from the spectrum defined in (3.17).

## 3.2 Introduction to many-body localization

Recent experimental progress in the control of cold atom quantum simulator platforms motivated the study of the statistical mechanics of isolated quantum many-body systems. From these considerations, the question arises whether localization can survive when interactions are introduced to an Anderson localized system? Already in the early 1980s, Fleishman and Anderson [114] researched the existence of localization in a weakly interacting system. More recent work [56, 58] confirmed that localization effects can occur in a disordered interacting system. Furthermore, these systems show signs of a new phase, the so-called many-body localized (MBL) phase. In the MBL phase, the system fails to thermalize and retains some memory of the initial state making these systems viable as quantum memory. Whether a system thermalizes or ends up in a localized state depends on its nature as well as the initial conditions. Changing the interaction or the disorder strength can instigate a quantum phase transition between a thermal and an MBL phase. Note, in order to change the thermalization properties of a system, the MBL transition must at least affect a great portion of the spectrum. The group of Immanuel Bloch observed MBL in a fermionic system with a quasi-random optical lattice [73]. A year later, it was possible to realize MBL in a quantum simulator with an Ising Hamiltonian and controlled random disorder [75]. The MBL phase transition was also verified in a two-dimensional bosonic system with a disordered optical lattice [76], as well as a two-dimensional fermionic lattice system [115].

In the following section, we introduce localization effects in isolated many-body systems in the presence of disorder and interactions, as well as the phase transition between an ergodic and an MBL system. We will use the concepts introduced in this chapter to investigate the localization effects of the quantum many-body model with the kinetic constraint from Chapter 6. A more detailed discussion about MBL can be found in [11, 116, 117].

### 3.2.1 Thermalization

A macroscopic system in thermal equilibrium typically displays properties that do not (or only weakly) depend on the details of the microscopic configuration and are functions instead of few macroscopic (or coarse-grained) parameters such as temperature [11, 118]. The system loses all information of the initial state in the process of thermalization by the spread of quantum entanglement; the memory of the system is fully erased (an exception being the mean energy which defines the

temperature). On macroscopic scales it is observed that, independently of the initial conditions, an isolated system typically settles/relaxes towards a thermal state. However, the information about the initial state of the system cannot be truly lost, as the time evolution is unitary. The actual thermalization of a state is a decoherent process. Thermalization in closed systems must be thought of in terms of local properties so that the system can effectively act as a reservoir for any of its smaller portions. Furthermore, the energy transport in a system undergoing thermalization has to be very efficient for states to relax to thermal equilibrium. Thermalizing quantum systems are ergodic, which means that in the long-time limit,  $t \rightarrow \infty$ , the trajectory of the system in phase space comes infinitesimally close to all possible phase space configurations.

The so-called eigenstate thermalization hypothesis (ETH) [117, 119] states in which cases the behavior of an isolated quantum system is captured by equilibrium statistical mechanics. Thus, it describes how an isolated quantum system initially prepared in a far-from equilibrium state, like a product state, can effectively approach thermal equilibrium in terms of the properties of the system's energy eigenstates. The long-time behavior of a thermalizing system following the ETH can be correctly described by a canonical, microcanonical or grand canonical ensemble. Note, there is no mathematical proof that thermalizing systems have to obey the ETH, however, many studies verify that thermalizing quantum system follow the hypothesis. Consider an isolated  $N$ -body quantum system described by the Hamiltonian  $\hat{H}$  with the eigenstates  $|\epsilon_\alpha\rangle$  and eigenenergies  $\epsilon_\alpha$ ,

$$\hat{H}|\epsilon_\alpha\rangle = \epsilon_\alpha|\epsilon_\alpha\rangle. \quad (3.18)$$

The first statement of the ETH argues that the diagonal matrix element of the local observable,  $\hat{O}_{\alpha\alpha} \simeq \langle\epsilon_\alpha|\hat{O}|\epsilon_\alpha\rangle$ , are smooth functions of the eigenenergies  $\epsilon_\alpha$ . The second ETH condition states that the off-diagonal matrix elements  $\langle\epsilon_\alpha|\hat{O}|\epsilon_\beta\rangle$  ( $\alpha \neq \beta$ ) decay exponentially fast with the microcanonical thermodynamic entropy  $S(\epsilon_{\alpha\beta})$ , where  $\epsilon_{\alpha\beta} = (\epsilon_\alpha + \epsilon_\beta)/2$  is the average energy between the levels  $|\epsilon_\alpha\rangle$  and  $|\epsilon_\beta\rangle$ . Combining the two statements the observable is given by [120, 121]

$$O_{\alpha\beta} = \mathcal{O}(\epsilon_{\alpha\beta})\delta_{\alpha,\beta} + e^{-S(\epsilon_{\alpha\beta})/2}f_O(\epsilon_{\alpha\beta},\omega_{\alpha\beta})R_{\alpha\beta}, \quad (3.19)$$

with  $\omega_{\alpha\beta} = (\epsilon_\alpha - \epsilon_\beta)$ ,  $\mathcal{O}(\epsilon_{\alpha\beta})$  and  $f_O(\epsilon_{\alpha\beta},\omega_{\alpha\beta})$  are smooth functions of the averaged energy, and  $R_{\alpha\beta}$  are random numbers with zero mean and variance one. As a result of the ETH, the expectation values of physical observables in ergodic systems, are identical with the thermal expectation values obtained by a microcanonical ensemble. The ETH also describes the behavior of the entanglement

entropy in a thermal system. We divide the quantum system into a subsystem  $A$  and the remaining system  $B$  acting as the environment. The density matrix of subsystem  $A$ ,  $\hat{\rho}_A(t) = \text{tr}_B\{\hat{\rho}(t)\}$ , is given by tracing out all the degrees of freedom of the remaining system  $B$ . In the limit of long times and large system sizes, the reduced density matrix of a thermalizing subsystem  $A$  takes the thermal form  $\hat{\rho}_A = Z^{-1} \exp(-\hat{H}/T)$  with  $\hat{H}$  being the Hamiltonian,  $T$  the temperature, and  $Z$  the partition function of the canonical ensemble. According to the ETH, subsystem  $A$  will reach thermal equilibrium in the thermodynamic limit. The Entanglement entropy between the subsystem  $A$  and the remaining system  $B$  is defined as the von Neumann entropy,  $S_A = -\text{tr}\{\hat{\rho}_A \ln \hat{\rho}_A\} = S_{A,\text{th}}$ . For a system obeying the ETH, the entanglement entropy of the subsystem  $A$  is equal to the thermodynamic entropy and therefore scales with the volume of subsystem  $A$ . The eigenstates of an ergodic system are therefore highly entangled.

### 3.2.2 Many-body localization

Disordered quantum many-body systems show non-ergodic behavior even in the presence of interactions leading to interesting localization effects. In the many-body localized phase, the system is unable to act as its own reservoir, it violates the ETH and fails to thermalize. Accordingly, the long-time behavior depends on the initial condition; the system keeps its memory and, if appropriately devised, can be utilized as storage for quantum information. The MBL phase features highly excited localized eigenstates at a finite energy density [56, 60, 72] which exhibit properties similar to those previously attributed to ground states such as area law entanglement. One of the most studied models in the context of MBL is the spin 1/2 Heisenberg chain in a random magnetic field

$$\hat{H}_{\text{HM}} = \sum_k \left( \hat{S}_k^x \hat{S}_{k+1}^x + \hat{S}_k^y \hat{S}_{k+1}^y + \hat{S}_k^z \hat{S}_{k+1}^z \right) - \sum_k h_k \hat{S}_k^z, \quad (3.20)$$

where  $\hat{S}^\alpha = \hat{\sigma}^\alpha/2$  with the standard Pauli matrices  $\hat{\sigma}^\alpha$ ,  $\alpha \in \{x, y, z\}$ , and the random magnetic fields  $h_k$  drawn from a uniform distribution with strength  $W$ ,  $h_k \in [-W, W]$ . This is a spin chain example with short-range interactions and no coupling to a bath. Depending on the initial state, the system can undergo a transition between the thermal and MBL phase by varying the disorder strength or the energy density. This phase transition is dynamic, therefore, it cannot be determined by equilibrium statistical mechanics where the quantities are averaged over an ensemble of states. However, the exact eigenstates of the many-body Hamiltonian have distinct properties in the two different phases and can be used to detect the phase transition.

Figure 3.2 illustrates the difference between the ergodic and the MBL phase. Starting from a staggered initial configuration, depending on the existence of disorder in the system, the system can either thermalize (left) or many-body localize (right) under unitary time evolution. In the ergodic case, the potential  $V(x)$  is ordered leading to thermalization in the long-time limit. All features of the initial staggered configuration are washed out and all lattice sites are equally populated yielding the uniform density distribution  $n(x)$ . When a disordered potential  $V(x)$  is introduced, the system keeps some memory of the initial configuration which can be extracted from the structured density distribution.

Analogous to the localization of the wavefunction in an Anderson-localized system, MBL states are localized in Fock or configuration space. MBL states are unable to explore the entire Fock space of a system and have a non-zero amplitude only on a small subspace consisting of the low entanglement states which are localized single-particles states. Table 3.1 gives a short summary of these properties of the MBL phase and compares them to the thermal and the Anderson localized phase.

MBL systems are closely related to integrable systems, also featuring an extensive amount of conservation laws, the so-called local integrals of motion (LIOM). The theory of LIOMs [63, 122, 123] provides a phenomenological analysis of the eigenstates in the MBL phase. We give only a brief introduction to LIOMs, as they are not used for the description of the system in Chapter 6 (due to the non-local description of our system in dual space, it is not clear how to construct LIOMs). In order to characterize an MBL system in terms of conserved quantities, we examine the regime of strong disorder, where the system is fully localized. In a spin system, the degrees of freedom are defined by Pauli operators  $\{\sigma_i^z\}$  which are referred to as p-bits (physical bits). In the MBL phase, we can introduce a complete set of localized Pauli operators  $\{\tau_i^z\}$ , the so-called l-bits which can be seen as effective spins. Defining a unitary transformation which diagonalizes the Hamiltonian  $\hat{H}_{\text{diag}} = \hat{U}^\dagger \hat{H} \hat{U}$ , allows us to introduce a representation for the complete set of local integrals of motion  $\hat{\tau}_i^z = \hat{U} \hat{\sigma}_i^z \hat{U}^\dagger$ . In the MBL phase, the  $\hat{\tau}_i$  operator is quasi-local, having support around site  $i$ , whose amplitude decreases exponentially with an increasing distance. To allow the definition of arbitrary operators in the l-bit picture, we introduce  $\hat{\tau}_i^\alpha = \hat{U} \hat{\sigma}_i^\alpha \hat{U}^\dagger$  for  $\alpha \in \{x, y, z\}$ . The Hamiltonian can be defined in terms of a complete set of LIOMs

$$\hat{H} = \hat{h}_0 + \sum_i h_i \hat{\tau}_i^z + \sum_{ij} h_{ij} \hat{\tau}_i^z \hat{\tau}_j^z + \sum_{ijk} h_{ijk} \hat{\tau}_i^z \hat{\tau}_j^z \hat{\tau}_k^z + \dots \quad (3.21)$$

The set of l-bits is complete and therefore we are able to uniquely determine

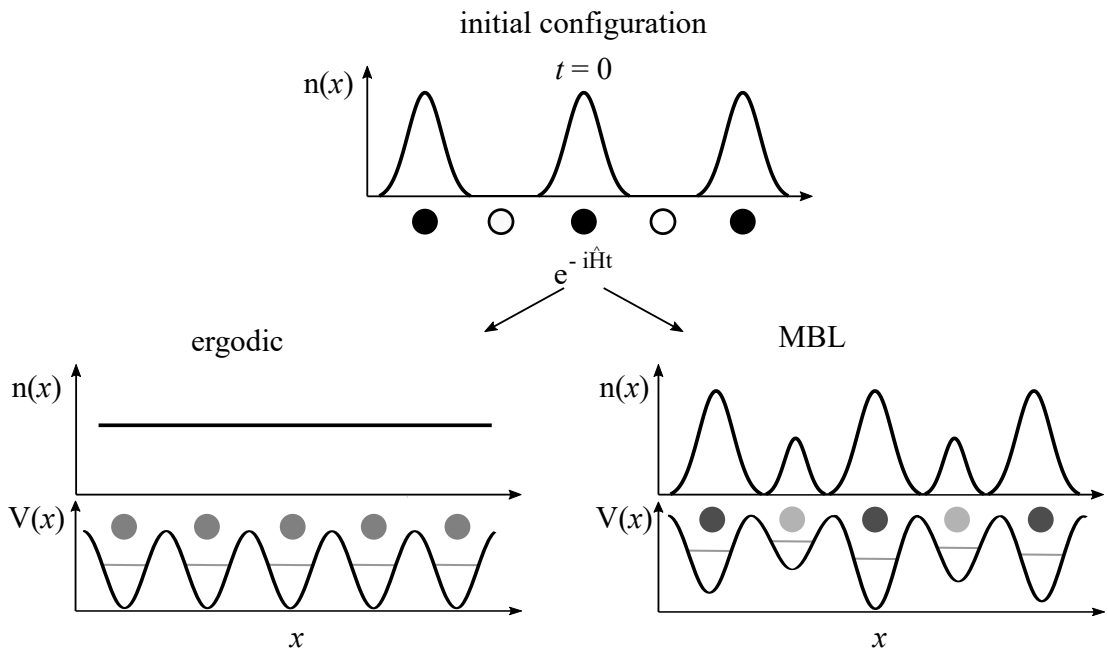


**Figure 3.2: Comparison of the density profile of an ergodic and an MBL system.** An interacting quantum system initially prepared in a staggered configuration. In a disorder-free system (left), the system thermalizes under unitary time evolution, and each lattice site is equally populated leading to a uniform density. On the other hand, when the atoms are located in a disordered potential  $V(x)$  (right), the system evolves into a many-body localized state retaining some memory of the initial state. Adapted from Ref. [5].

Thermal Phase	Anderson Localization	Many-Body Localization
No memory of initial state extractable Memory is hidden in global operators	Memory of local initial conditions preserved	Memory of local initial conditions preserved
ETH true	ETH false	ETH false
Eigenstates show volume-law scaling of EE	Eigenstates show area-law scaling of EE	Eigenstates show area-law scaling of EE
Power-law growth of entanglement in time	No entanglement growth in time	Logarithmic entanglement growth in time
Dephasing Dissipation	No dephasing No dissipation	Dephasing No dissipation
No Localization	Localization in real space	Localization in Fock/configuration space

**Table 3.1: Properties of the thermal, Anderson and MBL phase.** Comparison of the properties of the ETH, the Anderson localized and the MBL-phase (taken from Ref. [11]). Note, the third row compares the properties of the entanglement entropy (EE) as a function of system size.

the fully localized eigenstates of the Hamiltonian which are closely related to the eigenstates in the non-interacting case. From this, we can directly see, that the l-bits commute with the Hamiltonian,  $[\hat{\tau}_i^z, \hat{H}] = 0$ . Unitary time-evolution conserves the extensive number of LIOMs, thus the l-bits adopt the function of conservation laws in an integrable system, explaining the ergodicity breaking of MBL states. This results in the retaining of memory of the initial conditions. The framework of LIOMs can explain the logarithmic spread of entanglement in an MBL system in the absence of energy/particle transport [122]. In the MBL case local integrals of motion are present and the interaction between two l-bits ( $\alpha, \beta$ ) decays exponentially with the distance  $L$ ,  $V_{\alpha,\beta} \propto V_0 \exp(-L/\xi_{\text{MB}})$ , where  $\xi_{\text{MB}}$  is the MB localization length, defining the range of support of the  $\hat{\tau}^z$ . Thus, local information is distributed in a set of quantities which do not extend much beyond the original domain while in the case of an ergodic system, local information distributes on globally-extended modes and can therefore expand throughout the system. Since entanglement only spreads through an MBL system via direct local interactions the entanglement entropy (EE) shows an area-law scaling. With the framework of local integrals of motion, it is possible to obtain a full phenomenological description of MBL systems, as can be seen in Ref. [123].

As already mentioned, the phase transition between the thermal and MBL phase is very difficult to describe because it cannot be governed by equilibrium statistical mechanics. The thermal to MBL phase transition is often referred to as an *eigenstate phase transition*, as the properties of an exponential number of eigenstates at the same energy density change suddenly. The transition between an MBL to thermal phase is called a *dynamical phase transition* because it can be captured by dynamical measures.

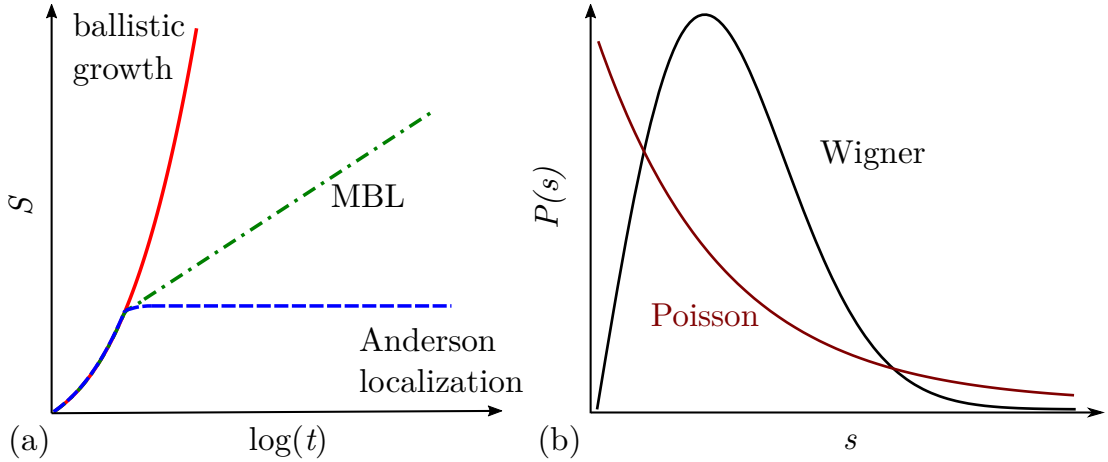


**Figure 3.3: Entanglement entropy and distribution of energy levels for ergodic and localized systems.** (a) Entanglement entropy (EE) as a function of the logarithm of the time. An ergodic system shows a ballistic growth of the EE (red). The EE in an MBL system is strongly suppressed compared to the thermalizing case; the EE growth logarithmically (green). In the case of Anderson localization, the EE saturates and does not spread through the system (blue) even for  $t \rightarrow \infty$ . (b) The spacing between adjacent energy levels  $s = \epsilon_\alpha - \epsilon_{\alpha+1}$ , in a MBL system follows a Poisson distribution (dark red), while the spacing in an ergodic system follows the Wigner distribution (black).

### Entanglement entropy

The first measure we are considering to distinguish between an ergodic and an integrable system is the entanglement entropy. We describe the properties of the EE for the example of a one-dimensional system (chain). The EE defines the spread of entanglement, hence, the spread of information throughout a system. Therefore, we partition our system in two halves  $A$  and  $B$ , with  $N = N_A + N_B$ , and determine the amount of entanglement between the two subsystems. We trace out the degrees of freedom of the second subsystem  $B$ ,  $\hat{\rho}_A = \text{tr}_B\{\hat{\rho}\}$  to define the von Neumann half-chain entanglement entropy,  $S = -\text{tr}\{\hat{\rho}_A \ln \hat{\rho}_A\}$ . In contrast to the volume-law scaling of the entanglement with subsystem size found in the ETH phase, the entanglement scales slower in the MBL phase. It shows area-law behavior even for high-energy eigenstates which is usually a ground state property of gapped Hamiltonians. Considering the time-evolution of a system, the half-chain entanglement entropy shows a logarithmic growth as a function of time in the MBL phase. Figure 3.3(a) illustrates the time-dependence of EE for an ergodic, an MBL, and an Anderson localized phase. For small times, the three phases show the same behavior, a rapid increase of the half-chain EE caused by

the expansion of the wave function. This increase of the EE continues until the wave function reaches a size of the order of the localization length. As the localization length is infinite in an ergodic system and the wavefunction is a Bloch wave extended over the entire lattice, the EE shows a ballistic growth in the long-time limit (red, solid). In the case of a non-interacting system that undergoes Anderson localization, the EE reaches, after the initial growth, a saturation value (blue, dashed) and the spread of entanglement fully stops. On the other hand, for an infinite system in the MBL phase, the logarithmic growth of the EE would continue for all times (green, dash-dotted), while in a finite system, the EE increases logarithmically until a finite saturation value is reached which depends on the system size. In the non-interacting case there is neither transport nor spread of entanglement, while in the interacting case the entanglement can still slowly spread through the system leading to the logarithmic growth in time.

### Imbalance

The imbalance can be used as a measure of the memory that a system retains of its initial conditions by determining the spatial structure. Therefore, it can distinguish between the ergodic phase, where the system thermalizes and all memory of the initial conditions are lost, and the MBL phase, where some memory of the initial state is retained. Starting in a staggered configuration,  $|\psi_S\rangle = |\uparrow\downarrow\uparrow\downarrow\cdots\rangle$ , the imbalance  $\mathcal{I}(t)$  gives the divergence as a function of time. Therefore, when the system is initially prepared in  $|\psi_S\rangle$ , the MBL phase is characterized by a non-vanishing value of the imbalance even at long times. Considering a cold-atom experiment, the imbalance is defined as the normalized difference between numbers of particles in an odd or even site

$$\mathcal{I}(t) = \frac{|N_{\text{odd}} - N_{\text{even}}|}{N_{\text{odd}} + N_{\text{even}}}. \quad (3.22)$$

### Statistics of the eigenvalue spacing

A additional measure to distinguish between the two phases is the statistical distribution of the spacing between adjacent energy levels,  $s = \epsilon_\alpha - \epsilon_{\alpha+1}$ , of the Hamiltonian. In an ergodic system, the distribution of the level spacing  $P(s)$  can be described by random matrices following the GOE, where the level spacing is distributed according to the Wigner-Dyson level statistics,

$$P_{\text{Wigner}}(s) \propto s \exp(-\pi s^2/4). \quad (3.23)$$

The probability of the spacing between neighboring energy levels is close to the Wigner surmise Fig. 3.3(b) (black) which approaches zero for a very small level

spacing. The small  $s$  behaviour of this distribution can be qualitatively explained by realizing that symmetries must be present for energy levels to cross. In their absence, crossings are avoided, resulting in a vanishing probability of finding closing gaps. This causes the strong level repulsion of the correlated energy levels. On the other hand, the level spacing of a localized and therefore integrable system, which exhibits independent random energy levels, follows Poisson statistics

$$P_{\text{Poisson}}(s) \propto \exp(-s). \quad (3.24)$$

For  $s \rightarrow 0$ , the Poisson distribution, Fig. 3.3(b) (red), gives a finite value which agrees with the observation that there is no level repulsion in a many-body localized system. Both distributions decay fast with increasing level spacing, however, the Wigner distribution decays faster than the Poisson distribution. The level statistic ratio (LSR) introduced by Oganesyanyan and Huse [58], a measure for the distribution of the energy levels which is often used for the distinction between the two phases, is independent of local averaging effects. The LSR will be introduced in more detail in Chapter 6 on the example of a spin chain with facilitation.

# Chapter 4

## Non-adiabatic quantum state preparation and quantum state transport in chains of Rydberg atoms

### 4.1 Introduction

This chapter is adapted from Ref. [1].

Building on the capabilities of optical tweezer arrays with Rydberg atoms introduced in Chapter 2, and single-site addressing for quantum information processing (QIP), we consider the engineering of the maximally entangled Greenberger-Horne-Zeilinger (GHZ) and matrix product state (MPS), and quantum state transport in a one-dimensional geometry. This particular choice is motivated by the fact that all three examples play a fundamental role in QIP, and constitute an ideal benchmark in order to assess the performance of the experimental platform we consider - an array of Rydberg atoms - for our theoretical and numerical analysis. Specifically, the GHZ state serves as a reference in quantum estimation theory yielding the Heisenberg scaling [124]. Various proposals exist in the literature for the creation of GHZ states [21, 125, 126], some of which have been realized experimentally, for example using ultracold ions [127]. Similarly, MPSs play a central role in classical simulations of quantum Hamiltonians in one dimension [128–130] and are naturally realized as ground states of some finite-range interaction spin chains [131–133], which are related to the problem of classical hardcore dimers [134]. For that reason we refer to the class of MPS considered in this thesis as dimer-MPS. Importantly, the dimer-MPS features the so-called

Rydberg crystal as a special case [28, 135–137]. Finally, faithful transport of a quantum state between different nodes of a quantum network is an essential requirement for QIP schemes such as quantum computation [138]. Various methods to achieve quantum state transport between spatially separated qubits have been proposed. These include schemes based on atoms connected through an optical link [139] or Rydberg atoms, where the transport is achieved through interaction between the Rydberg atoms and atomic ensembles which communicate through a photon exchange [140].

In this chapter, QIP is based on the Rydberg blockade mechanism, which we discussed in Chapter 2.3.3, that relies on the strong repulsive interaction between atoms excited to a Rydberg state [21]. We first introduce the protocols for the GHZ state, a dimer-MPS generation (where the dimer-MPS state is a superposition state of every possible configuration with no neighboring Rydberg excitations) and quantum state transport in the idealized limit of perfect blockade, in Chapter 4.2. In this regime the blockade mechanism can be effectively described by a three-body Hamiltonian which constitutes the basic building blocks of the studied protocols. In Section 4.3, we then investigate the influence of more realistic conditions, such as the non-perfect blockade due to the finite value of the interaction energy and the tails of the interaction. Moreover, we consider the positional disorder coming from the atoms held in optical tweezers [6] as we have seen in Chapter 2.4. There, we relax the requirement of strict blockade and consider instead an evolution guided by a more realistic system Hamiltonian including a van der Waals interatomic potential. This allows us to verify the predictions of the effective description of Section 4.2. To this end we evaluate the fidelity of the produced states with respect to the target as a function of various parameters, such as the Rabi frequency of the laser pulses, interaction strength, length and parity of the chain or the strength of the disorder. We summarize and discuss the results in Section 4.4.

## 4.2 Setup, state preparation and state transport protocols

We consider a one-dimensional chain (with open boundaries) along the  $x_3$ -direction of  $N$  optical traps, each occupied with a single atom see Fig. 4.1(a). The setup for the case of two atoms is similar to the one shown in Fig. 2.3(a). The optical

traps are separated by equal spacing  $R_0$  so that the position of the  $k$ -th atom reads  $\mathbf{r}_k = (0, 0, kR_0)$ . Each atom is described as an effective two level system, where the electronic ground state  $|\downarrow\rangle$  is coupled to the highly excited Rydberg state  $|\uparrow\rangle$  via a laser pulse with Rabi frequency  $\Omega$ . In this section we are interested in the state preparation and state transport in the context of quantum information and quantum computation, hence we use the ground state of the system as logical zero  $|\downarrow\rangle = |0\rangle$ , and the Rydberg state is used as logical one  $|\uparrow\rangle = |1\rangle$  as depicted in Fig. 4.1(b). We later account for the presence of a second hyperfine ground state  $|\tilde{1}\rangle$  coupled to the Rydberg state via a second laser with different polarization and Rabi frequency  $\tilde{\Omega}$ , see Fig. 4.1(c).

Considering that the atoms in Rydberg states interact through the van der Waals potential, the Hamiltonian of the system is given by (in the rotating wave approximation)

$$\hat{H} = \sum_{k=1}^N \hat{h}_k(\Omega_k, \Delta_k) + \hat{H}_{\text{int}}, \quad (4.1)$$

where

$$\hat{h}_k(\Omega_k, \Delta_k) = \Omega_k \hat{\sigma}_y^{(k)} + \Delta_k \hat{n}_k \quad (4.2a)$$

$$\hat{H}_{\text{int}} = \frac{1}{2} \sum_{\substack{k=1 \\ m \neq k}}^N V(d_{km}) \hat{n}_m \hat{n}_k. \quad (4.2b)$$

Here,  $k$  is the atomic position in the lattice,  $V(d_{km}) = V_0/|k - m|^6$ ,  $\hat{\sigma}_y^{(k)} = i(|1_k\rangle\langle 0_k| - |0_k\rangle\langle 1_k|)$ ,  $\hat{n}_k = |1_k\rangle\langle 1_k|$ , the parameter  $\Delta_k$  is the relative detuning of the laser from the resonant transition between the states  $|0_k\rangle$  and  $|1_k\rangle$ , and  $V_0 = C_6/R_0^6$  is the interaction strength proportional to the van der Waals coefficient  $C_6$ . Note that in (4.1) we have allowed for site-dependent Rabi frequencies and detunings  $\Omega_k, \Delta_k$ . In principle more general unitaries can be obtained by considering  $\hat{h}_k(\Omega_k, \Delta_k) = \Omega_k^x \hat{\sigma}_x^{(k)} + \Omega_k^y \hat{\sigma}_y^{(k)} + \Delta_k \hat{n}_k$ . We restrict our considerations to a coupling term proportional to  $\hat{\sigma}_y$ . This choice of the coupling term results in real GHZ and dimer-MPS states without unwanted imaginary prefactors as it would happen in the case of a coupling term  $\propto \hat{\sigma}_x^{(k)}$ . In the blockade regime where  $V_0 \gg \Omega_k, \forall k$ , the laser driving, which is proportional to  $\Omega_k$ , cannot overcome the energy cost of having two neighboring Rydberg excitations preventing two adjacent atoms from being in a Rydberg state at the same time. In this limit, it becomes convenient to adiabatically eliminate blockaded processes by applying a

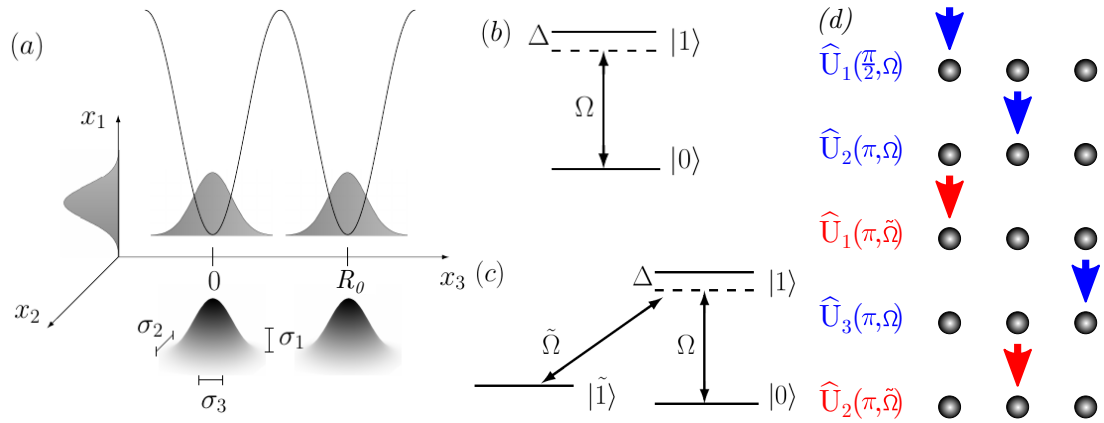


**Figure 4.1: Setup, level schemes for two and three level systems, and GHZ protocol.** (a): Setup for  $N = 2$  atoms. The optical traps are arranged along the  $x_3$  direction and are separated by  $R_0$ . The atomic positions are spread with uncertainty  $\sigma_i$  around their equilibrium values [6]. (b): Level scheme for an effective two level system, where the state  $|0\rangle$  is coupled to the Rydberg state  $|1\rangle$  by a laser with Rabi frequency  $\Omega$ . (c): Energy levels of an effective three-level system as it is assumed in the GHZ protocol, where  $\tilde{\Omega}$  couples the Rydberg state  $|1\rangle$  to another hyperfine state  $|\tilde{1}\rangle$ . (d) GHZ protocol in the three-level scheme. The blue arrows represent laser pulses coupling the  $|0\rangle \rightarrow |1\rangle$  state, while the red arrows represent laser pulses driving the  $|1\rangle \rightarrow |\tilde{1}\rangle$ . This figure is adapted from Ref. [1].

unitary transformation

$$\hat{U} = \exp \left( -itV_0 \sum_k \hat{n}_k \hat{n}_{k+1} \right), \quad (4.3)$$

on the full Hamiltonian (4.1) as introduced in Sec. 2.4. The Hamiltonian transforms in the usual way (Eq. 2.34)

$$\hat{\tilde{H}} = \hat{U}^\dagger \hat{H} \hat{U} - i\hat{U}^\dagger \left( \partial_t \hat{U} \right), \quad (4.4)$$

where the second term is trivially given by

$$-i\hat{U}^\dagger \left( \partial_t \hat{U} \right) = -V_0 \sum_k \hat{n}_k \hat{n}_{k+1}. \quad (4.5)$$

In order to calculate the first term in (4.4), we consider the action of the unitary operator on the Hamiltonian  $\hat{h}_k$  acting on site  $k$ ,  $\hat{U}^\dagger \hat{h}_k \hat{U} = \hat{U}^\dagger \left( \Omega_k \hat{\sigma}_y^{(k)} + \Delta_k \hat{n}_k \right) \hat{U}$ . The term proportional to the detuning  $\Delta$  commutes with the unitary operator  $\hat{U}$  and is therefore unaffected, thus we only need to find an expression for

$$\hat{U}^\dagger \hat{\sigma}_y \hat{U} = e^{iV_0 t \sum_k \hat{n}_k \hat{n}_{k+1}} \hat{\sigma}_y^{(k)} e^{-iV_0 t \sum_k \hat{n}_k \hat{n}_{k+1}}. \quad (4.6)$$

For this purpose, we perform a Taylor expansion of the unitary operator  $\hat{U}^\dagger$  (and analogously on  $\hat{U}$ )

$$e^{iV_0 t \sum_k \hat{n}_k \hat{n}_{k+1}} = 1 + \sum_{m=1}^{\infty} \frac{1}{m!} (iV_0 t)^m \left( \sum_k \hat{n}_k \hat{n}_{k+1} \right)^m. \quad (4.7)$$

Neglecting terms oscillating at the frequencies  $V_0$  (RWA) we obtain

$$\hat{U}^\dagger \hat{\sigma}_y^{(k)} \hat{U} \approx \hat{P}_{k-1} \hat{\sigma}_y^{(k)} \hat{P}_{k+1}, \quad (4.8)$$

where  $\hat{P}_k = (\mathbb{1} - \hat{n}_k)$  are the projectors on ground-state atoms. This leads to the Hamiltonian in the interaction picture

$$\hat{H}_I \approx \sum_{k=1}^N \left( \Omega \hat{\sigma}_y^{(k)} (1 - \hat{n}_{k-1})(1 - \hat{n}_{k+1}) + \Delta_k \hat{n}_k + \frac{V_0}{64} \hat{n}_k \hat{n}_{k+2} \right). \quad (4.9)$$

The nearest-neighbour term is by construction cancelled in this picture (see Eq. 4.5). Since all remaining terms are rapidly suppressed with increasing distance between excited atoms, we neglect them. Furthermore, considering a resonant excitation of the atoms  $\Delta_k = 0$ ,  $\forall k$ , one can derive an effective three-body Hamiltonian making the blockade mechanism manifest [131]

$$\hat{H} = \sum_{k=1}^N \hat{h}_k^{\text{3body}}, \quad (4.10)$$

with  $\hat{h}_k^{3\text{body}} = \Omega_k \hat{P}_{k-1} \hat{\sigma}_y^{(k)} \hat{P}_{k+1}$ . The associated unitary evolution corresponding to the application of a laser pulse of duration  $t_k$ , and area  $A_k = \Omega_k t_k$ , on the  $k$ -th atom on the  $|l\rangle - |l'\rangle$  transition reads

$$\hat{U}_k^{ll'}(A_k) = \exp(-i t_k \hat{h}_k^{3\text{body}}) = \mathbb{1} - \hat{P}_{k-1} \hat{P}_{k+1} + \hat{P}_{k-1} \hat{P}_{k+1} e^{-i t_k \Omega_k \hat{\sigma}_y^{(k)}}, \quad (4.11)$$

and represents the basic building block of the protocols studied in this thesis. The indices  $ll' \in \{01, 1\tilde{1}\}$  on the left-hand side of (4.11) label the basis in which the operators are expressed as defined in Fig. 4.1 (c). For example,  $\hat{U}_k^{01}$  means that the operators  $\hat{P}_k = \mathbb{1} - \hat{n}_k$  and  $\hat{\sigma}_y^{(k)}$  on the right-hand side of (4.11) act upon the  $\{|0\rangle, |1\rangle\}$  basis. We note that for  $A_k = \pi$ , the unitary (4.11) corresponds to the Toffoli gate, which we recall in Appendix B.1, with  $k$  the target and  $k-1, k+1$  the control atoms. In the following we shall refer to the preparation procedure as *non-adiabatic* meaning that the state of the system evolves in a step-wise manner after every application of a gate of the form (4.11), or any other local gate, and in general is not an eigenstate of the Hamiltonian (4.1). This has to be contrasted with adiabatic protocols, where the final state is the ground state of the Hamiltonian whose parameters are adiabatically deformed, starting from an initial ground state that is easy to prepare.

Before we introduce the state preparation and state transport protocols, a comment is in place. The reason for considering the auxiliary hyperfine state  $|\tilde{1}\rangle$  is to avoid undesirable effects such as spontaneous emission from atoms in the Rydberg levels or atomic loss, and dephasing due to mechanical forces acting on the atoms like van der Waals repulsion [141, 142], and collisions with the background gas. This can be achieved in the three-level scheme when the atomic population is transferred from the Rydberg level  $|1\rangle$ , after it has been used to implement a particular gate, as fast as possible to the stable hyperfine state  $|\tilde{1}\rangle$ . However, in order to reduce the complexity of the experiments, which may be important for first proof-of-principle demonstrations, and to further reduce the number of applied gates, we will consider the two-level configuration as well, where only the ground and Rydberg levels  $|0\rangle, |1\rangle$  are involved. More specifically, we describe the use of both the three and two-level schemes on the example of the GHZ state preparation protocol in Section 4.2.1 and discuss the differences between the two schemes in Section 4.3.1. For the reasons mentioned above, we limit the discussion of the dimer-MPS preparation and state transport protocols to the two-level scheme only.

### 4.2.1 GHZ state preparation

We consider the non-adiabatic preparation of antiferromagnetic GHZ states of the form

$$|\text{GHZ}\rangle = \frac{1}{\sqrt{2}} (|0_1 \tilde{1}_2 0_3 \dots \tilde{1}_N\rangle + |\tilde{1}_1 0_2 \tilde{1}_3 \dots 0_N\rangle). \quad (4.12)$$

They are robust with respect to global noise, such as magnetic or electric field fluctuations on length-scales larger than the length of the chain, as the two components of the state are energetically degenerate. Using encoding in the basis  $|0\rangle, |\tilde{1}\rangle$  (see Fig. 4.1 (c)), this is only strictly true when  $N$  is even as there is the same number of excitations, atoms in the state  $|\tilde{1}\rangle$ , in both components of the GHZ state (4.12).

Initially all atoms are prepared in the ground state  $|\Psi_{\text{in}}\rangle = |000\dots 0\rangle$ . First we apply a  $\pi/2$  pulse  $\hat{U}_1^{01}(\frac{\pi}{2})$  on the first atom to generate a superposition state

$$|\Psi_1\rangle = \hat{U}_1^{01}\left(\frac{\pi}{2}\right) |\Psi_{\text{in}}\rangle = \frac{1}{\sqrt{2}}(|000\dots 0\rangle + |100\dots 0\rangle). \quad (4.13)$$

This is followed by the application of a  $\pi$ -pulse  $\hat{U}_2^{01}(\pi)$  on the second atom

$$|\Psi_2\rangle = \hat{U}_2^{01}(\pi) |\Psi_1\rangle = \frac{1}{\sqrt{2}}(|010\dots 0\rangle + |100\dots 0\rangle). \quad (4.14)$$

Note that, due to the blockade mechanism, the second term on the right hand side of (4.13) is not affected by the second pulse. We then return to the first atom and apply a  $\pi$ -pulse on the  $|\tilde{1}\rangle - |1\rangle$  transition in order to transfer any population in its Rydberg level to the hyperfine state  $|\tilde{1}\rangle$  so that

$$|\Psi_3\rangle = \hat{U}_1^{1\tilde{1}}(\pi) |\Psi_2\rangle = \frac{1}{\sqrt{2}}(|010\dots 0\rangle - |\tilde{1}00\dots 0\rangle). \quad (4.15)$$

This is followed by the application of  $\hat{U}_3^{01}(\pi)$  on the third atom and  $\hat{U}_2^{1\tilde{1}}(\pi)$  on the second atom and so forth until the end of the chain is reached after  $2N - 1$  gates (unitaries) have been applied. The procedure is summarized in Table 4.1 and illustrated in Fig. 4.1(d). We note that a similar proposal for the preparation of a ferromagnetic GHZ state was put forward recently in [126].

With the GHZ state preparation protocol just described, the Rydberg state  $|1\rangle$  appears neither in the initial nor final state, Eq. (4.12). It is simply exploited to implement the constrained spin flipping which allows the reconstruction the GHZ pattern in the two components of the state. A simplified two-level version of this protocol, where only levels  $|0\rangle$  and  $|1\rangle$  are used, is obtained simply by neglecting the transfer from the Rydberg to the hyperfine state, i.e. omitting step (iv) in Table 4.1.

	GHZ	dimer-MPS	Transport
$ \Psi_{\text{in}}\rangle$	$ 000\dots 0\rangle$	$ 000\dots 0\rangle$	$ \psi 00\dots 0\rangle$
(i)	apply $\hat{U}_1^{01}(\frac{\pi}{2})$	set counter to $k = 1$	set counter to $k = 1$
(ii)	set counter to $k = 1$	apply pulse of area $A_k$ on atom $k$ [see Eqs. (4.24)]	apply $\pi$ -pulse on atom $k + 1$
(iii)	apply $\hat{U}_{k+1}^{01}(\pi)$ if $k = N$ do nothing	$k \Rightarrow k + 1$ go back to (ii) until $k = N$ then stop	apply $\pi$ -pulse on atom $k$
(iv)	apply $\hat{U}_k^{1\bar{1}}(\pi)$		$k \Rightarrow k + 1$ go back to (ii) until $k = N$ then stop
(v)	move to next atom  $k \Rightarrow k + 1$ repeat (iii) - (v) until $k = N$		apply $(i^{N-1}\hat{\sigma}_y^{(N)})$ for $N$ even, see end of Sec. 4.2.2
# of applied pulses	$2N - 1$	$N$	$2N - 2$

**Table 4.1: Protocol for the GHZ and MPS state preparation, and the state teleportation.** Pulse sequence for the preparation of a GHZ state (left column), the dimer-MPS state (middle column) and the state transport (right column) in a chain of  $N$  Rydberg atoms. In the case of the GHZ state, the Rydberg atoms are described as an effective three-level system. However, the GHZ protocol can also be adapted to a two-level description of the atoms by neglecting step (iv). For the dimer-MPS as well as the state transport protocol, each atom is approximated as a two-level system.  $|\Psi_{\text{in}}\rangle$  is the initial state for the particular protocol. Taken from Ref. [1].

### 4.2.2 Dimer-MPS preparation

It seems natural to explore the effective three-body interaction  $\hat{h}_k^{3\text{body}}$  used in the GHZ state preparation for the creation of various other quantum states. Specifically, we note that the perfect blockade and the associated Hamiltonian (4.10), in principle, allow the creation of all possible configurations which are compatible with the dimer-MPS protocol, given in Table 4.1. More precisely, in the blockade regime, simultaneous excitations of adjacent atoms are strongly suppressed, confining the dynamics to subspaces where the number of neighboring excitations is constant. In particular, the subspace we work in displays all Rydberg excitations separated by at least one site. We describe how to produce a specific example of such a quantum state which is defined as

$$|z\rangle = \frac{1}{\sqrt{Z_z}} \prod_{k=1}^N (\mathbb{1} + z \hat{P}_{k-1} \hat{\sigma}_k^+ \hat{P}_{k+1}) |0 \dots 0\rangle. \quad (4.16)$$

Here,  $z$  is a real number parametrizing the state,  $\hat{P}_k = (\mathbb{1} - \hat{n}_k) = |0_k\rangle \langle 0_k|$  is the projector on the atomic ground state introduced in Eq. (4.8) and  $Z_z$  is an overall normalization constant ensuring  $\langle z|z\rangle = 1$ . The state (4.16) is a superposition of all possible configurations without adjacent Rydberg excitations, where each configuration is weighted by  $z^n$  with  $n$  the total number of (isolated) excitations in it. An illustration of  $|z\rangle$  is provided in Fig. 4.2(a). Specifically, for  $z = 0$ ,  $|z\rangle$  is the product state  $|000 \dots 0\rangle$ , without any entanglement. For  $z = 1$ , all possible components are equally weighted, whereas for  $z \gg 1$  the ones with higher number of excitations dominate. Note that for odd  $N$  and  $z \rightarrow \infty$ , the corresponding dimer-MPS state is a single antiferromagnetic configuration where all odd sites, including the first and the last, have an excited atom. Such an alternating configuration constitutes an example of a so-called Rydberg crystal. However, this state is completely separable and holds no entanglement at all. For the scope of this work, it is therefore convenient to focus on the complementary case. For even  $N$ , the major contribution will instead be given by the  $N/2 + 1$  configurations with  $N/2$  excitations.

It has been shown in [132] that the state (4.16) admits a matrix product representation

$$|z\rangle = \frac{1}{N} \sum_{i_1, \dots, i_N=0,1} [\vec{l} \cdot \hat{X}_{i_1} \hat{X}_{i_2} \dots \hat{X}_{i_N} \cdot \vec{r}] |i_1 i_2 \dots i_N\rangle, \quad (4.17)$$

with the two  $2 \times 2$  matrices  $\hat{X}_0 = (\mathbb{1} - \hat{n}) + z \hat{\sigma}^-$ ,  $\hat{X}_1 = \hat{\sigma}^+$ , and the ladder operators  $\hat{\sigma}_\pm = (\hat{\sigma}_x \pm i \hat{\sigma}_y)/2$ . The vectors  $\vec{l} = (z, 1)$  and  $\vec{r} = (0, 1)$  are included to impose the correct boundary conditions.

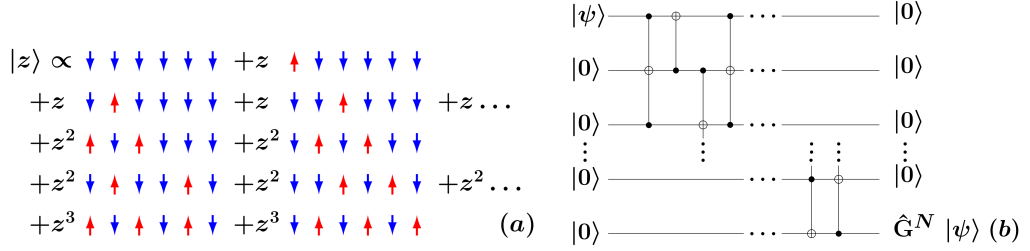


**Figure 4.2: Representation of the MPS preparation and state transport protocol.** (a): Representation of the dimer-MPS for a chain of  $N = 6$  atoms. This state is a superposition of all possible configurations without neighboring Rydberg excitations. The parameter  $z$  is weighting the number of excitations in the particular component of the superposition state. (b): Circuit for the transport of a single qubit state  $|\psi\rangle$  from the first to the  $N$ th qubit in the chain. All qubits except the first one, are prepared in the ground state. The CNOT gate as well as the Toffoli gate correspond to a  $\pi$ -pulse with Rabi frequency  $\Omega$  applied to the particular atom. In the post processing, the  $\hat{G}^N$ -gate is applied to the state on the  $N$ th qubit, in order to obtain the correct state  $|\psi\rangle$ . Taken from Ref. [1].

Furthermore, the same construction leading to (4.16) can be generalized to the case of a blockade extending over  $R$  sites, i.e. an excitation prevents its first  $R$  neighbors from being excited [133]. The analog of the state (4.16) then reads

$$|z\rangle = \frac{1}{\sqrt{Z_z}} \prod_{k=1}^N (\mathbb{1} + z \hat{P}_{k,\text{left}} \hat{\sigma}_k^+ \hat{P}_{k,\text{right}}) |0 \dots 0\rangle, \quad (4.18)$$

where  $\hat{P}_{k,\text{left}} = \prod_{j=1}^R \hat{P}_{k-j}$ ,  $\hat{P}_{k,\text{right}} = \prod_{j=1}^R \hat{P}_{k+j}$  and  $Z_z$  is the corresponding normalization constant. This state again admits a MPS representation (4.17) in which  $\hat{X}_0$  and  $\hat{X}_1$  are  $(R+1) \times (R+1)$  matrices and  $\vec{l}$  and  $\vec{r}$  are  $(R+1)$ -vectors [133]. As a final remark before describing the state preparation protocol, we would like to mention that the states (4.16) and (4.18) are directly related to the ground states of the Hamiltonian (4.1).

In the following, we show that a state of the form (4.16), for  $R = 1$ , can be generated via an appropriate sequence of pulses. Appendix B.2.1 introduces a more general procedure which applies to generic  $R$ . As a first step, we consider how a local pulse of area  $A_k = \Omega_k t_k$  acts on a ground state atom located in site  $k$ . If the  $k$ -th atom is blockaded, i.e., if there is an excitation to its left and/or right, then

$$\hat{U}_k^{01}(A_k) |0_k\rangle = |0_k\rangle, \quad (4.19)$$

whereas if it is not

$$\hat{U}_k^{01} |0_k\rangle (A_k) = \cos A_k |0_k\rangle + \sin A_k |1_k\rangle. \quad (4.20)$$

The excited component in  $k$  will then blockade the following site, so that

$$\begin{aligned} \hat{U}_{k+1}^{01}(A_{k+1}) \hat{U}_k^{01}(A_k) |0_k 0_{k+1}\rangle &= \cos A_k \cos A_{k+1} |0_k 0_{k+1}\rangle + \cos A_k \sin A_{k+1} |0_k 1_{k+1}\rangle \\ &+ \sin A_k |1_k 0_{k+1}\rangle. \end{aligned} \quad (4.21)$$

Applying an ordered sequence of local pulses from the first to the last atom  $\hat{U} = \prod_{k=N}^1 \hat{U}_k^{01}$  on the global atomic ground state  $|0_1 \dots 0_N\rangle$  will generally yield components on all elements of the basis in which no neighboring pairs of excitations appear. From Eq. (4.20) it is not difficult to see that the component over the initial state will be  $C_0 \equiv \prod_{k=N}^1 \cos A_k$ . An excitation in, site  $j$  will instead obtain a  $\sin A_j$  and will lose, with respect to the coefficient  $C_0$ , a factor  $\cos A_{j+1}$ . Using this simple rule, we can work out that the ratio between the component of a generic basis element  $C^{(\vec{n})}$  with  $n$  (non-neighboring) excitations in  $\vec{n} = \{j_1, \dots, j_n\}$  and  $C_0$  will be given by

$$\frac{C^{(\vec{n})}}{C_0} = \prod_{\mu=1}^n \left( \frac{\sin A_{j_\mu}}{\cos A_{j_\mu} \cos A_{j_\mu+1}} \right). \quad (4.22)$$

In order to correctly reproduce state  $|z\rangle$ , this ratio must be set to be equal to  $z^n$ . The only way for this to hold for every possible number  $n$  of excitations is to have

$$\frac{\sin A_j}{\cos A_j \cos A_{j+1}} = z \quad \forall j. \quad (4.23)$$

This defines a recursion relation for  $A_j$  in terms of  $A_{j+1}$ . The natural boundary condition to provide a seed to the recursion is

$$\cos(A_{N+j}) = 1 \quad \forall j > 0, \quad (4.24)$$

which corresponds to requiring that, should the excitation protocol stop before reaching the actual end of the chain, all atoms which have not been addressed should still be in their ground state. Equations (4.23) and (4.24) can be analytically solved to yield

$$\cos A_k = \sqrt{2 \frac{(1 + \sqrt{1 + 4z^2})^{N+2-k} - (1 - \sqrt{1 + 4z^2})^{N+2-k}}{(1 + \sqrt{1 + 4z^2})^{N+3-k} - (1 - \sqrt{1 + 4z^2})^{N+3-k}}}. \quad (4.25)$$

Together with the relation  $\text{sign}(\sin A_k) = \text{sign}(z)$ , the above expressions provide a unique way to extract the pulse areas  $A_k$ . Using the values so obtained in the protocol described in Table 4.1 will yield state  $|z\rangle$ .

### 4.2.3 Quantum state transport

In this section we discuss a protocol for the coherent transport of a single qubit state between the two ends of the chain (last column of Table 4.1). We consider a state  $|\psi_1\rangle = \alpha|0\rangle + \beta|1\rangle$  to be initialized at the first qubit so that the total initial state reads

$$|\Psi_{\text{in}}\rangle = (\alpha|0\rangle + \beta|1\rangle)_1 \otimes |0_2 0_3 \dots 0_N\rangle. \quad (4.26)$$

The circuit representation of the state transport protocol is shown in Fig. 4.2(b). The protocol relies on a sequence of three-body Toffoli gates (cf. Eq. (4.10) and Appendix B.1), which, when applied at the two ends of the chain, become effectively CNOT gates due to the absence of one of the sites. In our implementation, the Toffoli and the CNOT gate flip the target qubit if the controlled qubits are in the ground state  $|0\rangle$ .

The first step is the application of a  $\pi$  pulse on the second qubit

$$|\Psi_1\rangle = \hat{U}_2^{01}(\pi) |\Psi_{\text{in}}\rangle = \alpha|010\dots 0\rangle + \beta|100\dots 0\rangle. \quad (4.27)$$

As a second step, a  $\pi$ -pulse is applied on the first atom

$$|\Psi_2\rangle = \hat{U}_1^{01}(\pi) |\Psi_1\rangle = \alpha|010\dots 0\rangle + \beta|000\dots 0\rangle, \quad (4.28)$$

which is then followed by the application of a  $\pi$  pulse on the third qubit

$$|\Psi_3\rangle = \hat{U}_3^{01}(\pi) |\Psi_2\rangle = \alpha|010\dots 0\rangle + \beta|001\dots 0\rangle, \quad (4.29)$$

and so on, cf. the steps (ii)-(iv) in Table 4.1, which are repeated until the end of the chain is reached. At this stage, the initial state  $|\psi_1\rangle$  has been successfully transferred so that the state of the  $N$ -th qubit reads

$$|\psi_N\rangle = \begin{cases} i^{N+1} \hat{\sigma}_y |\psi_1\rangle & N \text{ even} \\ |\psi_1\rangle & N \text{ odd.} \end{cases} \quad (4.30)$$

The presented state transport protocol requires  $(2N-2)$  laser pulses and is deterministic since the only required information is the length of the spin chain, with no need for a classical communication between the two ends of the chain [143].

## 4.3 Imperfections

The above presented protocols for quantum state transport, GHZ and dimer-MPS preparation rely on two important assumptions, namely that the blockade

mechanism between two adjacent atoms excited to a Rydberg state is perfect and that the atoms are equally spaced in the chain. Here we analyze in detail the limitations of the protocols when these assumptions are relaxed. Namely when the blockade becomes non-perfect due to the finite interaction strength between nearest-neighbors, and when accounting for interactions beyond nearest-neighbors. Furthermore, disorder in atomic positions coming from the finite temperature of the atoms and non-vanishing width of the optical traps can cause a non-perfect Rydberg blockade. We comment on other sources of imperfections, such as the influence of relaxation processes, at the end of this section.

### 4.3.1 Non-perfect Rydberg blockade

The non-perfect blockade is accounted for by considering the full Hamiltonian (4.2) featuring van der Waals interaction between all of the atoms excited to a Rydberg state. In this case, when a pulse of area  $A_k = \Omega_k t_k$  is applied to the  $k$ -th atom, the idealized unitary gate (4.11) becomes

$$\hat{W}_k^{01}(A_k = \Omega_k t_k) = \exp \left[ -i t_k \left( \hat{h}_k(\Omega_k, \Delta_k = 0) + \hat{H}_{\text{int}} \right) \right]. \quad (4.31)$$

We find that, the full Hamiltonian (4.2) amounts simply to replacing the unitary gates  $\hat{U} \rightarrow \hat{W}$  in Table 4.1, which are operators acting on the full Hilbert space of dimension  $2^N$ . The non-perfect blockade results in configurations with adjacent Rydberg excitations. This limits the fidelity of the produced states defined as

$$F \equiv \langle \Psi_{\text{target}} | \rho_{\text{final}} | \Psi_{\text{target}} \rangle, \quad (4.32)$$

where  $\rho_{\text{final}}$  is the state at the output of the particular protocol described in Table 4.1, and  $|\Psi_{\text{target}}\rangle$  is the desired target state. We note that  $\rho_{\text{final}} = |\Psi_{\text{final}}\rangle \langle \Psi_{\text{final}}|$  is pure by construction for the GHZ and dimer-MPS protocol as it is defined on all atoms of the chain; on the other hand, it is generally mixed for the transport protocol as we trace over all but the last qubit. We will then consider the Rabi frequency  $\Omega$  to be identical for all atoms. We also neglect the effect of the decay of the Rydberg states, which we justify in Section 4.3.3.

### GHZ state preparation

We start our analysis by examining the influence of the non-perfect Rydberg blockade on the GHZ state preparation described in the first column of Table 4.1 with the replacement  $\hat{U}^{01} \rightarrow \hat{W}^{01}$ , and where  $|\Psi_{\text{target}}\rangle = |\text{GHZ}_N\rangle$  (we recall that here  $N$  is even). The effect of the finite interaction strength can be seen in

Fig. 4.3, where we plot the fidelity (4.32) as a function of the ratio of the nearest-neighbor interaction strength and the Rabi frequency  $V_0/\Omega$ . Fig. 4.3a shows a situation when using the two-level scheme. Fig. 4.3(b) then the fidelity in the three-level scheme, where the atoms are transferred from the Rydberg state  $|1\rangle$  to the hyperfine state  $|\tilde{1}\rangle$ .

It is apparent from Fig. 4.3 that in the limit  $V_0/\Omega \rightarrow 0$ , i.e. in the absence of the blockade, the fidelity goes to zero in all cases (except  $N = 2$  in the three-level scenario, where it is straightforward to show that  $F \rightarrow 1/4$ ). In the opposite limit of the infinite blockade  $V_0/\Omega \rightarrow \infty$ , the vanishing of the fidelity in the two-level scenario can be easily understood as the blockade length extends over the whole chain, thus allowing for at most a single Rydberg excitation to be present. In contrast, in the three-level scenario there is never more than one atom in the Rydberg level at any given time, which results in unit fidelity in that limit.

For intermediate values of  $V_0/\Omega$ , one can observe oscillations of the fidelity  $F$ . The origin of those oscillations can be understood using the example of two atoms (cf. the magenta line in Fig. 4.3). Here the final state is obtained after application of one pulse at each atom and reads

$$|\Psi_{\text{final}}\rangle = \hat{W}_2^{01}(\pi) \hat{W}_1^{01}\left(\frac{\pi}{2}\right) |00\rangle = \frac{1}{\sqrt{2}} (|01\rangle + \gamma |10\rangle + \delta |11\rangle), \quad (4.33)$$

where

$$\gamma = e^{-i\frac{\pi V_0}{8\Omega}} \left( \cos\left(\pi\frac{\tau}{8\Omega}\right) + \frac{iV_0 \sin\left(\frac{\pi\tau}{8\Omega}\right)}{\tau} \right), \quad (4.34a)$$

$$|\delta| = \sqrt{1 - |\gamma|^2}, \quad (4.34b)$$

$$\tau = \sqrt{V_0^2 + 16\Omega^2}. \quad (4.34c)$$

The term  $\delta |11\rangle$  in (4.33) occurs due to the finiteness of the interaction strength  $V_0$ , and reduces the fidelity of the produced state (4.32), which reads

$$F_{N=2} = \frac{1}{4} |1 + \gamma|^2. \quad (4.35)$$

If the argument of the trigonometric functions (4.34)(a) is chosen in such a way that the second term ( $\propto \sin$ ) vanishes then one obtains the maximal fidelity. Although the fidelity depends on atom number, the position of the oscillation maxima are robust. Thus the expressions (4.34) provide accurate estimates (which become exact for  $N = 2$ ) for the values of  $V_0/\Omega$  that maximize the fidelity.

### Dimer-MPS preparation

In analogy to the GHZ case, we investigate the effect of the non-perfect Rydberg blockade on the fidelity of the dimer-MPS state by applying the protocol described

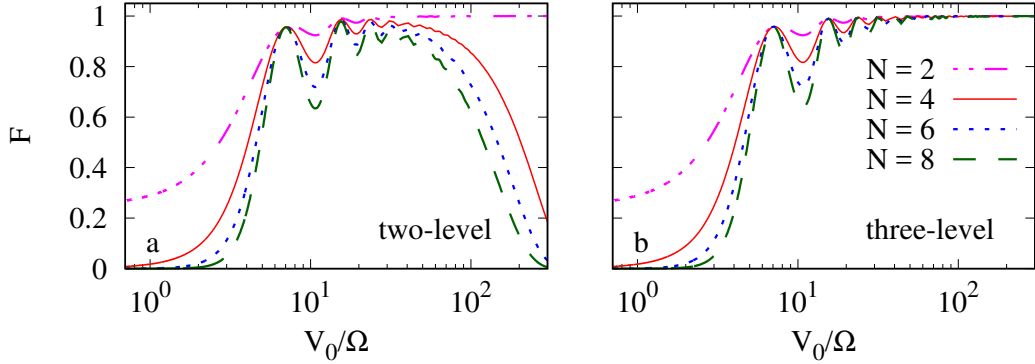


**Figure 4.3: Fidelity of the GHZ state preparation protocol for a two-level, and three-level atom.** Fidelity of the GHZ state preparation protocol for a two-level description of the atoms (a), as well as the three-level scheme (b) as a function of  $V_0/\Omega$ . In the three-level implementation of the protocol, atoms are excited to the Rydberg state to effectuate the blockade mechanism and are subsequently transferred to a stable hyperfine state, see text for details. The fidelity is given for chains of length  $N = 2, 4, 6, 8$ , respectively. Taken from Ref. [1].

in the second column of Table 4.1, where  $|\Psi_{\text{final}}\rangle = |z\rangle$ , using Eq. (4.17) and replacing  $\hat{U}^{01} \rightarrow \hat{W}^{01}$ . Fig. 4.4 shows the influence of the non-perfect Rydberg blockade on the dimer-MPS state preparation protocol on the example of  $z = 0.1, 0.5, 1, 10$ , for  $N = 2$  to  $N = 7$  atoms in a chain, respectively. For  $z = 0.1$  (Fig. 4.4(a)) the fidelity is approximately one over the whole parameter range. This is a consequence of the dominant term in the state (4.17), for  $z \ll 1$ , being the vacuum state where all atoms are in the ground state  $|0\rangle$  and therefore not affected by the blockade mechanism.

When increasing  $z$ , terms containing more and more atoms in the Rydberg state  $|1\rangle$  are becoming relevant. In the limiting situation  $z \gg 1$ , the dimer-MPS is dominated by terms containing  $N/2$  excitations for even and  $(N+1)/2$  excitations for odd chains. Similarly to the GHZ case, the drop of fidelity for small (large)  $V_0/\Omega$  is due to non-perfect blockade where the blockade extends beyond nearest-neighbor.

We indicate by vertical lines in Fig. 4.4(b-d) the values of  $\Omega = V_{\text{NN}} = V_0$  and  $\Omega = V_{\text{NNN}}$  corresponding to the interaction energies of nearest neighbor and next-to-nearest neighbor excitations, respectively. We expect to find the optimal fidelity within the region of these two boundaries. In fact, for  $\Omega \gg V_{\text{NN}}$  the blockade is relaxed and pairs of neighboring excitations are frequently produced.

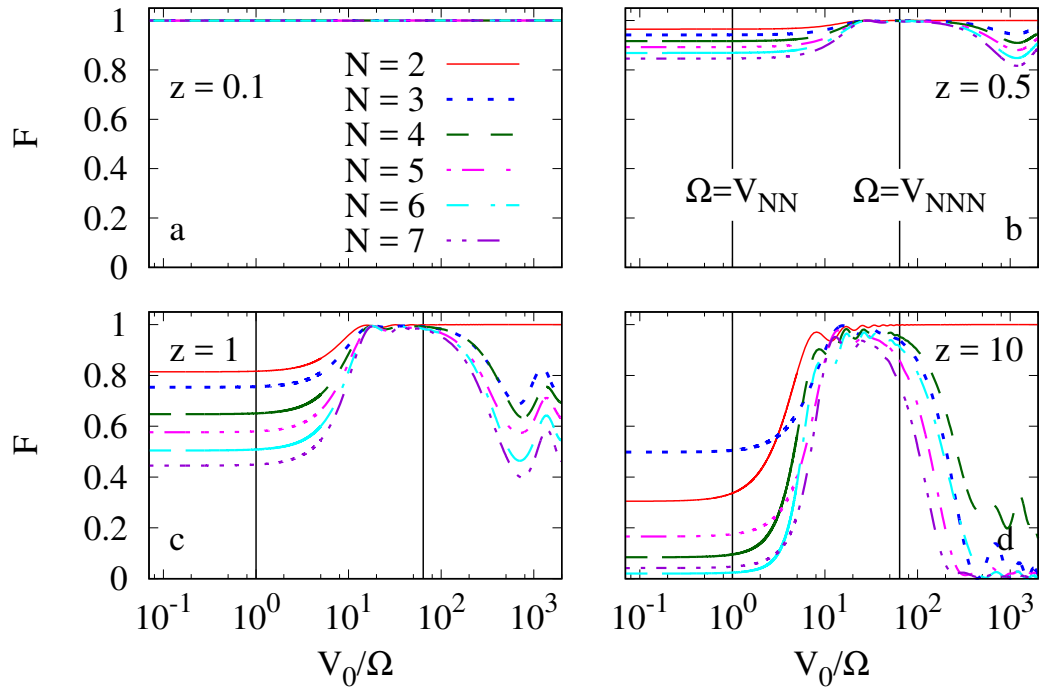


**Figure 4.4: Fidelity of the dimer-MPS preparation protocol.** Fidelity of the dimer-MPS preparation protocol for  $N = 2$  up to  $N = 7$  atoms as a function of  $V_0/\Omega$  and for  $z=0.1, 0.5, 1, 10$  (a-d). See text for details (Taken from Ref. [1]).

Conversely, for  $\Omega \ll V_{\text{NNN}}$ , the next-to-nearest neighbor interaction (partially) blockades atoms two lattice sites away from an excitation, again negating the state preparation procedures described above.

### Quantum state transport

Using the notation from Sec. 4.2.2, the target state is the state of the first atom,  $|\Psi_{\text{target}}\rangle = |\psi_1\rangle$ , while the final, single-qubit state,  $\rho_{\text{final}} = \text{Tr}_{\neq N}(|\psi_t\rangle\langle\psi_t|)$ , is obtained by tracing out all but the  $N$ -th atom. The state  $|\psi_t\rangle$  is obtained when applying the transport protocol with  $\hat{U}^{01} \rightarrow \hat{W}^{01}$  on the target state. Fig. 4.5a shows the fidelity of the transport process for an initial state

$$|\psi_1\rangle = \frac{1}{\sqrt{2}}(|0\rangle + |1\rangle)$$

at the first atom, for  $N = 4, 5, 6$ . The decrease in the fidelity and the oscillations in the small and large  $V_0/\Omega$  limit have the same origin as in the case of dimer-MPS and GHZ state preparation. A vanishing blockade for  $V_0/\Omega \rightarrow 0$  and an imperfect blockade due to the finiteness of  $V_0$ , respectively. Next, in order to demonstrate the influence of the initial state on the resulting fidelity, we plot the fidelity as a function of  $V_0/\Omega$  in Fig. 4.5(b) for  $|\psi_1\rangle = \alpha|0\rangle + \beta|1\rangle$ ,  $\beta = \sqrt{1 - |\alpha|^2}$ , for  $\alpha = -0.7, 0, 0.7$ . It can be seen that in the parameter regime of interest ( $V_0/\Omega \gtrsim 5$ ), the maxima of the fidelity coincide for the considered  $\alpha$ . As in the GHZ case, the nature of the observed oscillations can be exemplified on the elementary example of two atoms for which we get

$$\hat{W}_1^{01}(\pi)\hat{W}_2^{01}(\pi)|\Psi_1\rangle = \alpha(\gamma|01\rangle + \gamma'|11\rangle) + \beta(\delta|00\rangle + \delta'|11\rangle + \delta''|01\rangle),$$

where  $\gamma, \delta$  are given by (4.34) and

$$|\gamma'| = \sqrt{1 - |\gamma|^2}, \quad (4.36a)$$

$$\delta' = \frac{2e^{-\frac{i\pi V_0}{4\Omega}} \Omega \left( -iV_0 + iV_0 \cos\left(\frac{\pi\tau}{4\Omega}\right) + \tau \sin\left(\frac{\pi\tau}{4\Omega}\right) \right)}{\tau^2}, \quad (4.36b)$$

$$\delta'' = \sqrt{1 - |\delta|^2 - |\delta'|^2}. \quad (4.36c)$$

In the case of a perfect Rydberg blockade, only the terms  $\alpha\gamma|01\rangle$  and  $\beta\delta|00\rangle$  would occur after the application of the two laser pulses.

### 4.3.2 Non-perfect blockade and position disorder

As described in Section 2.4, a source of disorder in a realistic experiment originates from the uncertainty of the position of the atoms in the trap  $\mathbf{r}_k = \mathbf{r}_k^{(0)} + \delta\mathbf{r}_k$  due

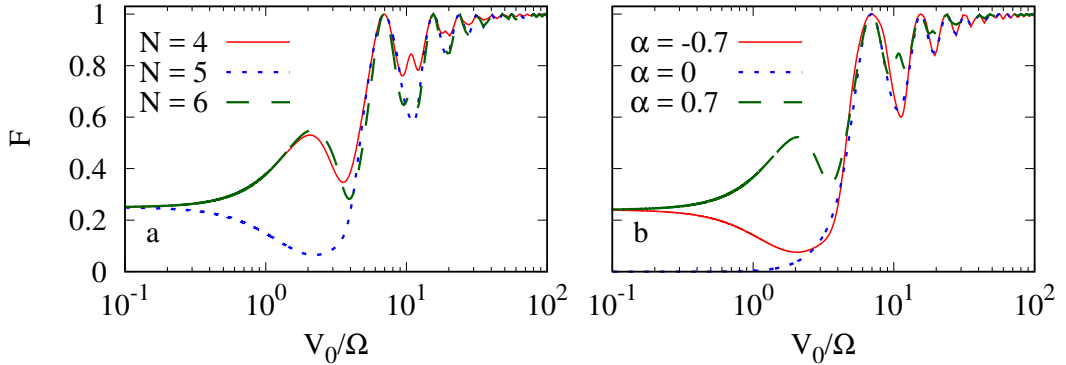


**Figure 4.5: Fidelity of the transport process for different initial states.**

(a): Fidelity of a coherent transport process for  $N = 4, 5, 6$  as a function of  $V_0/\Omega$ . The transferred state is  $|\psi_1\rangle = 1/\sqrt{2}(|0\rangle + |1\rangle)$ . (b): Comparison of the fidelity of the transport process for different initial states  $|\psi_1\rangle$  for  $N = 4$ . The parameter  $\alpha$  ( $\beta = \sqrt{1 - \alpha^2}$ ) of the state  $|\psi_1\rangle = \alpha|0\rangle + \beta|1\rangle$  is varied (Taken from Ref. [1]).

to the finite temperature  $T$  of the system. This results in a three-dimensional Gaussian distribution of the  $\delta\mathbf{r}_k$  given in equation (A.14), with widths  $\sigma_i$ ,  $i \in \{1, 2, 3\}$  in the three spatial directions. Taking, for our comparison, parameters from recent experiments [6], we set the trap separation to  $R_0 = 4.1 \mu\text{m}$ . We consider two scenarios for the disorder, one with isotropic disorder ( $\sigma_i = 120 \text{ nm}$ ,  $i = 1, 2, 3$ ) and one with anisotropic disorder ( $\sigma_1 = 1 \mu\text{m}$  and  $\sigma_{2,3} = 120 \text{ nm}$ ). The results presented below are obtained by averaging over 1000 realizations of the disorder unless stated otherwise.

In Figs. 4.6-4.8 we show the fidelity for the GHZ, dimer-MPS, and state transport protocols, respectively (we take the initial state  $|\psi_1\rangle = 1/\sqrt{2}(|0\rangle + |1\rangle)$  in the transport protocol). In all plots we compare the non-perfect blockade and three different choices of disorder: absent (red), isotropic (dotted blue) and anisotropic (dashed green).

The common feature to all plots is that, for the parameters considered, in the large  $V_0/\Omega$  limit, the blockade mechanism dominates and is only weakly affected by the disorder: here, all three cases show only small differences and sit well on top of each other. Conversely, in the limit of  $V_0/\Omega \sim O(1)$ , the disorder has much stronger impact and in general decreases the fidelity significantly. This limit is of interest for fast application of the protocols such that it still yields high-fidelity outputs (the larger the  $\Omega$ , the shorter the time needed to apply a pulse of a given area).

In that regime, the decrease of fidelity is more pronounced with increasing disorder

(situation in all Figs. (4.6)-(4.8)), and also with increasing atom number (compare Fig. 4.6(a) and Fig. 4.6(b), Fig. 4.7(a,c) and Fig. 4.7(b,d) and all the panels in Fig. 4.8). The decrease of fidelity with the atom number stems from the fact that all of our procedures address the atoms sequentially. Therefore each pulse, under imperfect conditions, will make the state diverge more from the target state. In the case of the dimer-MPS protocol, we note that the fidelity decreases also with increasing  $z$ , which can be easily understood as higher  $z$  correspond to larger number of excitations in the state, which in turn is more sensitive to the disorder.

The main message to be extracted from these results is that all of the considered protocols are becoming more sensitive to the positional disorder when approaching the fast operation regime  $V_0/\Omega \sim O(1)$  from the large  $V_0/\Omega$  side.

In order to further quantify the sensitivity to the disorder and the corresponding decrease in fidelity, we study the fidelity as a function of the length of the chain for all three protocols. Here we consider a system with non-perfect Rydberg blockade without disorder (red crosses), with isotropic disorder (blue squares), and anisotropic disorder (green diamonds). As we are interested in the fast application of the protocols, for the GHZ state preparation we have fixed the ratio  $V_0/\Omega = 7.2, 15.5$  in Figs. 4.9(a,b), and for the state transport protocol to  $V_0/\Omega = 6.9, 15.5$  in Figs. 4.11(a,b). These values correspond to the leftmost and second leftmost peaks in the fidelity (Figs. 4.3 and 4.5). The optimal values of  $V_0/\Omega$  used can be extracted numerically or using (4.34) and (4.36), respectively. The solid lines correspond to an exponential function  $f(N) = a \exp(-b(N - 2))$  fitted to the respective data points. Since we consider chains of length  $N \geq 2$  we set the exponent of the function  $f(N)$  to  $-b(N - 2)$  rather than  $-bN$ . With such a choice of the fitting function, the parameter  $a$  in Table 4.2 states the maximal fidelity of the protocol achievable in the simplest possible system  $N = 2$  for different types of disorder. Table 4.2 shows that the protocols do not reach a fidelity of one when disorder is considered. Figs. 4.9 and 4.11 further quantify the above discussed observation, that the resulting performance is a trade off between how fast the protocol can be applied and the resulting fidelity. Interestingly, in the absence of disorder and for  $V_0/\Omega$  corresponding to the optimal fidelity regions, the final fidelity of the protocols is essentially insensitive to the exact atom number, i.e. it is not affected by the tails of the interaction potential, see also Figs. 4.3, 4.5. For the dimer-MPS protocol, we consider  $z = 10$ , in order to emphasize the effect of the long-range (algebraically-decaying) nature of the interactions on the resulting fidelity. The choice of  $V_0/\Omega$ , corresponding to the two leftmost peaks of

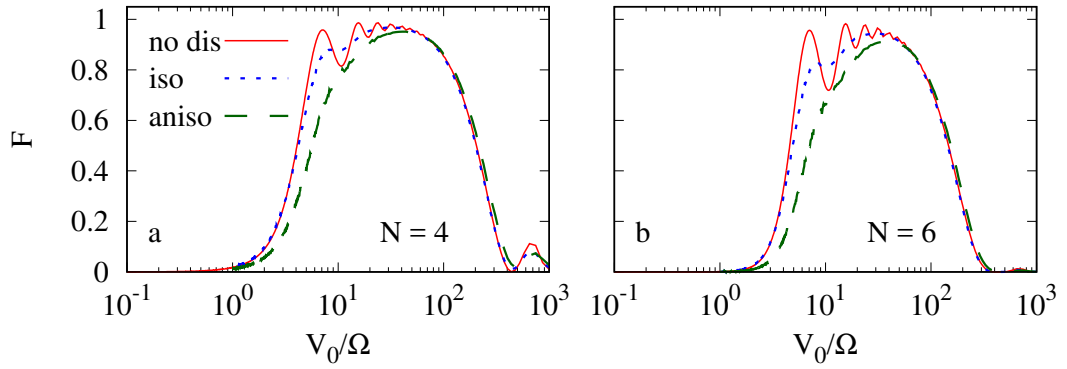


**Figure 4.6: Fidelity of the GHZ protocol including the effect of non-perfect blockade and disorder.** Fidelity of the GHZ state preparation protocol including the effect of non-perfect blockade and disorder for  $N = 4$  (a) and  $N = 6$  (b) as a function of  $V_0/\Omega$  with no (solid red), isotropic (dotted blue) and anisotropic (dashed green) disorder (Taken from Ref. [1]).

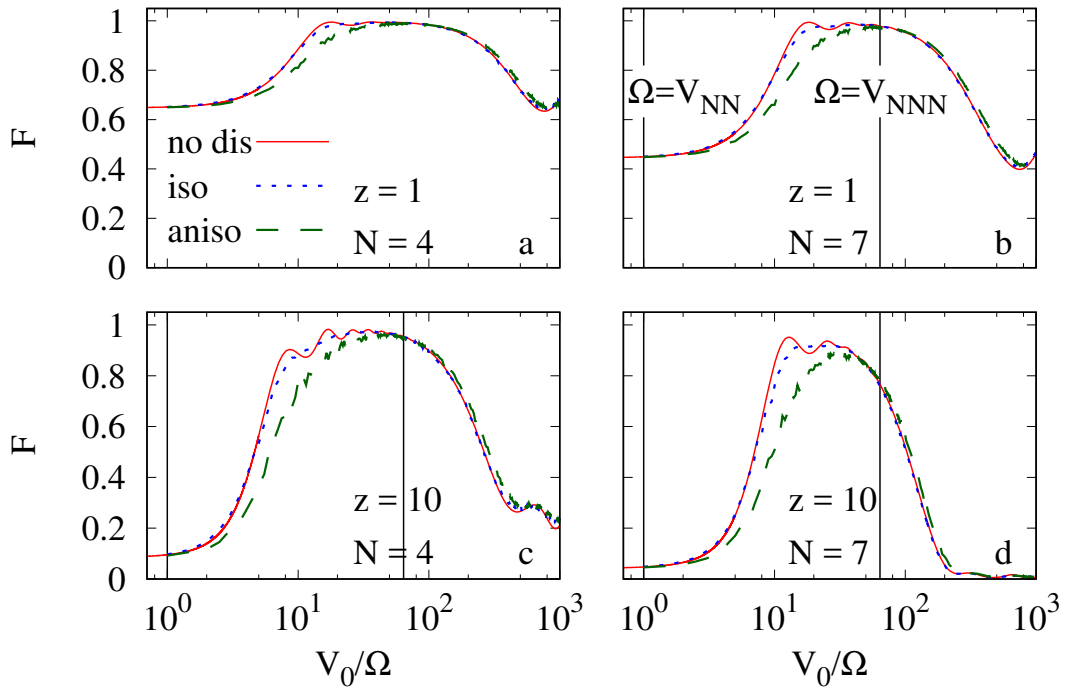


**Figure 4.7: Fidelity of the dimer-MPS protocol including a non-perfect Rydberg blockade and disorder.** Fidelity of the dimer-MPS protocol as a function of  $V_0/\Omega$  including the effect of a non-perfect Rydberg blockade and disorder for  $N = 4$  (a,c),  $N = 7$  (b,d), and  $z = 1$  (a,b) and  $z = 10$  (c,d). The solid red, dotted blue and dashed green lines correspond to no, isotropic and anisotropic disorder, respectively. Here,  $F$  is obtained for 100 realizations of the disorder. (Taken from Ref. [1].)

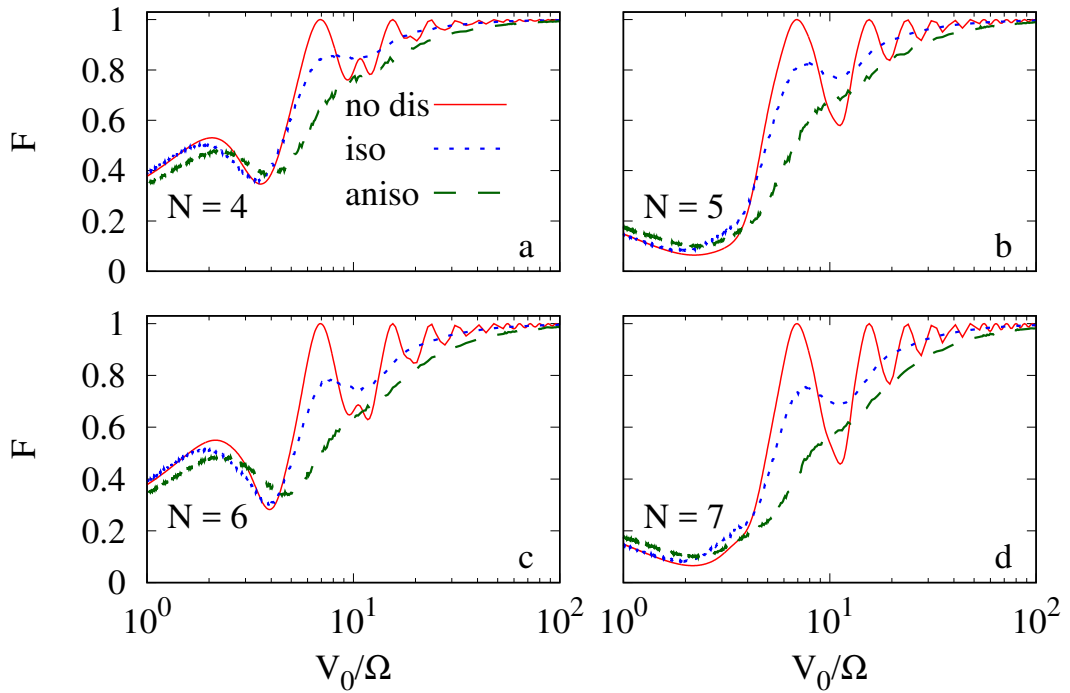


**Figure 4.8: Fidelity of the state transport protocol including a non-perfect Rydberg blockade and disorder.** Fidelity of the state transport protocol as a function of  $V_0/\Omega$  for the initial state  $|\psi_1\rangle = 1/\sqrt{2}(|0\rangle + |1\rangle)$  and for  $N = 4$  (a),  $N = 5$  (b),  $N = 6$  (c), and  $N = 7$  (d). The solid red, dotted blue and dashed green lines correspond to no, isotropic and anisotropic disorder, respectively. (Taken from Ref. [1].)

the fidelity, for the GHZ preparation and state transport protocols is motivated by the fact that in the absence of disorder these values provide a satisfactory trade-off between the achievable fidelity, and the speed of operation independently of the atom number. On the other hand, for the dimer-MPS protocol it is clear from Fig. 4.4 ( $z = 10$ ) that  $V_0/\Omega$  corresponding to the leftmost peak of  $N = 2$  yields a rather rapid drop in the fidelity for higher  $N$  even in the absence of the disorder. For this reason we consider only the values of  $V_0/\Omega$  corresponding to the second leftmost peak of the fidelity in Fig. 4.4. Here we note that the corresponding value of  $V_0/\Omega$  slightly varies for odd and even  $N$  unlike for the GHZ state preparation and transport protocols. Specifically, we find that the peaks appear around  $V_0/\Omega \approx 15.6$  and  $V_0/\Omega \approx 17.1$  for odd and even  $N$  which we use in Fig. 4.10.

### 4.3.3 Limitations due to spontaneous decay

In Sec. 4.3 we have considered two sources of imperfections introducing errors in the state preparation and state transport protocols, namely the effect of the finiteness of the interaction potential resulting in non-perfect blockade, and the effect of positional disorder of the atoms. We have neglected other noise sources such as spontaneous decay of the atoms from the Rydberg state or loss and dephasing mechanisms due to the interaction of the lattice atoms with the background gas. The reason for this is that we are interested in the short-time dynamics, where these effects become essentially negligible. To give a specific example of a constraint such considerations impose on the evolution of the system, we consider here the example of spontaneous decay.

Motivated by [6], we set the total duration of the experiment to  $\tau_{\text{exp}} = 2 \mu\text{s}$ , in order to avoid effects due to the spontaneous photon emission, atom loss, and mechanical effects induced by the forces between atoms. As we are considering non-adiabatic state-preparation protocols, we want to find a parameter regime where the protocol can be performed as fast as possible with a high fidelity. Thus, we choose  $(V_0/\Omega)^* = 6.9$ , corresponding to the position of the leftmost maximum fidelity peak in each protocol (Figs. 4.3-4.5). Finally, we fix  $V_0 = 2\pi \times 8.4 \text{ MHz}$  [6]. We can now estimate, with the help of the Table 4.1 and the relations (4.24), the maximal number of atoms  $N_{\text{max}}$  so that the total duration of each protocol is smaller than  $\tau_{\text{exp}}$ . The result can be summarized as

$$N_{\text{max}} = (\text{GHZ} \rightarrow 9; \text{MPS}(z = 1) \rightarrow 13, \text{MPS}(z = 10) \rightarrow 7; \text{transport} \rightarrow 6). \quad (4.37)$$

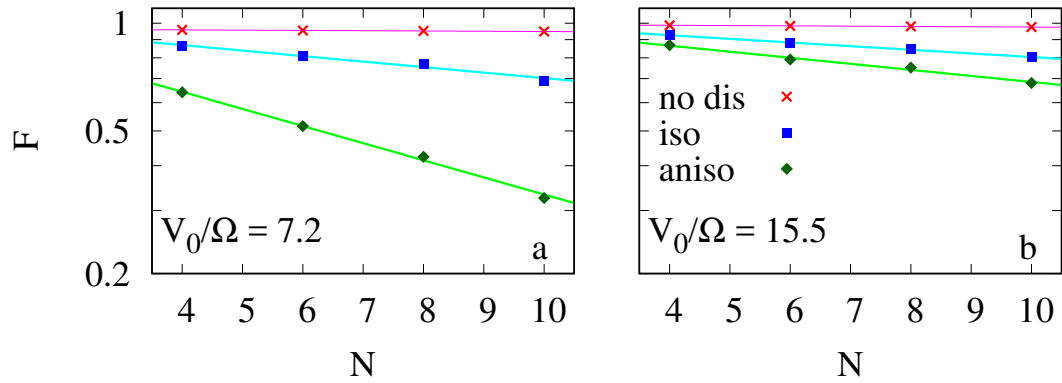


**Figure 4.9: Fidelity of the GHZ protocol as a function of the system size.** Fidelity of the GHZ protocol as a function of the number of atoms in the chain  $N$  for  $V_0/\Omega = 7.2$  (a) and  $V_0/\Omega = 15.5$  (b). The red crosses, blue squares and green diamonds correspond to no, isotropic and anisotropic disorder, respectively. The solid lines represent an exponential function fitted to the data points, see text for details. Data obtained by averaging over 100 realizations of the disorder. (Taken from Ref. [1].)

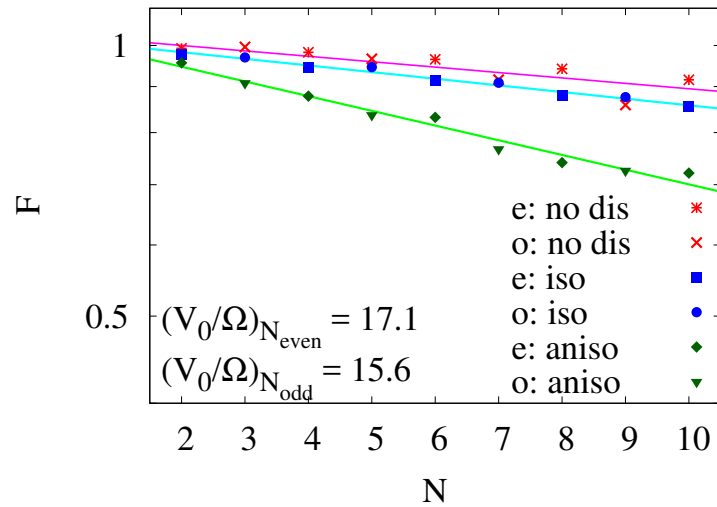


**Figure 4.10: Fidelity of the dimer-MPS protocol as a function of the system size.** Fidelity of the dimer-MPS protocol as a function of the number of atoms in the chain  $N$  for  $V_0/\Omega = 17.1$  for even (e) and  $V_0/\Omega = 15.6$  for odd (o) number of atoms in the chain and  $z = 10$  in a logarithmic scale. The red crosses, blue squares and green diamonds correspond to no, isotropic and anisotropic disorder, respectively. The solid lines represent an exponential function fitted to the data points, see text for details. Data obtained by averaging over 100 realizations of the disorder. (Taken from Ref. [1].)

GHZ state		
$\frac{V_0}{\Omega} = 6.9$		
	$a$	$b$
no disorder	$0.961015 \pm 6 \cdot 10^{-6}$	$(1739 \pm 1) \cdot 10^{-6}$
isotropic	$0.93 \pm 0.02$	$0.035 \pm 0.004$
anisotropic	$0.80 \pm 0.01$	$0.110 \pm 0.004$
$\frac{V_0}{\Omega} = 15.5$		
	$a$	$b$
no disorder	$0.990331 \pm 7 \cdot 10^{-6}$	$(1911 \pm 1) \cdot 10^{-6}$
isotropic	$0.970 \pm 0.003$	$0.0234 \pm 0.0006$
anisotropic	$0.94 \pm 0.01$	$0.039 \pm 0.003$
dimer-MPS state		
$(\frac{V_0}{\Omega})_{N_{\text{odd}}} = 15.6$ and $(\frac{V_0}{\Omega})_{N_{\text{even}}} = 17.1$		
	$a$	$b$
no disorder	$1.00 - 0.02$	$0.0139 \pm 0.004$
isotropic	$0.983 \pm 0.004$	$0.0170 \pm 0.0009$
anisotropic	$0.947 \pm 0.009$	$0.037 \pm 0.002$
State transport		
$\frac{V_0}{\Omega} = 6.9$		
	$a$	$b$
no disorder	$0.999988 \pm 4 \cdot 10^{-6}$	$(7.6 \pm 0.8) \cdot 10^{-7}$
isotropic	$0.94 \pm 0.05$	$0.051 \pm 0.003$
anisotropic	$0.73 \pm 0.04$	$0.09 \pm 0.01$
$\frac{V_0}{\Omega} = 15.5$		
	$a$	$b$
no disorder	$0.999989 \pm 4 \cdot 10^{-6}$	$(6.8 \pm 0.8) \cdot 10^{-7}$
isotropic	$0.97 \pm 0.01$	$0.036 \pm 0.002$
anisotropic	$0.93 \pm 0.02$	$0.055 \pm 0.003$

**Table 4.2: Fit of the system size dependence for the GHZ, dimer-MPS state preparation and state transport protocols.** The coefficients of the function  $f(N) = a \exp(-b(N-2))$  fitted to the data points in Figs. 4.9, 4.10 and 4.11 for the GHZ, dimer-MPS state preparation and state transport protocols, respectively. The abbreviations correspond to “no dis” = no disorder, “iso” = isotropic disorder, “aniso” = anisotropic disorder parameterized according to the values reported in the main text. (Taken from Ref. [1].)

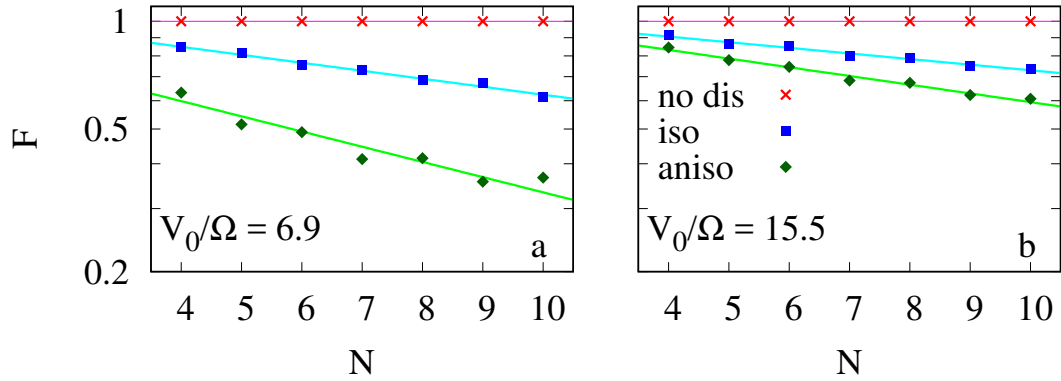


**Figure 4.11: Fidelity of the state transport protocol as a function of the number of atoms.** Fidelity of the state transport protocol as a function of the number of atoms in the chain  $N$  for  $V_0/\Omega = 6.9$  (a) and  $V_0/\Omega = 15.5$  (b) in a logarithmic scale. The red crosses, blue squares and green diamonds correspond to no, isotropic and anisotropic disorder, respectively. The solid lines represent an exponential function fitted to the data points, see text for details. Data obtained by averaging over 1000 realizations of the disorder. (Taken from Ref. [1].)

One can see, that in the specific example with  $\tau_{\text{exp}} = 2 \mu\text{s}$ , the protocols are limited to rather small numbers of atoms of the order of 10. In the case of the two-level scheme, the coherence time of the system is dominated by the lifetime  $\tau_l$  of a single Rydberg atom divided by the number of atoms  $\tau_l/N$ . At the same time, Rydberg atoms provide multiple possibilities with relaxation timescales ranging over several orders of magnitude, typically from  $\mu\text{s}$  to  $\text{ms}$  regime [10,21] depending on the Rydberg state. It would thus be interesting to identify the transitions with sufficiently large interaction strength  $V_0$  and long relaxation times. That allows significantly higher  $N_{\text{max}}$ , which can in principle be achieved by analyzing higher principal quantum number  $n$  states (we recall that the interaction strength and relaxation timescales obey approximately the scaling relations  $V_0 \propto n^{11}$ ,  $\tau \propto n^3$  [22], while  $n = 56$  was used in [6] in the repulsive interaction regime). However, when the three level scheme is used, where the excited Rydberg states are transferred to an atomic hyperfine ground state  $|\tilde{1}\rangle$ , the coherence time can last up to several tens of seconds as outlined in reference [144].

## 4.4 Outlook and Conclusion

We have described three different protocols for quantum information processing based on non-adiabatic manipulation of atoms. The protocols exploit the Ryd-

berg blockade mechanism and require single-site addressability, which is now an available experimental tool. Specifically, we have shown how to generate antiferromagnetic GHZ states, a class of matrix product states - the dimer-MPS - which include the Rydberg crystals, and quantum state transport in chains of Rydberg atoms. We have evaluated the effect of the full interaction potential on the quality of the protocols identifying a parameter regime yielding optimal performance in terms of fast operation resulting in output states with high fidelity. We then evaluated the experimentally relevant effect of positional disorder stemming from the finite temperature of the atoms and the width of the optical traps. Finally, we have discussed the constraints imposed on the presented protocols by other sources of imperfections, namely the spontaneous decay of the Rydberg states.

After studying the effects of disorder on quantum information protocols due to imperfections, we now turn our attention to the influence of disorder on the transport properties of Rydberg quantum simulator systems. The special properties of interacting Rydberg atoms result in localization effects that are unusual compared to the standard Anderson localization explained in Chapter 3.

# Chapter 5

## Synthetic lattices, flat bands and localization in Rydberg quantum simulators

This chapter is based on Ref. [2] and its supplementary material.

### 5.1 Introduction

As discussed in Chapter 3, transport in quantum systems can be heavily affected by the presence of quenched disorder via *Anderson localization* [54]. In one and two dimensions, the effect of Anderson localization is so significant that for arbitrarily small disorder, all energy eigenstates are localized and transport is effectively impossible [145, 146]. Apart from the case of quenched disorder, localized states can also arise in tight-binding models from particular lattice geometries. In these cases, destructive interference comes not from the random nature of the phases acquired along different trajectories, but from a specific careful arrangement of the lattice, leading to the emergence of flat bands. Models with flat bands allow the construction of localized eigenstates, and have been experimentally realized with cold atoms [147], photonic lattices [148], and synthetic solid-state structures [149, 150]. When disorder is introduced in such systems, these pre-existing localized states couple to the dispersive, delocalized ones and start acting like scatterers. The ensuing richer phenomenology includes localization enhancement [8], Anderson transitions in lower-dimensional systems [151], and disorder-induced delocalization [152].

In this chapter we demonstrate that Rydberg lattice quantum simulators [28, 35, 153] permit the exploration of these anomalous disorder phenomena. We show

that under facilitation conditions the Hilbert space acquires a regular (synthetic) lattice structure supporting flat bands. In this picture, the uncertainty of atomic positions translates into a disordered potential acting on its sites. Similar scenarios were previously theoretically analyzed in Ref. [8, 151]. Here we show that they emerge naturally in Rydberg quantum simulators employing optical tweezer arrays [35, 153, 154]. We illustrate our findings for the case of a so-called ‘‘Lieb ladder’’. We analyze the scaling of the localization lengths and discuss the spreading dynamics of a local flat-band eigenstate under the action of different disorder strengths.

## 5.2 Facilitation, Hilbert space structure and flat bands

We consider a lattice of  $N$  optical tweezers, each loaded with a single Rydberg atom, and with nearest-neighbor distance  $R_0$ . We shine a laser with Rabi frequency  $\Omega$  and detuning  $\Delta$ , with respect to an atomic transition between the electronic ground state  $|\downarrow\rangle$  and a Rydberg level  $|\uparrow\rangle$ , onto the system. Atoms in the Rydberg state  $|\uparrow\rangle$  interact, at distance  $d$ , via an algebraically-decaying potential  $V(d) = C_\alpha/d^\alpha$ , with  $\alpha = 3$  for dipole-dipole interactions (the facilitation mechanism does not depend on the sign of the potential, so without loss of generality we choose  $C_\alpha > 0$ ). As already mentioned, within the rotating wave approximation the Hamiltonian of this system reads

$$\hat{H} = \Omega \sum_{k=1}^N \hat{\sigma}_x^{(k)} + \Delta \sum_{k=1}^N \hat{n}_k + \frac{1}{2} \sum_{\substack{k=1 \\ m \neq k}}^N V(d_{km}) \hat{n}_m \hat{n}_k, \quad (5.1)$$

where  $k$  and  $m$  are lattice indices,  $d_{km}$  denotes the distance between atoms in sites  $k$  and  $m$ ,  $\hat{\sigma}_x^{(k)} = |\uparrow_k\rangle \langle \downarrow_k| + |\downarrow_k\rangle \langle \uparrow_k|$  and  $\hat{n}_k = |\uparrow_k\rangle \langle \uparrow_k|$ . The facilitation condition is obtained by setting  $\Delta = -V(R_0)$ , so that an isolated excited atom makes its neighbors’ transitions resonant with the laser. In the following, we consider  $|\Delta| \gg \Omega$ , so that non-facilitated atoms are sufficiently off-resonant to neglect their excitation. Furthermore, we require  $V(2R_0) \gg \Omega$  which implies that a pair of neighboring excitations is unable to facilitate any nearby site. Neglecting these strongly suppressed transitions effectively splits the Hilbert space into subspaces, each comprises a set of *quasi-resonant* states, separated by energy scales  $\gg \Omega$ , as shown in Fig. 5.3(a) [6, 155]. This splitting of the Hilbert space into energy sectors will be derived later in this chapter (see 5.2.1). Intuitively, this means that an isolated excitation can at most produce one more in the neighborhood,

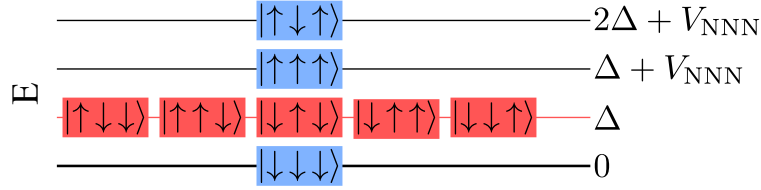


**Figure 5.1: Splitting of the Hilbert space.** Under the facilitation condition the Hilbert space splits into subspaces separated by energies much larger than the Rabi frequency (adapted from Ref. [6]).

after which either the former facilitates the de-excitation of the latter, or vice versa:

$$|\dots \downarrow\uparrow\downarrow\dots\rangle \xleftarrow{\hat{H}} |\dots \downarrow\uparrow\uparrow\downarrow\dots\rangle \xleftarrow{\hat{H}} |\dots \downarrow\downarrow\uparrow\downarrow\dots\rangle. \quad (5.2)$$

Here we work in the simplest non-trivial subspace, which contains all configurations with either a single excitation or a single pair of neighboring ones (red layer in Fig. 5.1). These states can be obtained by repeatedly applying the Hamiltonian to, e.g., a state with a single excitation at one end of the chain via the mechanism highlighted above. In the following, we will be interested in reconstructing the connectivity structure of these states in the Hilbert space; we shall therefore imagine that each classical (i.e., eigenstate of all  $\hat{\sigma}_z^{(k)}$ s) spin configuration is represented by a lattice site, while we identify as *nearest neighbors* those states which are connected by the Hamiltonian. To avoid confusion, we shall refer to this emerging lattice structure as the *synthetic lattice*, while we call the lattice formed by the actual traps the *real lattice*. The construction of the synthetic lattice is illustrated in Fig. 5.2 and can be performed pictorially in a few steps: (i) we recognize that there is a one-to-one correspondence between states with a single excitation and the position of that excitation in the real lattice. Hence, we dispose these state of the synthetic lattice in the same structure adopted by the real lattice (i.e., in a square ordering if the traps form a square lattice). (ii) for later convenience we draw links between each pair of neighbors in this partial structure. (iii) we see from (5.2) that the Hamiltonian does not directly connect any states with a single excitation, implying that in this partial structure (we are still missing the two-neighboring-excitation states, or *pair*, states) no nearest neighbors (according to our definition above) can be found. (iv) From (5.2), we see that single-excitation states are indirectly connected by pair states. Furthermore, each pair state connects *exclusively* to the two single excitation states in either of the positions of the pair. Finally, these two states have excitations in contiguous positions and are therefore, by (ii), connected by one of the links we

drew. Hence, we add an extra synthetic lattice site, on the midpoint of each link which represents a pair state and completes the synthetic lattice. For a square lattice, the new structure (see Fig. 5.2) is the *Lieb lattice* and is known to feature one flat and two dispersive bands which meet with linear dispersion at the edges of the first Brillouin zone. With an eye to this Dirac-cone-like band structure, this lattice has been theoretically studied before in [156], although in a framework where the Lieb lattice is directly realized by the traps. The construction we summarized above is general and can be extended to any kind of regular lattice. Most choices will support flat bands as well; we show in Appendix C.1 that, calling  $n_1$  ( $n_2$ ) the number of one-excitation (pair) states in a unit cell, the number of flat bands is bounded by  $n_{\text{flat}} \geq |n_1 - n_2|$ . For the square, triangular and honeycomb lattices in Fig. 5.2,  $(n_1, n_2, n_{\text{flat}}) = (1, 2, 1)$ ,  $(1, 3, 2)$  and  $(2, 3, 1)$  respectively. These flat bands constitute extensively-degenerate eigenspaces of the Hamiltonian; as such, it is often possible to recombine the usual (plane-wave-like) Bloch solutions to form a set of localized eigenstates.

### 5.2.1 Hilbert space reduction and restricted Hamiltonian

In this section we describe the reduction of the Hilbert space which results from the splitting of the Hilbert space into disconnected subspace. From this we obtain the restricted Hamiltonian acting on the subspace which consists of either a single excitation or a single pair of neighboring excitations. In order to exploit the large energy separations between the subspaces present in the system, we switch from the Schrödinger picture Eq.(5.1) to the interaction picture as introduced in Sec. 2.4. Therefore, we separate the Hamiltonian in the Schrödinger picture into two parts

$$\hat{H}_I(t) = e^{i\hat{H}_0 t} \hat{H}_1 e^{-i\hat{H}_0 t} = \Omega \sum_k e^{i\hat{H}_0 t} \hat{\sigma}_x^{(k)} e^{-i\hat{H}_0 t}, \quad (5.3)$$

where

$$\hat{H}_0 = \Delta \sum_k \hat{n}_k + \frac{1}{2} \sum_{m \neq k} V(d_{km}) \hat{n}_m \hat{n}_k, \quad \text{and} \quad H_1 = \Omega \sum_{k=1} \hat{\sigma}_x^{(k)}. \quad (5.4)$$

Recalling that  $[\hat{\sigma}_x^{(k)}, \hat{n}_m] = 0$  for every  $k \neq m$ , one can perform a partial cancellation of exponential terms in (5.3), keeping only those which are proportional to  $\hat{n}_k$ , all other terms cancel out as they commute with  $\hat{\sigma}_x^{(k)}$ ,

$$e^{i\hat{H}_0 t} \hat{\sigma}_x^{(k)} e^{-i\hat{H}_0 t} = e^{it\hat{n}_k \left( \Delta + \sum_{m \neq k} V(d_{km}) \hat{n}_m \right)} \hat{\sigma}_x^{(k)} e^{-it\hat{n}_k \left( \Delta + \sum_{m \neq k} V(d_{km}) \hat{n}_m \right)}. \quad (5.5)$$

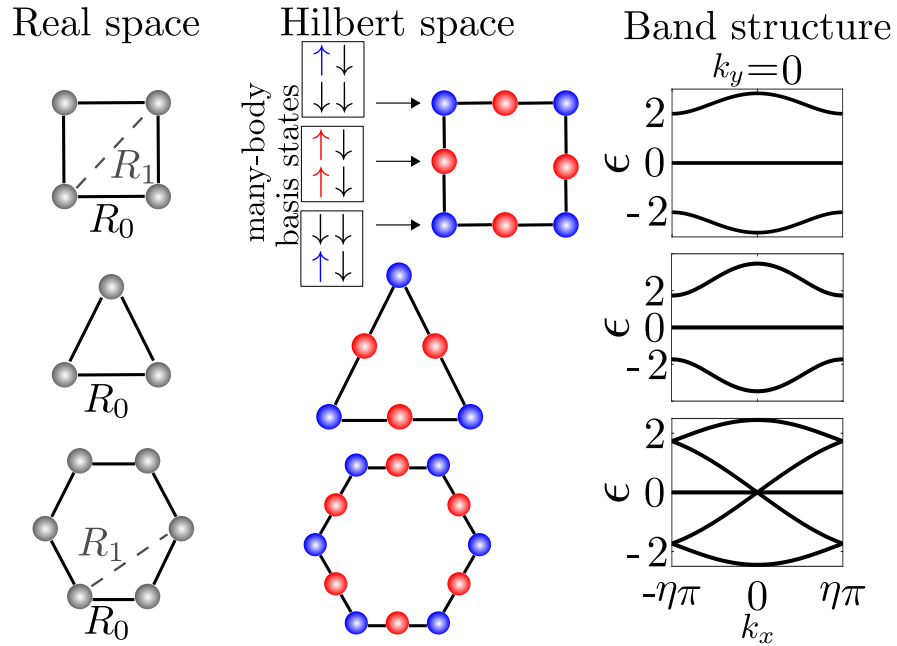


**Figure 5.2: Real space lattice, synthetic Lieb lattice and the respective band structure.** Left column: basic local site configuration within a square, triangular, and honeycomb lattices. The gray dots depict the positions of the optical tweezers, while the lines provide a guide to the eye.  $R_0$  and  $R_1$  represent nearest and next-nearest neighbor distances, respectively. Middle column: respective "synthetic lattices" in the Hilbert space under facilitation conditions. The blue dots represent one-excitation states while the red ones are pair states. Right column: Cut through the Brillouin zone for each lattice geometries at  $k_y = 0$ . Each lattice features (at least) a flat band. The momentum scales for the three lattices (from top to bottom) are  $\eta = (1, \frac{4}{3}, \frac{4}{3})$ . This figure is taken from Ref. [2].

We expand the term in the exponentials that is proportional to the detuning (analogous to the term proportional to  $V(d_{km})$ ) resulting in

$$e^{it\Delta\hat{n}_k} = \sum_{j=0}^{\infty} \frac{(it\Delta\hat{n}_k)^j}{j!} = 1 + \hat{n}_k \sum_{j=1}^{\infty} \frac{(it\Delta)^j}{j!} = 1 + \hat{n}_k (e^{it\Delta} - 1), \quad (5.6)$$

rewrite the commutator as  $\hat{\sigma}_x^{(k)}\hat{n}_k = (\mathbb{1} - \hat{n}_k)\hat{\sigma}_x^{(k)}$ , and simplify the  $k$ -th term in Eq. (5.3)

$$e^{i\hat{H}_0 t} \hat{\sigma}_x^{(k)} e^{-i\hat{H}_0 t} = e^{it(2\hat{n}_k - 1) \left( \Delta + \sum_{m \neq k} V(d_{km}) \hat{n}_m \right)} \hat{\sigma}_x^{(k)}. \quad (5.7)$$

With that, the Hamiltonian  $\hat{H}_I$  can then be written as

$$\hat{H}_I(t) = \Omega \sum_k e^{it(2\hat{n}_k - 1) \left( \Delta + \sum_{m \neq k} V(d_{km}) \hat{n}_m \right)} \hat{\sigma}_x^{(k)}. \quad (5.8)$$

We apply a rotating-wave approximation to discard all terms which oscillate fast in time. This implies that the oscillation frequency  $\zeta$  should be much larger than the Rabi frequency  $\zeta \gg \Omega$  for a term to be neglected. Note that the frequency  $\zeta$  is however operator-valued

$$\zeta = (2\hat{n}_k - \mathbb{1}) \left( \Delta + \sum_{m \neq k} V(d_{km}) \hat{n}_m \right). \quad (5.9)$$

Since the prefactor  $-\mathbb{1} \leq 2\hat{n}_k - \mathbb{1} \leq \mathbb{1}$  is of order  $O(1)$ , it is the second factor which is decisive for the selection. We now introduce for every site  $k$  a projector  $\hat{P}_k$  over all states where there is a single excitation among the neighbors of  $k$  and no additional one within a radius  $2R_0$ . Its specific structure depends clearly on the structure of the lattice, but if we define by  $\mathcal{F}_k$  the set of nearest-neighboring sites of  $k$  and by  $\mathcal{S}_k$  the set of sites within a distance  $2R_0$  from  $k$  which are neither site  $k$  itself nor one of the sites in  $\mathcal{F}_k$ , as illustrated in Fig. 5.3(b), (i.e.,  $k \notin \mathcal{S}_k$ ,

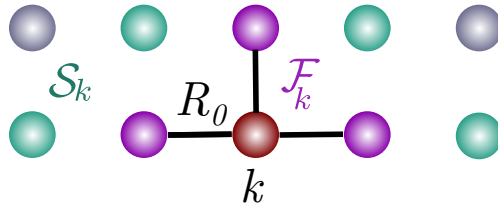


**Figure 5.3: Definition of the set of  $\mathcal{F}_k$  and  $\mathcal{S}_k$**  We define the set  $\mathcal{F}_k$  (violet) which consists of all nearest-neighbor sites of site  $k$  (dark red). The set  $\mathcal{S}_k$  (green) are all sites within a distance of  $2R_0$  from  $k$ , which are not site  $k$  itself, or site in set  $\mathcal{F}_k$ .

$\mathcal{F}_k \cap \mathcal{S}_k = \emptyset$ ), then we can give an implicit definition according to

$$\hat{P}_k = \sum_{q \in \mathcal{F}_k} \hat{n}_q \prod_{q' \in \mathcal{F}_k, q' \neq q} (1 - \hat{n}_{q'}) \prod_{q'' \in \mathcal{S}_k} (1 - \hat{n}_{q''}). \quad (5.10)$$

The operator  $\hat{P}_k \hat{\sigma}_x^{(k)}$  flips the spin on site  $k$  depending on the presence of a single excitation in  $\mathcal{F}_k$  and no additional one in  $\mathcal{S}_k$ . Checking that the expression above satisfies  $(\hat{P}_k)^2 = \hat{P}_k$  is straightforward if one recalls that  $\hat{n}_q^2 = \hat{n}_q$ ,  $(\mathbb{1} - \hat{n}_q)^2 = \mathbb{1} - \hat{n}_q \forall q$ , and  $n_q(\mathbb{1} - n_q) = 0$ . The relevance of the projector  $\hat{P}_k$  is that it precisely identifies the constraints under which a spin (or atom) is able to flip (or be excited/de-excited). Slightly more formally,

$$\left( \Delta + \sum_{m \neq k} V(d_{km}) \hat{n}_m \right) \hat{P}_k \approx (\Delta - V(R_0)) \hat{P}_k = 0, \quad (5.11)$$

where we have neglected all contributions from excitations beyond a distance of  $2R_0$ . Furthermore, note that according to definition (5.10),  $\hat{P}_k$  acts trivially on site  $k$  and thus commutes with all local operators which instead exclusively act on that site; in particular,  $[\hat{\sigma}_x^{(k)}, \hat{P}_k] = 0$ . To simplify the interaction Hamiltonian (5.8), we define the operator  $\hat{Q}_k = \mathbb{1} - \hat{P}_k$ , which is the projector onto the orthogonal subspace ( $\hat{Q}_k^2 = \hat{Q}_k$ ,  $\hat{Q}_k \hat{P}_k = 0$ ). With this, we obtain

$$\begin{aligned} \hat{\sigma}_x^{(k)} &= (\hat{P}_k + \hat{Q}_k) \hat{\sigma}_x^{(k)} (\hat{P}_k + \hat{Q}_k) \\ &= \hat{P}_k \hat{\sigma}_x^{(k)} \hat{P}_k + \underbrace{\hat{Q}_k \hat{\sigma}_x^{(k)} \hat{P}_k}_{=0} + \underbrace{\hat{Q}_k \hat{\sigma}_x^{(k)} \hat{P}_k}_{=0} + \hat{Q}_k \hat{\sigma}_x^{(k)} \hat{Q}_k \\ &= \hat{P}_k \hat{\sigma}_x^{(k)} + \hat{Q}_k \hat{\sigma}_x^{(k)}. \end{aligned} \quad (5.12)$$

Hence, we can separate the interaction Hamiltonian  $\hat{H}_I$  into two contributions using Eq. (5.11)

$$\hat{H}_I(t) \approx \Omega \sum_k \hat{P}_k \hat{\sigma}_x^{(k)} + e^{it(2\hat{n}_k - 1)} \left( \Delta + \sum_{m \neq k} V(d_{km}) \hat{n}_m \right) \hat{Q}_k \hat{\sigma}_x^{(k)}. \quad (5.13)$$

The space of configurations onto which  $\hat{Q}_k$  has support can be further split into three classes:

- (A) States where site  $k$  has two or more excited nearest neighbors;
- (B) States where site  $k$  has only one excited neighbor, but there is at least another excitation within a radius  $2R_0$ ;
- (C) States where no neighbors of  $k$  are excited.

In case (A) the interaction potential on site  $k$  is  $\geq 2V(R_0)$ . Accounting for the facilitation condition,  $\Delta = -V(R_0)$ , we find  $\zeta \gtrsim V(R_0) \gg \Omega$ . These terms oscillate very fast and can be discarded under the RWA. Terms of type (B) are facilitated by the single neighboring excitation, but the presence of an additional one within a distance  $2R_0$  implies that

$$\Delta + \sum_{m \neq k} V(d_{km}) \hat{n}_m \geq V(2R_0), \quad (5.14)$$

and therefore  $\zeta \gtrsim V(2R_0) \gg \Omega$ , which allows us to neglect all type-(B) contributions as well. Terms belonging to class (C) are instead more delicate, since an appropriate combination of the interactions with many excitations at different distances could approximately cancel out the detuning  $\Delta$ . For instance, for dipole-dipole interactions ( $\alpha = 3$ ) the potential obeys  $V(\alpha R_0) = V(R_0)\alpha^{-3}$ . Considering a honeycomb lattice with 5 excited next-nearest neighbors at distance  $R_1 = \sqrt{3}R_0$  and a single excited fourth-nearest neighbor at distance  $R_4 = 3R_0$  one finds

$$\begin{aligned} \Delta + \sum_{m \notin \mathcal{F}_k} V(d_{km}) &\rightarrow -V(R_0) + 5V(R_1) + V(R_4) \\ &= V(R_0) \left( -1 + \frac{5}{3\sqrt{3}} + \frac{1}{3^3} \right) \approx -0.00071 V(R_0). \end{aligned} \quad (5.15)$$

However, configurations such as this one always require a large local density of excitations, and hence can only affect Hilbert subspaces at higher energies than the ones considered in this chapter, separated at least by some factors of  $V(R_1) \gg \Omega$ . As long as we consider the low-energy Hilbert subspaces, it is justified to neglect terms of type (C) as well. Overall, in the subspaces we are interested in, we can approximate the interaction Hamiltonian as

$$\hat{H}_I(t) \approx \Omega \sum_k \hat{P}_k \hat{\sigma}_x^{(k)}. \quad (5.16)$$

Going back to the original Schrödinger representation is now straightforward and yields

$$\hat{H} \approx \Omega \sum_k \hat{P}_k \hat{\sigma}_x^{(k)} + \Delta \sum_k \hat{n}_k + \sum_{\substack{k=1 \\ m \neq k}}^N \frac{1}{2} V(d_{km}) \hat{n}_m \hat{n}_k. \quad (5.17)$$

Note that in the specific subspace (let us call it  $\mathcal{H}_1$ ) considered here, the one including all possible one-excitation states plus all possible pairs of neighboring ones, the diagonal part  $\hat{H}_0$  acts trivially as the null operator and can thus be discarded, implying

$$\hat{H}_{\mathcal{H}_1} = \Omega \sum_k \hat{P}_k \hat{\sigma}_x^{(k)}. \quad (5.18)$$

We remark that the same derivation can be followed in the presence of weak disorder by changing the definition of  $\hat{H}_1$  (Eq. (5.3)) to

$$\hat{H}_1 = \Omega \sum_k \hat{\sigma}_x^{(k)} + \frac{1}{2} \sum_{k \neq q} \delta V(d_{kq}) \hat{n}_k \hat{n}_q. \quad (5.19)$$

Since the second term is diagonal and commutes with  $\hat{H}_0$ , the calculation of the interaction picture is straightforward

$$\hat{H}_I(t) = \Omega \sum_k e^{it(2\hat{n}_k-1)} \left( \Delta + \sum_{m \neq k} V(d_{km}) \hat{n}_m \right) \hat{\sigma}_x^{(k)} + \frac{1}{2} \sum_{k \neq q} \delta V(d_{kq}) \hat{n}_k \hat{n}_q, \quad (5.20)$$

and one can follow the same steps outlined above.

## 5.2.2 Hilbert space lattice structure

Having derived the restricted Hamiltonian (5.18) we can now identify the geometric structure of the Hilbert space in the basis of eigenstates of  $\hat{\sigma}_z^{(k)}$ . To start with, we introduce the following definitions for the basis itself: we call  $|M_k\rangle$  states with a single excitation present on site  $k$ , whereas we denote by  $|N_{kq}\rangle$  states with a pair of excitations on sites  $k$  and  $q$ . Fixing the number  $N$  of tweezers, the Hilbert subspace we work in is therefore defined as

$$\mathcal{H}_1 = \text{Span} \{ |M_k\rangle, |N_{kq}\rangle \mid k = 1, \dots, N; q \in \mathcal{F}_k \}, \quad (5.21)$$

where we recall that  $\mathcal{F}_k$  is the set of nearest neighbors of site  $k$  (see Fig. 5.3(b)). Note that, since  $|N_{kq}\rangle = |N_{qk}\rangle$  denote the same state, the pair states are doubly counted, however, this clearly still leads to the generation of the same vector space. Alternatively, one can also define an equivalence relation  $|N_{kq}\rangle \sim |N_{ml}\rangle \Leftrightarrow (k = m \wedge q = l) \vee (k = l \wedge q = m)$  and take the quotient of the r.h.s. above. In the following, it is understood that the states  $|N_{kq}\rangle$  are always taken from this space, i.e., we do not consider states with two isolated excitations at distance  $d > R_0$ .

By construction, the image of Hamiltonian  $\hat{H}_{\mathcal{H}_1}$  (Eq. (5.18)) onto the subspace  $\mathcal{H}_1$  is a subset of  $\mathcal{H}_1$ ,  $\hat{H}_{\mathcal{H}_1} \mathcal{H}_1 \subseteq \mathcal{H}_1$ . As a reminder,  $\hat{P}_k \hat{\sigma}_x^{(k)}$  flips the spin in site  $k$  conditioned on the presence of a single excitation in  $\mathcal{F}_k$  and no additional one in  $\mathcal{S}_k$ . This implies

$$\hat{P}_k \hat{\sigma}_x^{(k)} |M_l\rangle = \begin{cases} 0 & \text{if } l = k, \\ |N_{kl}\rangle & \text{if } l \in \mathcal{F}_k, \\ 0 & \text{otherwise.} \end{cases} \quad (5.22)$$

Considering that  $l \in \mathcal{F}_k \Leftrightarrow k \in \mathcal{F}_l$ , one can see that

$$\hat{H}_{\mathcal{H}_1} |M_l\rangle = \Omega \sum_{k \in \mathcal{F}_l} |N_{kl}\rangle. \quad (5.23)$$

Similarly,

$$\hat{P}_k \hat{\sigma}_x^{(k)} |N_{ql}\rangle = \begin{cases} |M_l\rangle & \text{if } q = k, \\ |M_q\rangle & \text{if } l = k, \\ 0 & \text{otherwise,} \end{cases} \quad (5.24)$$

since by construction the only facilitated spins are in sites  $q$  and  $l$ . Hence,

$$\hat{H}_{\mathcal{H}_1} |N_{ql}\rangle = \Omega (|M_q\rangle + |M_l\rangle). \quad (5.25)$$

Collecting these considerations, we can find the Hamiltonian matrix elements:

$$\langle M_q | \hat{H}_{\mathcal{H}_1} |M_k\rangle = 0 \quad (5.26a)$$

$$\langle N_{ml} | \hat{H}_{\mathcal{H}_1} |N_{kq}\rangle = 0 \quad (5.26b)$$

$$\langle N_{ml} | \hat{H}_{\mathcal{H}_1} |M_k\rangle = \begin{cases} \Omega & \text{if } l = k, \\ \Omega & \text{if } m = k, \\ 0 & \text{otherwise.} \end{cases} \quad (5.26c)$$

Now, there are as many states  $|M_k\rangle$  as there are real-lattice sites, so it is natural to make a connection: starting from the real-space geometry of the tweezer array, which defines the original lattice structure, we place each state  $|M_k\rangle$  on the corresponding site  $k$ . Crucially, each pair state  $|N_{kq}\rangle$  is exclusively connected (via the Hamiltonian) to the two one-excitation states  $|M_k\rangle$  and  $|M_q\rangle$ , so it is placed as a mid-point between sites  $k$  and  $q$ , changing the structure to a generalized Lieb lattice. Now, by drawing a link between any pair of sites every time the corresponding states yield a non-zero Hamiltonian matrix element, one precisely reconstructs the kind of lattices we displayed in Fig. 5.2.

### 5.3 Disordered Lieb ladder

As introduced in Sec. 2.4.1, disorder enters the picture through uncertainty in the atomic positions which create random shifts  $\delta V$  in the interaction potential. In the case of the Lieb lattice, the interaction only affects pair states (red sites in Fig. 5.2) leading to an alternating disorder potential landscape over the synthetic lattice.

In the remainder of our discussion, we shall focus on a ladder configuration, i.e. a quasi-one-dimensional lattice formed by two parallel linear chains at a distance  $R_0$ . For this example, the synthetic lattice (a “1D Lieb lattice”) in the Hilbert space is sketched in Fig. 5.4(a). The unit cell consists of five sites with  $n_1 = 2$  site with a single excitation and  $n_2 = 3$  sites with a pair of neighboring excitations. The band structure features one zero-energy flat band  $E_{\text{FB}} = 0$ , and four

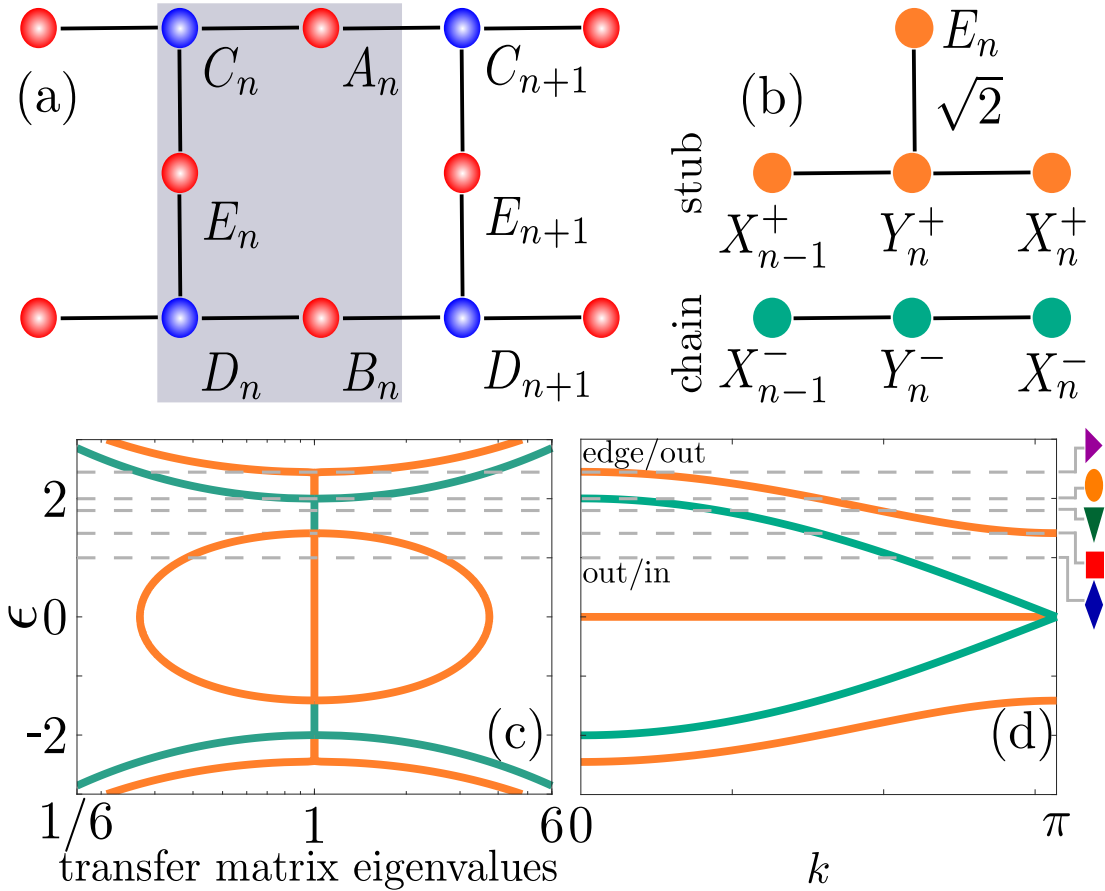


**Figure 5.4: Lieb ladder, “detangled” Lieb ladder, eigenvalues of the transfer matrix and band structure.** (a) Lieb ladder; blue (red) dots correspond to one-excitation (pair) states. We denote by  $A_n, B_n, C_n, D_n, E_n$  the five sites in the  $n$ -th unit cell (shaded in gray). (b) A change of basis – the so-called “detangling”, introducing the new linear combinations  $X_n^\pm = (A_n \pm B_n)/\sqrt{2}$  and  $Y_n^\pm = (C_n \pm D_n)/\sqrt{2}$  [7, 8] maps the Lieb ladder onto two decoupled chains; a stub lattice (orange) and a chain (green). The  $\sqrt{2}$  factor denotes that the hopping amplitude on the vertical link of each unit cell is amplified by that same amount. (c) Eigenvalues of the transfer matrix in log-linear scale. The dotted lines corresponds to the energies  $\epsilon = \{1, \sqrt{2}, 1.8, 2, \sqrt{6}\}$  at which the scaling of the localization lengths is investigated in Fig. 5.5. (d) Band structure of the Lieb ladder. The bands corresponding to the stub lattice are given in orange and bands of the ordinary 1D chain are shown in green. This figure can be found in Ref. [2]

dispersive ones,

$$\begin{aligned} E(k) &= \pm 2 \cos\left(\frac{a k}{2}\right) \\ E(k) &= \pm \sqrt{4 + 2 \cos(a k)}, \end{aligned} \quad (5.27)$$

with  $a = 2\pi/N$ , as can be seen in Fig. 5.4(d). This Lieb ladder constitutes one of the simplest examples where flat bands produce a non-trivial interplay with the on-site disorder [8]. In a Rydberg quantum simulator, however, the disorder only appears on pair states, i.e. all the one-excitation sites (blue in Fig. 5.2 and 5.4) of the synthetic lattice are unaffected by it. To investigate the effect of this unusual disorder scenario we study in the following the scaling behavior of the *localization length*  $\xi$  for small disorder strengths. This quantity encodes the localization properties of the energy eigenstates, whose amplitude is typically peaked somewhere within the lattice and decays exponentially as  $e^{-r/\xi}$  at large distances  $r$ .

For a ladder configuration, one can perform an appropriate change of basis (*detangling transformation* [7,8] introduced in the next section) through which the Lieb ladder is mapped onto two uncoupled one-dimensional lattices [see Fig. 5.4(b)], a chain (in green, supporting the two innermost dispersive bands) and a “stub” lattice (in orange, supporting the flat and two outermost dispersive bands). Thus, two different values of  $\xi$  can be extracted at any given energy, which we denote by  $\xi_{1/2}$  and order according to  $\xi_1 < \xi_2$ . At small disorder, each localization lengths can be associated to either detangled chain.

### 5.3.1 Transfer matrix approach

Due to the tight-binding structure of  $\hat{H}_{\mathcal{H}_1}$ , we can introduce the *synthetic lattice states*  $|A_i\rangle$ ,  $|B_i\rangle$ ,  $|C_i\rangle$ ,  $|D_i\rangle$  and  $|E_i\rangle$ , which define the sites in the  $n$ -th unit cell as illustrated in Fig. 5.4. The  $|C_i\rangle$ ,  $|D_i\rangle$  belong to the one-excitation states, and the  $|A_i\rangle$ ,  $|B_i\rangle$ ,  $|E_i\rangle$  are pair states. Hence, we can rewrite the eigenstate  $|\psi\rangle$  of the tight-binding Hamiltonian in terms of the synthetic lattice states

$$|\psi\rangle = \sum_i \left[ A_i |A_i\rangle + B_n |B_i\rangle + C_i |C_i\rangle + D_i |D_i\rangle + E_i |E_i\rangle \right]. \quad (5.28)$$

As already mentioned in Chapter 2, only the pair states are affected by the disorder which is described by the random variables  $\delta_{A_n}$ ,  $\delta_{B_n}$ ,  $\delta_{E_n}$ . With this, the time-independent Schrödinger equation  $\hat{H}|\varphi\rangle = \epsilon|\varphi\rangle$  with the Hamiltonian

(5.18) can be converted into

$$\begin{aligned}
\epsilon A_n &= \delta_{A_n} A_n + C_n + C_{n+1} \\
\epsilon B_n &= \delta_{B_n} B_n + D_n + D_{n+1} \\
\epsilon C_n &= A_n + A_{n-1} + E_n \\
\epsilon D_n &= B_n + B_{n-1} + E_n \\
\epsilon E_n &= \delta_{E_n} E_n + C_n + D_n,
\end{aligned} \tag{5.29}$$

describing the connectivity of the synthetic lattice states as well as the action of the disorder on the pair states. Applying the so-called *detangling* transformation

$$\begin{aligned}
X_n^\pm &= \frac{A_n \pm B_n}{\sqrt{2}}, & Y_n^\pm &= \frac{C_n \pm D_n}{\sqrt{2}}, \\
\delta_{X_n^\pm} &= \frac{\delta_{A_n} \pm \delta_{B_n}}{2},
\end{aligned} \tag{5.30}$$

which partly detangles the lattice into a one-dimensional *stub* lattice and a simple chain results in

$$\begin{aligned}
\epsilon X_n^+ &= \delta_{X_n^+} X_n^+ + \delta_{X_n^-} X_n^- + Y_n^+ + Y_{n+1}^+ \\
\epsilon X_n^- &= \delta_{X_n^-} X_n^- + \delta_{X_n^+} X_n^+ + Y_n^- + Y_{n+1}^- \\
\epsilon Y_n^+ &= X_n^+ + X_{n-1}^+ + \frac{2}{\epsilon - \delta_{E_n}} Y_n^+ \\
\epsilon Y_n^- &= X_n^- + X_{n-1}^- \\
\epsilon E_n &= \frac{\sqrt{2}}{\epsilon - \delta_{E_n}} Y_n^+.
\end{aligned} \tag{5.31}$$

As sketched in Fig. 5.4(b), the “+” variables live on the one-dimensional stub lattice and “−” ones on the remaining simple chain. It is also clear that they are only partly detangled as the random numbers  $\delta_{X_n^-}$  effectively act as random hopping amplitudes between  $X$  sites from the chain to the stub lattice and vice versa. The last equation in (5.31) has been substituted into the third one to replace  $E_n$ , so that we can now close the equations without the variables  $E_n$ . By combining the first two equations with the third and fourth, and going one step to the right ( $n \rightarrow n + 1$ ), we obtain for the  $Y_{n+1}^\pm, X_{n+1}^\pm$  variables,

$$\begin{aligned}
Y_{n+1}^+ &= (\epsilon - \delta_{X_n^+}) X_n^+ - \delta_{X_n^-} X_n^- - Y_n^+ \\
Y_{n+1}^- &= (\epsilon - \delta_{X_n^-}) X_n^- - \delta_{X_n^+} X_n^+ - Y_n^- \\
X_{n+1}^+ &= -X_n^+ + \left( \epsilon - \frac{2}{\epsilon - \delta_{E_{n+1}}} \right) Y_{n+1}^+ \\
X_{n+1}^- &= -X_n^- + \epsilon Y_{n+1}^-.
\end{aligned} \tag{5.32}$$

Substituting the first two equations (5.32) in the third and fourth ones and introducing the shorthand notation

$$\alpha_n^\pm = \epsilon - \delta_{X_n^\pm} \quad \text{and} \quad \gamma_n = \epsilon - \frac{2}{\epsilon - \delta_{E_{n+1}}}, \quad (5.33)$$

we obtain a recursive set of linear equations

$$\begin{aligned} X_{n+1}^+ &= -X_n^+ + \gamma_n \alpha_n^+ X_n^+ - \gamma_n \delta_{X_n^-} X_n^- - \gamma_n Y_n^+ \\ X_{n+1}^- &= -X_n^- + \epsilon \alpha_n^+ X_n^- - \epsilon \delta_{X_n^-} X_n^+ - \epsilon Y_n^- \\ Y_{n+1}^+ &= \alpha_n^+ X_n^+ - \delta_{X_n^-} X_n^- - Y_n^+ \\ Y_{n+1}^- &= \alpha_n^+ X_n^- - \delta_{X_n^-} X_n^+ - Y_n^-. \end{aligned} \quad (5.34)$$

This can be now interpreted as a transfer matrix  $\hat{T}_i$  propagating the state through the system as introduced in Section 3.1.1

$$\begin{pmatrix} X^+ \\ X^- \\ Y^+ \\ Y^- \end{pmatrix}_{i+1} = T_i \begin{pmatrix} X^+ \\ X^- \\ Y^+ \\ Y^- \end{pmatrix}_i, \quad (5.35)$$

where the transfer matrix is defined as

$$T_i = \begin{pmatrix} \gamma_i \alpha_i^+ - 1 & -\gamma_i \delta_{X_i^-} & -\gamma_i & 0 \\ -\epsilon \delta_{X_i^-} & -1 + \epsilon \alpha_i^+ & 0 & -\epsilon \\ \alpha_i^+ & -\delta_{X_i^-} & -1 & 0 \\ -\delta_{X_i^-} & \alpha_i^+ & 0 & -1 \end{pmatrix}.$$

At any fixed value of the energy  $\epsilon$ , these transfer matrices can be used in a sequence to iteratively reconstruct the components of the vector  $|\psi\rangle$

$$\begin{pmatrix} X^+ \\ X^- \\ Y^+ \\ Y^- \end{pmatrix}_n = \left( \prod_{i=n}^1 T_i \right) \begin{pmatrix} X^+ \\ X^- \\ Y^+ \\ Y^- \end{pmatrix}_1. \quad (5.36)$$

The boundary conditions then distinguish which values of  $\epsilon$  are actually part of the spectrum of  $\hat{H}_{\mathcal{H}_1}$ . Products of random matrices such as  $\prod_{i=n}^1 T_i$  are of course dependent on the specific realization of the disorder. However, their asymptotic properties (for  $n \gg 1$ ) are often more general and only depend on the probability distribution function the disorder is satisfying. In particular, taking a randomly-selected ‘‘seed’’ vector  $\vec{v}_0$ , the norm is

$$\|\vec{v}_n\| = \left\| \prod_{i=n}^1 T_i \vec{v}_0 \right\|. \quad (5.37)$$

Typically it decays exponentially with the number of matrices in the product as  $e^{-n/\xi}$ , with the localization length  $\xi$  at energy  $\epsilon$ . Each matrix  $T_i$  is  $4 \times 4$  and symplectic, i.e., if we define

$$J = \begin{pmatrix} 0 & 0 & 1 & 0 \\ 0 & 0 & 0 & 1 \\ 1 & 0 & 0 & 0 \\ 0 & 1 & 0 & 0 \end{pmatrix}, \quad (5.38)$$

then  $(T_i)^T J T_i = J$ , which implies in particular that its determinant is 1 and that its spectrum comes in pairs of inverse eigenvalues  $\Lambda_i, 1/\Lambda_i$  ( $i = 1, 2$ ). This is a particular case of a more general class of systems [157]. It is intuitive to understand that, at every matrix multiplication, (at most) two directions in the four-dimensional space it acts upon get stretched, suggesting a long-distance exponential scaling of the form  $e^{n/\xi_1 + n/\xi_2}$  with  $\xi_1 < \xi_2$ , where therefore  $\xi_1$  is the dominant scale and  $\xi_2$  the subleading one. The specific numerical method employed for the extraction of  $\xi_{1/2}$  can be found in Ref. [158].

### 5.3.2 Localization and scaling exponents

The localization lengths  $\xi_{1/2}$  are found numerically via the transfer matrix formalism and are displayed in Fig. 5.5(a) as a function of the disorder strength  $s \equiv \sigma/R_0$  and the energy  $\epsilon$ . In Fig. 5.5(b) we display log-log plots of  $\xi_{1/2}$  at selected energies as functions of  $s$ , which illustrate algebraic scaling  $\xi_i \sim s^\nu$ , for sufficiently small  $s$ . Where possible, we connect our findings to those presented in Ref. [8], where the same geometry is studied with independent disorder on all sites.

In Table 5.1 we list the scaling exponents  $\nu_i$  extracted from the scaling of the localization lengths  $\xi_i \sim s^{\nu_i}$ ,  $i = 1, 2$  in the limit  $s \rightarrow 0$  as described in Fig. 5.5. For comparison, we list in the second and third columns scaling exponents obtained with a *flat* disorder distribution, where the disorder energies  $\delta V$  affecting the sites of the (synthetic) Lieb ladder are drawn uniformly from an interval  $[-W/2, W/2]$ . The second (third) column accounts for a situation where only pair sites (all sites of the Lieb ladder) are affected. Finally, we list in the last column the values presented in Ref. [8]. An admixture of the dispersive states with the flat band causes the anomalous scaling exponent of  $\nu = 4/3$  which was originally found in a diamond ladder [159]. The usual scaling for Anderson localization corresponds to  $\nu = 0$  at energies outside a band (“out”),  $\nu = 2/3$  at a band edge (“edge”) and  $\nu = 2$  inside a band (“in”). The energies selected in Fig. 5.4 correspond to  $\epsilon = 1$

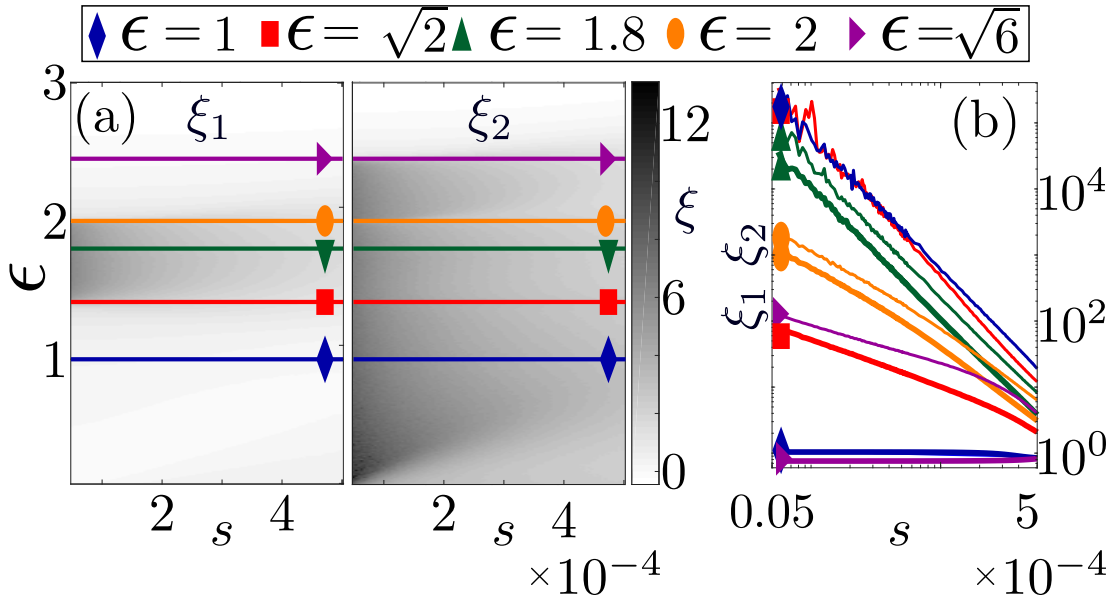


**Figure 5.5: Localization lengths.** (a) Color map of the localization lengths  $\xi_1$ ,  $\xi_2$  as a function of the energy  $\epsilon$  and the disorder strength  $s = \sigma/R_0$ . (b) Localization lengths  $\xi_1$  (thick lines),  $\xi_2$  (thin lines) in log-log scale for five different values of the energy, reported above the panel and highlighted in (a) via horizontal, solid lines. For small disorder all curves are approximately linear, making it possible to assign power law exponents  $\nu$  characterizing the small-disorder behavior  $\xi_i \sim s^\nu$ : grouping them by energy  $\epsilon$ , they read  $\nu(\epsilon = 1) \approx \{0, 2.2\}$ ,  $\nu(\epsilon = \sqrt{2}) \approx \{0.7, 2.2\}$ ,  $\nu(\epsilon = 1.8) \approx \{2.0, 1.9\}$ ,  $\nu(\epsilon = 2) \approx \{1.1, 1.1\}$ ,  $\nu(\epsilon = \sqrt{6}) \approx \{0, 0.6\}$ . Here we have chosen a dipole-dipole interaction ( $\alpha = 3$ ) with an interaction strength of  $V(R_0) = 300\Omega$ . It is apparent that the lowermost curves bend down in the rightmost part of panel (b). For the estimation of the slope, we have considered the data between  $s = 5 \times 10^{-6}$  and  $s = 5 \times 10^{-5}$ . This Figure is adapted from Ref. [2].

	experimental disorder $s \in$ $[5 \cdot 10^{-6}, 5 \cdot 10^{-4}]$	flat disorder on pair-state sites $(A_i, B_i, E_i)$ $W \in [5 \cdot 10^{-2}, 1]$	flat disorder on all sites $(A_i, B_i, C_i,$ $D_i, E_i) W \in$ $[1 \cdot 10^{-1}, 1]$	flat disorder on all sites $(A_i, B_i, C_i,$ $D_i, E_i)$ values from Ref. [8]
$\epsilon = 1$	(0, 2.2)	(0, 2.0)	(0, 1.8)	(0, 2)
$\epsilon = \sqrt{2}$	(0.7, 2.2)	(0.7, 2.0)	(0.8, 1.4)	(2/3, 4/3)
$\epsilon = 1.8$	(2.0, 1.9)	(2.0, 1.8)	(2.0, 2.0)	(2, 2)
$\epsilon = 2$	(1.1, 1.1)	(0.7, 1.3)	(0.7, 1.3)	(2/3, 4/3)
$\epsilon = \sqrt{6}$	(0, 0.6)	(0, 0.6)	(0, 0.6)	(0, 2/3)

**Table 5.1: Scaling exponents.** Scaling exponents  $\nu$  for different energies  $\epsilon$  obtained from fitting the behaviour of the localization lengths  $\xi$ .  $\xi_i \sim s^{\nu_i}$  for the first and  $\xi_i \sim W^{\nu_i}$  for the second to fourth columns, see text for details. Experimental disorder refers to disorder stemming from the Gaussian position distribution of the atoms which acts only on the pair states in the system. The range of  $s$  and  $W$  in the first row denote the interval of the disorder parameter over which the fit was performed. Values in the first column are obtained for  $\alpha = 3$  and  $n = 10^6$ , where  $n$  is the number of random matrix realizations entering (5.37). In the third and fourth column we used  $n = 10^6$  and  $10^5$ , respectively (see Ref. [2]).

(out/in),  $\sqrt{2}$  (edge/in), 1.8 (in/in), 2 (in/edge) and  $\sqrt{6}$  (edge/out). The entries within brackets refer to the two sets of bands depicted in Fig. 5.4(c,d), where the orange bands correspond to the sub lattice and the green band to the chain. So, for instance, the first value (out/in) is an energy lying within the green band (in), but outside of the orange ones (out).

For  $\epsilon = 1, \sqrt{2}, 1.8,$  and  $2$ , the leading localization lengths  $\xi_1$  belongs to the stub lattice and the second leading exponent belongs to the chain. This changes for  $\epsilon = \sqrt{6}$ , where the leading localization length can be associated to the chain and the second exponent to the stub lattice. In Ref. [8] an “anomalous” scaling  $\nu = 4/3$  was found at  $\epsilon = \sqrt{2}$  and  $2$ . This was attributed to the fact that disorder, in the detangled picture, is not merely on-site but couples the two chains. This in turn may produce resonances between states in the middle of a band and states at the edge of the other when the latter display vanishing group velocity. Comparing these values with the ones obtained for our situation, we observe reasonable agreement at  $\epsilon = 1, \epsilon = 1.8$  and  $\epsilon = \sqrt{6}$ , plus for the “edge” scaling

at  $\epsilon = \sqrt{2}$ . The anomalous “in” scaling of  $4/3$  at  $\epsilon = \sqrt{2}$  seems instead to be “cured” as we retrieve a result compatible with the usual Anderson one ( $\nu \approx 2$ ). This anomaly appears only when the disorder is present on all sites as in Ref. [8] and is likely to be due to the alternating structure of the disorder in the synthetic lattice, which in the detangled picture results in the absence of random couplings between  $Y_n^\pm$  sites as shown in Fig. 5.4(b). However, when the disorder affects only the pair sites it corresponds to the Anderson value of two (both when the disorder is flat and drawn from the distribution (A.13)). In contrast, we remark that for  $\epsilon = 2$ , for the flat distribution the result is independent on whether it acts on all or only on pair state sites and matches the expected values  $2/3$  (edge) or  $4/3$  (in, anomalous). On the other hand, the values we obtain for the disorder distribution drawn from (A.13), i.e.  $\nu(\epsilon = 2) \approx \{1.1, 1.1\}$  do not seem to be close to either the anomalous or the edge scaling exponents and, based solely on the present analysis, cannot be simply attributed to the disorder acting on only the pair state sites.

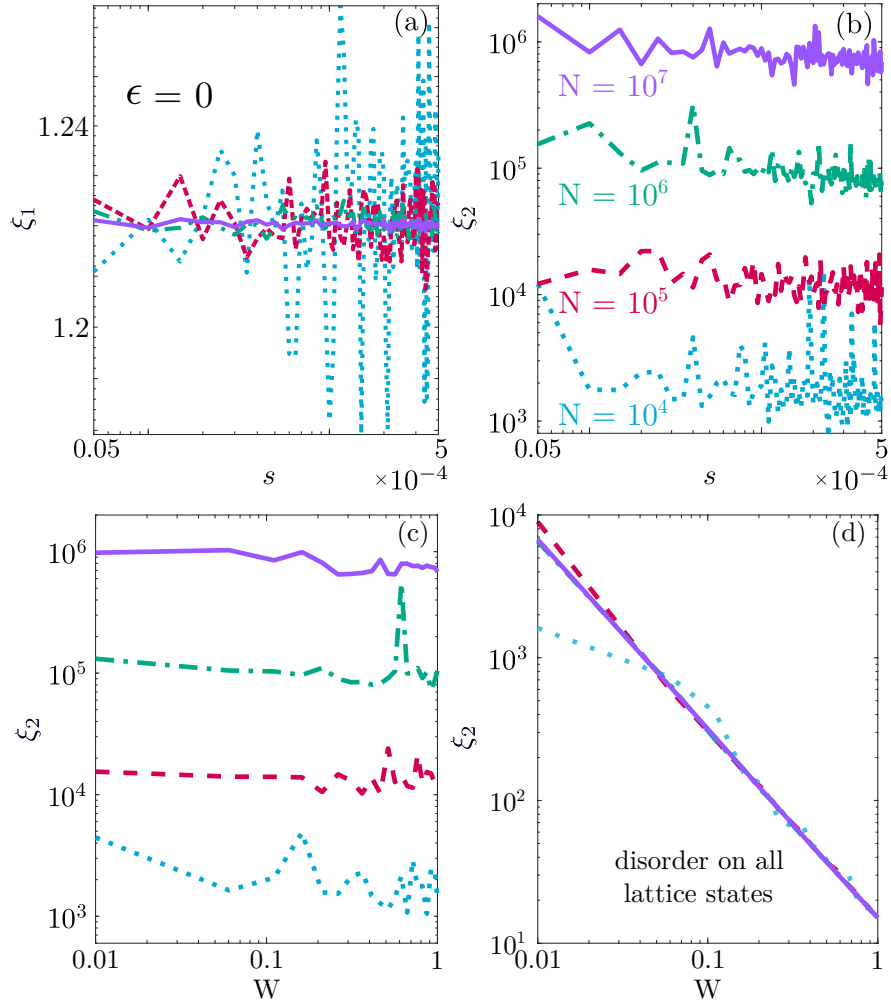
### Localization length $\xi_2$ at zero energy

Figure 5.6(a,b) shows the localization length  $\xi_1, \xi_2$  for zero energy  $\epsilon = 0$ . The localization length  $\xi_1$  shows the expected behavior, scaling with a power law exponent of  $\nu = 0$ . However,  $\xi_2$  behaves in an anomalous way as it is independent of the disorder strength  $s$  but scales with the system size  $N$ .

This anomalous behaviour also appears when considering flat disorder, with the random variable drawn from the interval  $[-W/2, W/2]$  as shown in Fig. 5.6(c). Nevertheless, the anomaly can be lifted by forcing the disorder to act on all lattice sites as shown in Fig. 5.6(d) for flat disorder. In this case the localization length  $\xi_2$  shows the typical power law scaling with disorder strength  $W$ . This scaling behavior of  $\xi_2$  caused by the alternating disorder.

## 5.4 Localized flat band state dynamics

Note, this chapter is adapted from the supplementary material in Ref. [2]. Experimentally measuring the localization lengths studied above is challenging due to the required large system size and small disorder amplitudes. However, one can probe the influence of disorder by initializing the system in a specific state and tracking the subsequent dynamics by measuring the on-site excitation densities  $\langle \hat{n}_i \rangle$  [28, 35, 153]. A particularly interesting choice for an initial state is one of the localized eigenstates of the flat band which is immobile in the absence of disorder.



**Figure 5.6: Localization length  $\xi_2$  for zero energy.** Localization lengths (a)  $\xi_1$  and (b)  $\xi_2$  for zero energy  $\epsilon = 0$  and experimental disorder acting on the pair states of the lattice (red sites in Fig. 5.4). We used a dipole-dipole interaction ( $\alpha = 3$ ) with an interaction strength of  $V(R_0) = 300\Omega$ . (c) Localization length  $\xi_2$  with flat disorder drawn from the interval  $[-W/2, W/2]$  acting on the pair states (red sites in Fig. 5.4). (d)  $\xi_2$  with flat disorder forced to act on all lattice states (all sites in Fig. 5.4). In all panels, the colours correspond to the system sizes listed in (b).

The state

$$|\psi_{\text{loc}}\rangle = \frac{1}{\sqrt{4}} (|A_i\rangle + |B_i\rangle - |E_i\rangle - |E_{i+1}\rangle) \quad (5.39)$$

is entirely localized between the  $i$ -th and  $(i+1)$ -th rungs of the ladder [see Fig. 5.7(a)] and can be prepared experimentally via single site addressing. Specifically, we will address the atoms individually with a laser pulse of Rabi frequency  $\Omega_R$  and duration  $\tau$  so that the atomic spin evolves according to

$$U(\theta \equiv \Omega_R \tau) = e^{-i\frac{\theta}{2}\sigma_x} = \begin{pmatrix} \cos \frac{\theta}{2} & -i \sin \frac{\theta}{2} \\ -i \sin \frac{\theta}{2} & \cos \frac{\theta}{2} \end{pmatrix}$$

The laser detuning  $\Delta$  is chosen to be resonant with the transition of the addressed atom. If  $\Delta \gg \Omega_R$ , instead, it acts trivially like an identity operator. Specifically, we will distinguish two special cases, namely  $\Delta = 0$  and  $\Delta = -V(R_0)$  corresponding to the blockade and facilitation condition, respectively. The state  $|\psi_{\text{loc}}\rangle$  can be obtained by the application of six pulses on an initial state with all atoms in the spin-down state as

$$|\psi_{\text{loc}}\rangle = \mathcal{F}_2(2\pi)\mathcal{F}_4(2\pi)\mathcal{F}_3(\pi)\mathcal{F}_2\left(\frac{\pi}{2}\right)\mathcal{B}_4(\pi)\mathcal{B}_1\left(\frac{\pi}{2}\right)|\psi_{\downarrow\dots\downarrow}\rangle. \quad (5.40)$$

Here,  $\mathcal{B}_j(\theta), \mathcal{F}_j(\theta)$  stand for the laser pulse of area  $\theta = \Omega_R \tau$  in the blockaded ( $\mathcal{B}$ ) and facilitated ( $\mathcal{F}$ ) regime applied at site  $j = 1, \dots, 4$  labeling the effective plaquette formed by the four sites corresponding to two adjacent rungs of the ladder (see Eq. (5.41)). The first pulse creates an excitation at site 1, the second pulse then exploits the blockade mechanism to create a superposition of spin-up states at sites 1 and 4. Next, the pulse in the facilitated regime applied at site 2 creates a superposition of the form  $-i|\uparrow\rangle + |\downarrow\rangle$  if and only if a single nearest-neighbor is already excited, and so forth. We have omitted the global  $-i$  factors in the second, and fourth lines of (5.41). In practice the choice of  $\Omega_R$  is a trade-off between the need to keep the state-preparation time to a minimum (implying higher values of  $\Omega_R$ ) and the upper bounds imposed for keeping the blockade and facilitation conditions preserved, see Ref. [1] for details of these issues.

Once the state  $|\psi_{\text{loc}}\rangle$  has been prepared,

$$\begin{array}{l}
\begin{array}{|c|c|} \hline \downarrow_1 & \downarrow_2 \\ \hline \downarrow_3 & \downarrow_4 \\ \hline \end{array} \xrightarrow{\mathcal{B}_1(\frac{\pi}{2})} -i \begin{array}{|c|c|} \hline \uparrow & \downarrow \\ \hline \downarrow & \downarrow \\ \hline \end{array} + \begin{array}{|c|c|} \hline \downarrow & \downarrow \\ \hline \downarrow & \downarrow \\ \hline \end{array} \\
\xrightarrow{\mathcal{B}_4(\pi)} \begin{array}{|c|c|} \hline \uparrow & \downarrow \\ \hline \downarrow & \downarrow \\ \hline \end{array} + \begin{array}{|c|c|} \hline \downarrow & \downarrow \\ \hline \downarrow & \uparrow \\ \hline \end{array} \\
\xrightarrow{\mathcal{F}_2(\frac{\pi}{2})} -i \begin{array}{|c|c|} \hline \uparrow & \uparrow \\ \hline \downarrow & \downarrow \\ \hline \end{array} + \begin{array}{|c|c|} \hline \uparrow & \downarrow \\ \hline \downarrow & \downarrow \\ \hline \end{array} - i \begin{array}{|c|c|} \hline \downarrow & \uparrow \\ \hline \downarrow & \uparrow \\ \hline \end{array} + \begin{array}{|c|c|} \hline \downarrow & \downarrow \\ \hline \downarrow & \uparrow \\ \hline \end{array} \\
\xrightarrow{\mathcal{F}_3(\pi)} \begin{array}{|c|c|} \hline \uparrow & \uparrow \\ \hline \downarrow & \downarrow \\ \hline \end{array} + \begin{array}{|c|c|} \hline \uparrow & \downarrow \\ \hline \uparrow & \downarrow \\ \hline \end{array} + \begin{array}{|c|c|} \hline \downarrow & \uparrow \\ \hline \downarrow & \uparrow \\ \hline \end{array} + \begin{array}{|c|c|} \hline \downarrow & \downarrow \\ \hline \uparrow & \uparrow \\ \hline \end{array} \\
\xrightarrow{\mathcal{F}_4(2\pi)} \begin{array}{|c|c|} \hline \uparrow & \uparrow \\ \hline \downarrow & \downarrow \\ \hline \end{array} + \begin{array}{|c|c|} \hline \uparrow & \downarrow \\ \hline \uparrow & \downarrow \\ \hline \end{array} - \begin{array}{|c|c|} \hline \downarrow & \uparrow \\ \hline \downarrow & \uparrow \\ \hline \end{array} - \begin{array}{|c|c|} \hline \downarrow & \downarrow \\ \hline \uparrow & \uparrow \\ \hline \end{array} \\
\xrightarrow{\mathcal{F}_2(2\pi)} \begin{array}{|c|c|} \hline \uparrow & \uparrow \\ \hline \downarrow & \downarrow \\ \hline \end{array} - \begin{array}{|c|c|} \hline \uparrow & \downarrow \\ \hline \uparrow & \downarrow \\ \hline \end{array} - \begin{array}{|c|c|} \hline \downarrow & \uparrow \\ \hline \downarrow & \uparrow \\ \hline \end{array} + \begin{array}{|c|c|} \hline \downarrow & \downarrow \\ \hline \uparrow & \uparrow \\ \hline \end{array},
\end{array} \tag{5.41}$$

where the picture of configurations is given in real space, it evolves according to  $\hat{H}_{\mathcal{H}_1}$ , Eq. (5.18), using the following algorithm. The spin dynamics is simulated with the effective Hamiltonian expressed in the basis of the Lieb lattice of length  $L$

$$\{|A_1\rangle, \dots, |A_L\rangle, |B_1\rangle, \dots, |B_L\rangle, \dots, \dots, |E_L\rangle\}, \tag{5.42}$$

resulting in

$$\Omega^{-1}\hat{H}_{\text{eff}} = \hat{H}_0 \otimes \mathbf{1}_L + \hat{H}_0^{\text{dis}} + \left[ \hat{H}_1 \otimes \hat{G}_L + \text{H.c.} \right], \tag{5.43}$$

where the tilde labels dimensionless quantities ( $\tilde{V}(R_0) = V(R_0)/\Omega$ ). The first term in Eq. 5.43 accounts for the hopping within a unit cell, the second term records the disorder, and the third term describes hopping between contiguous unit cells. In matrix representation,  $\hat{H}_0$  takes the form

$$\hat{H}_0 = \begin{pmatrix} 0 & 0 & 1 & 0 & 0 \\ 0 & 0 & 0 & 1 & 0 \\ 1 & 0 & 0 & 0 & 1 \\ 0 & 1 & 0 & 0 & 1 \\ 0 & 0 & 1 & 1 & 0 \end{pmatrix}, \tag{5.44}$$

$\hat{H}_1$  is a  $5 \times 5$  matrix with only non-zero entries  $(\hat{H}_1)_{1,3} = (\hat{H}_1)_{2,4} = 1$ ,  $(G_L)_{ij} = \delta_{i,j-1}$  is a  $L \times L$  matrix with ones on the first upper diagonal and the disorder

matrix

$$\hat{H}_0^{\text{dis}} = \text{diag} \left( \tilde{\delta}_{A_1}, \dots, \tilde{\delta}_{A_{L-1}}, \tilde{\delta}_{A_L} = 0, \tilde{\delta}_{B_1}, \dots, \tilde{\delta}_{B_{L-1}}, \tilde{\delta}_{B_L} = 0, \right. \\ \left. \tilde{\delta}_{C_1} = 0, \dots, \tilde{\delta}_{C_L} = 0, \tilde{\delta}_{D_1} = 0, \dots, \tilde{\delta}_{D_L} = 0, \tilde{\delta}_{E_1}, \dots, \tilde{\delta}_{E_L} \right) \quad (5.45)$$

is a  $5L \times 5L$  diagonal matrix. We impose open boundary conditions (OBC) by requiring that  $\tilde{\delta}_{A_L} = \tilde{\delta}_{B_L} = 0$  because  $A_L$  and  $B_L$  correspond to pair states that would require an additional spin on the non-existent site  $L + 1$ . Analogously, we enforce the OBC in the coupling matrix by setting all Hamiltonian elements corresponding to the  $L$ -th and  $2L$ -th rows and columns to 0. Here,  $\tilde{\delta}_{\Xi_j} = \Omega^{-1} (V(d_{\Xi_j}) - V(R_0))$ , where  $\Xi_j = A_j, \dots, E_j$  and  $d_{\Xi_j}$  is a shorthand for the spin separation in the given configuration  $\Xi_j$ . We note that since configurations  $C, D$  correspond to single spin excitation, the associated disorder is vanishing by definition,  $\tilde{\delta}_{C_j} = \tilde{\delta}_{D_j} = 0, \forall j$ . The disorder energies  $\tilde{\delta}_{\Xi_j}$  are generated from first drawing a specific realization of atomic positions at each site of the lattice in all three spatial directions with isotropic Gaussian distribution of width  $s$ . We then exactly evolve an initial state

$$|\psi_0\rangle = \sum_{j=1}^{5L} c_j |b_j\rangle, \quad (5.46)$$

as  $|\psi(t)\rangle = \exp[-it\hat{H}_{\text{eff}}] |\psi_0\rangle$ , where  $b_j$  are the elements of the basis (5.42) (strictly speaking there are only  $5L - 2$  non-trivial elements due to the OBC). We note that the result of the evolution depends on two independent parameters,  $s$  and the ratio  $V(R_0)/\Omega$ , where the Rabi frequency should further satisfy  $\Omega \ll V(2R_0)$  for the effective Hamiltonian (5.43) to be valid.

To establish how much an initially-localized configuration spreads through the system, we define a set of effective probabilities

$$P_i^\gamma = \frac{n_i^\gamma}{\sum_{i=1}^L n_i^\gamma}. \quad (5.47)$$

Here  $n_i^\gamma = \langle \psi(t) | \hat{n}_i^\gamma | \psi(t) \rangle$ ,  $\gamma = u, l$  for the upper and lower leg of the ladder respectively and  $L$  denotes the length of the ladder. The probability of finding an excitation at position  $i$ , is by definition  $n_i^\gamma$ . These probabilities are then averaged over the disorder  $P_i^\gamma \rightarrow \langle P_i^\gamma \rangle_{\delta V} \equiv p_i^\gamma$  and used to define the average

position and the standard deviation of the excitations according to

$$\bar{x}^\gamma = \sum_{i=1}^L p_i^\gamma i \quad (5.48)$$

$$(\Delta x^\gamma)^2 = \sum_{i=1}^L p_i^\gamma i^2 - (\bar{x}^\gamma)^2 = \sum_{i=1}^L p_i^\gamma (i - \bar{x}^\gamma)^2. \quad (5.49)$$

We show the time evolution of the excitation density in Fig. 5.7(b). The effect of the disorder becomes apparent in the width  $\Delta x$  of the density packet which quickly reaches a stationary state. It is interesting to observe that, as shown in Fig. 5.7(c), the stationary value of  $\Delta x$  displays a non-monotonic behavior as a function of  $s$ . This can be understood as follows: at very small but finite disorder strength  $s$ , the initial state (energy  $\epsilon \approx 0$ ) is almost a flat band eigenstate and it therefore only minimally spreads (see e.g. Refs. [152, 160]). As  $s$  is increased, this state hybridizes either with neighboring localized states, or with delocalized states, allowing transport over larger distances to occur. At the same time, however, the localization lengths at  $\epsilon \approx 0$  decrease, binding the maximal spread  $\Delta x$  of the state. Once the decrease in the localization scale catches up with the increase of  $\Delta x$ , the behavior is dominated by localization and, as expected,  $\Delta x$  decreases with increasing disorder strength.

In Fig. 5.8(a) we present the results of the simulation, analogous to those performed in Fig. 5.7, showing  $\Delta x$  in the  $s - \Omega/V(R_0)$  plane. We observe that the maximum of  $\Delta x$  as a function of the disorder gets shifted towards higher disorder strengths as  $\Omega$  is increased. The dependence of  $\Delta x$  in Fig. 5.8(a) can be intuitively understood as follows. Smaller values of  $\Omega/V(R_0)$  correspond to larger diagonal disorder elements  $\tilde{\delta}$ . Since the disorder couples the flat and dispersive bands, the smaller the  $s$ , the smaller the  $\Omega$  that is sufficient to cause the propagation of excitations and thus the increase in  $\Delta x$ . As  $s$  is increased, Anderson localization becomes more and more relevant and, correspondingly, the localization length at  $\epsilon = 0$  shrinks. Eventually, the state becomes capable of propagating over distances comparable to the localization length. Further increasing  $s$  reduces this scale, corresponding to the decrease in  $\Delta x$ . Clearly, by increasing  $\Omega/V(R_0)$  the hopping amplitude becomes more relevant with respect to the typical energy shifts and the localization length is increased. Higher values of  $s$  are then required to localize the state again. In Fig 5.8(b,c) we show a comparison between the exact evolution according to the full Hamiltonian (5.1), dashed line, and  $H_{\text{eff}}$ , solid line. As expected, the predictions of the two models show an agreement in the regime where  $\Omega \ll V(2R_0)$ , Fig. 5.8(c) ( $V(R_0)/\Omega = 200$ ). On the other hand for larger  $\Omega$ , the two models start to differ as shown in Fig. 5.8(b) ( $V(R_0)/\Omega = 20$ ).

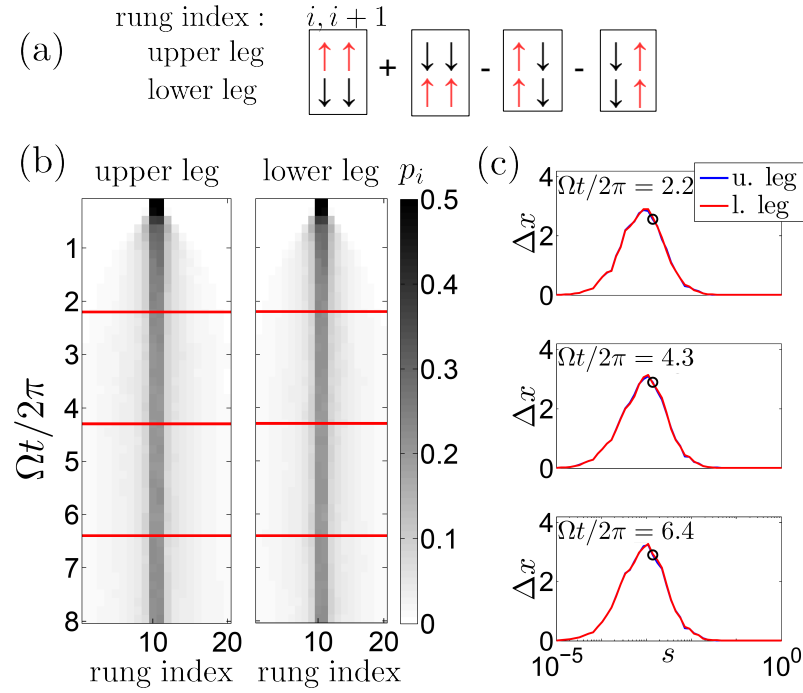


**Figure 5.7: Time evolution of the localized state.** (a) Schematic representation of the spin configuration corresponding to the initial state  $|\psi_{\text{loc}}\rangle$  localized at rungs  $i, i+1$  of the ladder. (b) The averaged probability of excitations  $p_i$  given by the time evolution of the localized state. Initially the state has support in the middle (rungs 10 and 11) of the ladder of length 20 for  $s = 0.0014$ . The left (right) panel shows the time evolution in the upper (lower) leg of the ladder. The horizontal red lines denote three different times for which the respective value of  $\Delta x$  is shown as a black circle in (c). (c) Standard deviation of the excitation positions  $\Delta x$  as a function of the disorder strength  $s$  for three different times. Blue (red) solid lines, which are virtually indistinguishable correspond to upper (lower) leg of the ladder respectively. Results obtained for 100 disorder realizations and  $V(R_0) = 200\Omega$ . This plot can be found in Ref. [2].

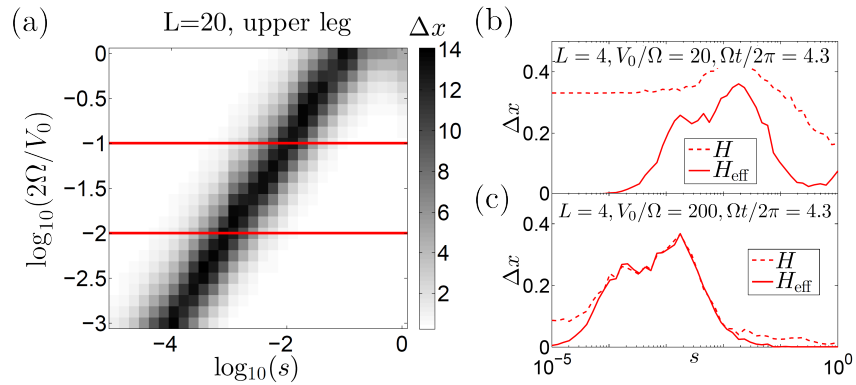


**Figure 5.8: Spin dynamics in the effective and full model.** (a) Width  $\Delta x$ , Eq. (5.49), of the excitation positions in the  $s - \Omega/V(R_0)$  plane. Here,  $\Delta x$  was obtained by evolving the initial state  $|\psi_{\text{loc}}\rangle$  located at rungs 10 and 11 in the middle of the ladder of length  $L = 20$  by the effective Hamiltonian  $H_{\text{eff}}$ . The two red solid lines correspond to a cut for fixed values of  $\Omega/V(R_0)$ ,  $\Omega/V(R_0) = 1/20$  (upper line) and  $\Omega/V(R_0) = 1/200$  (lower line). (b) Comparison between the evolution of  $|\psi_{\text{loc}}\rangle$  generated by  $H$ , Eq. (5.1), dashed line and  $H_{\text{eff}}$ , solid line, in a ladder of  $L = 4$  and for  $\Omega/V(R_0) = 1/20$ . (c) Same as (b) with  $\Omega/V(R_0) = 1/200$ . Here we have fixed the time so that  $\Omega t/2\pi = 4.3$  irrespective  $\Omega$  and averaged over 100 disorder realizations. This Figure is taken from the supplementary material in Ref. [2].

## 5.5 Outlook and Conclusion

In this chapter we have shown that Rydberg quantum simulators allow us to explore localization phenomena. The current chapter focuses on the Lieb ladder and on a particular excitation sector. Key features of the phenomenology discussed for this case are however more general and would apply to higher-dimensional lattices as well. In particular, these would give rise to effective synthetic lattices with flat bands and localized eigenstates capable of aiding the localization. In two dimensions, a similar behavior to the one observed in the Lieb ladder is expected to occur. In three dimensions, according to the standard properties of Anderson localization, a transition is expected at the critical disorder strength, from a regime that allows transport to a fully-localized one. This transition is related to the appearance of mobility edges in the spectrum.

From the single-particle localization investigated in this chapter we will now expand our considerations to the many-body system in a disordered one-dimensional Rydberg system subject to the constraints imposed by facilitation.

# Chapter 6

## Localization in spin chains with facilitation constraints and disordered interactions

This chapter is adapted from Ref. [3].

### 6.1 Introduction

In this chapter we are interested in understanding localization in disordered spin chains in the presence of facilitation, a mechanism already encountered in previous chapters and regarded here as an example for a kinetic constraint [161]. Such a scenario was recently realized experimentally [6] within an optical lattice quantum simulator consisting of individually trapped Rydberg atoms [13,153,162,163]. As previously explained, in a facilitated setting [48,49,51,53], atoms are excited in a way that the excitation of a Rydberg atom is strongly enhanced by an already excited neighbor. Under these conditions, an initial excitation can “seed” the nucleation of an excitation cluster [52,164,165] (for the classical origin of ideas about facilitation dynamics see Refs. [161,166–168]). Disorder enters in this scenario due to the fact that the position of each atom is thermally distributed within its trap. We show that in this situation the system maps onto a disordered and interacting XX-spin chain, which is the typical starting point for many MBL studies. However, in our case disorder and interactions are non-local and intertwined, which makes the analysis of localization effects rather involved. We characterize the localization properties via the imbalance, the half-chain entanglement entropy and the energy level statistics and find signatures of a crossover between a delocalized and a localized phase. Our study demonstrates a need to

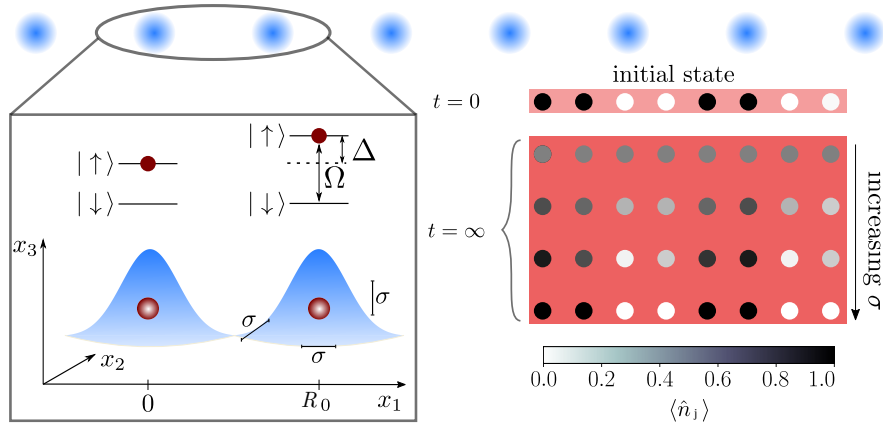


**Figure 6.1: Setup of the one-dimensional Rydberg lattice with kinetic facilitation constraints.** Setup and basic principle. In a one-dimensional lattice atoms in their electronic ground state,  $|\downarrow\rangle$ , are coupled to a highly-excited Rydberg state,  $|\uparrow\rangle$ , with a laser of Rabi frequency  $\Omega$  and detuning  $\Delta$ . The atomic positions in the local traps are distributed according to a Gaussian distribution of width  $\sigma$ . For small values of  $\sigma$  excitations, initially prepared at time  $t = 0$  in a state  $|\uparrow\uparrow\downarrow\downarrow\uparrow\uparrow\downarrow\downarrow\rangle$ , spread throughout the chain. With increasing value of  $\sigma$  localization sets in and the systems remains localized in a state close to the initial configuration. (Taken from Ref. [3]).

consider situations that differ from the standard settings for MBL, namely local on-site disorder and clean interactions, in order to study possible localization in constrained systems realizable in experiments.

## 6.2 Setup

Our setup consists of a one-dimensional chain of  $N$  traps, such as optical tweezers, each loaded with a single atom, and separated by the nearest-neighbor distance  $R_0$  (see Fig. 6.1). The atoms are described as effective two-level systems, where the electronic ground state  $|\downarrow\rangle$  is coupled to the Rydberg state  $|\uparrow\rangle$  via a laser with Rabi frequency  $\Omega$  and detuning  $\Delta$ . The many-body Hamiltonian is given, in the rotating wave approximation (RWA) by (2.33)

$$\hat{H} = \Omega \sum_k \hat{\sigma}_k^x + \Delta \sum_k \hat{n}_k + \frac{C_\alpha}{2} \sum_{\substack{k=1 \\ m \neq k}}^N \frac{\hat{n}_m \hat{n}_k}{|\mathbf{r}_k - \mathbf{r}_m|^\alpha}, \quad (6.1)$$

where  $C_\alpha$  is for  $\alpha = 6$  the so-called dispersion coefficient of the van der Waals interaction (we are considering different values for  $\alpha$  in Section 6.5.) and  $\mathbf{r}_k$  are the atomic positions [21]. The spin-operators are defined through  $\hat{\sigma}_k^x = |\uparrow\rangle_k \langle\downarrow|_k + |\downarrow\rangle_k \langle\uparrow|_k$  and  $\hat{n}_k = |\uparrow\rangle_k \langle\uparrow|_k = \frac{1}{2} (\mathbb{1} + \hat{\sigma}_k^z)$  with  $\hat{\sigma}_k^z = |\uparrow\rangle_k \langle\uparrow|_k - |\downarrow\rangle_k \langle\downarrow|_k$ .

### 6.3 Constrained spin chain

The facilitation (anti-blockade) condition [26, 48–53, 169] is imposed by setting the laser detuning such that it cancels exactly the nearest-neighbor interaction,  $\Delta = -V_0 \equiv -\frac{C_6}{R_0^6}$ . In other words,  $\Delta$  is chosen so that the facilitation radius is  $R_0$  (see Fig. 6.1). Furthermore, we assume that the detuning is large,  $|\Delta| \gg \Omega$ , so that unfacilitated transitions are suppressed and can be neglected [6]. Under these conditions, the dynamics is effectively constrained to allow spin flips only on sites contiguous to already present excitations.

Accounting for this constraint and neglecting interactions beyond nearest-neighbors, which is justified by the rapid decay of the van der Waals interaction, the Hamiltonian can be approximated by

$$\hat{H}_{\text{eff}} = \Omega \sum_{k=1}^N \hat{P}_k \hat{\sigma}_k^x, \quad (6.2)$$

where the projector  $\hat{P}_k = \frac{1}{2} (\mathbb{1} - \hat{\sigma}_{k-1}^z \hat{\sigma}_{k+1}^z)$  implements the constraint. To avoid defining different projectors for the boundaries we assume that there are two fictitious down-spins at the ends of the chain, so that  $\hat{n}_0 \equiv \hat{n}_{N+1} \equiv 0$ .

Formally, Eq. (6.2) is derived by adopting an interaction picture, introduced in Sec. 2.4 and similar to the one in Sec. 5.2.1, via the unitary

$$\hat{U} = \exp \left[ -it\Delta \sum_{k=1}^N \hat{n}_k (\mathbb{1} - \hat{n}_{k+1}) \right], \quad (6.3)$$

and subsequently dropping all terms oscillating with frequency  $V_0$  (RWA). We can now introduce the operator

$$\hat{N}_{\text{cl}} = \sum_{k=1}^N \hat{n}_k (1 - \hat{n}_{k+1}), \quad (6.4)$$

which can be interpreted as the number of clusters of uninterrupted domains of excitations terminated by down spins, and is by construction a conserved quantity,  $[\hat{H}_{\text{eff}}, \hat{N}_{\text{cl}}] = 0$ . Its conservation makes it possible to adopt a dual description in terms of *domain walls*. The detailed derivation can be found in details elsewhere [170]. We use the notation  $|\bullet\rangle$  for a domain wall and  $|\circ\rangle$  for a hole (absence of domain wall). The relation between real and dual space is a two-to-one mapping given by

$$|\uparrow\downarrow\rangle, |\downarrow\uparrow\rangle \rightarrow |\bullet\rangle \quad \text{and} \quad |\uparrow\uparrow\rangle, |\downarrow\downarrow\rangle \rightarrow |\circ\rangle. \quad (6.5)$$

Note, a chain of  $N + 2$  sites has  $N + 1$  bonds yielding a discrepancy between the dimension of the real space ( $2^N$ ) and dual space ( $2^{N+1}$ ). This is caused by the

domain-wall parity conservation, which separates the domain-wall Hilbert space in two subspaces with even and odd numbers of domain walls. In our convention, only the subspace with an even number of domain walls is physical. This results in a one-to-one mapping between real and dual space and the two pictures are equivalent. The dual space operators are standard Pauli matrices given by

$$\hat{\mu}_k^x = |\bullet\rangle_k \langle \circ|_k + |\circ\rangle_k \langle \bullet|_k, \quad (6.6)$$

$$\hat{\mu}_k^y = -i |\bullet\rangle_k \langle \circ|_k + i |\circ\rangle_k \langle \bullet|_k, \quad (6.7)$$

$$\hat{\mu}_k^z = |\bullet\rangle_k \langle \bullet|_k - |\circ\rangle_k \langle \circ|_k, \quad (6.8)$$

and are related to the Pauli operators defined in real space by a Kramers-Wannier transformation

$$\begin{aligned} \hat{\sigma}_k^x &= \hat{\mu}_k^x \hat{\mu}_{k+1}^x, \\ \hat{\sigma}_k^y &= (-1)^{k+1} \prod_{l=1}^{k-1} \hat{\mu}_l^z \hat{\mu}_k^y \hat{\mu}_{k+1}^x, \\ \hat{\sigma}_k^z &= (-1)^{k+1} \prod_{l=1}^k \hat{\mu}_l^z. \end{aligned} \quad (6.9)$$

Note, the  $k$ th bond connects the  $(k-1)$ th spin with the  $k$ th one. The operators in dual as well as real space fulfill the standard (anti-)commutation relations

$$\left[ \hat{\mu}_k^\alpha, \hat{\mu}_l^\beta \right] = 2i \delta_{kl} \epsilon_{\alpha\beta\gamma} \hat{\mu}_k^\gamma \quad \text{and} \quad \left\{ \hat{\mu}_k^\alpha, \mu_k^\beta \right\} = 2 \delta_{\alpha,\beta} \mathbb{1}_k, \quad (6.10)$$

with the Kronecker symbol  $\delta_{\alpha,\beta}$  and the three-dimensional Levi-Civita tensor  $\epsilon_{\alpha\beta\gamma}$ . Substituting (6.9) into the Hamiltonian (6.2) yields the Hamiltonian in dual space

$$\begin{aligned} \hat{H}_{\text{eff}} &= \Omega \sum_{k=1}^N \hat{P}_k \hat{\sigma}_k^x = \frac{\Omega}{2} \sum_{k=1}^N (\mathbb{1} - \hat{\sigma}_{k-1}^z \hat{\sigma}_{k+1}^z) \hat{\sigma}_k^x = \frac{\Omega}{2} \sum_{k=1}^N (\mathbb{1} - \hat{\mu}_k^z \hat{\mu}_{k+1}^z) \hat{\mu}_k^x \hat{\mu}_{k+1}^x \\ &= \frac{\Omega}{2} \sum_{k=1}^N (\hat{\mu}_k^x \hat{\mu}_{k+1}^x + \hat{\mu}_k^y \hat{\mu}_{k+1}^y), \end{aligned} \quad (6.11)$$

which corresponds to a special case of the  $XY$  model with zero transverse field. The  $XX$  model is a special case of the class of  $XY$  models

$$\hat{H}_{XY} = \sum_{k=1}^N \left( \frac{1+\gamma}{2} \hat{\mu}_k^x \hat{\mu}_{k+1}^x + \frac{1-\gamma}{2} \hat{\mu}_k^y \hat{\mu}_{k+1}^y \right) - h \sum_{k=1}^{N-1} \hat{\mu}_k^z \quad (6.12)$$

which are integrable and can be solved via a Jordan-Wigner transformation to fermionic degrees of freedom followed by a Bogoliubov transformation. The

Hamiltonian (6.2) is then mapped to that of an XX-model, equivalent to free fermions [171],

$$\hat{H}_{\text{XX}} = \frac{\Omega}{2} \sum_{k=1}^N (\hat{\mu}_k^x \hat{\mu}_{k+1}^x + \hat{\mu}_k^y \hat{\mu}_{k+1}^y), \quad (6.13)$$

where the  $\hat{\mu}_k^\alpha$  are spin operators ( $\alpha = x, y, z$ ) living on the  $k$ -th bond. Note, that in this domain wall picture the index  $k$ , labeling the bonds, runs from 1 to  $N + 1$  as we introduced to fictitious spins, so that the first and last bonds connect them to the actual chain.

### 6.3.1 Constrained Rydberg gas with disorder

As we have seen in Chapter 2.4, disorder emerges in our setting due to the finite temperature  $T$  of the kinetic degrees of freedom of the atoms [2, 6]. The atomic positions are statistically distributed and given by  $\mathbf{r}_k = k\mathbf{R}_0 + \delta\mathbf{r}_k$  with  $\mathbf{r}_0 = (0, 0, R_0)$  and  $\delta\mathbf{r}_k$  the displacement from the center of the  $k$ -th trap. For low enough temperatures — such that each atom is still well confined within its trap — the displacements  $\delta\mathbf{r}_k$  obey an approximately Gaussian distribution of vanishing mean and width  $\sigma = \sqrt{k_B T / (m\omega^2)}$ , with  $m$  the atomic mass,  $\omega$  the trapping frequency, and  $k_B$  Boltzmann's constant. For simplicity, we assume the traps to be isotropic.

From Hamiltonian (6.1) one recognizes that the randomness of the atomic positions affects the interaction term through the distances  $|\mathbf{r}_{k+l} - \mathbf{r}_k| = |l\mathbf{r}_0 + \delta\mathbf{r}_{k+l} - \delta\mathbf{r}_k|$ . In our approximation, where we neglect the tails of the interaction and only retain the nearest-neighbor contribution, disorder generates a random term of the form

$$\hat{V}_{\text{dis}} = \sum_{k=1}^{N-1} \delta V_k \hat{n}_k \hat{n}_{k+1}, \quad (6.14)$$

where  $\delta V_k = C_6 / |\mathbf{r}_0 + \delta\mathbf{r}_k - \delta\mathbf{r}_{k+1}|^6 - V_0$ . Note that, while the displacements  $\delta\mathbf{r}_k$  are independent random variables, this is not true for the energy shifts  $\delta V_k$  [6].

Transforming into the dual domain wall picture the interaction becomes non-local

$$\begin{aligned} \hat{V}_{\text{dis}} &= \frac{1}{4} \sum_{k=1}^{N-1} \delta V_k \left( \left[ (-1)^{k+1} \prod_{l=1}^k \hat{\mu}_l^z \right] + \mathbb{1} \right) \\ &\quad \times \left( \left[ (-1)^{k+2} \prod_{j=1}^{k+1} \hat{\mu}_j^z \right] + \mathbb{1} \right), \end{aligned} \quad (6.15)$$

i.e. includes strings of operators of arbitrary length (up to the system size).

This last feature marks a difference with standard MBL models, where the parameters that control disorder and interactions are typically independent. Yet, the system we study is by no means exotic as it represents a standard spin model in real space [see Eqs. (6.2) and (6.14)]. It does not only have a connection to Rydberg gases but more broadly to disordered spin systems, for example in the context of nuclear magnetic resonance [172, 173]. This suggests that the study of non-local disorder may be more relevant than it would seem at first glance.

## 6.4 Numerical results

In order to characterize localization in our system, described by the combined Hamiltonian  $\hat{H} = \hat{H}_{\text{eff}} + \hat{V}_{\text{dis}}$  [see Eqs. (6.2) and (6.14)], we study the following quantities introduced in Chapter 3.2.2: (i) the imbalance  $\mathcal{I}$ , defined further below, which tracks the memory of an initial alternating structure at long times; (ii) the time evolution of the half-chain entanglement entropy (EE)  $S(t)$ ; and (iii) the level statistics ratio (LSR) of the spectrum of the Hamiltonian. In our simulations we measure all distances in units of the trap spacing  $R_0$ , and energy scales (time) in units of the (inverse) Rabi frequency  $\Omega$ . All quantities presented are averaged over 100 disorder realizations.

Unless stated otherwise, simulations start from an initial state with alternating pairs of up and down spins,

$$|\Psi(t=0)\rangle_{\text{spin}} = |\uparrow\uparrow\downarrow\downarrow\uparrow\uparrow\downarrow\downarrow\cdots\rangle, \quad (6.16)$$

which translates into a staggered configuration of domain walls [see Fig. 6.2(c)]. A reason for choosing this initial state is that the system we study features eigenstates which are decoupled from the disorder. We can construct one of them per possible number of clusters  $N_{\text{cl}}$ . These are of the form  $\hat{\Phi}^{N_{\text{cl}}} |\downarrow\downarrow \dots \downarrow\rangle$  ( $N_{\text{cl}} = 0, \dots, N/2$ ), with

$$\hat{\Phi} = \sum_{k=1}^N (-1)^k (1 - \hat{n}_{k-1}) \sigma_k^+ (1 - \hat{n}_{k+1}). \quad (6.17)$$

They are linear combinations of configurations with isolated excitations, and they remain (zero-energy) eigenstates of  $H_{\text{eff}}$  (6.2), even after the introduction of the interactions. Thus, they display uniform densities and always remain delocalized. There is one such state per sector at fixed number of clusters (see Section 6.4.4). To avoid spurious localization effects, we have constructed our initial state in such a way that it has no overlap with any of these special states.

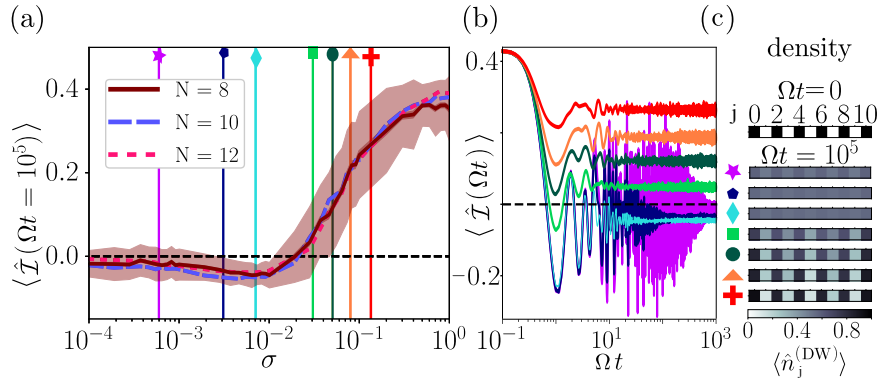


**Figure 6.2: Domain wall imbalance and average of the local density of domain walls.** (a) Domain wall imbalance in the long-time limit ( $\Omega t = 10^5$ ) for a chain of  $N = 8$  (brown, solid line),  $N = 10$  (blue, long dashes) and  $N = 12$  (red, short dashes) atoms. The shaded area is plus/minus the standard deviation for 100 disorder realizations at  $t = 10^5$  for a chain of  $N = 8$  atoms. (b) Imbalance as a function of time (up to  $\Omega t = 10^3$ ) for seven values of the trap width  $\sigma$  for  $N = 8$  atoms; in increasing order:  $\sigma = 0.0006$  (purple, star),  $0.0031$  (dark blue, pentagon),  $0.0071$  (light blue, rhombus),  $0.0306$  (green, square),  $0.0506$  (dark green, circle),  $0.08$  (orange, triangle),  $0.135$  (red, cross). (c) Average local density of domain walls  $\langle \hat{n}_j^{(DW)} \rangle$  in the initial state and at long times ( $\Omega t = 10^5$ ) for all values of the disorder displayed on the left and  $N = 10$ . A crossover from a quasi-uniform and delocalized average to configurations more and more similar to the initial state is observed as  $\sigma$  is increased. (This figure can be found in Ref. [3]).

### 6.4.1 Domain wall imbalance

Generally, an imbalance estimates how close the state of the system is to a staggered (alternating) configuration and thus measures the change of the spatial structure. The comparison of its value at long times with its initial value provides a measure of how much memory the system retains of its initial state [74, 174], provided the initial state is chosen so that the imbalance is large, and thus gives an indication of the non-ergodicity of the dynamics. We define the imbalance as

$$\hat{\mathcal{I}} = \frac{1}{N-1} \sum_{k=1}^{N-1} (-1)^k [\hat{n}_k (\mathbb{1} - \hat{n}_{k+1}) + (\mathbb{1} - \hat{n}_k) \hat{n}_{k+1}] .$$

On the state (6.16) (with  $N$  even), it evaluates to  $(N-2)/(2N-2)$  and tends to  $1/2$  for  $N \gg 1$ . Using  $\hat{n}_k = \mathbb{1} + \hat{\sigma}_k^z$ , the imbalance can be rewritten as

$$\hat{\mathcal{I}} = \frac{1}{2} \frac{1}{N-1} \sum_{k=1}^{N-1} (-1)^{k+1} (\mathbb{1} - \hat{\sigma}_k^z \hat{\sigma}_{k+1}^z) , \quad (6.18)$$

which can be transformed into the domain wall picture

$$\begin{aligned} \hat{\mathcal{I}} &= \frac{1}{2} \frac{1}{N-1} \sum_{k=1}^{N-1} (-1)^{k+1} \left[ \mathbb{1} - \left( (-1)^{k+1} \prod_{l=1}^j \hat{\mu}_l^z \right) \left( (-1)^k \prod_{l=1}^{k+1} \hat{\mu}_l^z \right) \right] \\ &= \frac{1}{2} \frac{1}{N-1} \sum_{k=1}^{N-1} (-1)^{k+1} \left[ \mathbb{1} + \left( \prod_{l=1}^k (\hat{\mu}_l^z)^2 \right) \hat{\mu}_{k+1}^z \right] \\ &= \frac{1}{2} \frac{1}{N-1} \sum_{k=1}^{N-1} (-1)^{k+1} (\mathbb{1} + \hat{\mu}_{k+1}^z) . \end{aligned}$$

Introducing the domain wall density operator,  $\hat{n}_k^{(\text{DW})} = \frac{1}{2} [\hat{\mu}_k^z + \mathbb{1}]$ , the domain wall representation of the imbalance reads

$$\hat{\mathcal{I}} = \frac{1}{N-1} \sum_{k=1}^{N-1} (-1)^{k+1} \hat{n}_{k+1}^{(\text{DW})} . \quad (6.19)$$

In Fig. 6.2(a) we show the average expectation value of  $\hat{\mathcal{I}}$  at long times,  $\Omega t = 10^5$ , and for different system sizes as a function of the trap width  $\sigma$ . The latter parametrizes the disorder strength, with  $\sigma = 0$  being the disorder-free limit. For small disorder, the excitations are able to move and spread over the whole chain, as can be extracted from panel (c): at the smallest values of  $\sigma$ , a nearly homogeneous distribution of domain walls is reached, with the residual negative value of the imbalance being a finite size effect.

Fig 6.4 shows the imbalance of an equal superposition state of all basis vectors with  $N_{cl} = 2$  clusters at  $\Omega t = 0$  as a function of system size. The imbalance of the

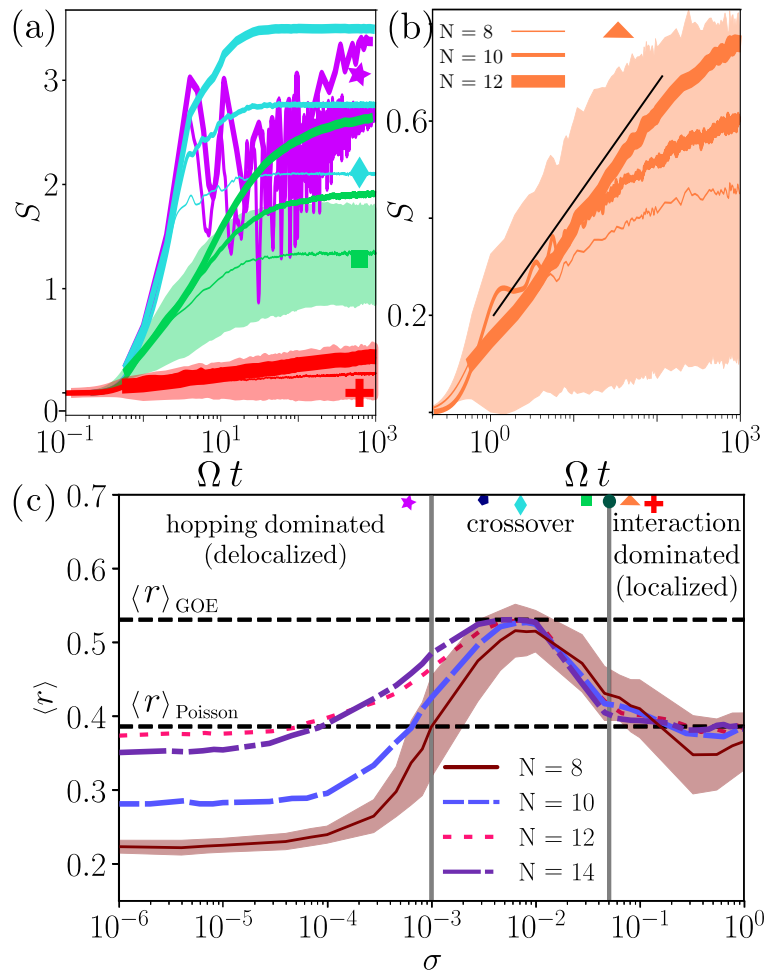


**Figure 6.3: Half-chain entanglement entropy (HCEE), and level statistic ratio.** (a,b) HCEE as a function of time in a chain for various  $N = 8, 10, 12$ , and  $\sigma$ . The color code and symbols correspond to those in Fig. 6.2(a), i.e.  $\sigma = 0.0006$  (purple) [only  $N = 10, 12$  shown],  $0.0071$  (light blue),  $0.0306$  (green) and  $0.135$  (red) [ $N = 10$  and  $N = 12$  overlap]. (b) The  $\sigma = 0.08$  (orange) case, is displayed on its own to highlight the emergence of a logarithmic growth of the HCEE as  $N$  is increased (the black curve, indicating logarithmic behavior, is a guide to the eye). (c) LSR of the effective disordered Hamiltonian in the restricted Hilbert space containing  $N_{\text{cl}} = 2$  clusters as a function of  $\sigma$  for different  $N$ . The LSR is compatible with a Poissonian distribution of level spacings at very low and large disorder. In the former case, the system is close to being integrable, whereas in the latter this is due to the effects of the disorder and the phase is MBL-like. In between there is a crossover regime in which the LSR shows GOE statistics, suggesting the presence of an ergodic window at intermediate values of  $\sigma \approx 10^{-2}$ . Shaded areas: plus/minus the standard deviation for 100 disorder realizations for  $N = 8$  atoms. (This figure is adapted from Ref. [3]).

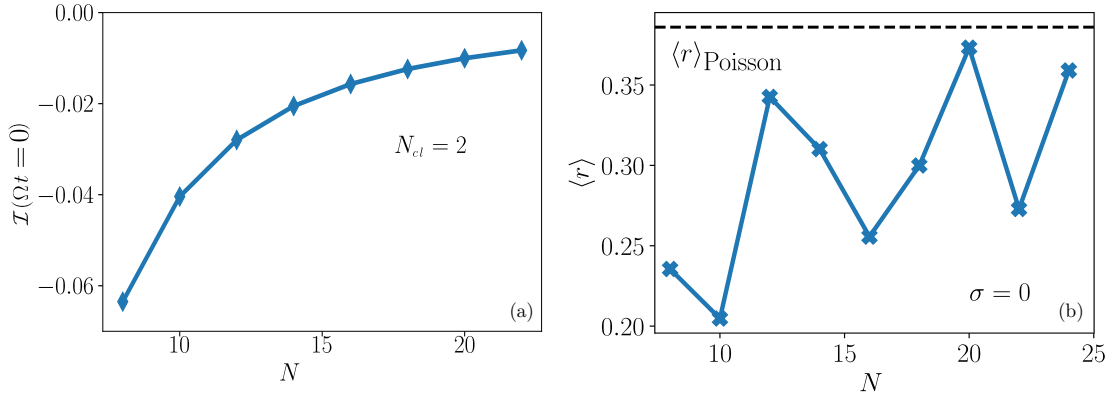


**Figure 6.4: Finite size effects of the level statistic ratio and the imbalance.** (a): Imbalance of an equal superposition state containing  $N_{cl} = 2$  clusters at  $\Omega t = 0$  as a function of system size  $N$ . (b): Level statistic ratio for zero disorder in the restricted Hilbert space containing  $N_{cl} = 2$  clusters as a function of system size  $N$ . The dashed line gives the LSR of a Poissonian distribution of the level spacing.

equal superposition state  $\mathcal{I}(\Omega t = 0)$  is approaching zero with increasing system size. Starting in a structured product state (6.16), the state will approximately stay the same during the time evolution. Therefore, the imbalance will remain at its initial value (close to 0.5) and is therefore a good measure for ergodicity. However, at an intermediate disorder strength  $\sigma \approx 10^{-2}$ , Anderson localization into spatially extended modes occurs and the imbalance can take any value in the interval  $[-0.5, 0.5]$ . Thus, the small negative value of the imbalance could indicate non-ergodicity. At this point this is difficult to establish, though, due to finite size effects. Finally, when the disorder is large the domain wall density at long times ( $\Omega t = 10^5$ ) remains close to that of the initial configuration ( $t = 0$ ), suggesting that the system localizes.

It may be challenging to probe the very long times investigated here in an experimental setting. In Fig. 6.2(b) we show a few instances of the averaged imbalance as a function of time, highlighting that at shorter times, ( $\Omega t \approx 10^3$ ),  $\langle \hat{\mathcal{I}} \rangle$  still displays oscillations for small disorder, and only becomes stationary from  $\sigma \gtrsim 10^{-2}$  onwards. Experiments should thus in principle operate beyond a certain disorder threshold to avoid the strong oscillations in the early dynamics.

### 6.4.2 Half-chain entanglement entropy (HCEE)

A prototypical measure to detect the spreading of quantum correlations through the system is the entanglement entropy of a subsystem [61, 62, 118]. It tracks how

much information about the chosen subsystem is lost when the complement is traced away. For an initial pure state  $|\Psi(t=0)\rangle$  evolving under  $\hat{H}$  it is defined as  $S(t) = -\text{tr}\{\hat{\rho}_{1/2}(t) \ln \hat{\rho}_{1/2}(t)\}$ , where  $\hat{\rho}_{1/2}(t) = \text{tr}_{N/2, \dots, N}\{|\Psi(t)\rangle \langle \Psi(t)|\}$  denotes the trace over the Hilbert subspace corresponding to the right half of the chain (in the spin picture).

Fig. 6.3(a) shows the evolution of the HCEE as a function of time for some of the trap widths chosen in Fig. 6.2. For very small values of  $\sigma$ , excitations can hop and spread entanglement over the entire system, causing a substantial increase in entropy. For intermediate disorder  $\sigma = 0.0071$  the average over different realizations becomes sufficient to damp the oscillations, but the entropy still saturates at long times at a value comparable to the smaller-disorder cases, suggesting extensive spread of entanglement. As the disorder strength is increased further, the long time value of the HCEE monotonically decreases, suggesting localization of excitations close to their initial position, and therefore limited spread of information from one half of the chain to the other. In this regime the growth of the entropy is visibly slower and, within the addressed range of timescales, appears to be logarithmic in nature. To highlight this, we show in Fig. 6.3(b) three curves (for  $N = 8, 10, 12$ ) at  $\sigma = 0.08$  which display how, increasing the system size, the HCEE growth tends to acquire an apparently linear behavior in log-linear scale. A logarithmic growth of the HCEE towards its stationary value is a characteristic feature of MBL systems [61], suggesting the presence of an MBL phase (for  $\sigma \gtrsim 0.01$ ), although it is not straightforward in our case to disentangle the effects of interactions and disorder, and we are restricted to rather small system sizes.

### 6.4.3 Level statistic ratio

A further measure often used in the context of both MBL and integrable systems is the level statistic ratio (LSR) [58, 175], which characterizes the statistical distribution of energy gaps in the spectrum of the Hamiltonian [176, 177] and is therefore basis independent. In the presence of interactions, one expects the system to show signs of thermalization, with a distribution of the eigenvalues similar to the one found for the so-called Gaussian orthogonal ensemble (GOE). Conversely, in an MBL phase the system cannot redistribute energy effectively, the level repulsion of the GOE is absent and the distribution of levels is closer to a Poissonian. This difference is typically quantified via the dimensionless ratio

$$r_n = \frac{\min\{\Delta_n, \Delta_{n+1}\}}{\max\{\Delta_n, \Delta_{n+1}\}}, \quad (6.20)$$

where  $\Delta_n = |\epsilon_n - \epsilon_{n+1}|$  is the spacing between adjacent eigenenergies of the Hamiltonian, listed in ascending order ( $\epsilon_n \geq \epsilon_{n-1}$ ). To get the LSR  $\langle r \rangle$ , one takes the arithmetic mean of the  $r_n$  ( $n = 1, 2, 3, \dots$ ) and then averages over the disorder distribution. The predictions for GOE and Poissonian ensembles are  $\langle r \rangle_{\text{GOE}} \simeq 0.5307$  and  $\langle r \rangle_{\text{Poisson}} = 2 \ln(2) - 1 \simeq 0.386$ , respectively.

Fig. 6.3(c) shows the LSR of the effective Hamiltonian (6.2) in the reduced Hilbert space with  $N_{\text{cl}} = 2$  as a function of the trap width  $\sigma$ . For very small disorder  $\sigma \lesssim 10^{-3}$ , the system, which is in the regime dominated by the hopping term (6.2), is still close to its integrable regime. Hence, it can be described as free fermions, and the LSR approaches a Poissonian value. Deviations from the Poissonian value for very small disorder are a finite size effect as can be seen in Fig. 6.4(b) which shows the LSR for zero disorder as a function of lattice size  $N$ . The deviations from the Poissonian value are not monotonic, but collectively show a tendency to decrease as the system size grows  $N$ . In the large disorder limit,  $\langle r \rangle$  also approaches the Poissonian value, presumably entering an MBL phase, however the mechanism is different, as the system does not map on free fermions. In this limit, the diagonal interaction terms dominate and the system can be approximately diagonalized in the basis of classical configurations (of spin product states). The effective detunings introduced by the disorder are very large which makes the system trivially integrable and the LSR is Poissonian. Between these two regimes,  $\langle r \rangle$  rises to “GOE-like” values, suggesting that in this crossover window — for the system sizes studied here — ergodic behavior and (effective) thermalization are present.

#### 6.4.4 ETH plots

As a reminder, the basic conditions of ETH states that the expectation value of an observable  $\hat{O}$  for a system in the eigenstate  $|\epsilon_\alpha\rangle$  of the Hamiltonian is a smooth function of the energy  $\epsilon$ . It is possible to utilize this ETH condition as a measure to distinguish between a thermalizing and an MBL system. A thermalizing system satisfies the ETH, thus  $O(\epsilon_\alpha)$  will be a smooth function of the energy, while in the MBL phase, where the ETH breaks down, the  $\hat{O}(\epsilon_\alpha)$  will exhibit a fundamentally different behavior.

The magnetization  $\langle M_z \rangle$  is defined as

$$\langle M_z \rangle^{(\alpha)} = \frac{1}{N} \left\langle \epsilon_\alpha \left| \sum_{k=1}^N \hat{\sigma}_k^z \right| \epsilon_\alpha \right\rangle, \quad (6.21)$$

where  $|\epsilon_\alpha\rangle$  is the eigenstate of the Hamiltonian with eigenenergy  $\epsilon_\alpha$ . Fig. 6.5

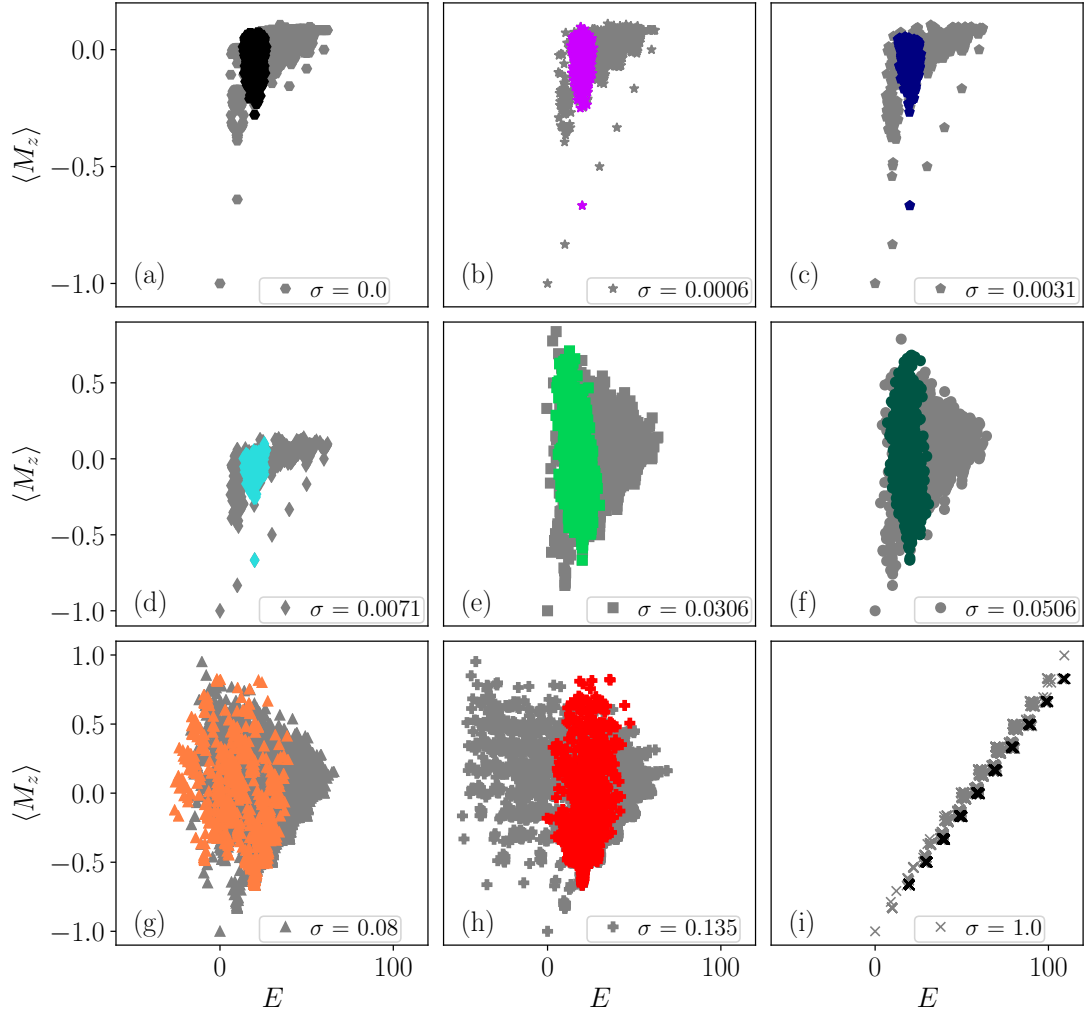


**Figure 6.5: ETH plot of the magnetization.** ETH plot of the magnetization  $\langle M_z \rangle$  for a chain of  $N = 12$  atoms for nine different trap width, where  $|E_\alpha\rangle$  is the eigenstate of the Hamiltonian with eigenenergies  $E_\alpha$ . We compare the magnetization for the full Hilbert space (gray) and the restricted Hilbert space containing  $N_{cl} = 2$  clusters (colored) for nine different disorder strengths. (b-h) The colors and the symbols correspond to the trap width in Fig. 6.2. (a,i) Magnetization for zero disorder and the maximal disorder  $\sigma = 1$ .

shows the ETH plot for the magnetization for nine different disorder strengths. The gray data is taken for the full Hilbert space, while the colored data is for the restricted Hilbert space containing  $N_{cl} = 2$  clusters. Considering the full Hilbert space (gray), the magnetization splits into sectors of fixed numbers of clusters. For small disorder  $\sigma < 0.0306$ , where the system is close to integrability, these sectors can be easily distinguished from each other. Increasing the disorder, these characteristics are washed out and the different sectors start to overlap.

Each sector corresponding to a fixed  $N_{cl} = m$ , shows a disconnected point in the

magnetization unaffected by the disorder. The corresponding states are equal superposition states of all possible configurations with  $N_{cl} = m$  clusters, where each cluster consists of only a single spin. This is the reason that the disorder does not affect the disconnected states as only states with neighboring Rydberg excitations feel the disorder. These states were already introduced in Section 6.4 as states produced by  $\hat{\Phi}^{N_{cl}} |\downarrow\downarrow \cdots \downarrow\rangle$ . The magnetization with  $\langle M_z \rangle = -1$  belongs to the sector with  $N_{cl} = 0$  clusters and corresponds to the state with all spins in the  $|\downarrow\rangle$  state,  $|\Psi_{N_{cl}=0}\rangle = |\downarrow\downarrow \cdots \downarrow\rangle$ . The disconnected states with higher numbers of cluster  $N_{cl} > 0$  can be constructed by applying the  $\hat{\Phi}$  operator (6.17)  $m$  times to the zero-cluster state  $|\Psi_{N_{cl}=0}\rangle$  to obtain the  $N_{cl} = m$  state. For  $m = 1$  clusters in the state the disconnected state takes the form,  $\hat{\Phi} |\Psi_{N_{cl}=0}\rangle = |\Psi_{N_{cl}=1}\rangle \propto |\uparrow\downarrow\downarrow \cdots \downarrow\rangle - |\downarrow\uparrow\downarrow \cdots \downarrow\rangle + \cdots + |\downarrow\downarrow \cdots \downarrow\uparrow\rangle$ . Adjacent states in the superposition appear with alternating signs, thus neighboring states cancel each other when the Hamiltonian is applied. As already mentioned, the disconnected states have no overlap with the initial state in Eq. (6.16), therefore all localization effects occur due to the kinetic constraint.

In standard MBL systems the disorder is local in space, so one can conveniently define local observables. In our system, the disorder is non-local in the dual space so it is not clear that space-local observables should follow the behaviour predicted for local ones in usual MBL setups. This is presumably the reason that we cannot get a clear distinction between the thermal and MBL regime when studying the magnetization as a function of energy.

## 6.5 Localization in the full model

Our constrained model is based on the restriction that a spin can only be flipped next to an already excited neighbor. So far we only considered nearest-neighbor interactions and a perfect facilitation condition of the atoms. Here, we analyze how the full dynamics of the Hamiltonian (6.1) changes the localization behavior in the spin chain assuming van der Waals interaction ( $\alpha = 6.0$ ). Furthermore, we are considering a long ranged interaction potential ( $\alpha = 1.0$ ) in order to analyze the localization behavior when both, the interactions and the disorder are non-local. It has to be mentioned that the number of clusters  $N_{cl}$  is no longer a conserved quantity in the full model. The Rabi frequency  $\Omega$  as well as the interatomic separation  $R_0$  are set to unity, and the detuning is equal to the nearest-neighbor interaction energy  $V_0 = -\Delta = 10$ . Figure 6.6(a,b) shows the half-chain entanglement entropy as a function of time and disorder strength for

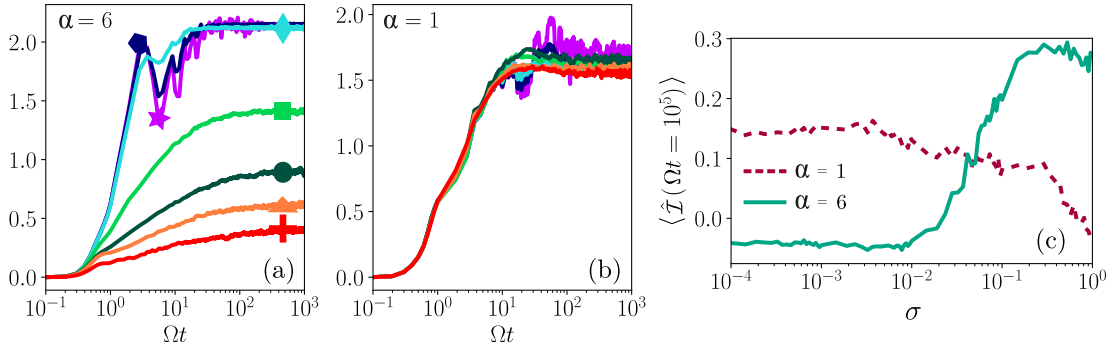


**Figure 6.6: Half-chain entanglement entropy and imbalance under the full dynamics.** Half-chain entanglement entropy as a function of time and trap width  $\sigma$  for a chain of  $N = 8$  atoms. The full dynamics is considered (6.1) for van der Waals interaction  $\alpha = 6.0$  and for a long ranged interaction with exponent,  $\alpha = 1.0$  (b). The color code and the symbols correspond to the ones in Fig. 6.2. (c) Imbalance  $\langle I(\Omega t = 10^5) \rangle$  of the full Hamiltonian for  $\alpha = 6, 1$ .

two different interaction exponents.

In the case of a van der Waals interaction,  $\alpha = 6$ , the HCEE is in good agreement with the results from our effective model (6.2) (see Fig. 6.3). However, for the long-range interaction, the behavior does not conform with the one found in the effective model where we only considered nearest neighbor interaction. We can still observe the ballistic growth for very short times ( $\Omega t < 1$ ), followed by the linear behavior (on the logarithmic scale) over two orders of magnitude, although the HCEE for different disorder strengths lie on top of each other. Furthermore, for all considered disorder strengths, the HCEE reaches approximately the same plateau value in the long-time limit.

Figure 6.6(c) compares the imbalance of the full Hamiltonian for van der Waals interaction with the long-ranged interaction potential ( $\alpha = 1$ ). In case of a van der Waals potential, the imbalance agrees qualitatively with the imbalance in the effective model. For very small disorder  $\sigma < 10^{-2}$ , where the excitations can spread over the whole chain, the imbalance takes a small negative value. In the limit of strong disorder, the imbalance reaches a plateau value and the final state will be close to the initial configuration (6.16). The plateau value of the imbalance in the limit of large disorder is approximately  $\langle \mathcal{I}(\Omega t = 10^5) \rangle \approx 0.3$ , and therefore smaller than in the effective model. The deviations of the imbalance can be explained by the fact that the number of clusters is not a conserved quantity. Considering the long-ranged interaction potential, we can see the imbalance shows a fundamentally different behavior. For small disorder strength, the disorder takes an intermediate value keeping some memory of the initial configuration.

For intermediate disorder strength the imbalance slowly decreases, reaching zero in the large disorder limit.

From the analysis of the full model we can conclude that the effective Hamiltonian gives a good description of the full system considering a van der Waals potential. However, in the case of a long-ranged interaction the effective model breaks down, which is not surprising as it only considers nearest-neighbor interactions which is not justified with a long-ranged interaction potential.

## 6.6 Outlook and Conclusion

We analyzed the effects of disorder on an interacting Rydberg chain under the facilitation constraint. Within a dual domain wall picture the system is described by an XX-spin model and randomness in the atomic positions translates into a non-local disordered interaction potential. This unconventional disordered many-body system shows signatures of a crossover between an ergodic, thermalizing phase and what appears to be a many-body localized one. The model studied here differs from a more standard MBL model because non-local interactions and disorder are intrinsically interconnected, a feature that should nevertheless naturally arise in experimental settings exploiting Rydberg facilitation.

The constraints in this model emerged from energy barriers which restrict the dynamics to only allow a spin flip next to an excited spin (facilitation). In the following chapter, we redirect our focus to dissipation induced constraints in a hard-core boson model that can be realised with Rydberg atoms.

# Chapter 7

## Dynamics of hard-core bosons on a two-dimensional lattice with non-local loss

### 7.1 Introduction

In the previous chapters, kinetic constraints emerged in cold lattice gases due to energy barriers caused by the interplay between the off-resonant laser excitation of Rydberg atoms and the interaction between Rydberg states. [48,49]. In this chapter, we consider constraints originating from the quantum Zeno effect [178–180] in systems with strong dissipation. The Zeno effect projects the system onto a subspace (Zeno-subspace) where the occupation of specific (rapidly decaying) states is prohibited. Previous work on one-dimensional chains has found that strong distance-selective pair-loss can result in the dissipative binding of lattice bosons [9, 181] due to the Zeno effect. For the specific case of pair loss, the Zeno subspace prevents simultaneous occupation of two lattice sites at a particular distance. This boson model with non-local dissipation can be experimentally realized in cold Rydberg quantum simulators using the dependence of the Rydberg blockade on the interatomic separation to create the distance-selective loss process [9].

We study a two-dimensional system of hard-core bosons with strong non-local pair loss resulting in interesting out-of-equilibrium effects, such as dissipation induced localization. As in the one-dimensional case, the dynamics can be separated into two parts, the fast loss process that rapidly evolves the system into the Zeno subspace, followed by the coherent dynamics restricted to this subspace. We analyze the correlated particle loss process, which evolves a system initiated in a

Mott insulator state into the Zeno subspace, using Monte Carlo techniques. This is followed by a discussion of the coherent dynamics in the limit of strong loss processes which can be described as a hopping model with non-local constraints.

## 7.2 System

We consider a two-dimensional lattice gas (with  $N = N_x \cdot N_y$  lattice sites using open boundary conditions (OBC)) of hardcore-bosons (the occupation of a single lattice site by more than one particle is forbidden [182]) tunneling between adjacent lattice sites at rate  $J$ . The dynamics of the system is described by a hopping Hamiltonian (open boundary conditions) [9, 181]

$$\hat{H} = J \sum_{\langle ik \rangle}^N (\hat{\sigma}_i^+ \hat{\sigma}_k^- + \hat{\sigma}_i^- \hat{\sigma}_k^+) , \quad (7.1)$$

where  $J$  is the tunneling rate,  $\langle ij \rangle$  denotes nearest neighbor configurations, and  $\hat{\sigma}_k^\pm = (\hat{\sigma}_k^x \pm i\hat{\sigma}_k^y)$  are the standard spin-1/2 lowering and raising operators.

We are interested in a situation where the system experiences a non-local distance-selective loss resulting in the ejection of boson pairs out of the lattice that are separated by a critical distance  $R_c$ . This pair-loss process is illustrated in Fig. 7.1(a) for the specific case of a one-dimensional system with a critical distance  $R_c = 2$ . The two particles (black circles) initially occupying neighboring lattice sites are in a stable configuration. If the right atom were to hop to the right (red, crossed out lattice site) the two bosons would be separated by  $R_c$  which corresponds to a *forbidden* state and thus the bosons are ejected at rate  $\gamma$ .

Due to the dissipation the system being effectively open, the dynamics can be described via the density operator  $\hat{\rho}$  whose time evolution is governed by the Lindblad master equation (which is given for simplicity in one-dimensions)

$$\begin{aligned} \dot{\hat{\rho}} &= -i [\hat{H}, \hat{\rho}] + \sum_{k=1}^N \left( \hat{L}_k \hat{\rho} \hat{L}_k^\dagger - \frac{1}{2} \{ \hat{L}_k^\dagger \hat{L}_k, \hat{\rho} \} \right) \\ &= \mathcal{L}_c \hat{\rho} + \mathcal{L}_d \hat{\rho} , \end{aligned} \quad (7.2)$$

with the jump operator

$$\hat{L}_k = \sqrt{\gamma} \hat{\sigma}_k^- \sigma_{k+R_c}^- . \quad (7.3)$$

The Lindblad master equation describes the dynamics of Markovian systems which do not have any memory of their previous behavior. We are considering the limit of strong dissipation, where the dissipation rate  $\gamma$  is much larger

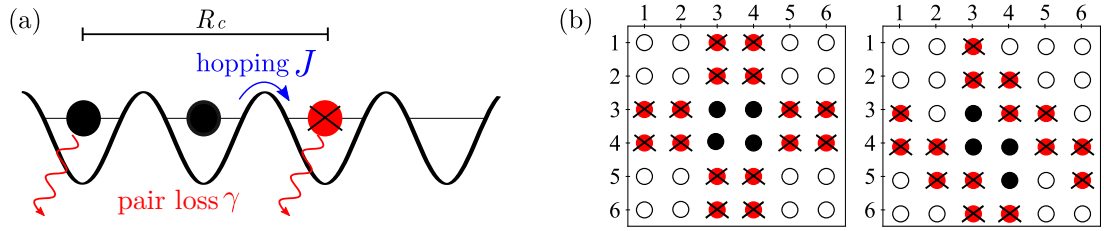


**Figure 7.1: Dynamics and constraint of the lattice bosons.** (a) Dynamics and constraint of the lattice bosons which leads to the non-local loss when two atoms are separated by the critical distance  $R_c$ . (Adapted from [9]). (b) Representation of the constrained hopping model on the example of a  $N = 6 \times 6$  lattice where the initial state consists of four occupied sites (black circles) forming a square (left) and a  $Z$  (right). The white and red circles show unoccupied and forbidden sites, respectively, for a critical distance  $R_c = 2$ . The square configuration is surrounded by forbidden sites and is therefore immobile for all times, while the  $Z$ -configuration has the ability to leave its initial configuration (in two directions).

than the tunneling rate  $J$  ( $\gamma \gg J$ ). This results in the separation of the dynamics in two parts, the fast dissipative dynamics described by  $\mathcal{L}_d$ , and the much slower coherent dynamics described by  $\mathcal{L}_c$ . Thus, it is not necessary to solve the Lindblad master equation as a whole and instead we solve the two processes independently of each other.

This specific kind of loss process can be realized in Rydberg lattice systems utilizing the Rydberg blockade, i.e. that the excitation to a doubly excited Rydberg state depends on the interatomic separation [9]. In the case of the pair loss process, the doubly excited state is reached via a resonant two-photon process coupling the collective ground state  $|\downarrow\downarrow\rangle$  to the pair state  $|\uparrow\uparrow\rangle$  via a laser with detuning  $\Delta$  ( $|\downarrow\downarrow\rangle \rightarrow |\uparrow\downarrow\rangle, |\downarrow\uparrow\rangle$  transition). The energy difference between the pair state and the ground state is given by the two-atom detuning  $\Delta_2(R_0) = 2\Delta + V(R_0)$ , which can be tuned by either adjusting  $\Delta$  or the interatomic separation  $R_0$ . By fixing the detuning  $\Delta$ , we can determine the critical distance  $R_c$  at which two atoms can be excited to the pair state. For the pair state there exist two different decay channels, a mechanical loss channel caused by the strong repulsive interaction between the Rydberg atoms resulting in the atoms escaping their traps, and a radiative loss where the atoms gain momentum by spontaneously decaying into a lower lying state. Both decay processes result in the loss of the atom pair.

We first analyze the fast dissipative dynamics of the system when prepared in a Mott-insulator state, i.e. with a fully occupied lattice. The end result is a Zeno subspace spanned by all configurations where no bosons are separated by the critical distance.

After the Zeno subspace is reached, the slow coherent evolution can be described by the constrained Hamiltonian

$$\hat{H}_{\text{Zeno}} = \sum_{k=1}^N \hat{Q}_0 (\hat{\sigma}_k^+ \hat{\sigma}_{k+1}^- + \hat{\sigma}_k^- \hat{\sigma}_{k+1}^+) \hat{Q}_0, \quad (7.4)$$

where the projector onto the reduced space is

$$\hat{Q}_0 = \prod_{k=1}^N (\mathbb{1} - \hat{n}_k \hat{n}_{k+R_c}), \quad (7.5)$$

with  $\hat{n}_k = \hat{\sigma}_k^+ \hat{\sigma}_k^-$ . Figure 7.1(b) illustrates the constraints given by the Hamiltonian (7.4) on the example of a square lattice  $N = 6 \times 6$  with  $N_p = 4$  bosons and a constraint of  $R_c = 2$ . The black circles indicate some example configurations of bosons, and the red and white circle show the forbidden and allowed sites for that particular configuration. A bosons can only move from its initial position if it has a white neighboring lattice site. The square configuration (left) is trivially localized due to the constraint; the bosons cannot move in any direction as all neighboring lattice sites are forbidden. The  $Z$ -configuration (right), however is not fully restricted in its motion as two of the particles are allowed to hop to neighboring (white) lattice site.

Due to the particle number conservation (in the limit of  $\gamma \gg J$ ) that emerges in the constrained description, we restrict the Hilbert space to the sector with fixed  $N_p$  yielding a Hilbert space dimension of  $\binom{N}{N_p}$ . The Hilbert space can be restricted further by removing all states that are forbidden by the constraint and would not be populated throughout the course of the dynamics. If not stated otherwise, we will restrict our considerations to a critical distance of  $R_c = 2$ .

### 7.3 Classical loss dynamics

In this section, we focus on the fast, dissipative dynamics of the system,  $\mathcal{L}_d$  in Eq. 7.2, which evolves from an initial Mott insulator state into the Zeno subspace. In order to quantify the atom loss, we are studying the boson density  $p(t)$  as a function of time

$$p(t) = \sum_{k=1}^N \frac{\langle \hat{n}_k(t) \rangle}{N}, \quad (7.6)$$

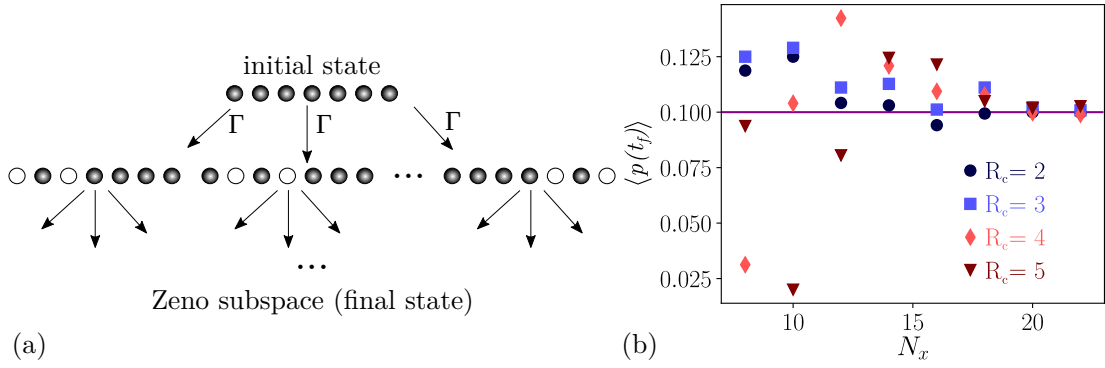


**Figure 7.2: Kinetic Monte Carlo method and final boson density.** (a) Illustration of the kinetic Monte Carlo (MC) method. The system is initially prepared in a Mott insulator state. In every jump two bosons at the critical distance  $R_c$  are removed from the system. In our model, any jump happens with transfer rate  $\Gamma = 1$  but the choice of jump is randomly selected. This process is repeated until the Zeno subspace is reached; i.e. there no longer exists particles separated by the critical distance  $R_c$ . (b) Final boson density  $\langle p(t_f) \rangle$  as a function of  $N_x$  (with  $N = N_x \times N_x$ ) for various constraints  $R_c$ . Initially, the system is prepared in a Mott insulator state and atoms located at the critical distance  $R_c$  are removed until the Zeno subspace is reached. The density is averaged over 20 MC runs.

with  $\hat{n}_k = \hat{\sigma}_k^+ \hat{\sigma}_k^-$ . The pair loss process can be simulated by kinetic Monte Carlo as illustrated in Fig. 7.2(a). The evolution of the initial (fully occupied) state is given via a jump processes where in each jump, a pair of bosons separated by  $R_c$  is expelled out of the lattice until the Zeno subspace (final state) is reached. In our model, all jumps are equally likely, hence the probability  $\Gamma$  for any possible jump is equal to one,  $\Gamma = 1$ . The probability that no jump has happened at time  $t$  is then given by

$$P_{\text{no jump}}(t) = e^{-N_f t}, \quad (7.7)$$

where  $N_f$  is the number of states that can be reached via a jump (indicated as arrows in Fig.7.2(a)). In a kinetic Monte Carlo approach, we generate the waiting time before a jump occurs  $t_{\text{jump}}$  as follows

$$\mu = e^{-N_f t_{\text{jump}}}, \quad (7.8)$$

where we pick the random number  $\mu$  from a uniform distribution  $\mu \in [0, 1]$ . After a jump occurs, which is also randomly picked, the initial state is updated and the next jump time is generated. This process is repeated until the Zeno subspace is reached. This completed evolution, from Mott insulator to Zeno subspace, is

one possible route (trajectory) the system can take. To produce an average of the dynamics, and in turn an average value for the observable, the process must be repeated many times until the average converges. Figure 7.2(b) shows the final average boson density  $\langle p(t_f) \rangle$  as a function of the lattice size  $N = N_x \times N_x$  for four critical distances  $R_c$ . The final time  $t_f$  is the point at which a configuration is reached which admits no further jumps. In the limit of large  $N$ , a Mott insulator state reaches a steady state with approximately ten percent filling  $p(t \rightarrow \infty) \approx 0.1$  (purple line). It is important to note that this is independent of the critical distance  $R_c$ , a result previously found in the one-dimensional case [181].

### 7.3.1 Quantum evolution

After the Zeno subspace is reached the dynamics can be described as a coherent evolution with kinetic constraints. We are interested in the effect the constraint has on the relaxation properties of the system. Therefore, we study the normalized two-times correlation function [79], to be more precise the autocorrelation function,

$$c(t) = \frac{1}{N} \sum_k \frac{\langle \Psi(t_0) | \hat{n}_k(t) \hat{n}_k(t_0) | \Psi(t_0) \rangle}{\phi(1-\phi)} - \frac{\phi}{(1-\phi)}, \quad (7.9)$$

where  $\hat{n}_k(t)$  is the number operator in the Heisenberg picture,  $\phi = N_p/N$  is the filling fraction, and  $t_0 = 0$  is the initial time. The subtracted constant ensures that, if the correlation factorizes at long times, it vanishes. Note, the autocorrelation function  $c(t \rightarrow \infty)$  is expected to vanish in a thermalizing system (in the thermodynamic limit), however, it can take a finite value for a localized final state.

Figure 7.3 (upper panel) shows the autocorrelator of a  $N = 4 \times 4$  square lattice with  $N_p = 4$  particles for a constrained system ( $R_c = 2$ ) (red), and an unconstrained system (blue). The unconstrained dynamics is free and described by the hopping Hamiltonian (7.1), while the constrained dynamics is governed by Eq. (7.4). Initially, the system is prepared in a  $Z$ -configuration as shown in the inset, and then evolves under its respective dynamics. Both autocorrelation functions show an initial decay on short time-scales, however in the free case the decay is much faster. For the free evolution, the correlation function vanishes in the long-time limit indicating that all information of the initial state is lost and that the system thermalizes. For the constrained dynamics on the other hand, the

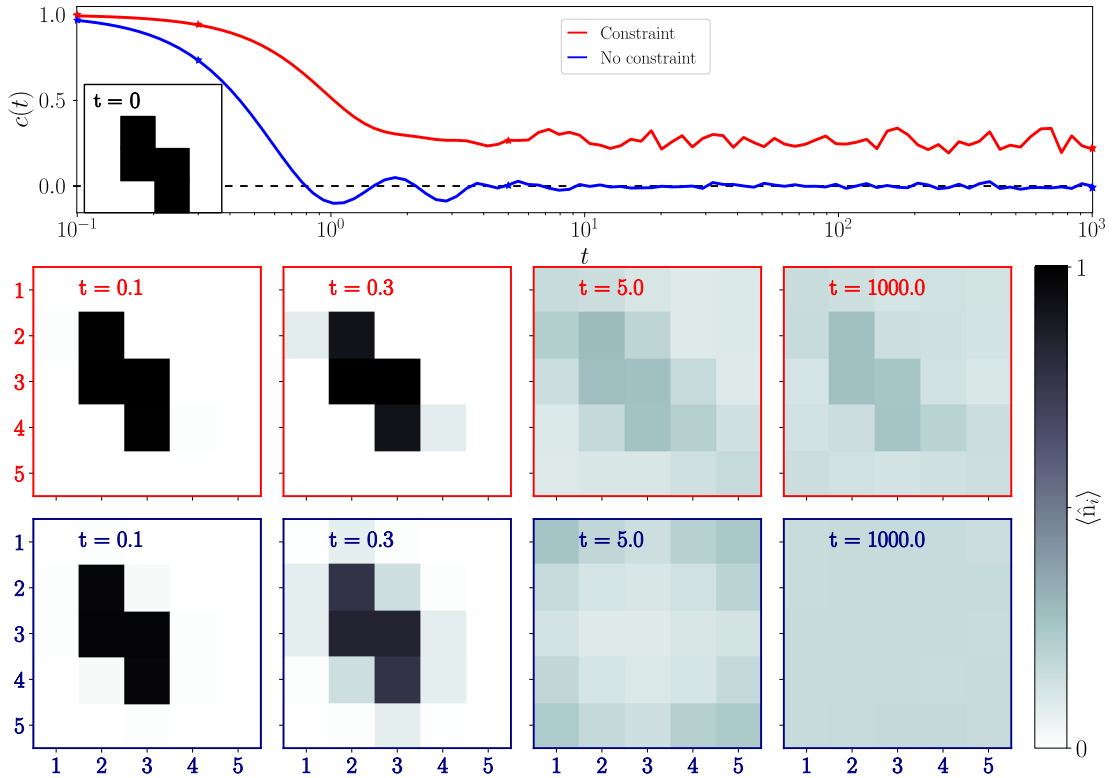


**Figure 7.3: Comparison of the constrained and free dynamics for a  $Z$ -configuration.** Upper panel: Autocorrelator as a function of time  $c(t)$  for a constrained system (red) with a critical distance of  $R_c = 2$  and a system without any constraints (blue) as a function of time. We are considering  $N = 4 \times 4$  lattice sites with  $N_p = 4$  particles initially prepared in the  $Z$ -configuration shown in the inset. Lower panel: Evolution of the populations  $\langle \hat{n}_i \rangle$  for a constrained (red) and an unconstrained system (blue) on a  $N = 5 \times 5$  lattice with  $N_p = 4$  particles initially prepared in a  $Z$ -configuration. We are using OBC for both the simulation of the autocorrelation function and the evolution of the population.

autocorrelator saturates to a non-zero plateau value implying the preservation of some memory, thus non-ergodic behavior.

The difference in the dynamics between the free and constrained system can be confirmed by Fig. 7.3 (lower panel), which shows the population  $\langle \hat{n}_i \rangle$  of a square lattice  $N = 5 \times 5$  with  $N_p = 4$  particles for four different times. We study the time evolution of the populations on a larger lattice than previously to ensure that the survival of the initial configuration in the constrained case is not purely a boundary effect. For the free dynamics this is the largest system which we are able to simulate due to computational limits. The simulation of the autocorrelation function is computationally more demanding, thus the maximal system we can simulate is  $N = 4 \times 4$  lattice with  $N_p = 4$  particles.

In the constrained system, we can see that the  $Z$ -configuration initially deteriorates until reaching a plateau that is stable for long times. On the other hand, in the unconstrained case, the population vanishes rapidly until the configuration can no longer be detected at all. For both measures, the constraint seems to introduce some sort of localization effect dependent on the initial state. This effect may be diminished for larger system sizes, however, this proved to be too demanding for our currently accessible computing facilities. The localization in the case of the constrained model can be explained by considering the spectrum of the Hamiltonian, which has a manifold of degenerate zero-energy eigenstates that do not evolve in time and are therefore localized. These localized states are similar to the frozen states in [183]. The energy spectrum is symmetric around the zero-energy manifold, every state with energy  $\epsilon$  has a partner state at  $-\epsilon$  indicating a particle-hole-symmetry. The localization effect of the time-evolved  $Z$ -configuration can be explained by decomposing the time-evolved state  $|\Psi(t_f)\rangle$  at some time  $t_f$  into the eigenstates  $|E_n\rangle$  of the Hamiltonian

$$|\Psi(t_f)\rangle = \sum_n \langle \epsilon_n | \Psi(t_0) \rangle e^{-i\epsilon_n t} | \epsilon_n \rangle , \quad (7.10)$$

where  $|\Psi(t_0)\rangle$  is the initial state. The index  $n$  runs over all eigenstates of the entire spectrum including the immobile zero-energy eigenstates. Considering the long time limit, we see that only the zero-energy components have a contribution to the time-evolution of the state as the time-dependent terms interfere destructively, letting the time-independent terms dominate the behavior

$$\lim_{t \rightarrow \infty} \langle \Psi(t_0) | \Psi(t_f) \rangle = \sum_{i \in \epsilon_0} \langle \epsilon_0^{(i)} | \Psi(t_0) \rangle . \quad (7.11)$$

Thus the zero-energy eigenstates are responsible for the localization effect in the constrained model due to destructive interference effects.

### 7.3.2 Quantum dynamics versus classical diffusion

To explore the role of quantum effects and constraint on localization found in our system, we study the constrained dynamics as a classical diffusive process. The time evolution is described in terms of the classical probability state,

$$|p(t_f)\rangle = \exp(Wt) |p(t_0)\rangle, \quad (7.12)$$

where  $W$  is the transition rate matrix. In general, the transition rate matrix defines the evolution of a stochastic process in a continuous-time Markov chain. Each component of the vector  $|p(t_k)\rangle$  gives the probability of the corresponding classical configuration. Note, the  $|p(t_k)\rangle$  are normalized such that the sum over all elements is one. The matrix  $W$  can be constructed in the following way: the off-diagonal elements of the stochastic matrix are equal to the constrained Hamiltonian in Eq. 7.4,  $W_{km} = H_{km}$  for  $k \neq m$ ; the diagonal elements of the transition rate matrix are chosen such that the sum of each row in  $W$  is equal to zero  $W_{kk} = -\sum_{m \neq k} W_{km}$ . With this, we define the autocorrelator for the classical diffusion process analogously to the quantum case,

$$c^c(t) = \frac{1}{N} \sum_k \frac{\langle \mathcal{P} | \hat{n}_k^c(t) \hat{n}_k^c(t_0) | p(t_0) \rangle}{\phi(1-\phi)} - \frac{\phi}{(1-\phi)} \quad \text{with} \quad |\mathcal{P}\rangle = \begin{pmatrix} 1 \\ 1 \\ \vdots \\ 1 \end{pmatrix}, \quad (7.13)$$

where the classical number operators in the Heisenberg picture are given by  $\hat{n}_k^c(t) = \exp(-Wt) \hat{n}_k \exp(Wt)$ .

In Fig. 7.4, we compare the autocorrelation function for (a) the constrained quantum dynamics, (b) the free quantum dynamics, (c) and the constrained classical diffusion for the whole spectrum of initial states. We restrict our considerations to  $N_p = 2$  particles as the computation of the entire spectrum for a larger system would be too computationally demanding for the free model. In the constrained quantum case in Fig. 7.4(a), the spectrum of the autocorrelation function indicates localized states through a non-vanishing plateau value in the long time limit  $c(t \rightarrow \infty) \neq 0$ . The constraint prevents the system from thermalizing which results in localized states with some memory of the initial conditions. In the case of the freely evolving quantum system (b), we can see some structure in  $c(t)$ , however these are most likely residues of the finite size of the system. The free model is ergodic and the system thermalizes. Also in the classical constrained model, the autocorrelation function vanishes on a short time scale, which confirms that the localization of the states is a result of quantum interference effects.

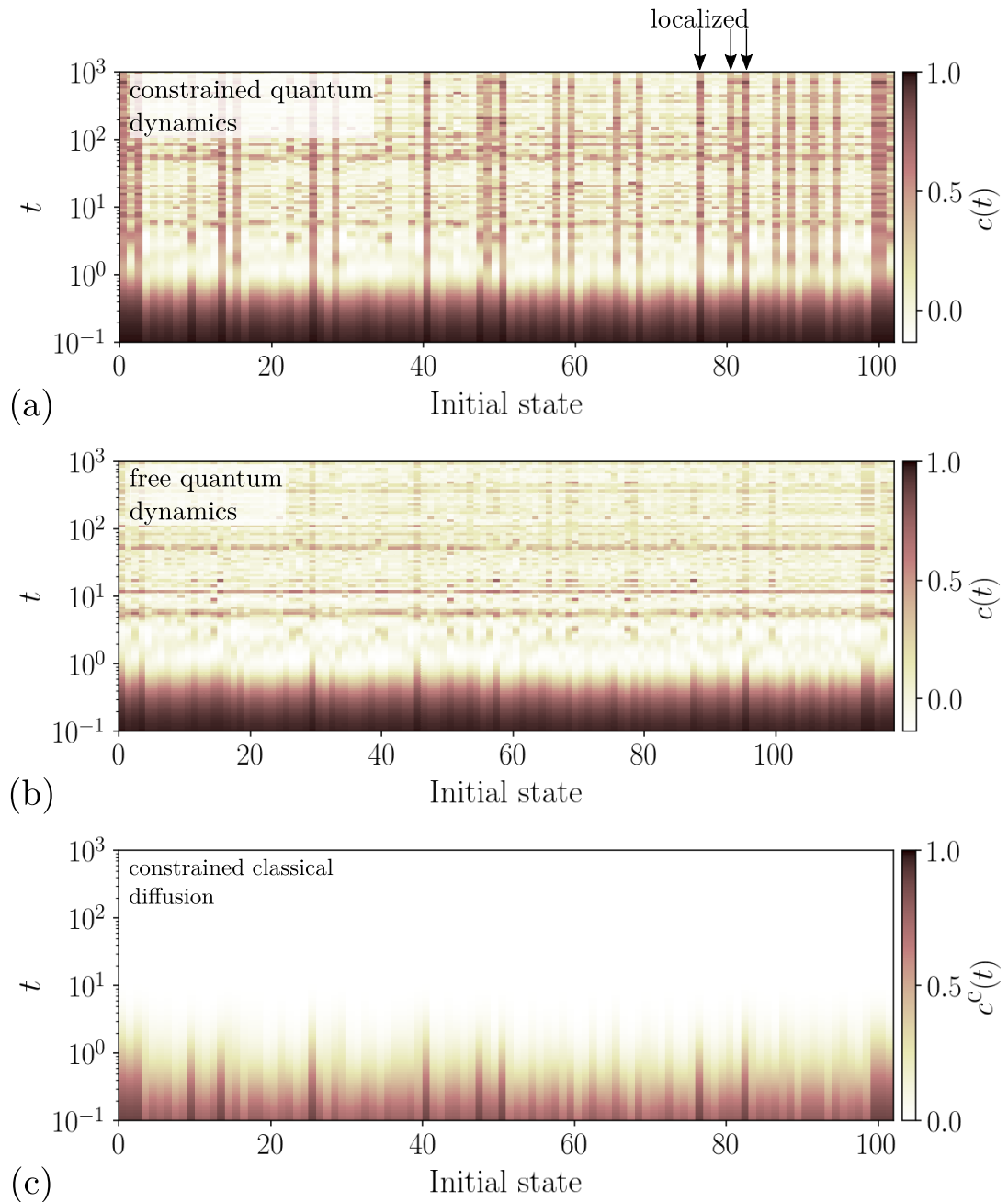


**Figure 7.4: Scan of the autocorrelation function for constrained and free quantum dynamics, and constrained classical diffusion.** Scan of the two-time correlation function  $c(t)$  over all possible initial product states for a  $N = 4 \times 4$  lattice sites with  $N_p = 2$  particles and open boundary conditions. We are considering a system under (a) quantum dynamics with constraint  $R_c = 2$ , (b) quantum dynamics without constrained and (c) classical diffusion with constraint. We indicate three of the localized states in the quantum dynamics.

We now study the localization phenomena in a system with a higher boson density ( $N = 4 \times 4$ ,  $N_p = 4$ ). Figure 7.5 compares the autocorrelation function of (a) the constrained quantum evolution with (b) the classical diffusion process. In both cases we can see trivially localized states, where the autocorrelor stays constant  $c(t) = 1$  ( $c^c(t) = 1$ ) for all times. These fully localized states are zero-energy eigenstates of the constrained Hamiltonian. They are trivially localized and belong to immobile square configurations where the particles are trapped as illustrated in Fig. 7.1(b) ( $N_p = 4$  particles and  $R_c = 2$ ). They are localized by the constraint and therefore appear also in the classical model. These states are a special feature of systems with  $N_p = 2 \cdot x$  and  $R_c = x$ .

As we have already seen in Fig. 7.4(a), destructive quantum interference results in localization effects. Additionally, in the quantum case, we can observe states with a vanishing autocorrelation function on short timescales which show a revival followed by strong oscillations for  $t \rightarrow \infty$ . In the classical case, the autocorrelation vanishes, except for the trivially localized states, which indicates ergodic behavior.

In a two-dimensional lattice, the configurations of the zero-energy eigenstates (in the product state basis) are, for reasonable system sizes and boson densities, far too complicated to find an underlying structure or to construct them in an experiment. Therefore we will focus our considerations on a quasi-one dimensional lattice to understand how to construct the localized eigenstates of the Hamiltonian.

## 7.4 Ladder system

For a more detailed analysis of the structure of the zero-energy eigenstates, we consider a simplified system — a quasi-one dimensional lattice or ladder. As illustrated in Fig 7.6(a), in a ladder, the particles are restricted in their motion by the ladder geometry (in the  $y$ -direction) in addition to the restrictions imposed by the constraint (along the  $x$ -direction). Considering that the particle number is a conserved quantity, we can construct the graph of the constrained Hilbert space to analyze the structure of the localized zero-energy eigenstates. Figure 7.6(b) shows the graph for a ladder with  $N = 4 \times 2$  sites, two particles  $N_p = 2$ , critical distance  $R_c = 2$  and periodic boundary conditions (PBC). Each vertex represents a product state and the edges define the connection between configurations under the action of the Hamiltonian. The four-fold rotational symmetry of the graph is caused by the periodic boundary conditions and corresponds to the invariance

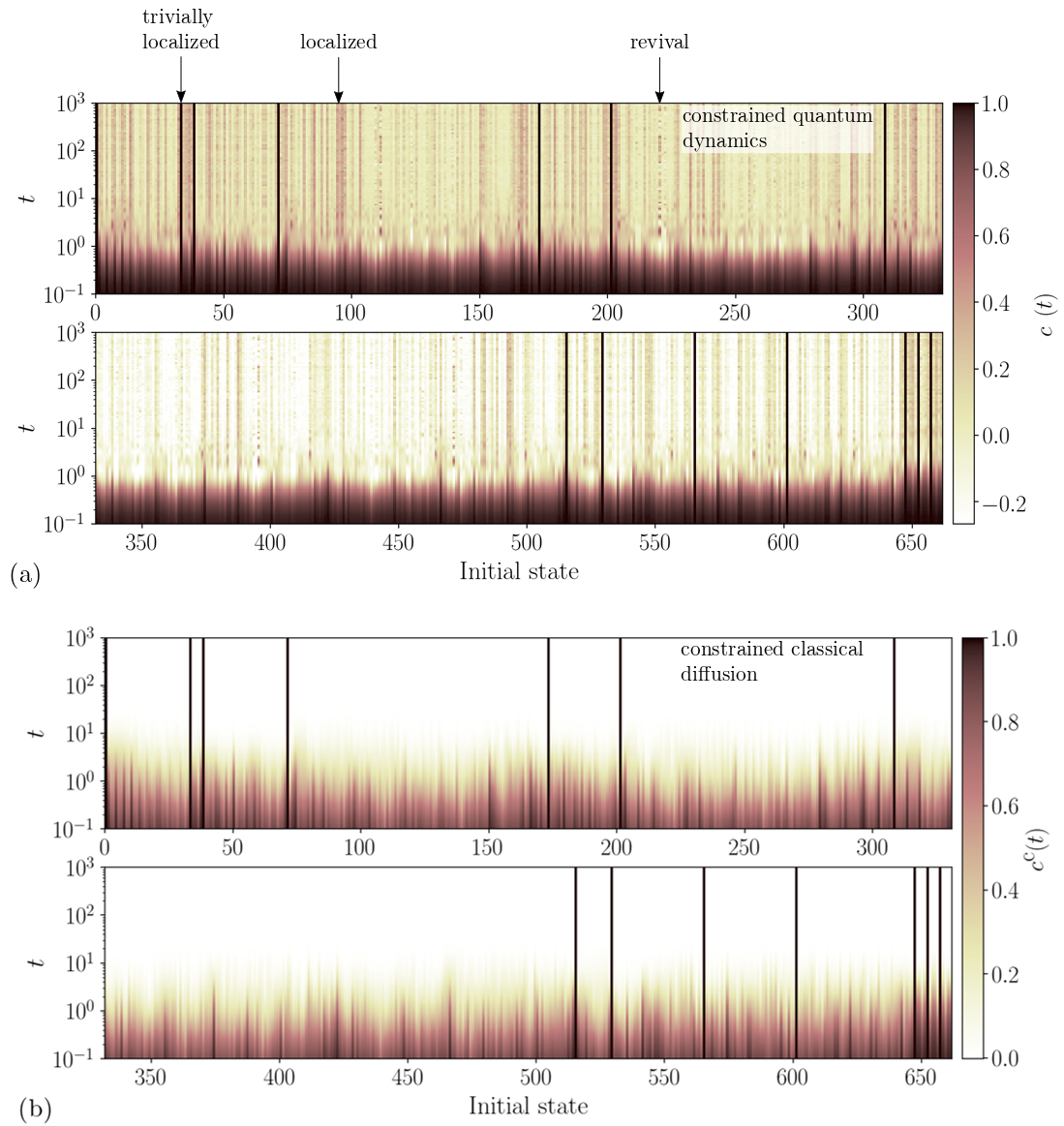


**Figure 7.5: Scan of the autocorrelation function for a system with high boson density.** Scan of the two-time correlation function  $c(t)$  over all possible product states of a constrained system ( $R_c = 2$ ) of  $N = 4 \times 4$  lattice sites with  $N_p = 4$  particles (OBC) under (a) quantum dynamics, and (b) under classical diffusion. The trivially localized states (black bands) coincide in the quantum and the classical case.

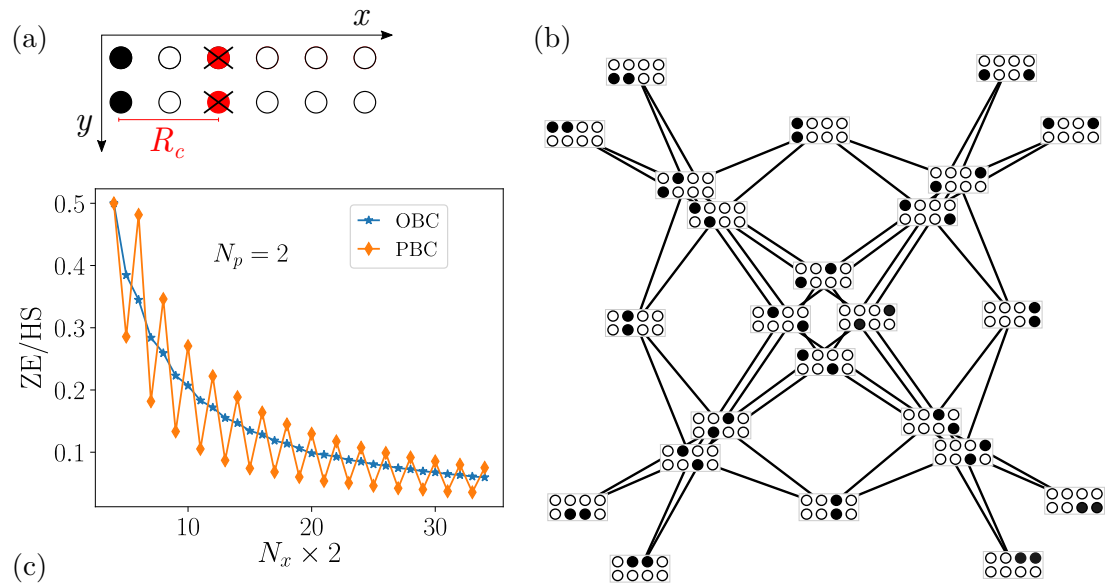


**Figure 7.6: Constrained model on a ladder.** (a) Quasi one-dimensional lattice expanding in the  $x$ -direction and restricted in the  $y$ -direction to two rows (ladder). We are considering two particles (black) in the lattice, the red spheres indicate the lattice sites that are forbidden for this specific configuration with  $R_c = 2$ . (b) Graph representation of the constrained model for a  $N = 4 \times 2$  ladder with PBC ( $N_p = 2$ ). We show all allowed product state configurations and their connections under the action of the constrained Hamiltonian. (c) Ratio of the number of zero-energy eigenstates (ZE) and the size of the reduced Hilbert space (HS) as a function of system size  $N = N_x \times 2$  for  $R_c = 2$  for open (blue) and periodic (orange) boundary conditions.

under discrete translations (or cyclic permutations) of a configuration along the  $x$ -axes.

### 7.4.1 Localized zero-energy states

We consider the system size scaling of the dimension of the zero energy eigenstate (ZE) space with respect to the dimension of the restricted Hilbert space (HS). Figure 7.6(c) shows the ratio ZE/HS as a function of the length of the ladder  $N_x \times 2$  for  $N_p = 2$  particles (for open and periodic boundary conditions). In the thermodynamic limit, the ratio ZE/HS vanishes. However it seems that the dimension of the ZE subspace still increases with system size, albeit in a subleading fashion, with respect to the restricted Hilbert space dimension.

For a ladder with even  $N_x$  ( $N_x = 2n$  for  $n \in \mathbb{N}$ ), we obtain from the progression of the results in Fig. 7.6(c) the number of zero-energy eigenstates,  $\text{ZE}^{\text{PBC}} = 8(n - 1) + 4$ , and  $\text{ZE}^{\text{OBC}} = 10(n - 1) + 4$  (for  $n \geq 3$ ). In the case that  $n < 3$ , the number of zero energy eigenstates for periodic and open boundaries is equal,  $\text{ZE} = 8(n - 1) + 4$ .

Knowing the number of zero-energy states in a system, we now want to illustrate how to construct those localized states as a superposition of a small number of product states. Figure 7.7 illustrates the configuration of some localized zero-energy states for the example of a  $N = 4 \times 2$  (a) and  $N = 6 \times 2$  ladder with  $N_p = 2$  bosons (PBC). We can construct zero-energy states by superimposing two dimer configurations with opposite phases (indicated as blue and red circles) located at the same rung ( $x$ -direction) of the ladder. Thus, the action of the Hamiltonian on these superposition states results in the cancellation of the wavefunctions indicating a zero-energy eigenstate. In a  $N = N_x \times 2$  ladder with  $N_p = 2$  particles, we can construct  $N_x$  localized zero-energy states by translating the superposition state through the system along the  $x$ -direction. The remaining zero-energy eigenstates cannot be systematically constructed and become increasingly more complicated with increasing system size making them experimentally unfeasible to construct. Figure 7.8 compares the autocorrelation of a ladder ( $N = 10 \times 2$ ) with  $N_p = 2$  particles under (a) constrained quantum dynamics, and (b) constrained classical diffusion. The system is described using PBC, thus we can construct ten zero-energy eigenstates analogously to the states shown in Fig. 7.7. In the quantum case, we can observe non-zero plateau values of the autocorrelation function indicating localization. The localized eigenstates appear in a periodic pattern which can be attributed to the periodic structure of the Hilbert space. As expected, the autocorrelator describing the classical diffusion shows a similar behavior as

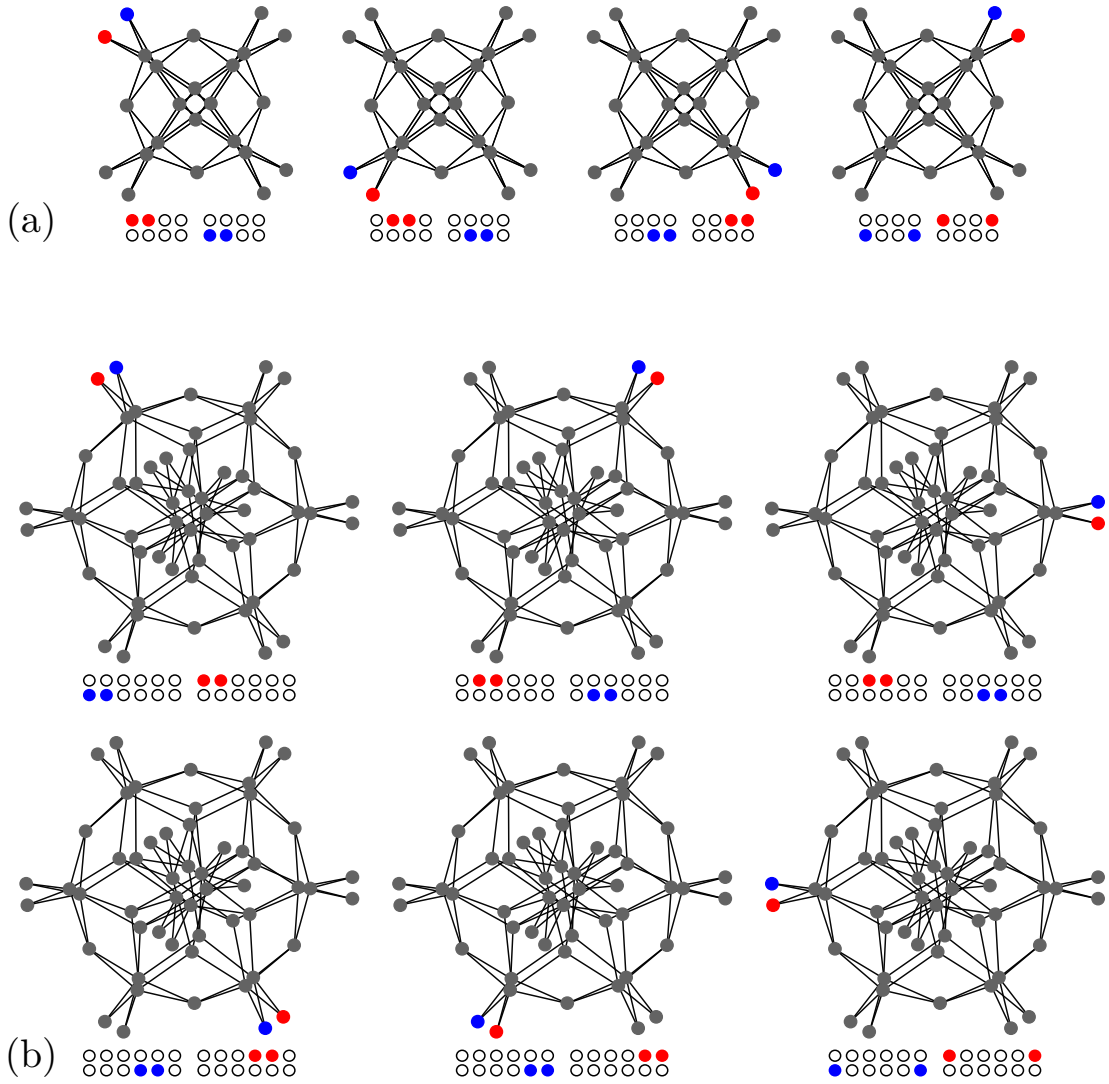


**Figure 7.7: Graph representation of the Hilbert space and localized zero-energy eigenstates.** Graph of the adjacency matrix for a  $N = 4 \times 2$  (a) and  $N = 6 \times 2$  (b) ladder with two particles ( $R_c = 2$ , PBC). We show the configurations of the  $N_x$  translationally invariant zero-energy eigenstates which can be constructed in any  $N_x \times 2$  ladder with PBC.

in the case of the square lattice;  $c^\ell(t)$  rapidly decays on short timescales ( $t < 10$ ) before vanishing indicating that the system has thermalized.

## 7.5 Conclusion and Outlook

We studied the effect of non-local particle loss on the dynamics of a two-dimensional hard-core lattice gas. In the regime of strong dissipation, the model can be effectively described as a hopping model with the constraint that two particles cannot be separated by the critical distance  $R_c$ . This constraint results in non-equilibrium dynamics and localization effects that are caused by an interplay of the classical constraint and quantum interference effects.

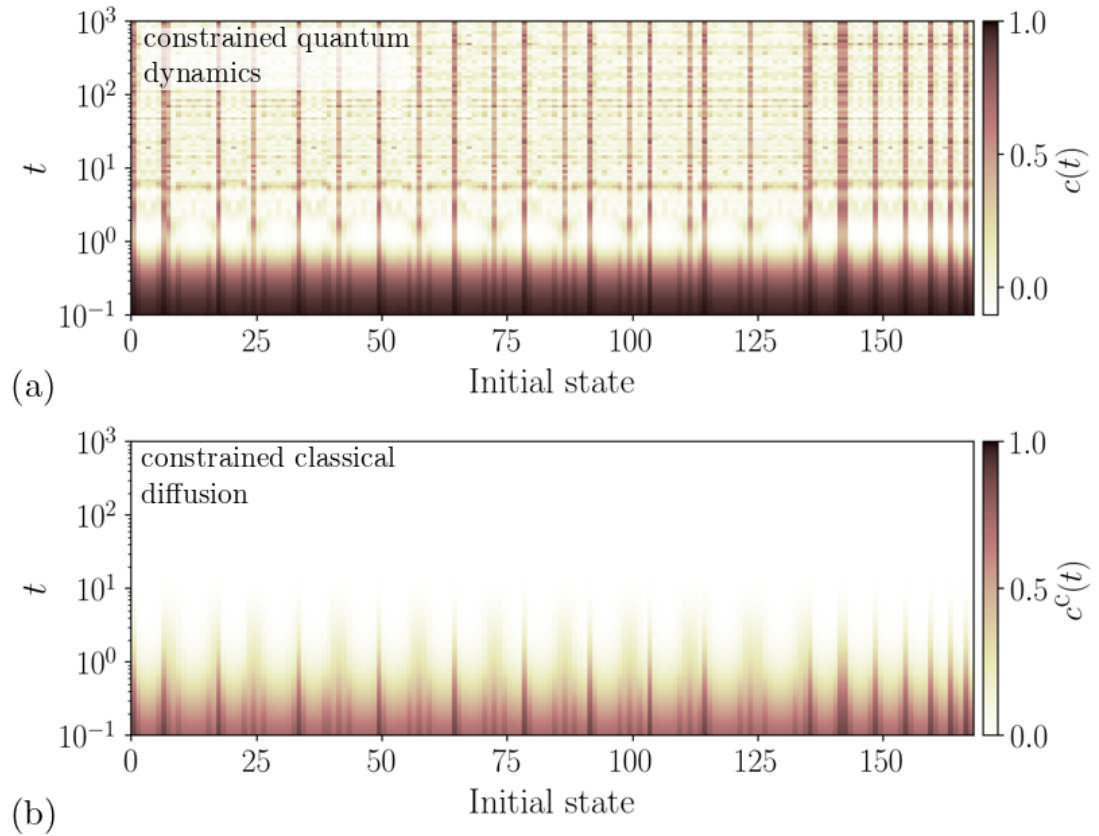


**Figure 7.8: Scan of the autocorrelation function for a ladder.** Scan of the two-time correlation function  $c(t)$  over all possible product states of a constrained system ( $R_c = 2$ ) of  $N = 10 \times 2$  lattice sites with  $N_p = 2$  particles evolving under (a) quantum dynamics, and (b) under classical diffusion (PBC).

# Chapter 8

## Outlook and Conclusions

Recent advances in the trapping and the manipulation of cold atoms in optical tweezer arrays have allowed for the production of Rydberg quantum simulators. This experimental progress enables the creation of one-, two- and three-dimensional lattices of arbitrary geometry with close-to-unit filling [163] thus offering a novel platform to study the dynamics of many-body quantum systems [153]. We based our theoretical models on these Rydberg quantum simulators to investigate the many-body dynamics of Rydberg lattice systems in the presence of constraints and disorder. Additionally, we designed and simulated three protocols for the non-adiabatic engineering and transport of quantum states in one-dimensional chains of Rydberg atoms [1].

Chapter 4 introduced state-preparation protocols based on the Rydberg blockade which prevents the excitation of two adjacent atoms to a Rydberg state. In particular, we discussed the preparation of a maximally entangled quantum state known as the antiferromagnetic GHZ state which is used as a reference in quantum estimation theory. Furthermore, we considered a protocol to prepare a specific kind of matrix product state, the dimer-MPS state, which is related to a Rydberg crystal and can be treated analytically. The last protocol we considered allows the transport of a single-qubit state between different nodes of a network. We studied how the performance of these protocols is influenced by imperfections such as non-perfect Rydberg blockade and disorder arising from the randomness of the atomic positions in the traps due to the finite temperature of the setup. This research could be continued by improving the performance of the protocols by reducing the sensitivity to imperfections resulting in a higher fidelity for long chains. Furthermore, the state transport protocol could be extended to transport many-qubit states between nodes of a quantum network or to expand the network

to various two-dimensional geometries.

Our next project then focused on the dynamics of Rydberg quantum simulator systems with constraints caused by the strong interactions between the Rydberg atoms. In particular, we were considering models based on the facilitation mechanism, where the excitation of an atom to a Rydberg state is strongly enhanced by an already excited neighbor, thus defining the constrained dynamics of the system. In order for the facilitation mechanism to work it is not sufficient to simply have strong interactions. In fact, it requires a fine-tuning of the parameters and control of the setup. Even small variations in the atomic positions, when the lattice is not perfectly regular, can dramatically shift the energy levels and hinder the facilitation mechanism. This means that the facilitation is very sensitive to disorder. However, disorder in a system can lead to interesting effects such as single-particle localization also called Anderson localization.

In chapter 5, we were studying disorder induced Anderson localization in a quasi one-dimensional Rydberg lattice under the facilitation constraint. We focused on the single-particle regime, where the Hilbert space forms a synthetic lattice, a Lieb ladder, featuring a flat band which supports localized states. Such flat bands result in interesting phenomena such as disorder induced delocalization. In order to quantify the localization effect in the Lieb ladder, we calculated the localization lengths as a function of the disorder strengths. The Lieb ladder decouples into two lattices, a stub lattice and a chain, with corresponding transmission channels and localization lengths. Therefore, the localization behavior in a Lieb ladder is described by two localization lengths. We found anomalous scaling behavior of the localization lengths. The model we considered in this chapter can be applied to higher dimensional lattices which will, as in the Lieb ladder case, result in a synthetic lattice featuring flat bands and localized eigenstates. Future work might study the effect of flat bands on the localization behavior for the three-dimensional case, where the system undergoes a phase transition at a critical disorder strength from a delocalized to a fully-localized regime.

After focusing on single-particle or Anderson localization, we considered in chapter 6 localization phenomena in the many-body sector with facilitation constraints. In this sector the system can be described in terms of a dual domain wall picture. The randomness in the atomic positions translates in the domain wall picture into a non-local disordered interaction, where the disorder and interaction are intertwined and cannot be tuned independently from each other. This differs from standard MBL systems where the disorder and the interactions strength are

independent parameters. This model is relevant and not just an exotic theoretical construct as it arises naturally in Rydberg quantum simulator experiments. In this many-body model we find signatures of a crossover between a thermalizing and a many-body localized phase. Future research on many-body localization in constrained Rydberg lattice systems might consider the dynamics on higher dimensional lattices with various lattice geometries. Investigating different types of disorder, such as correlated and uncorrelated disorder, and their influence on the many-body localization might also be of interest. Further research on this topic that is about coupling the degrees of freedom of the spin system with the lattice vibrations of the atomic traps leading to the formation of polarons [184]. The previous chapters considered constraints emerging from energy barriers restricting the dynamics to only allow a spin flip next to an already excited spin. In chapter 7, we studied dissipation induced constraints in a hard-core boson model that can be realized in a Rydberg lattice system. The system exhibits interesting localization effects even in the absence of disorder. Further work might consider the role of dissipation in a constrained Rydberg lattice system with disorder and how the combination of these two effects influences the dynamics of localized system.

# Bibliography

- [1] Maike Ostmann, Jiří Minář, Matteo Marcuzzi, Emanuele Levi, and Igor Lesanovsky. Non-adiabatic quantum state preparation and quantum state transport in chains of Rydberg atoms. *New Journal of Physics*, 19(12):123015, Dec 2017.
- [2] Maike Ostmann, Matteo Marcuzzi, Jiří Minář, and Igor Lesanovsky. Synthetic lattices, flat bands and localization in Rydberg quantum simulators. *Quantum Science and Technology*, 4(2):02LT01, Jan 2019.
- [3] Maike Ostmann, Matteo Marcuzzi, Juan P. Garrahan, and Igor Lesanovsky. Localization in spin chains with facilitation constraints and disordered interactions. *Phys. Rev. A*, 99:060101, Jun 2019.
- [4] Beatriz Olmos and Igor Lesanovsky. Rydberg rings. *Phys. Chem. Chem. Phys.*, Jan 2011.
- [5] Dmitry A. Abanin, Ehud Altman, Immanuel Bloch, and Maksym Serbyn. Colloquium: Many-body localization, thermalization, and entanglement. *Rev. Mod. Phys.*, 91:021001, May 2019.
- [6] Matteo Marcuzzi, Jiří Minář, Daniel Barredo, Sylvain de Léséleuc, Henning Labuhn, Thierry Lahaye, Antoine Browaeys, Emanuele Levi, and Igor Lesanovsky. Facilitation Dynamics and Localization Phenomena in Rydberg Lattice Gases with Position Disorder. *Phys. Rev. Lett.*, 118:063606, Feb 2017.
- [7] Sergej Flach, Daniel Leykam, Joshua D. Bodyfelt, Peter Matthies, and Anton S. Desyatnikov. Detangling flat bands into Fano lattices. *EPL (Europhysics Letters)*, 105(3):30001, Feb 2014.
- [8] Daniel Leykam, Joshua D. Bodyfelt, Anton S. Desyatnikov, and Sergej Flach. Localization of weakly disordered flat band states. *The European Physical Journal B*, 90(1):1, Jan 2017.

- [9] Cenap Ates, Beatriz Olmos, Weibin Li, and Igor Lesanovsky. Dissipative Binding of Lattice Bosons through Distance-Selective Pair Loss. *Phys. Rev. Lett.*, 109:233003, Dec 2012.
- [10] Thomas F. Gallagher. *Rydberg Atoms*. Cambridge Monographs on Atomic, Molecular and Chemical Physics. Cambridge University Press, 1994.
- [11] Rahul Nandkishore and David A. Huse. Many-Body Localization and Thermalization in Quantum Statistical Mechanics. *Annu. Rev. Condens. Matter Phys.*, 6(1):15–38, Mar 2015.
- [12] Immanuel Bloch, Jean Dalibard, and Wilhelm Zwerger. Many-body physics with ultracold gases. *Rev. Mod. Phys.*, 80:885–964, Jul 2008.
- [13] Immanuel Bloch, Jean Dalibard, and Sylvain Nascimbene. Quantum simulations with ultracold quantum gases. *Nat. Phys.*, 8(4):267–276, 2012.
- [14] Sebastian Hofferberth, Igor Lesanovsky, Thorsten Schumm, Adilet Imambekov, Vladimir Gritsev, Eugene Demler, and Jorg Schmiedmayer. Probing quantum and thermal noise in an interacting many-body system. *Nature Physics*, Apr 2008.
- [15] Toshiya Kinoshita, Trevor Wenger, and David S. Weiss. Observation of a One-Dimensional Tonks-Girardeau Gas. 305(5687):1125–1128, Aug 2004.
- [16] Markus Greiner, Olaf Mandel, Tilman Esslinger, Theodor W. Hänsch, and Immanuel Bloch. Quantum phase transition from a superfluid to a Mott insulator in a gas of ultracold atoms. *Nature*, 415(6867):39–44, Jan 2002.
- [17] Michael Köhl, Henning Moritz, Thilo Stöferle, Kenneth Günter, and Tilman Esslinger. Fermionic atoms in a three dimensional optical lattice: Observing fermi surfaces, dynamics, and interactions. *Phys. Rev. Lett.*, 94:080403, Mar 2005.
- [18] Markus Greiner, Olaf Mandel, Theodor W. Hänsch, and Immanuel Bloch. Collapse and revival of the matter wave field of a Bose–Einstein condensate. *Nature*, 419(6902):51–54, Sep 2002.
- [19] Marc Cheneau, Peter Barmettler, Dario Poletti, Manuel Endres, Peter Schauß, Takeshi Fukuhara, Christian Gross, Immanuel Bloch, Corinna Kollath, and Stefan Kuhr. Light-cone-like spreading of correlations in a quantum many-body system. *Nature*, 481(7382):484–487, Jan 2012.

- [20] Zoran Hadzibabic, Peter Krüger, Marc Cheneau, Baptiste Battelier, and Jean Dalibard. Berezinskii–Kosterlitz–Thouless crossover in a trapped atomic gas. *Nature*, 441(7097):1118–1121, Jun 2006.
- [21] M. Saffman, T. G. Walker, and K. Mølmer. Quantum information with Rydberg atoms. *Rev. Mod. Phys.*, 82:2313–2363, Aug 2010.
- [22] Robert Löw, Hendrik Weimer, Johannes Nipper, Jonathan B Balewski, Björn Butscher, Hans Peter Büchler, and Tilman Pfau. An experimental and theoretical guide to strongly interacting Rydberg gases. *Journal of Physics B: Atomic, Molecular and Optical Physics*, 45(11):113001, May 2012.
- [23] Hendrik Weimer and Hans Peter Büchler. Two-stage melting in Systems of Strongly Interacting Rydberg Atoms. *Phys. Rev. Lett.*, 105:230403, Nov 2010.
- [24] Emanuele Levi, Jiří Minář, and Igor Lesanovsky. Crystalline structures in a one-dimensional two-component lattice gas with  $1/r^\alpha$  interactions. *Journal of Statistical Mechanics: Theory and Experiment*, 2016(3):033111, Mar 2016.
- [25] Zhihao Lan, Jiří Minář, Emanuele Levi, Weibin Li, and Igor Lesanovsky. Emergent Devil’s Staircase without Particle-Hole Symmetry in Rydberg Quantum Gases with Competing Attractive and Repulsive Interactions. *Phys. Rev. Lett.*, 115:203001, Nov 2015.
- [26] Hanna Schempp, Georg Günter, Martin Robert-de Saint-Vincent, Christoph S. Hofmann, David Breyel, Andreas Komnik, David W. Schönleber, Martin Gärttner, Jörg Evers, Shannon Whitlock, and Matthias Weidemüller. Full Counting Statistics of Laser Excited Rydberg Aggregates in a One-Dimensional Geometry. *Phys. Rev. Lett.*, 112:013002, Jan 2014.
- [27] Zhihao Lan, Weibin Li, and Igor Lesanovsky. Quantum melting of two-component Rydberg crystals. *Phys. Rev. A*, 94:051603, Nov 2016.
- [28] Peter Schauß, Johannes Zeiher, Takeshi Fukuhara, S Hild, M Cheneau, T Macrì, T Pohl, Immanuel Bloch, and Christian Groß. Crystallization in Ising quantum magnets. *Science*, 347(6229):1455–1458, Mar 2015.

- [29] Christopher Carr, Ralf Ritter, Christopher G. Wade, Charles S. Adams, and Kevin J. Weatherill. Nonequilibrium Phase Transition in a Dilute Rydberg Ensemble. *Phys. Rev. Lett.*, 111:113901, Sep 2013.
- [30] Nikola Šibalić, Christopher G. Wade, Charles S. Adams, Kevin J. Weatherill, and Thomas Pohl. Driven-dissipative many-body systems with mixed power-law interactions: Bistabilities and temperature-driven nonequilibrium phase transitions. *Phys. Rev. A*, 94:011401, Jul 2016.
- [31] Robert Löw, Hendrik Weimer, Ulrich Krohn, Rolf Heidemann, Vera Bendkowsky, Björn Butscher, Hans Peter Büchler, and Tilman Pfau. Universal scaling in a strongly interacting Rydberg gas. *Phys. Rev. A*, 80:033422, Sep 2009.
- [32] Matteo Marcuzzi, Emanuele Levi, Sebastian Diehl, Juan P. Garrahan, and Igor Lesanovsky. Universal Nonequilibrium Properties of Dissipative Rydberg Gases. *Phys. Rev. Lett.*, 113:210401, Nov 2014.
- [33] Ricardo Gutiérrez, Juan P. Garrahan, and Igor Lesanovsky. Self-similar nonequilibrium dynamics of a many-body system with power-law interactions. *Phys. Rev. E*, 92:062144, Dec 2015.
- [34] Michael Schecter and Thomas Iadecola. Many-body spectral reflection symmetry and protected infinite-temperature degeneracy. *Phys. Rev. B*, 98:035139, Jul 2018.
- [35] Henning Labuhn, Daniel Barredo, Sylvain Ravets, Sylvain de Léséleuc, Tommaso Macrì, Thierry Lahaye, and Antoine Browaeys. Tunable two-dimensional arrays of single Rydberg atoms for realizing quantum Ising models. *Nature*, 534:667, Jun 2016.
- [36] Mark Saffman. Quantum computing with atomic qubits and Rydberg interactions: progress and challenges. *Journal of Physics B: Atomic, Molecular and Optical Physics*, 49(20):202001, Oct 2016.
- [37] Larry Isenhower, Erik Urban, Xianli. L. Zhang, Alex T. Gill, Thomas Henage, T. A. Johnson, Thad G. Walker, and Mark Saffman. Demonstration of a Neutral Atom Controlled-Not Quantum Gate. *Phys. Rev. Lett.*, 104:010503, Jan 2010.

- [38] Kara M. Maller, Marc T. Lichtman, Tian-long Xia, Yue Sun, Michał J. Piotrowicz, A. W. Carr, Larry Isenhower, and Mark Saffman. Rydberg-blockade controlled-not gate and entanglement in a two-dimensional array of neutral-atom qubits. *Phys. Rev. A*, 92:022336, Aug 2015.
- [39] Florence Nogrette, Henning Labuhn, Sylvain Ravets, Daniel Barredo, Lucas Béguin, Aline Vernier, Thierry Lahaye, and Antoine Browaeys. Single-Atom Trapping in Holographic 2D Arrays of Microtraps with Arbitrary Geometries. *Phys. Rev. X*, 4:021034, May 2014.
- [40] Daniel Barredo, Sylvain de Léséleuc, Vincent Lienhard, Thierry Lahaye, and Antoine Browaeys. An atom-by-atom assembler of defect-free arbitrary two-dimensional atomic arrays. 354(6315):1021–1023, Nov 2016.
- [41] Manuel Endres, Hannes Bernien, Alexander Keesling, Harry Levine, Eric R. Anschuetz, Alexandre Krajenbrink, Crystal Senko, Vladan Vuletic, Markus Greiner, and Mikhail D. Lukin. Atom-by-atom assembly of defect-free one-dimensional cold atom arrays. *Science*, 354(6315):1024–1027, Nov 2016.
- [42] Henning Labuhn, Sylvain Ravets, Daniel Barredo, Lucas Béguin, Florence Nogrette, Thierry Lahaye, and Antoine Browaeys. Single-atom addressing in microtraps for quantum-state engineering using Rydberg atoms. *Phys. Rev. A*, 90:023415, Aug 2014.
- [43] Martin Boll, Timon A. Hilker, Guillaume Salomon, Ahmed Omran, Jacopo Nespolo, Lode Pollet, Immanuel Bloch, and Christian Gross. Spin- and density-resolved microscopy of antiferromagnetic correlations in fermi-hubbard chains. *Science*, 353(6305):1257–1260, Sep 2016.
- [44] Waseem S. Bakr, Jonathon I. Gillen, Amy Peng, Simon Fölling, and Markus Greiner. A quantum gas microscope for detecting single atoms in a Hubbard-regime optical lattice. *Nature*, 462(7269):74–77, Nov 2009.
- [45] Lawrence W. Cheuk, Matthew A. Nichols, Melih Okan, Thomas Gersdorf, Vinay V. Ramasesh, Waseem S. Bakr, Thomas Lompe, and Martin W. Zwierlein. Quantum-gas microscope for fermionic atoms. *Phys. Rev. Lett.*, 114:193001, May 2015.
- [46] David Petrosyan, Klaus Mølmer, and Michael Fleischhauer. On the adiabatic preparation of spatially-ordered Rydberg excitations of atoms in a one-dimensional optical lattice by laser frequency sweeps. *Journal of Physics B: Atomic, Molecular and Optical Physics*, 49(8):084003, Apr 2016.

- [47] Jian Cui, Rick van Bijnen, Thomas Pohl, Simone Montangero, and Tommaso Calarco. Optimal control of Rydberg lattice gases. *Quantum Science and Technology*, 2(3):035006, Aug 2017.
- [48] Caner Ates, Thomas Pohl, Thomas Pattard, and Jan M. Rost. Antiblockade in Rydberg Excitation of an Ultracold Lattice Gas. *Phys. Rev. Lett.*, 98:023002, Jan 2007.
- [49] Thomas Amthor, Christian Giese, Christoph S. Hofmann, and Matthias Weidemüller. Evidence of Antiblockade in an Ultracold Rydberg Gas. *Phys. Rev. Lett.*, 104:013001, Jan 2010.
- [50] David W. Schönleber, Martin Gärttner, and Jörg Evers. Coherent versus incoherent excitation dynamics in dissipative many-body Rydberg systems. *Phys. Rev. A*, 89:033421, Mar 2014.
- [51] Igor Lesanovsky and Juan P. Garrahan. Out-of-equilibrium structures in strongly interacting Rydberg gases with dissipation. *Phys. Rev. A*, 90:011603, Jul 2014.
- [52] Alban Urvoy, Fabian Ripka, Igor Lesanovsky, Donald Booth, James P. Shaffer, Tilman Pfau, and Robert Löw. Strongly Correlated Growth of Rydberg Aggregates in a Vapor Cell. *Phys. Rev. Lett.*, 114:203002, May 2015.
- [53] M. M. Valado, C. Simonelli, M. D. Hoogerland, I. Lesanovsky, J. P. Garrahan, E. Arimondo, D. Ciampini, and O. Morsch. Experimental observation of controllable kinetic constraints in a cold atomic gas. *Phys. Rev. A*, 93:040701, Apr 2016.
- [54] Philip W. Anderson. Absence of Diffusion in Certain Random Lattices. *Phys. Rev.*, 109:1492–1505, Mar 1958.
- [55] Boris L. Altshuler, Yuval Gefen, Alex Kamenev, and Leonid S. Levitov. Quasiparticle Lifetime in a Finite System: A Nonperturbative Approach. *Phys. Rev. Lett.*, 78:2803–2806, Apr 1997.
- [56] Denis M. Basko, Igor L. Aleiner, and Boris L. Altshuler. Metal-insulator transition in a weakly interacting many-electron system with localized single-particle states. *Ann. Phys.*, 321:1126, May 2006.
- [57] Igor. V. Gornyi, Alexander D. Mirlin, and Dmitry G. Polyakov. Interacting Electrons in Disordered Wires: Anderson Localization and Low- $T$  Transport. *Phys. Rev. Lett.*, 95:206603, Nov 2005.

- [58] Vadim Oganesyan and David A. Huse. Localization of interacting fermions at high temperature. *Phys. Rev. B*, 75:155111, Apr 2007.
- [59] Marko Žnidarič, Tomaž Prosen, and Peter Prelovšek. Many-body localization in the Heisenberg  $XXZ$  magnet in a random field. *Phys. Rev. B*, 77:064426, Feb 2008.
- [60] Arijeet Pal and David A. Huse. The many-body localization phase transition. *Phys. Rev. B*, 82:174411, Oct 2010.
- [61] Jens H. Bardarson, Frank Pollmann, and Joel E. Moore. Unbounded Growth of Entanglement in Models of Many-Body Localization. *Phys. Rev. Lett.*, 109:017202, Jul 2012.
- [62] Maksym Serbyn, Z. Papić, and Dmitry A. Abanin. Universal Slow Growth of Entanglement in Interacting Strongly Disordered Systems. *Phys. Rev. Lett.*, 110:260601, Jun 2013.
- [63] David A. Huse, Rahul Nandkishore, and Vadim Oganesyan. Phenomenology of fully many-body-localized systems. *Phys. Rev. B*, 90:174202, Nov 2014.
- [64] Felix Andraschko, Tilman Enss, and Jesko Sirker. Purification and Many-Body Localization in Cold Atomic Gases. *Phys. Rev. Lett.*, 113:217201, Nov 2014.
- [65] Norman Y. Yao, Chris R. Laumann, Sarang Gopalakrishnan, Michael Knap, Markus Müller, Eugene A. Demler, and Mikhail D. Lukin. Many-Body Localization in Dipolar Systems. *Phys. Rev. Lett.*, 113:243002, Dec 2014.
- [66] Maksym Serbyn, Zlatko Papić, and Dmitry A. Abanin. Quantum quenches in the many-body localized phase. *Phys. Rev. B*, 90:174302, Nov 2014.
- [67] Chris R. Laumann, Arijeet Pal, and Antonello Scardicchio. Many-Body Mobility Edge in a Mean-Field Quantum Spin Glass. *Phys. Rev. Lett.*, 113:200405, Nov 2014.
- [68] Valentina Ros, Markus Müller, and Antonello Scardicchio. Integrals of motion in the many-body localized phase. *Nuclear Physics B*, 891:420 – 465, Feb 2015.

- [69] Romain Vasseur, Siddharth A. Parameswaran, and Joel E. Moore. Quantum revivals and many-body localization. *Phys. Rev. B*, 91:140202, Apr 2015.
- [70] Kartiek Agarwal, Sarang Gopalakrishnan, Michael Knap, Markus Müller, and Eugene Demler. Anomalous Diffusion and Griffiths Effects Near the Many-Body Localization Transition. *Phys. Rev. Lett.*, 114:160401, Apr 2015.
- [71] Yevgeny Bar Lev, Guy Cohen, and David R. Reichman. Absence of Diffusion in an Interacting System of Spinless Fermions on a One-Dimensional Disordered Lattice. *Phys. Rev. Lett.*, 114:100601, Mar 2015.
- [72] John Z Imbrie. On many-body localization for quantum spin chains. *J. Stat. Phys.*, 163(5):998–1048, 2016.
- [73] Michael Schreiber, Sean S. Hodgman, Pranjal Bordia, Henrik P. Lüschen, Mark H. Fischer, Ronen Vosk, Ehud Altman, Ulrich Schneider, and Immanuel Bloch. Observation of many-body localization of interacting fermions in a quasi-random optical lattice. *Science*, 349:842, Jan 2015.
- [74] Pranjal Bordia, Henrik P. Luschen, Sean S. Hodgman, Michael Schreiber, Immanuel Bloch, and Ulrich Schneider. Coupling identical one-dimensional many-body localized systems. *Phys. Rev. Lett.*, 116:140401, Apr 2016.
- [75] Jacob Smith, Aaron Lee, Philip Richerme, Brian Neyenhuis, Paul W Hess, Philipp Hauke, Markus Heyl, David A Huse, and Christopher Monroe. Many-body localization in a quantum simulator with programmable random disorder. *Nature Phys.*, 12(10):907–911, Jun 2016.
- [76] Jae-yoon Choi, Sebastian Hild, Johannes Zeiher, Peter Schauß, Antonio Rubio-Abadal, Tarik Yefsah, Vedika Khemani, David A. Huse, Immanuel Bloch, and Christian Gross. Exploring the many-body localization transition in two dimensions. *Science*, 352(6293):1547–1552, Jun 2016.
- [77] Merlijn van Horssen, Emanuele Levi, and Juan P. Garrahan. Dynamics of many-body localization in a translation-invariant quantum glass model. *Phys. Rev. B*, 92:100305, Sep 2015.
- [78] James M Hickey, Sam Genway, and Juan P Garrahan. Signatures of many-body localisation in a system without disorder and the relation to a glass transition. *J. Stat. Mech.*, (5):054047, May 2016.

- [79] Zhihao Lan, Merlijn van Horssen, Stephen Powell, and Juan P. Garrahan. Quantum slow relaxation and metastability due to dynamical constraints. *Phys. Rev. Lett.*, 121:040603, Jul 2018.
- [80] Giuseppe Carleo, Federico Becca, Marco Schiró, and Michele Fabrizio. Localization and glassy dynamics of many-body quantum systems. *Scientific reports*, 2:243, Jan 2012.
- [81] Wojciech De Roeck and Francois Huveneers. Scenario for delocalization in translation-invariant systems. *Phys. Rev. B*, 90:165137, Oct 2014.
- [82] Mauro Schiulaz, Alessandro Silva, and Markus Müller. Dynamics in many-body localized quantum systems without disorder. *Phys. Rev. B*, 91:184202, May 2015.
- [83] Zlatko Papić, Edwin Miles Stoudenmire, and Dmitry A. Abanin. Many-body localization in disorder-free systems: The importance of finite-size constraints. *Ann. Phys.*, 362:714–725, Nov 2015.
- [84] Luca Barbiero, Chiara Menotti, Alessio Recati, and Lezie Santos. Out-of-equilibrium states and quasi-many-body localization in polar lattice gases. *Phys. Rev. B*, 92:180406, Nov 2015.
- [85] Norman Y. Yao, Chris R. Laumann, J. Ignacio Cirac, Mikhail D. Lukin, and Joel E. Moore. Quasi-Many-Body Localization in Translation-Invariant Systems. *Phys. Rev. Lett.*, 117:240601, Dec 2016.
- [86] Abhinav Prem, Jeongwan Haah, and Rahul Nandkishore. Glassy quantum dynamics in translation invariant fracton models. *Phys. Rev. B*, 95:155133, Apr 2017.
- [87] Adam Smith, Johannes Knolle, Dmitry L. Kovrizhin, and Roderich Moessner. Disorder-free localization. *Phys. Rev. Lett.*, 118:266601, Jun 2017.
- [88] H. Yarloo, Abdollah Langari, and Abolhassan Vaezi. Anyonic self-induced disorder in a stabilizer code: Quasi many-body localization in a translational invariant model. *Phys. Rev. B*, 97:054304, Feb 2018.
- [89] Rubem Mondaini and Zi Cai. Many-body self-localization in a translation-invariant Hamiltonian. *Phys. Rev. B*, 96:035153, Jul 2017.

- [90] Naoto Shiraishi and Takashi Mori. Systematic construction of counterexamples to the eigenstate thermalization hypothesis. *Phys. Rev. Lett.*, 119:030601, Jul 2017.
- [91] Chun Chen, Fiona Burnell, and Anushya Chandran. How Does a Locally Constrained Quantum System Localize? *Phys. Rev. Lett.*, 121:085701, Aug 2018.
- [92] Richard P Feynman. Simulating physics with computers. *International journal of theoretical physics*, 21:467–488, Jun 1982.
- [93] Benjamin Schumacher. Quantum coding. *Phys. Rev. A*, 51:2738–2747, Apr 1995.
- [94] David Deutsch and Roger Penrose. Quantum theory, the Church-Turing principle and the universal quantum computer. *Proceedings of the Royal Society of London. A. Mathematical and Physical Sciences*, 400(1818):97–117, Jul 1985.
- [95] David Deutsch and Richard Jozsa. Rapid solution of problems by quantum computation. *Proceedings of the Royal Society of London. Series A: Mathematical and Physical Sciences*, 439(1907):553–558, 1992.
- [96] Lov K. Grover. A fast quantum mechanical algorithm for database search. *arXiv e-prints*, pages quant-ph/9605043, May 1996.
- [97] P. Shor. Polynomial-Time Algorithms for Prime Factorization and Discrete Logarithms on a Quantum Computer. *SIAM Journal on Computing*, 26(5):1484–1509, Oct 1997.
- [98] Pieter Kok, W. J. Munro, Kae Nemoto, T. C. Ralph, Jonathan P. Dowling, and G. J. Milburn. Linear optical quantum computing with photonic qubits. *Rev. Mod. Phys.*, 79:135–174, Jan 2007.
- [99] Yuriy Makhlin, Gerd Schön, and Alexander Shnirman. Quantum-state engineering with Josephson-junction devices. *Rev. Mod. Phys.*, 73:357–400, May 2001.
- [100] Immanuel Bloch. Quantum coherence and entanglement with ultracold atoms in optical lattices. *Nature*, 453(7198):1016–1022, Jun 2008.
- [101] R. Blatt and Christian F. Roos. Quantum simulations with trapped ions. *Nature Physics*, 8:277 EP, Apr 2012.

- [102] Daniel Barredo, Henning Labuhn, Sylvain Ravets, Thierry Lahaye, Antoine Browaeys, and Charles S. Adams. Coherent Excitation Transfer in a Spin Chain of Three Rydberg Atoms. *Phys. Rev. Lett.*, 114:113002, Mar 2015.
- [103] Igor I Ryabtsev, Denis B Tretyakov, and Ilya I Beterov. Applicability of Rydberg atoms to quantum computers. *Journal of Physics B: Atomic, Molecular and Optical Physics*, 38(2):S421–S436, Jan 2005.
- [104] Antoine Browaeys, Daniel Barredo, and Thierry Lahaye. Experimental investigations of dipole–dipole interactions between a few Rydberg atoms. *Journal of Physics B: Atomic, Molecular and Optical Physics*, 49(15):152001, Jun 2016.
- [105] Mark Saffman and Thad G. Walker. Analysis of a quantum logic device based on dipole-dipole interactions of optically trapped Rydberg atoms. *Phys. Rev. A*, 72:022347, Aug 2005.
- [106] Marlan O. Scully and M. Suhail Zubairy. *Quantum Optics*. Cambridge University Press, 1997.
- [107] Daniel Comparat and Pierre Pillet. Dipole blockade in a cold Rydberg atomic sample. *J. Opt. Soc. Am. B*, 27(6):A208–A232, Jun 2010.
- [108] Barry R. Holstein. The van der Waals interaction. *American Journal of Physics*, 69(4):441–449, Oct 2001.
- [109] F. London. Zur Theorie und Systematik der Molekularkräfte. *Zeitschrift für Physik*, 63(3):245–279, Mar 1930.
- [110] Cenap Ates, Thomas Pohl, Thomas Pattard, and Jan M. Rost. Many-body theory of excitation dynamics in an ultracold Rydberg gas. *Phys. Rev. A*, 76:013413, Jul 2007.
- [111] John B. Pendry. Symmetry and transport of waves in one-dimensional disordered systems. *Advances in Physics*, 43(4):461–542, Feb 1994.
- [112] E. Abrahams, P. W. Anderson, D. C. Licciardello, and T. V. Ramakrishnan. Scaling Theory of Localization: Absence of Quantum Diffusion in Two Dimensions. *Phys. Rev. Lett.*, 42:673–676, Mar 1979.
- [113] A. Vulpiani A. Crisanti, G. Paladin. *Products of Random Matrices in Statistical Physics*, chapter 2, pages 26–29. Springer, 1st edition, 1993.

- [114] L. Fleishman and P. W. Anderson. Interactions and the Anderson transition. *Phys. Rev. B*, 21:2366–2377, Mar 1980.
- [115] Pranjal Bordia, Henrik Lüschen, Sebastian Scherg, Sarang Gopalakrishnan, Michael Knap, Ulrich Schneider, and Immanuel Bloch. Probing slow relaxation and many-body localization in two-dimensional quasiperiodic systems. *Phys. Rev. X*, 7:041047, Nov 2017.
- [116] Ehud Altman and Ronen Vosk. Universal dynamics and renormalization in many body localized systems. *Annu. Rev. Condens. Matter Phys.*, 6:383, Aug 2015.
- [117] Dmitry A. Abanin and Zlatko Papić. Recent progress in many-body localization. *Annalen der Physik*, 529(7):1700169, Jul 2017.
- [118] Fabien Alet and Nicolas Laflorencie. Many-body localization: An introduction and selected topics. *Comptes Rendus Physique*, 19(6):498 – 525, Sep 2018.
- [119] Marcos Rigol and Mark Srednicki. Alternatives to eigenstate thermalization. *Phys. Rev. Lett.*, 108:110601, Mar 2012.
- [120] Mark Srednicki. Thermal fluctuations in quantized chaotic systems. *Journal of Physics A: Mathematical and General*, 29(4):L75–L79, Feb 1996.
- [121] Rubem Mondaini and Marcos Rigol. Eigenstate thermalization in the two-dimensional transverse field Ising model. II. Off-diagonal matrix elements of observables. *Phys. Rev. E*, 96:012157, Jul 2017.
- [122] Maksym Serbyn, Z. Papić, and Dmitry A. Abanin. Local Conservation Laws and the Structure of the Many-Body Localized States. *Phys. Rev. Lett.*, 111:127201, Sep 2013.
- [123] John Z. Imbrie, Valentina Ros, and Antonello Scardicchio. Local integrals of motion in many-body localized systems. *Annalen der Physik*, 529(7):1600278, May 2017.
- [124] Vittorio Giovannetti, Seth Lloyd, and Lorenzo Maccone. Quantum-enhanced measurements: Beating the standard quantum limit. *Science*, 306(5700):1330–1336, Nov 2004.
- [125] Klaus Mølmer and Anders Sørensen. Multiparticle entanglement of hot trapped ions. *Phys. Rev. Lett.*, 82:1835–1838, Mar 1999.

- [126] Da-Wei Wang. Sewing Greenberger-Horne-Zeilinger states with a quantum zipper. *arXiv e-prints*, page arXiv:1609.08589, Sep 2016.
- [127] Thomas Monz, Philipp Schindler, Julio T. Barreiro, Michael Chwalla, Daniel Nigg, William A. Coish, Maximilian Harlander, Wolfgang Hänsel, Markus Hennrich, and Rainer Blatt. 14-Qubit Entanglement: Creation and Coherence. *Phys. Rev. Lett.*, 106:130506, Mar 2011.
- [128] U. Schollwöck. The density-matrix renormalization group. *Rev. Mod. Phys.*, 77:259–315, Apr 2005.
- [129] David Pérez-García, Frank Verstraete, Michael M. Wolf, and J. Ignacio Cirac. Matrix product state representations. *Quantum Information & Computation*, 7(5):401–430, Jul 2007.
- [130] Ulrich Schollwöck. The density-matrix renormalization group in the age of matrix product states. *Annals of Physics*, 326(1):96 – 192, Jan 2011.
- [131] Igor Lesanovsky. Many-Body Spin Interactions and the Ground State of a Dense Rydberg Lattice Gas. *Phys. Rev. Lett.*, 106:025301, Jan 2011.
- [132] Igor Lesanovsky. Liquid Ground State, Gap, and Excited States of a Strongly Correlated Spin Chain. *Phys. Rev. Lett.*, 108:105301, Mar 2012.
- [133] Emanuele Levi and Igor Lesanovsky. Non-classical correlations in a class of spin chains with long-range interactions and exactly solvable ground states. *New Journal of Physics*, 16(9):093053, Sep 2014.
- [134] Daniel S. Rokhsar and Steven A. Kivelson. Superconductivity and the quantum hard-core dimer gas. *Phys. Rev. Lett.*, 61:2376–2379, Nov 1988.
- [135] Johannes Schachenmayer, Igor Lesanovsky, Andrea Micheli, and Andrew J Daley. Dynamical crystal creation with polar molecules or Rydberg atoms in optical lattices. *New Journal of Physics*, 12(10):103044, Oct 2010.
- [136] Rick M W van Bijnen, Steef Smit, K A H van Leeuwen, E J D Vredenburg, and S J J M F Kokkelmans. Adiabatic formation of Rydberg crystals with chirped laser pulses. *Journal of Physics B: Atomic, Molecular and Optical Physics*, 44(18):184008, Sep 2011.
- [137] Thomas Pohl, Eugene Demler, and Mikhail D. Lukin. Dynamical Crystallization in the Dipole Blockade of Ultracold Atoms. *Phys. Rev. Lett.*, 104:043002, Jan 2010.

- [138] Charles H. Bennett and David P. DiVincenzo. Quantum information and computation. *Nature*, 404(6775):247–255, Mar 2000.
- [139] J. Ignacio Cirac, Peter Zoller, H. J. Kimble, and Hideo Mabuchi. Quantum State Transfer and Entanglement Distribution among Distant Nodes in a Quantum Network. *Phys. Rev. Lett.*, 78:3221–3224, Apr 1997.
- [140] Mark Saffman and Thad G. Walker. Entangling single- and N-atom qubits for fast quantum state detection and transmission. *Phys. Rev. A*, 72:042302, Mar 2005.
- [141] Nithiwadee Thaicharoen, Andrew Schwarzkopf, and Georg Raithel. Measurement of the van der Waals interaction by atom trajectory imaging. *Phys. Rev. A*, 92:040701, Oct 2015.
- [142] Riccardo Faoro, Cristiano Simonelli, Matteo Archimi, Guido Masella, Valado María Martínez, Ennio Arimondo, Riccardo Mannella, Donatella Ciampini, and Oliver Morsch. van der waals explosion of cold Rydberg clusters. *Phys. Rev. A*, 93:030701, Mar 2016.
- [143] Charles H. Bennett, Gilles Brassard, Claude Crépeau, Richard Jozsa, Asher Peres, and William K. Wootters. Teleporting an unknown quantum state via dual classical and Einstein-Podolsky-Rosen channels. *Phys. Rev. Lett.*, 70:1895–1899, Mar 1993.
- [144] Ramon Szmuk, Vincent Dugrain, Wilfried Mainault, Jakob Reichel, and Peter Rosenbusch. Stability of a trapped-atom clock on a chip. *Phys. Rev. A*, 92:012106, Jul 2015.
- [145] Nevill F. Mott and W.D. Twose. The theory of impurity conduction. *Advances in Physics*, 10(38):107–163, Jun 1961.
- [146] Kazushige Ishii. Localization of Eigenstates and Transport Phenomena in the One-Dimensional Disordered System. *Progress of Theoretical Physics Supplement*, 53:77–138, Jan 1973.
- [147] Shintaro Taie, Hideki Ozawa, Tomohiro Ichinose, Takuei Nishio, Shuta Nakajima, and Yoshiro Takahashi. Coherent driving and freezing of bosonic matter wave in an optical Lieb lattice. *Science Advances*, 1(10), Nov 2015.
- [148] Sebabrata Mukherjee, Alexander Spracklen, Debaditya Choudhury, Nathan Goldman, Patrik Öhberg, Erika Andersson, and Robert R. Thomson. Ob-

- ervation of a localized flat-band state in a photonic lieb lattice. *Phys. Rev. Lett.*, 114:245504, Jun 2015.
- [149] Marlou R Slot, Thomas S Gardenier, Peter H Jacobse, Guido CP van Miert, Sander N Kempkes, Stephan JM Zevenhuizen, Cristiane Morais Smith, Daniel Vanmaekelbergh, and Ingmar Swart. Experimental realization and characterization of an electronic Lieb lattice. *Nature Physics*, 13:672–676, Apr 2017.
- [150] Robert Drost, Teemu Ojanen, Ari Harju, and Peter Liljeroth. Topological states in engineered atomic lattices. *Nature Physics*, 13:668, Mar 2017.
- [151] Joshua D. Bodyfelt, Daniel Leykam, Carlo Danieli, Xiaoquan Yu, and Sergej Flach. Flatbands under correlated perturbations. *Phys. Rev. Lett.*, 113:236403, Dec 2014.
- [152] Masaki Goda, Shinya Nishino, and Hiroki Matsuda. Inverse anderson transition caused by flatbands. *Phys. Rev. Lett.*, 96:126401, Mar 2006.
- [153] Hannes Bernien, Sylvain Schwartz, Alexander Keesling, Harry Levine, Ahmed Omran, Hannes Pichler, Soonwon Choi, Alexander S. Zibrov, Manuel Endres, Markus Greiner, Vladan Vuletic, and Mikhail D. Lukin. Probing many-body dynamics on a 51-atom quantum simulator. *Nature*, 551:579, Nov 2017.
- [154] Yuan-Yu Jau, A. M. Hankin, Tyler Keating, Ivan H. Deutsch, and Grant W. Biedermann. Entangling atomic spins with a Rydberg-dressed spin-flip blockade. *Nature Physics*, 12:71, Oct 2015.
- [155] Marco Mattioli, Alexander W. Glätzle, and Wolfgang Lechner. From classical to quantum non-equilibrium dynamics of rydberg excitations in optical lattices. *New Journal of Physics*, 17(11):113039, Nov 2015.
- [156] Ruohao Shen, L. Baigeng Shao, Baigeng Wang, and D. Y. Xing. Single Dirac cone with a flat band touching on line-centered-square optical lattices. *Phys. Rev. B*, 81:041410, Jan 2010.
- [157] Vatsal Dwivedi and Victor Chua. Of bulk and boundaries: Generalized transfer matrices for tight-binding models. *Phys. Rev. B*, 93:134304, Apr 2016.

- [158] A. Crisanti, G. Paladin, and A. Vulpiani. *Products of Random Matrices in Statistical Physics*. Springer Series in Solid-State Sciences. Springer-Verlag, 1993.
- [159] Daniel Leykam, Sergej Flach, Omri Bahat-Treidel, and Anton S. Desyatnikov. Flat band states: Disorder and nonlinearity. *Phys. Rev. B*, 88:224203, Dec 2013.
- [160] Rodrigo A. Vicencio, Camilo Cantillano, Luis Morales-Inostroza, Bastián Real, Cristian Mejía-Cortés, Steffen Weimann, Alexander Szameit, and Mario I. Molina. Observation of Localized States in Lieb Photonic Lattices. *Phys. Rev. Lett.*, 114:245503, Jun 2015.
- [161] Felix Ritort and Peter Sollich. Glassy dynamics of kinetically constrained models. *Advances in Physics*, 52(4):219–342, Jun 2003.
- [162] Hyosub Kim, YeJe Park, Kyungtae Kim, H.-S. Sim, and Jaewook Ahn. Detailed Balance of Thermalization Dynamics in Rydberg-Atom Quantum Simulators. *Phys. Rev. Lett.*, 120:180502, May 2018.
- [163] Daniel Barredo, Vincent Lienhard, Sylvain De Leseleuc, Thierry Lahaye, and Antoine Browaeys. Synthetic three-dimensional atomic structures assembled atom by atom. *Nature*, 561(7721):79, Sep 2018.
- [164] C Simonelli, M M Valado, G Masella, L Asteria, E Arimondo, D Ciampini, and O Morsch. Seeded excitation avalanches in off-resonantly driven Rydberg gases. *Journal of Physics B: Atomic, Molecular and Optical Physics*, 49(15):154002, Jul 2016.
- [165] Fabian Letscher, Oliver Thomas, Thomas Niederprüm, Michael Fleischhauer, and Herwig Ott. Bistability Versus Metastability in Driven Dissipative Rydberg Gases. *Phys. Rev. X*, 7:021020, May 2017.
- [166] Glenn H. Fredrickson and Hans C. Andersen. Kinetic ising model of the glass transition. *Phys. Rev. Lett.*, 53:1244–1247, Sep 1984.
- [167] Juan P. Garrahan and David Chandler. Geometrical explanation and scaling of dynamical heterogeneities in glass forming systems. *Phys. Rev. Lett.*, 89:035704, Jul 2002.
- [168] Juan P. Garrahan. Aspects of non-equilibrium in classical and quantum systems: Slow relaxation and glasses, dynamical large deviations, quantum

- non-ergodicity, and open quantum dynamics. *Physica A: Statistical Mechanics and its Applications*, 504:130 – 154, 2018. Lecture Notes of the 14th International Summer School on Fundamental Problems in Statistical Physics.
- [169] Jeremy T. Young, Thomas Boulier, Eric Magnan, Elizabeth A. Goldschmidt, Ryan M. Wilson, Steven L. Rolston, James V. Porto, and Alexey V. Gorshkov. Dissipation-induced dipole blockade and antiblockade in driven Rydberg systems. *Phys. Rev. A*, 97:023424, Feb 2018.
- [170] To be published.
- [171] Fabio Franchini. *An introduction to integrable techniques for one-dimensional quantum systems*, volume 940. Springer, 2017.
- [172] Andrea De Luca and Alberto Rosso. Dynamic Nuclear Polarization and the Paradox of Quantum Thermalization. *Phys. Rev. Lett.*, 115:080401, Aug 2015.
- [173] Andrea De Luca, Inés Rodríguez-Arias, Markus Müller, and Alberto Rosso. Thermalization and many-body localization in systems under dynamic nuclear polarization. *Phys. Rev. B*, 94:014203, Jul 2016.
- [174] Henrik P. Lüschen, Pranjal Bordia, Sebastian Scherg, Fabien Alet, Ehud Altman, Ulrich Schneider, and Immanuel Bloch. Observation of slow dynamics near the many-body localization transition in one-dimensional quasiperiodic systems. *Phys. Rev. Lett.*, 119:260401, Dec 2017.
- [175] Vedika Khemani, S. P. Lim, D. N. Sheng, and David A. Huse. Critical properties of the many-body localization transition. *Phys. Rev. X*, 7:021013, Apr 2017.
- [176] B. I. Shklovskii, B. Shapiro, B. R. Sears, Panos Lambrianides, and Herbert B. Shore. Statistics of spectra of disordered systems near the metal-insulator transition. *Phys. Rev. B*, 47:11487–11490, May 1993.
- [177] Maksym Serbyn and Joel E. Moore. Spectral statistics across the many-body localization transition. *Phys. Rev. B*, 93:041424, Jan 2016.
- [178] Sabrina Maniscalco, Francesco Francica, Rosa L. Zaffino, Nicola Lo Gullo, and Francesco Plastina. Protecting entanglement via the quantum zeno effect. *Phys. Rev. Lett.*, 100:090503, Mar 2008.

- [179] Baidyanath Misra and E. C. G. Sudarshan. The Zeno's paradox in quantum theory. *Journal of Mathematical Physics*, 18(4):756–763, Aug 1977.
- [180] Wayne M. Itano, D. J. Heinzen, J. J. Bollinger, and D. J. Wineland. Quantum zeno effect. *Phys. Rev. A*, 41:2295–2300, Mar 1990.
- [181] Benjamin Everest, Michael R. Hush, and Igor Lesanovsky. Many-body out-of-equilibrium dynamics of hard-core lattice bosons with nonlocal loss. *Phys. Rev. B*, 90:134306, Oct 2014.
- [182] J J García-Ripoll, S Dürr, N Syassen, D M Bauer, M Lettner, G Rempe, and J I Cirac. Dissipation-induced hard-core boson gas in an optical lattice. *New Journal of Physics*, 11(1):013053, Jan 2009.
- [183] Pablo Sala, Tibor Rakovszky, Ruben Verresen, Michael Knap, and Frank Pollmann. Ergodicity-breaking arising from Hilbert space fragmentation in dipole-conserving Hamiltonians. *arXiv e-prints*, page arXiv:1904.04266, Apr 2019.
- [184] Paolo P. Mazza, Richard Schmidt, and Igor Lesanovsky. Vibrational dressing in kinetically constrained spin systems. *arXiv e-prints*, page arXiv:2003.00034, February 2020.
- [185] Fabricio A. Barone, Henrique Boschi-Filho, and Carlos Farina. Three methods for calculating the Feynman propagator. *American Journal of Physics*, 71(5):483–491, May 2003.
- [186] Barry R. Holstein. The harmonic oscillator propagator. *American Journal of Physics*, 66(7):583–589, Jun 1998.
- [187] Carlos M. da Fonseca and J. Petronilho. Explicit inverses of some tridiagonal matrices. *Linear Algebra and its Applications*, 325(1–3):7 – 21, Mar 2001.
- [188] Guiseppe Grosso and Guiseppe Pastori Parravicini. *Solid State Physics*. Academic Press, London, 2000.

# Appendix A

## Interacting Rydberg gases

This chapter is taken from the supplementary material in Ref. [2].

### A.1 Approximate Gaussian distribution of the atoms

Based on reference [6], we recall the ideas needed for the study of the effect of disorder. In order to show how the Gaussian distribution of the atomic positions arises, we consider an atom of mass  $m$  sitting in a one-dimensional optical trap of frequency  $\omega$ . The results are straightforward to generalize to the three-dimensional case as the three cartesian coordinates decouple and can be treated independently. We work in a regime of temperatures  $T$  much lower than the trap depth, but larger than the trap frequency, i.e.,  $k_B T \gg \omega$ . As already briefly mentioned in Section 2.4, these assumptions allow us to treat the trap as a harmonic potential, yielding a Hamiltonian

$$\hat{H}_{\text{trap}} \approx \frac{\hat{p}^2}{2m} + \frac{m}{2}\omega^2 \hat{x}^2, \quad (\text{A.1})$$

where  $\hat{x}$  and  $\hat{p}$  are the quantum position and momentum operators, respectively. The thermal state of the system is described by the Gibbs form defined as

$$\rho_{\text{th}} = \frac{1}{Z} e^{-\beta \hat{H}_{\text{trap}}}, \quad (\text{A.2})$$

where  $\beta = 1/(k_B T)$  and  $Z$  is the partition function

$$Z = \text{tr} \left\{ e^{-\beta \hat{H}_{\text{trap}}} \right\}. \quad (\text{A.3})$$

Employing the standard mapping

$$\hat{p} = i\sqrt{\frac{m\omega}{2}}(\hat{b}^\dagger - \hat{b}), \quad \hat{x} = \sqrt{\frac{1}{2m\omega}}(\hat{b}^\dagger + \hat{b}) \quad (\text{A.4})$$

in terms of bosonic creation  $\hat{b}^\dagger$  and annihilation  $\hat{b}$  operators (as usual,  $[\hat{b}, \hat{b}^\dagger] = 1$ ), one obtains for the Hamiltonian of the trap

$$\hat{H}_{\text{trap}} = \omega \left( \hat{b}^\dagger \hat{b} + \frac{1}{2} \right), \quad (\text{A.5})$$

while for the partition function, which is derived by using a geometric power series to expand Eq. (A.3), we obtain

$$Z = \sum_n e^{-\beta\omega(n+1/2)} = \frac{1}{2 \sinh(\frac{\beta\omega}{2})}. \quad (\text{A.6})$$

Introducing  $|x\rangle$ , the position eigenstate satisfying  $\hat{x}|x\rangle = x|x\rangle$ , the probability density function of the atomic position is defined as

$$p_{\text{pos}}(x) = \langle x | \hat{\rho}_{\text{th}} | x \rangle. \quad (\text{A.7})$$

The analytical form of the atomic position can be extracted from the Feynman propagator [185] which is, for a time-independent, non-relativistic system, defined as  $K(x, y, t) = \Theta(t) \langle x | e^{-it\hat{H}} | y \rangle$ , where  $\hat{H}$  is the Hamiltonian of a system and  $\Theta(t)$  is the Heaviside function. For the harmonic oscillator, the Hamiltonian in the Feynman propagator is the trap Hamiltonian (A.1). The Feynman propagator for the harmonic oscillator, in the time interval  $t \in (0, \pi/\omega)$ , is given by

$$K(x, y, t) = \sqrt{\frac{m\omega}{2\pi i \sin(\omega t)}} \exp \left\{ i \frac{m\omega}{2 \sin(\omega t)} [(x^2 + y^2) \cos(\omega t) - 2xy] \right\}. \quad (\text{A.8})$$

A detailed derivation of the propagator can be found in Refs. [185, 186]. Substituting  $t \rightarrow -i\beta$  and  $y \rightarrow x$  one finds

$$\begin{aligned} K(x, x, -i\beta) &= \langle x | e^{-\beta\hat{H}_{\text{trap}}} | x \rangle \\ &= \sqrt{\frac{m\omega}{2\pi \sinh(\omega\beta)}} \exp \left\{ -\frac{m\omega}{\sinh(\omega\beta)} (\cosh(\omega\beta) - 1) x^2 \right\}. \end{aligned} \quad (\text{A.9})$$

Dividing the propagator (A.9) by the partition function (A.3), one finally finds the Gaussian position distribution of the atom in the trap

$$\begin{aligned} p_{\text{pos}}(x) &= \sqrt{\frac{m\omega(\cosh(\omega\beta) - 1)}{\pi \sinh(\omega\beta)}} \\ &\times \exp \left\{ -\frac{m\omega}{\sinh(\omega\beta)} (\cosh(\omega\beta) - 1) x^2 \right\}. \end{aligned} \quad (\text{A.10})$$

The variance  $\sigma$  can be trivially read off and amounts to

$$\sigma^2 = \frac{\sinh(\omega\beta)}{2m\omega(\cosh(\omega\beta) - 1)}. \quad (\text{A.11})$$

Since we assumed  $k_B T \gg \omega$ , we can expand this expression to lowest order  $\omega\beta \ll 1$ , which yields

$$\sigma^2 \approx \frac{1}{m\omega^2\beta} = \frac{k_B T}{m\omega^2}. \quad (\text{A.12})$$

The distribution (A.10) is straightforward to generalize to three-dimensions with traps centered along a single linear chain at positions  $k\mathbf{R}_0 = (0, 0, kR_0)$ , where  $k$  is an integer as illustrated in Fig. 2.4,

$$p_{\text{pos}}^{(k)}(\mathbf{r}) = \frac{1}{(2\pi)^{3/2} \sigma^3} \exp\left(\frac{1}{2\sigma^2} (-r_x^2 - r_y^2 - (r_z - (k-1) \cdot R_0)^2)\right). \quad (\text{A.13})$$

For clarity, we remark here that the indices in the above expression distinguish between Cartesian components only, e.g.  $r_x$  and  $r_y$  are the components of the same atom along the  $x$  and  $y$  directions. In the following, when necessary, the trap index will appear as superscript, e.g.  $r_i^{(k)}$  is the  $i$ th component of the  $k$ th atom's position. For a ladder, a second set of position distributions  $p_{\text{pos}}^{(k)(2)}(\mathbf{r})$  would be added with the same Gaussian form up to  $r_y \rightarrow r_y - R_0$ .

This result for the distribution can also be generalized for the case of an anisotropic trapping potential

$$p_{\text{pos}}^{(k)}(\mathbf{r}) = \frac{1}{(2\pi)^{2/3} \sigma_x \sigma_y \sigma_z} \exp\left(-\frac{(r_1^{(k)})^2}{2\sigma_x^2} - \frac{(r_2^{(k)})^2}{2\sigma_y^2} - \frac{(r_z^{(k)} - kr_0)^2}{2\sigma_z^2}\right), \quad (\text{A.14})$$

where the widths  $\sigma_i = \sqrt{k_B T / (m\omega_i^2)}$  in the three spatial directions  $i = x, y, z$  depend on the trap frequencies  $\omega_i$  (see [6] for details).

## A.2 Distribution of the distances and interactions for a single chain

In this section, we derive the correlated distribution of the energy shifts between atomic pairs which is, in turn, derived from the distribution of the interatomic distances. Here, we focus on a single one-dimensional chain, as most of the properties that affect results in the later considerations are due to the presence of an extended longitudinal direction (see Chapter 4, 5 and 6). Still, the considerations made for the marginal distributions of pairs of atoms directly apply to any regular lattice configuration as well.

### A.2.1 From the distribution of the atomic positions to the distribution of the distances

To begin with, we consider a one-dimensional system where we neglect the extension of the traps in the  $y$  and  $z$  directions. At the end of this section, we generalize the results to three dimensions. The one-dimensional distribution of a single atom is given by

$$p_{\text{pos}}^{(k)}(x) = \frac{1}{\sqrt{2\pi}\sigma} \exp\left[-\frac{x^2}{2\sigma^2}\right]. \quad (\text{A.15})$$

From here, we can determine the distribution of the interatomic distances by solving the following integrals

$$\begin{aligned} p_{\text{diff}}(d_1, \dots, d_{L-1}) &= \int dx_1 \dots dx_L \prod_{k=1}^L p_{\text{pos}}^{(k)}(x) \prod_{k'=1}^{L-1} \delta(d_{k'} - (x_{k'+1} - x_{k'})) \\ &= \frac{1}{(\sqrt{2\pi}\sigma)^L} \int dx_1 \dots dx_L \exp\left(-\frac{1}{2\sigma^2} \sum_{k=1}^L x_k^2\right) \\ &\quad \times \prod_{k'=1}^{L-1} \delta(d_{k'} - (x_{k'+1} - x_{k'})). \end{aligned}$$

Integrating out each of the  $L - 1$  delta-distributions  $dx_2 \dots dx_L$ , with the integration variable  $x_{k'+1} = x_1 + \sum_{m=1}^{k'} d_m$ , leaves the Gaussian integral

$$p_{\text{diff}}(d_1, \dots, d_{L-1}) = \frac{1}{(\sqrt{2\pi}\sigma)^L} \int dx_1 e^{-\frac{1}{2\sigma^2}(Lx_1^2 + 2Dx_1 + A)}, \quad (\text{A.16})$$

with the parameters  $D = \sum_{m=1}^{L-1} (L - m) d_m$ , and  $A = \sum_{k=1}^L \left(\sum_{m=1}^{k-1} d_m\right)^2$ . This integral can be easily solved

$$p_{\text{diff}} = \frac{\exp\left(-\frac{1}{2\sigma^2} \left(A - \frac{D^2}{L}\right)\right)}{\sqrt{L}(\sqrt{2\pi}\sigma)^{L-1}}. \quad (\text{A.17})$$

In order to simplify the solution, we rewrite  $A - D^2/L = \sum_{r,q} d_r M_{rq} d_q$ , using

$$\frac{D^2}{L} = \frac{1}{L} \sum_{r=1}^{L-1} \sum_{q=1}^{L-1} (L-r)(L-q) d_r d_q, \quad (\text{A.18})$$

$$A = \sum_{l=1}^{L-1} \left(\sum_{n=1}^{l-1} d_n\right) \left(\sum_{n'=1}^{l-1} d_{n'}\right), \quad (\text{A.19})$$

which directly follows from the definition of the parameters. Considering only ordered terms,  $d_r d_q$  terms satisfying  $(l > r) \wedge (l > q)$  contribute to the sum,

each with a contribution of one, we obtain

$$A = \sum_{r=1}^{L-1} \sum_{q=1}^{L-1} (L - \max(r, q)) d_r d_q. \quad (\text{A.20})$$

This results in the following expression for  $M_{rq}$ ,

$$M_{rq} = L - \max(r, q) - \frac{1}{L}(L - r)(L - q) = (L - \max(r, q)) \min(r, q)/L. \quad (\text{A.21})$$

In three dimensions, the joint distribution of the differences  $\mathbf{d}_k = \mathbf{r}_{k+1} - \mathbf{r}_k = (d_{k,x}, d_{k,y}, d_{k,z})$  can be found in the supplemental material of Ref. [6] and, for isotropic traps, reads

$$\begin{aligned} p_{\text{diff}}(\mathbf{d}_1, \dots, \mathbf{d}_{L-1}) &= \int \left[ \prod_{k=1}^L d^3 r_k p_{\text{pos}}^{(k)}(\mathbf{r}_k) \right] \left[ \prod_{k'=1}^{L-1} \delta^{(3)}(\mathbf{d}_{k'} - (\mathbf{r}_{k'+1} - \mathbf{r}_{k'})) \right] \\ &= \left[ \frac{\sigma^{1-L}}{\sqrt{L} (\sqrt{2\pi})^{L-1}} \right]^3 e^{-\frac{1}{2\sigma^2} \sum_{\mu,q} [d_{\mu,x} M_{\mu q} d_{q,x} + d_{\mu,y} M_{\mu q} d_{q,y} + (d_{\mu,z} - R_0) M_{\mu q} (d_{q,z} - R_0)]}. \end{aligned} \quad (\text{A.22})$$

The correlation properties between different components  $d_{k,i}$  can be worked out via the inverse of the tridiagonal matrix  $M$  [187]

$$C = M^{-1} = \begin{pmatrix} 2 & -1 & 0 & 0 & & \\ -1 & 2 & -1 & 0 & & \\ 0 & -1 & 2 & -1 & \dots & \\ 0 & 0 & -1 & 2 & & \\ & & \vdots & & \ddots & \end{pmatrix}, \quad (\text{A.23})$$

implying,

$$\langle d_{k,i} d_{q,j} \rangle - \langle d_{k,i} \rangle \langle d_{q,j} \rangle = \sigma^2 \delta_{ij} (2\delta_{k,q} - \delta_{k,q+1} - \delta_{k,q-1}). \quad (\text{A.24})$$

Adjacent distances are therefore (anti-)correlated, which can be easily understood by considering a system of three atoms. Moving the middle atom closer to the left atom increases the distance to the right atom. These correlations therefore also exist in any (non-trivial) function of the distances, a notable example being the energy displacements  $\delta V_k = V(d_k) - V(R_0)$ . As a consistency check, we remark that  $C(L)$  is an  $(L-1) \times (L-1)$  matrix, whose determinant satisfies the recursion relation

$$\det C(L) = 2 \det C(L-1) - \det C(L-2) \quad (\text{A.25})$$

with ‘‘seed’’ (or ‘‘initial conditions’’)  $\det C(2) = 2$  and  $\det C(3) = 3$ , which is solved by  $\det C(L) = L$ . Consequently, the factor  $(\det M)^{3/2}$  produced by the Gaussian integration over all variables exactly cancels the factor  $L^{-3/2}$  appearing in the normalization, as expected.

### A.2.2 Marginal distribution for a single pair of atoms

Each  $\mathbf{d}_k$  is drawn from an identical distribution and so we can select one, dropping the subscript for simplicity, and integrate over the remaining  $L - 2$  variables from equation (A.22), which yields for a chain along the  $z$ -direction

$$\begin{aligned} p_{\text{diff}}(\mathbf{d}) &= \frac{1}{(4\pi)^{3/2}\sigma^3} e^{-\frac{1}{4\sigma^2}[d_x^2+d_y^2+(d_z-R_0)^2]} \\ &= \frac{1}{(4\pi)^{3/2}\sigma^3} e^{-\frac{1}{4\sigma^2}[d^2+R_0^2-2d_zR_0]}, \end{aligned} \quad (\text{A.26})$$

where  $d = |\mathbf{d}|$  denotes the distance between a pair of neighboring atoms. The distribution for this new variable can then be obtained from a solid angle integration with the Jacobi determinant  $dA = d^2 \sin \theta d\theta d\phi$ , and reads

$$\begin{aligned} p_{\text{dist}}(d) &= \frac{d^2}{4\sqrt{\pi}\sigma^3} e^{-\frac{1}{4\sigma^2}(d^2+R_0^2)} \int_0^\pi d\theta \sin \theta e^{-\frac{R_0 d \cos \theta}{2\sigma^2}} \\ &= \frac{d}{\sqrt{\pi}\sigma R_0} e^{-\frac{1}{4\sigma^2}(d^2+R_0^2)} \sinh\left(\frac{R_0 d}{2\sigma^2}\right). \end{aligned} \quad (\text{A.27})$$

From this, the distribution of an energy shift  $\delta V = V(r) - V(R_0)$  can be found via a change of variables,  $d \rightarrow d(\delta V)$ , according to

$$P(\delta V) = |d'(\delta V)| p_{\text{dist}}(d(\delta V)). \quad (\text{A.28})$$

Though we keep the interaction exponent  $\alpha$  generic, we will assume long-range ( $\alpha = 1$ , see Chapter 6), dipole-dipole ( $\alpha = 3$ , see Chapter 5) or van der Waals ( $\alpha = 6$ , see Chapter 4, 6) behavior in our later considerations, resulting in

$$d(\delta V) = \left( \frac{C_\alpha}{V_0 + \delta V} \right)^{\frac{1}{\alpha}}, \quad (\text{A.29})$$

where  $V_0 = C_\alpha/R_0^\alpha$ , which implies

$$d'(\delta V) = -\frac{1}{\alpha} \frac{C_\alpha^{1/\alpha}}{(V_0 + \delta V)^{1+1/\alpha}}. \quad (\text{A.30})$$

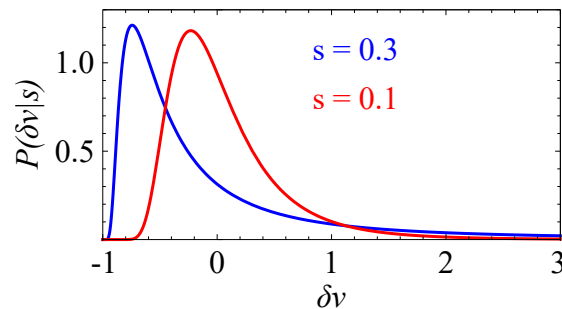


**Figure A.1: Distribution of energy shifts.** Probability distribution function for the dimensionless energy shift (A.32) for  $s = 0.3$  (blue) and  $s = 0.1$  (red).

Hence, the distribution of energy shifts for a pair of atoms in the Rydberg state is

$$P(\delta V|V_0, R_0, \sigma) = \frac{R_0}{\sigma\alpha\sqrt{\pi}V_0} \left(1 + \frac{\delta V}{V_0}\right)^{-(1+\frac{2}{\alpha})} \sinh \left[ \frac{R_0^2}{2\sigma^2} \left(1 + \frac{\delta V}{V_0}\right)^{-\frac{1}{\alpha}} \right] \\ \times \exp \left( -\frac{R_0^2}{4\sigma^2} \left[ 1 + \left(1 + \frac{\delta V}{V_0}\right)^{-\frac{2}{\alpha}} \right] \right). \quad (\text{A.31})$$

It is relatively simple to see that, if we define the dimensionless quantities  $\delta v = \delta V/V_0$  and  $s = \sigma/R_0$ , we can simplify this expression further

$$P(\delta v|s) = \frac{\exp \left( -\frac{1}{4s^2} \left[ 1 + (1 + \delta v)^{-\frac{2}{\alpha}} \right] \right)}{\alpha\sqrt{\pi}s(1 + \delta v)^{1+\frac{2}{\alpha}}} \sinh \left[ \frac{1}{2s^2} (1 + \delta v)^{-\frac{1}{\alpha}} \right]. \quad (\text{A.32})$$

The probability distribution function in Eq. (A.32) (see Fig. A.1) is defined in the domain  $\delta v \in [-1, +\infty)$ . For  $\delta v = -1 + \varepsilon$ , in the limit  $\varepsilon \rightarrow 0^+$ , it behaves as

$$P(\delta v|s) \propto \varepsilon^{-1-\frac{2}{\alpha}} \exp \left( -\frac{\varepsilon^{-\frac{2}{\alpha}}}{4s^2} \right) \sinh \left[ \frac{\varepsilon^{-\frac{1}{\alpha}}}{2s^2} \right] \rightarrow 0, \quad (\text{A.33})$$

as the (vanishing) exponential factor dominates. In the opposite limit  $\delta v \rightarrow \infty$ , the distribution behaves asymptotically as

$$P(\delta v|s) \approx \frac{1}{2\alpha\sqrt{\pi}s^3} e^{-\frac{1}{4s^2}} \delta v^{-1-3/\alpha}, \quad (\text{A.34})$$

showing that this distribution is fat-tailed. In particular, all moments of the distribution  $\langle \delta v^\beta \rangle$  with  $\beta \geq 3/\alpha$  are undefined. For both  $\alpha = 3$  and  $\alpha = 6$ , this includes both the mean and variance. These fat tails are the consequence of the approximation of the position distribution of an atom as a Gaussian everywhere in space, i.e., including points much further away from the center of a trap than several  $\sigma$ . In other words, it appears to be an artifact of the description, rather than a genuine feature of the system that would be found in a real experiment. The result of this approximation is to allow for an extremely small (but non-vanishing) probability that two atoms can be arbitrarily close, which, due to the algebraic scaling of the interactions, produces considerable energy shifts. Moments like the mean and variance are therefore dominated by the rare events in which two atoms lie very close to each other. The rarity of such events is encoded in the exponential suppression  $e^{-(1/4s^2)}$  in Eq. (A.34). In principle, these unphysical fat tails could affect theoretical predictions.

An important difference with our model is that the fat tails are strongly suppressed and one needs to assess how likely it is to actually probe them in a

simulation. Experiments will not probe them since they work with the “true” distribution and are not affected by the Gaussian approximation. For that purpose, let us first notice that the asymptotic behavior reported in (A.34) emerges when the argument of the sinh-function in Eq. (A.32) is small, i.e., still assuming  $\delta v \gg 1$ , for

$$\delta v \gg (2s^2)^{-\alpha}. \quad (\text{A.35})$$

The probability of generating an energy shift within the tails is

$$\mathbb{P}_s \equiv \mathbb{P} \left( \delta v > (2s^2)^{-\alpha} \right) = \int_{(2s^2)^{-\alpha}}^{\infty} d\delta v P(\delta v|s). \quad (\text{A.36})$$

Employing the asymptotic expression (A.34), we obtain

$$\mathbb{P}_s = \mathbb{P} \left( \delta v > (2s^2)^{-\alpha} \right) \approx \frac{4s^3}{3\sqrt{\pi}} e^{-\frac{1}{4s^2}}. \quad (\text{A.37})$$

This result suggests that  $\mathbb{P}_s$  does not depend on  $\alpha$ , but one should remember that the derivation assumes  $\delta v \gg 1$ , and is therefore only consistent if  $(2s^2)^{-\alpha} \gg 1$ . This assumption is satisfied already for  $\alpha = 3$  or  $6$  for rather large disorder amplitudes, e.g.,  $s = 0.3$ , which then yields  $\mathbb{P}_{0.3} \approx 0.0013$ . Due to the exponential factor, these probabilities decrease incredibly fast with increasing  $s$ . For instance, when  $s = 0.1$ , we get  $\mathbb{P}_{0.1} \approx 10^{-14}$ . For the values considered in Chapter 5,  $s \leq 5 \times 10^{-4}$ , this becomes  $\mathbb{P}_s \ll 10^{-400000}$ , which is clearly impossible to observe in any reasonable numerical procedure. Hence, we can safely assume the unphysical fat tails to be completely irrelevant in any sensible numerical simulation using the Gaussian approximation in this regime.

# Appendix B

## Non-Adiabatic quantum state preparation and quantum state transport

This chapter is taken from the supplementary material in Ref. [1].

### B.1 Toffoli gate

The basic building block of the protocols studied in Chapter 4 is the three-body Hamiltonian (4.10) and the associated unitary gate (4.11). The latter provides a tool to implement various three-body gates, where the specific properties of the gate are determined by the parameters of the Hamiltonian, namely the detuning  $\Delta_k$ , Rabi frequency  $\Omega_k$  and the duration of the pulse  $t_k$  on  $k$ -th atom. In the specific case, where  $\Delta_k = 0$  for all atoms, and the area of the pulse applied to the  $k$ -th atom is  $\Omega_k t_k = \pi$ , the unitary (4.11) corresponds to the Toffoli gate.

Here, in Table B.1, we list for completeness the properties of the Toffoli gate used in the quantum state transport protocol. The first and last qubits are the control ones while the second qubit is the target. Provided that both control qubits are in state  $|0\rangle$  the Toffoli gate acts like a  $\pi$ -pulse on the target qubit.

Input	Output
000	010
001	001
010	000
011	011
100	100
101	101
110	110
111	111

**Table B.1:** Truth table of the Toffoli gate. The first and the third qubits are the control qubits, while the second qubit is the target. When the control qubits are both in the ground state  $|0\rangle$ , the Toffoli gate corresponds to an application of a  $\pi$ -pulse on the target qubit.

## B.2 Dimer-MPS

### B.2.1 Derivation of the recurrence formulae

We discuss here how to retrieve a recursion formula for the areas  $A_k$  in the case where an excitation blocks its first  $R_b$  neighbors to the right and to the left. Equation (4.23) will correspond to the particular case  $R_b = 1$ . We start by recalling that the target state is expressed as

$$|z\rangle = \frac{1}{\sqrt{Z_z}} \prod_{k=1}^L \left( \mathbb{1} + z \hat{P}_{k,\text{left}} \hat{\sigma}_k^+ \hat{P}_{k,\text{right}} \right) |\downarrow \dots \downarrow\rangle, \quad (\text{B.1})$$

where  $\hat{P}_{k,\text{left}} = \hat{P}_{k-1} \dots \hat{P}_{k-R}$  and  $\hat{P}_{k,\text{right}} = \hat{P}_{k+1} \dots \hat{P}_{k+R_b}$ . The action of a local pulse on the  $k$ -th atom depends on whether the latter is blockaded (i.e. there are excitations within a radius  $R_b$ ) or not. In the former case, we have

$$\hat{U}_k^{01}(A_k) |0_k\rangle = |0_k\rangle. \quad (\text{B.2})$$

Conversely, if the atom is not blockaded,

$$\hat{U}_k^{01}(A_k) |0_k\rangle = \cos A_k |0_k\rangle + \sin A_k |1_k\rangle. \quad (\text{B.3})$$

We now think of applying an ordered sequence of these unitary operations addressing one atom at a time, from the first to the last  $\hat{U} = \prod_{k=N}^1 \hat{U}_k^{01}$ , to a ground-state configuration  $|0_1 \dots 0_N\rangle$ . This will yield a state with components

on all configurations in which no pairs of excitations appear at a distance  $\leq R_b$ . Note that, according to (B.3), the ground state configuration will come with a coefficient

$$C_0 \equiv \prod_{k=N}^1 \cos A_k. \quad (\text{B.4})$$

Every configuration with an excitation in site  $j$  will instead feature a factor  $\sin A_j$ . Furthermore, because of the blockade, the operations acting on  $j = k+1, \dots, k+R_b$  will behave as displayed in (B.2), i.e. they will trivially contribute 1 to the overall coefficient. In general, we can reconstruct the coefficient of a generic configuration via the following simple rules:

- (i) Choose a configuration and start reading it from the first atom to be addressed to the last one. Assign a coefficient 1 to start with.
- (ii) Until a  $|1_k\rangle$  is found, for every  $|0_k\rangle$  multiply the coefficient by  $\cos A_k$ .
- (iii) When a  $|1_k\rangle$  is found, multiply by  $\sin A_k$  and skip to position  $k + R_b + 1$ .
- (iv) Apply (ii) again.

Hence, if we call  $C_j^{(1)}$  the coefficient of the configuration with a single excitation in site  $j$  we have

$$\frac{C_j^{(1)}}{C_0} = \frac{\sin A_j}{\prod_{k=j}^{j+R_b} \cos A_k}. \quad (\text{B.5})$$

More general, the coefficient  $C^{(\vec{n})}$  of an allowed state with  $n$  excitations in positions  $\vec{n} = \{j_1, \dots, j_n\}$  will obey

$$\frac{C^{(\vec{n})}}{C_0} = \prod_{\mu=1}^n \frac{\sin A_{j_\mu}}{\prod_{k=j_\mu}^{j_\mu+R_b} \cos A_k}. \quad (\text{B.6})$$

The correct form of state  $|z\rangle$  is then reproduced by fixing the areas in such a way that

$$\frac{\sin A_j}{\prod_{k=j}^{j+R_b} \cos A_k} = z \quad \forall j. \quad (\text{B.7})$$

This defines a recursion for  $A_j$  in terms of  $A_{j+1}, \dots, A_{j+R}$ . In order to make the solution of the recursion unique, we need to also impose the boundary conditions

$$\cos A_{N+j} = 1 \quad \forall 1 \leq j \leq R_b. \quad (\text{B.8})$$

Note that the recursion relation can be also cast in the form

$$\tan A_j = z \prod_{k=j+1}^{j+R_b} \cos A_k. \quad (\text{B.9})$$

Since the tan function is  $\pi$ -periodic, we have the freedom to choose the sign of the cosines, which we choose to be positive. This means that the sign of the sines will instead coincide with the sign of the parameter  $z$ . This uniquely identifies the areas  $A_k$  modulo  $2\pi$ .

### Nearest-neighbor case

Here, we solve the recursion relation (4.23) in the simplest case  $R_b = 1$ . By defining

$$x_k = \cos^2 A_{L+1-k}, \quad (\text{B.10})$$

and  $a = z^2$  we find

$$x_{k+1} = \frac{1}{1 + a x_k}, \quad (\text{B.11})$$

with the initial condition  $x_0 = 1$ . We now rewrite  $x_k = p_k/q_k$ , which yields

$$\frac{p_{k+1}}{q_{k+1}} = \frac{q_k}{q_k + a p_k}, \quad (\text{B.12})$$

and assume that we can separate numerator and denominator as if they were independent, resulting in

$$p_{k+1} = q_k \quad (\text{B.13})$$

$$q_{k+1} = q_k + a q_{k-1}. \quad (\text{B.14})$$

In order to correctly reproduce the boundary condition for  $x_k$ , we ask  $q_0 = q_{-1} = p_0 = 1$ . Since  $a \geq 0$ , we see that if  $q_k > 0$  and  $q_{k-1} > 0$ , then  $q_{k+1} > 0$  as well. Given the initial conditions, it follows from induction that  $q_k > 0 \forall k$ . Furthermore, as expected we find that

$$q_{k+1} \geq q_k = p_{k+1}, \quad (\text{B.15})$$

since by definition  $x_k = p_k/q_k = q_{k-1}/q_k$  must be  $\leq 1$ .

The recursion equation for  $q_k$  is linear and can be solved exactly: the associated polynomial is  $\lambda^2 - \lambda - a$ , with

$$\lambda_{\pm} = \frac{1 \pm \sqrt{1 + 4a}}{2}. \quad (\text{B.16})$$

Therefore, the general solution is

$$q_k = A \lambda_+^k + B \lambda_-^k, \quad (\text{B.17})$$

with  $A$  and  $B$  fixed via the boundary conditions  $q_{-1} = q_0 = 1$ , which yields

$$A = \frac{1 + 2a + \sqrt{1 + 4a}}{2\sqrt{1 + 4a}} = \frac{1}{\sqrt{1 + 4a}} \left( \frac{1 + \sqrt{1 + 4a}}{2} \right)^2$$

$$B = \frac{-1 - 2a + \sqrt{1 + 4a}}{2\sqrt{1 + 4a}} = -\frac{1}{\sqrt{1 + 4a}} \left( \frac{1 - \sqrt{1 + 4a}}{2} \right)^2.$$

Using this result for  $A$  and  $B$ , we find

$$q_k = \frac{1}{\sqrt{1 + 4a}} \left[ \left( \frac{1 + \sqrt{1 + 4a}}{2} \right)^{k+2} - \left( \frac{1 - \sqrt{1 + 4a}}{2} \right)^{k+2} \right], \quad (\text{B.18})$$

and, consequently,

$$x_k = \frac{p_k}{q_k} = \frac{\left( \frac{1 + \sqrt{1 + 4a}}{2} \right)^{k+1} - \left( \frac{1 - \sqrt{1 + 4a}}{2} \right)^{k+1}}{\left( \frac{1 + \sqrt{1 + 4a}}{2} \right)^{k+2} - \left( \frac{1 - \sqrt{1 + 4a}}{2} \right)^{k+2}}$$

$$= 2 \frac{(1 + \sqrt{1 + 4a})^{k+1} - (1 - \sqrt{1 + 4a})^{k+1}}{(1 + \sqrt{1 + 4a})^{k+2} - (1 - \sqrt{1 + 4a})^{k+2}}, \quad (\text{B.19})$$

which exactly corresponds to Eq. (4.25), since we have chosen the cosines to be positive.

### Generic $R_b$ case

The general case is defined by

$$x_{k+1} = \frac{1}{1 + a \prod_{j=k}^{k+1-R_b} x_j}. \quad (\text{B.20})$$

The same trick as above can be applied  $x_k = p_k/q_k$ , resulting in

$$\frac{p_{k+1}}{q_{k+1}} = \frac{\prod_{j=k}^{k+1-R_b} q_j}{\prod_{j=k}^{k+1-R_b} q_j + a \prod_{j=k}^{k+1-R_b} p_j}. \quad (\text{B.21})$$

The same choice  $p_k = q_{k-1}$  gives

$$q_{k+1} = q_k + a q_{k-R_b}, \quad (\text{B.22})$$

which is associated with the polynomial

$$\lambda^{R_b+1} = \lambda^{R_b} + a, \quad (\text{B.23})$$

and cannot be solved analytically. However, it has  $R_b + 1$  (complex) roots  $\lambda_j$  and the general implicit solution of the recursion is

$$q_k = \sum_{j=1}^{R_b+1} A_j \lambda_j^k. \quad (\text{B.24})$$

Imposing the boundary conditions yields a system of equations for the coefficients  $A_j$  with equations of the form

$$\sum_{j=1}^{R_b+1} \frac{A_j}{\lambda_j^n} = 1, \quad (\text{B.25})$$

for  $n = -R_b, \dots, 0$ . This can be also written as

$$\sum_{j=1}^{R_b+1} M_{nj} A_j = 1 \quad \forall n, \quad (\text{B.26})$$

where  $M_{nj}$  is a matrix with entries  $M_{nj} = \lambda_j^{-n}$ , i.e. it is a Vandermonde matrix having a geometric progression in each row. By using Cramer's rule for the solution of linear systems of equations, we can write the coefficient  $A_k$  as

$$A_k = \frac{\det M^{(k)}}{\det M}, \quad (\text{B.27})$$

where  $M^{(k)}$  is constructed from  $M$  by substituting 1 to all entries on the  $k$ -th column. Note that  $M^{(k)} = M$  if  $\lambda_k = 1$ , which means that  $M^{(k)}$  is also a Vandermonde matrix. Exploiting the known structure of the determinants of Vandermonde matrices we can thus write

$$A_k = \frac{\prod_{1 \leq i < j \leq R_b+1} \left( \frac{1}{\lambda_j^{(k)}} - \frac{1}{\lambda_i^{(k)}} \right)}{\prod_{1 \leq i < j \leq R_b+1} \left( \frac{1}{\lambda_j} - \frac{1}{\lambda_i} \right)}, \quad (\text{B.28})$$

where  $\lambda_j^{(k)} = \lambda_j$  if  $j \neq k$  and 1 otherwise. By simplifying all common factors, this can also be rewritten as

$$A_k = \lambda_k^R \frac{\prod_{j \neq k} (1 - \lambda_j)}{\prod_{j \neq k} (\lambda_k - \lambda_j)}. \quad (\text{B.29})$$

# Appendix C

## Synthetic lattices, flat bands and localization in Rydberg quantum simulators

This chapter is taken from the supplementary material in Ref. [2].

### C.1 Bound on the number of flat bands

We provide an account of the lower bound of the number of flat bands  $n_{\text{flat}} \geq |n_1 - n_2|$  mentioned in the main text. We recall that  $n_{\text{flat}}$  denotes the number of flat bands in the model,  $n_1$  the number of one-particle states per unit cell and  $n_2$  the number of pair states per unit cell. Before working out the bound however, we briefly comment on the fact that the spectrum of the hopping Hamiltonians (5.18) is always symmetric with respect to  $\epsilon = 0$ . In fact, one can define the parity transformation

$$\hat{U} = \hat{U}^\dagger = (-1)^{\sum_k \hat{n}_k} \quad (\text{C.1})$$

which, in the subspace  $\mathcal{H}_1$ , acts according to  $\hat{U} |M_k\rangle = -|M_k\rangle$  on all one-excitation states and  $\hat{U} |N_{kq}\rangle = |N_{kq}\rangle$  on all pair states. Combined with Eqs. (5.26a)-(5.26c), this implies  $\hat{U}^\dagger \hat{H}_{\mathcal{H}_1} \hat{U} = -\hat{H}_{\mathcal{H}_1}$ . Hence, if  $|\epsilon\rangle$  is an eigenvector of the Hamiltonian at energy  $\epsilon$ , then  $\hat{U} |\epsilon\rangle$  is also an eigenvector, but at eigenvalue  $-\epsilon$ , proving the symmetry of the spectrum under reflection  $\epsilon \rightarrow -\epsilon$ .

We start directly from the synthetic lattice reconstructed in the Hilbert space according to the procedure described in the previous section. This structure is not in general a Bravais lattice and needs, as a first step, to be reduced to one

by identifying an appropriate “basis”. This is a standard procedure in crystallography and solid state physics and we refer the reader to any good introductory textbook (see e.g., [188]). For the reader’s convenience, we however recall here just a few of the most basic concepts: a Bravais lattice is a lattice structure where the positions  $\vec{l}$  of the lattice sites can be written as discrete combinations

$$\vec{l} = \sum_{i=1}^d z_i \vec{a}_i \quad \text{with } z_i \in \mathbb{Z}. \quad (\text{C.2})$$

of a set of  $d$  linearly-independent *primitive lattice vectors*  $\vec{a}_i$  ( $i = 1 \dots d$ ), where  $d$  is the dimensionality of the system. If a site is chosen as the origin, all sites can be found this way and all points at positions  $\vec{l}$  are lattice sites. Any lattice is, by definition, a periodically repeating pattern, and is therefore invariant under a certain set of translations by  $\vec{l}$  for some specific choice of the primitive lattice vectors. However, in many cases an additional set of  $B$  vectors  $\{\vec{b}_1, \dots, \vec{b}_B\}$ , called “basis”, is required. In such cases, and fixing conventionally  $\vec{b}_1 = 0$  which can be done without loss of generality, if one lattice point is located at the origin, every point at a position  $\vec{l}$  is also a lattice site, but not all lattice sites are at positions  $\vec{l}$ . All of them are instead found at positions  $\vec{l} + \vec{b}_j$  with  $j = 1, \dots, B$ . We also remark that distances between sites in the synthetic lattice are not meaningful, being just a convenient way to visualize the structure of the Hilbert space. Hence, we are free to rescale the length of all (dimensionless) vectors  $\vec{a}_i, \vec{b}_j$  by a common factor. In all the examples discussed below the primitive lattice vectors have the same length and we shall choose to normalize them to unit length ( $|\vec{a}_i| = 1$ ). Also, for brevity in the following we refer to the  $\mathbb{R}^d$  space where these vectors live as the *direct space*.

We also introduce the reciprocal lattice vectors  $\vec{a}_i^*$ ,  $i = 1 \dots d$  which satisfy the defining relations

$$\vec{a}_i^* \cdot \vec{a}_j = 2\pi \delta_{ij}. \quad (\text{C.3})$$

The reciprocal Bravais lattice is then reconstructed by taking integer combinations of these vectors, i.e.,

$$\vec{G} = \sum_{i=1}^d z_i^* \vec{a}_i^* \quad \text{with } z_i^* \in \mathbb{Z}. \quad (\text{C.4})$$

We define a unit cell  $\mathcal{U}^*$  which contains only one reciprocal lattice point. All possible translations  $\vec{G}$  of  $\mathcal{U}^*$  cover the whole space  $\mathbb{R}^d$  without any overlaps. It can be visualized as a tessellation with tile  $\mathcal{U}^*$ . From a slightly different (but equivalent) perspective, one can define the equivalence relation between vectors

$\vec{k}, \vec{q} \in \mathbb{R}^d$  living in reciprocal space

$$\vec{k} \sim \vec{q} \Leftrightarrow \exists \vec{G} \mid \vec{k} = \vec{q} + \vec{G} \quad (\text{C.5})$$

with  $\vec{G}$  a *reciprocal lattice* vector. Hence, the unit cell may be defined as a quotient  $\mathbb{R}^d / \sim$ . By defining quasi-momenta  $\vec{k}$  as reciprocal space vectors belonging to a unit cell  $\mathcal{U}^*$ , one can define a Fourier series in the usual way for any generic quantity  $A_{\vec{l}}$  living on the direct-space Bravais lattice

$$\tilde{A}_{\vec{k}} = \sum_{\vec{l}} e^{-i\vec{k} \cdot \vec{l}} A_{\vec{l}}. \quad (\text{C.6})$$

The corresponding inverse transform is also standard:

$$A_{\vec{l}} = \int_{\mathcal{U}^*} \frac{d^d k}{(2\pi)^d} e^{i\vec{k} \cdot \vec{l}} \tilde{A}_{\vec{k}}, \quad (\text{C.7})$$

as can be shown remembering that

$$\frac{\vec{G} \cdot \vec{l}}{2\pi} \in \mathbb{Z} \quad (\text{C.8})$$

and using the Poisson-summation-derived distributional identity

$$\sum_{z \in \mathbb{Z}} e^{-i\alpha z} = \sum_{m \in \mathbb{Z}} 2\pi \delta(\alpha + 2\pi m), \quad (\text{C.9})$$

with  $\alpha \in \mathbb{R}$  and  $\delta$  the Dirac delta. The choice of the unit cell is not unique; in the following we assume to be working in the *first Brillouin zone*  $\mathcal{B}$  [188].

Clearly, the definitions above do not hinge upon working in a specific space and, indeed, one can analogously define a unit cell in direct space which contains a single Bravais lattice point. Hence, such a unit cell includes  $B$  synthetic lattice points. It is quite natural to subdivide them according to whether they are of the “one-excitation” or “pair” kind. As done in the main text, we define  $n_1$  the number of one-excitation states in a unit cell and  $n_2 = B - n_1$  the number of pair ones. For example,

- Synthetic square lattice (Lieb lattice):  $n_1 = 1, n_2 = 2, B = 3$ .
- Synthetic triangular lattice:  $n_1 = 1, n_2 = 3, B = 4$ .
- Synthetic honeycomb lattice:  $n_1 = 2, n_2 = 3, B = 5$ .

Since each synthetic lattice point can be uniquely associated to a given primitive lattice vector  $\vec{l}$  and basis vector  $\vec{b}_i$ , we can unambiguously denote each

state in the Hilbert subspace  $\mathcal{H}_1$  as a tensor product  $|\vec{l}\rangle \otimes |\vec{b}_i\rangle$ . For later convenience, we introduce now a new notation distinguishing between the basis vectors identifying one-excitation states  $(|\vec{b}_i\rangle \rightarrow |\mu_j\rangle, j = 1, \dots, n_1)$  and pair states  $(|\vec{b}_i\rangle \rightarrow |\nu_j\rangle, j = 1, \dots, n_2)$ , so that the space of basis states is equivalently generated as

$$\text{Span} \{ |\mu_1\rangle, \dots, |\mu_{n_1}\rangle, |\nu_1\rangle, \dots, |\nu_{n_2}\rangle \}. \quad (\text{C.10})$$

Consequently, there is a bijective correspondence between states  $|M_k\rangle$  and states  $|\vec{l}\rangle \otimes |\mu_i\rangle$  and between states  $|N_{kq}\rangle$  and states  $|\vec{l}\rangle \otimes |\nu_i\rangle$ .

We also define the lattice translation operator  $T_{\vec{j}}$ , where  $\vec{j}$  is a Bravais lattice vector, which acts on the positional degrees of freedom according to

$$T_{\vec{j}}|\vec{l}\rangle = |\vec{l} + \vec{j}\rangle. \quad (\text{C.11})$$

By the straightforward quasi-momentum states definition

$$|\vec{k}\rangle = \sum_{\vec{l}} e^{-i\vec{k}\cdot\vec{l}} |\vec{l}\rangle \quad (\text{C.12})$$

one also gets

$$T_{\vec{j}}|\vec{k}\rangle = e^{i\vec{k}\cdot\vec{j}} |\vec{k}\rangle. \quad (\text{C.13})$$

The Hamiltonian can now be generically characterized as a sum of terms

$$\begin{aligned} \hat{H}_{\mathcal{H}_1} = \Omega \sum_{\vec{l}} \sum_{\vec{j}} \sum_{m=1}^{n_1} \sum_{n=1}^{n_2} & \left( C_{\vec{j},m,n} |\mu_m\rangle \langle \nu_n| + \right. \\ & \left. + D_{\vec{j},m,n} |\nu_n\rangle \langle \mu_m| \right) |\vec{l} + \vec{j}\rangle \langle \vec{l}|, \end{aligned} \quad (\text{C.14})$$

where  $C_{\vec{j}}$  and  $D_{\vec{j}}$  are collections of connectivity matrices with elements 1 (if two states are linked) and 0 (if the two states are not). For instance, if the Hamiltonian can cause a hop from  $\vec{l}$  to  $\vec{l} + \vec{a}_1$  accompanied by a change  $|\mu_1\rangle \rightarrow |\nu_1\rangle$ , then  $D_{\vec{a}_1,1,1} = 1$ . Note that these are, in general, rectangular matrices of size  $n_1 \times n_2$ . Furthermore, to ensure that  $H$  is Hermitian they must satisfy

$$C_{-\vec{j},m,n} = D_{\vec{j},m,n}^* = D_{\vec{j},m,n}, \quad (\text{C.15})$$

where the last equality comes from the fact that they are defined to be real (their elements being either 0 or 1). Note that no terms  $\propto |\mu_m\rangle \langle \mu_n|$  or  $|\nu_m\rangle \langle \nu_n|$  appear, as one-excitation states are exclusively connected to pair ones and vice versa (see Eqs. (5.26a)-(5.26c)). Neither  $C$  nor  $D$  depends explicitly on  $\vec{l}$ , as the form of the Hamiltonian is independent of the choice of the origin. In this form, it is not difficult to exploit this symmetry of the Hamiltonian under discrete lattice translations to partially diagonalize it in terms of Fourier modes:

$$\begin{aligned}
\hat{H}_{\mathcal{H}_1} &= \Omega \sum_{\vec{l}} \sum_{\vec{j}} \sum_{m=1}^{n_1} \sum_{n=1}^{n_2} \left( C_{\vec{j},m,n} |\mu_m\rangle \langle \nu_n| + C_{-\vec{j},m,n} |\nu_n\rangle \langle \mu_m| \right) T_{\vec{j}} |\vec{l}\rangle \langle \vec{l}| \\
&= \Omega \sum_{\vec{j}} \sum_{m=1}^{n_1} \sum_{n=1}^{n_2} \left( C_{\vec{j},m,n} |\mu_m\rangle \langle \nu_n| + C_{-\vec{j},m,n} |\nu_n\rangle \langle \mu_m| \right) T_{\vec{j}} \sum_{\vec{l}} |\vec{l}\rangle \langle \vec{l}| \\
&= \Omega \sum_{\vec{j}} \sum_{m=1}^{n_1} \sum_{n=1}^{n_2} \left( C_{\vec{j},m,n} |\mu_m\rangle \langle \nu_n| + C_{-\vec{j},m,n} |\nu_n\rangle \langle \mu_m| \right) T_{\vec{j}} \int_{\mathcal{B}} \frac{d^d k}{(2\pi)^d} |\vec{k}\rangle \langle \vec{k}| \\
&= \Omega \int_{\mathcal{B}} \frac{d^d k}{(2\pi)^d} \sum_{\vec{j}} \sum_{m=1}^{n_1} \sum_{n=1}^{n_2} \left( C_{\vec{j},m,n} |\mu_m\rangle \langle \nu_n| + C_{-\vec{j},m,n} |\nu_n\rangle \langle \mu_m| \right) e^{i\vec{k}\cdot\vec{j}} |\vec{k}\rangle \langle \vec{k}| \\
&= \Omega \int_{\mathcal{B}} \frac{d^d k}{(2\pi)^d} \sum_{m=1}^{n_1} \sum_{n=1}^{n_2} \left[ \left( \sum_{\vec{j}} C_{\vec{j},m,n} e^{i\vec{k}\cdot\vec{j}} \right) |\mu_m\rangle \langle \nu_n| \right. \\
&\quad \left. + \left( \sum_{\vec{j}} C_{\vec{j},m,n} e^{i\vec{k}\cdot\vec{j}} \right)^* |\nu_n\rangle \langle \mu_m| \right] |\vec{k}\rangle \langle \vec{k}| = \\
&= \Omega \int_{\mathcal{B}} \frac{d^d k}{(2\pi)^d} \sum_{m=1}^{n_1} \sum_{n=1}^{n_2} \left[ \tilde{C}_{-\vec{k},m,n} |\mu_m\rangle \langle \nu_n| + \left( \tilde{C}_{-\vec{k},m,n} \right)^* |\nu_n\rangle \langle \mu_m| \right] |\vec{k}\rangle \langle \vec{k}|,
\end{aligned} \tag{C.16}$$

where again

$$\tilde{C}_{-\vec{k},m,n} = \left( \sum_{\vec{j}} C_{\vec{j},m,n} e^{i\vec{k}\cdot\vec{j}} \right) \tag{C.17}$$

is, for every  $\vec{k} \in \mathcal{B}$ , a rectangular  $n_1 \times n_2$  matrix. Calling now

$$\hat{M}_{\vec{k}} = \sum_{m=1}^{n_1} \sum_{n=1}^{n_2} \left[ \tilde{C}_{-\vec{k},m,n} |\mu_m\rangle \langle \nu_n| + \text{h.c.} \right], \tag{C.18}$$

we can represent it as a matrix in the basis  $\{ |\mu_1\rangle, \dots, |\mu_{n_1}\rangle, |\nu_1\rangle, \dots, |\nu_{n_2}\rangle \}$ , which yields

$$M_{\vec{k}} = \left( \begin{array}{c|c} 0 & \tilde{C}_{-\vec{k}} \\ \hline \tilde{C}_{-\vec{k}}^\dagger & 0 \end{array} \right). \tag{C.19}$$

Due to this particular block structure,

$$\text{Rank} \{ M_{\vec{k}} \} = \text{Rank} \{ \tilde{C}_{-\vec{k}} \} + \text{Rank} \{ \tilde{C}_{-\vec{k}}^\dagger \}. \tag{C.20}$$

Furthermore, the rank of a rectangular matrix is never greater than its shortest side. In this case,

$$\text{Rank} \{ \tilde{C}_{-\vec{k}} \} \leq \min \{ n_1, n_2 \}, \tag{C.21}$$

which in turn implies that the rank of the square matrix  $M_{\vec{k}}$  is  $\leq 2 \min \{ n_1, n_2 \}$ . This means that the size of the kernel of  $M_{\vec{k}}$  has a lower bound

$$\begin{aligned} \dim (\text{Ker } M_{\vec{k}}) &= B - \text{Rank} \{ M_{\vec{k}} \} \geq \\ &\geq (n_1 + n_2) - 2 \min \{ n_1, n_2 \} = \\ &= \max \{ n_1, n_2 \} - \min \{ n_1, n_2 \} = \\ &= |n_1 - n_2|. \end{aligned} \tag{C.22}$$

Hence, if  $|n_1 - n_2| \geq 1$  then for every  $\vec{k}$  one can find a kernel vector  $|v_{\vec{k}}\rangle$  in the basis such that  $\hat{M}_{\vec{k}} |v_{\vec{k}}\rangle = 0$ . Correspondingly,  $\hat{H}_{\mathcal{H}_1} |\vec{k}\rangle \otimes |v_{\vec{k}}\rangle = 0 \forall \vec{k}$  and the set of all these states forms a zero-energy flat band. Clearly, if  $|n_1 - n_2| > 1$  then more than one choice of  $|v\rangle_{|\vec{k}\rangle}$  can be made per quasi-momentum  $\vec{k}$ , each identifying an independent flat band. Hence, calling the number of flat bands in the model  $n_{\text{flat}}$ , consistently with the main text notation,

$$n_{\text{flat}} = \dim (\text{Ker } M_{\vec{k}}) \geq |n_1 - n_2|, \tag{C.23}$$

which proves the bound.

The general rules for filling the matrix elements of  $\tilde{C}_{\vec{k}}$  are the following:

- Choose  $n$ -th column  $1 \leq n \leq n_2$ .
- Consider the *two* possible ways in which a particle can hop from the intermediate state  $|\nu_n\rangle$  within the basis to its neighbors  $|\mu_m\rangle$  and  $|\mu_p\rangle$ .
- Add  $e^{i\vec{k}\cdot\vec{j}_n}$  to  $C_{-\vec{k},m,n}$  and  $e^{i\vec{k}\cdot\vec{j}_p}$  to  $C_{\vec{k},p,n}$ , where  $\vec{j}_{m/p}$  are the lattice vectors pointing to the *arrival* lattice sites.

In the next sections we work out some examples among the ones displayed in the main text. For simplicity, we set  $\Omega = 1$ .

### C.1.1 Example: the triangular lattice

The triangular lattice is a two-dimensional Bravais lattice with primitive lattice vectors

$$\vec{a}_1 = a (1, 0)^\top \quad \text{and} \quad \vec{a}_2 = a \left( \cos \frac{\pi}{3}, \sin \frac{\pi}{3} \right)^\top, \tag{C.24}$$

with  $a$  the real-space lattice spacing. In the Hilbert space, we have again a triangular structure where a new site is added on each link.

It is not difficult to see that this reduces to a pure triangular lattice by choosing a basis of 4 sites, a single one-excitation one ( $n_1 = 1$ ) and 3 pair ones ( $n_2 = 3$ ). The primitive lattice vectors will be the same as above, where we fix for simplicity  $a = 1$ . The basis states can be chosen according to:

$|\mu_1\rangle$  : a one-excitation site at  $\vec{b} = 0$ .

$|\nu_1\rangle$  : a pair site at  $\vec{b} = \vec{a}_1/2$ .

$|\nu_2\rangle$  : a pair site at  $\vec{b} = \vec{a}_2/2$ .

$|\nu_3\rangle$  : a pair site at  $\vec{b} = (\vec{a}_1 - \vec{a}_2)/2$ .

The matrix  $\tilde{C}_{-\vec{k}}$  is now a  $1 \times 3$  matrix whose elements can be computed via the procedure outlined above:

$\tilde{C}_{-\vec{k},1,1}$  : from basis state  $|\nu_1\rangle$  one can reach state  $|\mu_1\rangle$  within the same Bravais lattice site ( $\Rightarrow +1$ ) or state  $|\mu_1\rangle$  at the neighboring site  $\vec{j} = \vec{a}_1$  ( $\Rightarrow +e^{i\vec{k}\cdot\vec{a}_1}$ ).

$\tilde{C}_{-\vec{k},1,2}$  : from basis state  $|\nu_2\rangle$  one can reach state  $|\mu_1\rangle$  within the same site ( $\Rightarrow +1$ ) or state  $|\mu_1\rangle$  at the neighboring site  $\vec{j} = \vec{a}_2$  ( $\Rightarrow +e^{i\vec{k}\cdot\vec{a}_2}$ ).

$\tilde{C}_{-\vec{k},1,3}$  : from state  $|\nu_3\rangle$  one can reach state  $|\mu_1\rangle$  within the same site ( $\Rightarrow +1$ ) or state  $|\mu_1\rangle$  at the neighboring site  $\vec{j} = \vec{a}_1 - \vec{a}_2$  ( $\Rightarrow +e^{i\vec{k}\cdot(\vec{a}_1 - \vec{a}_2)}$ ).

Collecting all terms, the matrix  $\tilde{C}_{-\vec{k}}$  reads

$$\tilde{C}_{-\vec{k}} = \left( 1 + e^{i\vec{k}\cdot\vec{a}_1}, \quad 1 + e^{i\vec{k}\cdot\vec{a}_2}, \quad 1 + e^{i\vec{k}\cdot(\vec{a}_1 - \vec{a}_2)} \right) \equiv \vec{w}_{\vec{k}}^\dagger \quad (\text{C.25})$$

and is equivalent to a three-dimensional vector  $\vec{w}_{\vec{k}}$ . Thus, the total matrix  $M_{\vec{k}}$  can be expressed as

$$M_{\vec{k}} = \left( \begin{array}{c|c} 0 & \vec{w}_{\vec{k}}^\dagger \\ \hline \vec{w}_{\vec{k}} & 0 \end{array} \right). \quad (\text{C.26})$$

There are two kernel states corresponding to four-dimensional vectors  $(0, \vec{v}_{\vec{k},1})$  and  $(0, \vec{v}_{\vec{k},2})$  with

$$\vec{w}_{\vec{k}}^\dagger \cdot \vec{v}_{\vec{k},1/2} = 0. \quad (\text{C.27})$$

These states thus reconstruct two flat bands, in line with the bound  $n_{\text{flat}} \geq 2$  of this case.

The remaining two bands can be calculated instead by squaring  $M_{\vec{k}}$ :

$$M_{\vec{k}}^2 = \left( \begin{array}{c|c} \vec{w}_{\vec{k}}^\dagger \cdot \vec{w}_{\vec{k}} & 0 \\ \hline 0 & \vec{w}_{\vec{k}} \otimes \vec{w}_{\vec{k}}^\dagger \end{array} \right). \quad (\text{C.28})$$

From the symmetric structure of the spectrum and the presence of two flat bands, we can simply infer the non-zero ones as (see Fig. 5.2 in the main text)

$$\begin{aligned}
\pm\sqrt{\vec{w}_k^\dagger \cdot \vec{w}_k} &= \pm\sqrt{\left|1 + e^{i\vec{k}\cdot\vec{a}_1}\right|^2 + \left|1 + e^{i\vec{k}\cdot\vec{a}_2}\right|^2 + \left|1 + e^{i\vec{k}\cdot(\vec{a}_1-\vec{a}_2)}\right|^2} \\
&= \pm\sqrt{2}\sqrt{3 + \cos(\vec{k}\cdot\vec{a}_1) + \cos(\vec{k}\cdot\vec{a}_2) + \cos(\vec{k}\cdot(\vec{a}_1-\vec{a}_2))}.
\end{aligned} \tag{C.29}$$

Choosing the reciprocal lattice vectors as

$$\vec{a}_1^* = \frac{4\pi}{\sqrt{3}} \left( \cos \frac{\pi}{6}, -\sin \frac{\pi}{6} \right)^\top \quad \text{and} \quad \vec{a}_2^* = \frac{4\pi}{\sqrt{3}} (0, 1)^\top \tag{C.30}$$

the first Brillouin zone  $\mathcal{B}$  is an hexagon in  $\vec{k}$  space identified by the conditions

$$\begin{aligned}
&\left( \left| \vec{k} \cdot \vec{a}_1^* \right| \leq \frac{1}{2} |\vec{a}_1^*|^2 \right) \cap \left( \left| \vec{k} \cdot \vec{a}_2^* \right| \leq \frac{1}{2} |\vec{a}_2^*|^2 \right) \cap \\
&\quad \cap \left( \left| \vec{k} \cdot (\vec{a}_1^* - \vec{a}_2^*) \right| \leq \frac{1}{2} |(\vec{a}_1^* - \vec{a}_2^*)|^2 \right).
\end{aligned} \tag{C.31}$$

### C.1.2 Example: the honeycomb lattice

The honeycomb lattice is a triangular Bravais lattice with primitive lattice vectors

$$\vec{a}_1 = a (1, 0)^\top \quad \text{and} \quad \vec{a}_2 = a \left( \cos \frac{\pi}{3}, \sin \frac{\pi}{3} \right)^\top, \tag{C.32}$$

where the lattice spacing  $a$  is  $\sqrt{3}$  times the edge of the hexagons, plus a basis of two vectors

$$\vec{b}_1 = 0 \quad \text{and} \quad \vec{b}_2 = \frac{2\vec{a}_2 - \vec{a}_1}{3}. \tag{C.33}$$

In the synthetic lattice, this gives rise to a structure with a basis of 5 elements: 2 one-excitation sites ( $n_1 = 2$ ) and 3 pair ones ( $n_2 = 3$ ), which we choose as follows:

$|\mu_1\rangle$  : a one-excitation site at  $\vec{b} = 0$ .

$|\mu_2\rangle$  : a one-excitation site at  $\vec{b} = \frac{2\vec{a}_2 - \vec{a}_1}{3}$ .

$|\nu_1\rangle$  : a pair site at  $\vec{b} = \frac{2\vec{a}_2 - \vec{a}_1}{6}$ .

$|\nu_2\rangle$  : a pair site at  $\vec{b} = \frac{2\vec{a}_1 - \vec{a}_2}{6}$ .

$|\nu_3\rangle$  : a pair site at  $\vec{b} = -\frac{\vec{a}_1 + \vec{a}_2}{6}$ .

We thus see that the  $\tilde{C}_{-\vec{k}}$  are  $2 \times 3$  matrices and that there is at least one flat zero-energy band. The matrix elements can be identified column by column as follows:

$|\nu_1\rangle$  : From  $|\nu_1\rangle$  one can jump to  $|\mu_1\rangle$  or to  $|\mu_2\rangle$  remaining in the same Bravais lattice site.

$|\nu_2\rangle$  : From  $|\nu_2\rangle$  one can jump to  $|\mu_1\rangle$  in the same site or to  $|\mu_2\rangle$  changing site by  $\vec{j} = \vec{a}_1 - \vec{a}_2$  ( $\Rightarrow e^{i\vec{k}\cdot(\vec{a}_1 - \vec{a}_2)}$ ).

$|\nu_3\rangle$  : From  $|\nu_3\rangle$  one can jump to  $|\mu_1\rangle$  in the same site or to  $|\mu_2\rangle$  changing site by  $\vec{j} = -\vec{a}_2$  ( $\Rightarrow e^{-i\vec{k}\cdot\vec{a}_2}$ ).

Hence,

$$\tilde{C}_{-\vec{k}} = \begin{pmatrix} 1 & 1 & 1 \\ 1 & e^{i\vec{k}\cdot(\vec{a}_1 - \vec{a}_2)} & e^{-i\vec{k}\cdot\vec{a}_2} \end{pmatrix} \equiv \begin{pmatrix} \vec{w}_{\vec{k},1}^\dagger \\ \vec{w}_{\vec{k},2}^\dagger \end{pmatrix}, \quad (\text{C.34})$$

with  $\vec{w}_{\vec{k},1/2}$  three-dimensional vectors. The matrix  $M_{\vec{k}}$  is thus

$$M_{\vec{k}} = \left( \begin{array}{cc|c} 0 & 0 & \vec{w}_{\vec{k},1}^\dagger \\ 0 & 0 & \vec{w}_{\vec{k},2}^\dagger \\ \hline \vec{w}_{\vec{k},1} & \vec{w}_{\vec{k},2} & 0 \end{array} \right). \quad (\text{C.35})$$

The kernel state is a five-dimensional vector  $(0, 0, \vec{v}_{\vec{k}})$  which satisfies  $\vec{w}_{\vec{k},1/2}^\dagger \cdot \vec{v}_{\vec{k}} = 0$ . To identify the remaining non-zero bands, we again take the square of the total matrix  $M_{\vec{k}}$ :

$$M_{\vec{k}}^2 = \left( \begin{array}{cc|c} \vec{w}_{\vec{k},1}^\dagger \cdot \vec{w}_{\vec{k},1} & \vec{w}_{\vec{k},1}^\dagger \cdot \vec{w}_{\vec{k},2} & 0 \\ \vec{w}_{\vec{k},2}^\dagger \cdot \vec{w}_{\vec{k},1} & \vec{w}_{\vec{k},2}^\dagger \cdot \vec{w}_{\vec{k},2} & 0 \\ \hline 0 & 0 & \vec{w}_{\vec{k},1} \otimes \vec{w}_{\vec{k},1}^\dagger + \vec{w}_{\vec{k},2} \otimes \vec{w}_{\vec{k},2}^\dagger \end{array} \right), \quad (\text{C.36})$$

where the first block is  $2 \times 2$  and the second one  $3 \times 3$ . We can now diagonalize the first block to find

$$\lambda_{\vec{k},\pm} = \frac{1}{2} \left[ \left( |\vec{w}_{\vec{k},1}|^2 + |\vec{w}_{\vec{k},2}|^2 \right) \pm \sqrt{\left( |\vec{w}_{\vec{k},1}|^2 - |\vec{w}_{\vec{k},2}|^2 \right)^2 + 4 \left| \vec{w}_{\vec{k},2}^\dagger \cdot \vec{w}_{\vec{k},1} \right|^2} \right], \quad (\text{C.37})$$

with  $\lambda_{\vec{k},\pm} \geq 0$ . The four non-trivial bands will thus correspond to  $\pm\sqrt{\lambda_{\vec{k},+}}$  and  $\pm\sqrt{\lambda_{\vec{k},-}}$ . Working out the scalar products

$$\left| \vec{w}_{\vec{k},1} \right|^2 = \left| \vec{w}_{\vec{k},2} \right|^2 = 3 \quad (\text{C.38})$$

and

$$\left| \vec{w}_{\vec{k},2}^\dagger \cdot \vec{w}_{\vec{k},1} \right| = \left| 1 + e^{i\vec{k}\cdot(\vec{a}_1 - \vec{a}_2)} + e^{-i\vec{k}\cdot\vec{a}_2} \right| \quad (\text{C.39})$$

we obtain by substitution

$$\begin{aligned}\lambda_{\vec{k},\pm} &= 3 \pm \left| 1 + e^{i\vec{k}\cdot(\vec{a}_1-\vec{a}_2)} + e^{-i\vec{k}\cdot\vec{a}_2} \right| \\ &= 3 \pm \sqrt{3 + 2 \cos(\vec{k}\cdot(\vec{a}_1 - \vec{a}_2)) + 2 \cos(\vec{k}\cdot\vec{a}_2) + 2 \cos(\vec{k}\cdot\vec{a}_1)}.\end{aligned}\quad (\text{C.40})$$

From the first equality we see that the second addend is always  $\leq 3$ . It is 3 only when  $\vec{k} = 0$  (up to reciprocal lattice translations  $\vec{G}$ , see (C.4)). Hence,  $\lambda_-(\vec{k} = 0) = 0$  is a minimum and  $\lambda_+(\vec{k} = 0) = 6$  is a maximum. The bands  $\pm\sqrt{\lambda_{\vec{k},-}}$  touch at  $\vec{k} = 0$  with linear dispersion. Second, the argument of the absolute value will vanish when

$$\vec{k}\cdot(\vec{a}_1 - \vec{a}_2) = \pm\frac{2\pi}{3} + 2\pi n, \quad -\vec{k}\cdot\vec{a}_2 = \pm\frac{4\pi}{3} + 2\pi m \quad (\text{C.41})$$

where the signs must be chosen consistently. Up to reciprocal lattice translations, one can choose

$$\vec{k} = \pm\frac{1}{3}(\vec{a}_2^* - \vec{a}_1^*), \quad (\text{C.42})$$

identifying the points at the vertices of the hexagonal first Brillouin zone (one can verify these points lie at the boundary of two of the conditions in (C.31)). Therefore, the two upper bands  $\sqrt{\lambda_{\vec{k},+}}$  and  $\sqrt{\lambda_{\vec{k},-}}$  touch at the vertices of the first Brillouin zone with linear dispersion and similarly do the lower bands  $-\sqrt{\lambda_{\vec{k},+}}$  and  $-\sqrt{\lambda_{\vec{k},-}}$ .

# Acknowledgements

First and foremost, I would like to thank my supervisor Professor Igor Lesanovsky. Many discussions and detailed answers to my questions helped me throughout my PhD and enabled me to complete this thesis.

Secondly, I want to thank Professor Juan P. Garrahan for his invaluable input and in general for his help.

Furthermore, I would like to thank Dr. Stephen Powell for being my internal examiner as well as Dr. Stephen Clark for being my external examiner.

I would like to thank Matteo Marcuzzi for his support and help with my research. Without his help it would not have been possible to complete this work. Thanks to Jiří Minář for his help especially at the start of my PhD.

Thanks to Katarzyna Macieszczak for insightful discussions.

Special thanks to all of my parents for their moral and financial support.

Many thanks to Matt Jessop, Jemma Needham, Dominic Rose, Neil Wilkins, Joe Wilkinson and Ellie Frampton for proofreading my thesis and for being great friends.